Surface Science and Catalysis Studies of the Structure and Reactivity of Model Catalysts

Elodie Fourré

Thesis submitted for PhD degree

Cardiff University, 2006

ProQuest LLC
789 East Eisenhower Parkway
P.O. Box 1346
Ann Arbor, MI 48106-1346

Form: PG/R/06/09

CARDIFF UNIVERSITY
PRIFYSGOL CAERDYDD

APPENDIX 1:
Specimen Layout for Thesis Summary and Declaration/Statements page to be included in a Thesis

DECLARATION

This work has not previously been accepted in substance for any degree and is not concurrently submitted in candidature for any degree.

Signed ..... (candidate) Date ...03/11/2006...

STATEMENT 1

This thesis is being submitted in partial fulfillment of the requirements for the degree of .....PhD.....(insert MCh, MD, MPhil, PhD etc, as appropriate)

Signed ..... (candidate) Date .....03/11/2006...

STATEMENT 2

This thesis is the result of my own independent work/investigation, except where otherwise stated.
Other sources are acknowledged by explicit references.

Signed ..... (candidate) Date ....03/11/2006...

STATEMENT 3

I hereby give consent for my thesis, if accepted, to be available for photocopying and for inter-library loan, and for the title and summary to be made available to outside organisations.

Signed ..... (candidate) Date .....03/11/2006.

STATEMENT 4 - BAR ON ACCESS APPROVED

I hereby give consent for my thesis, if accepted, to be available for photocopying and for inter-library loans **after expiry of a bar on access** approved by the Graduate Development Committee.

Signed ..... (candidate) Date .....03/11/2006 .

A ma Mère, à mon Père
et à mes Sœurs,

Acknowledgments

First, I would like to thank Professor Mike Bowker for giving me the opportunity to realise this work; his help, his trust and encouragement during all those years. I also thank the University of Reading and the University of Cardiff for their financial support.

I associate, in those acknowledgments, my work colleagues, in particular Rupert Smith who taught me the use of the equipment and helped me afterwards to resolves the various problems encountered; Federico for his precious help in my work and also for his patience, care and love that made my everyday life less complicated! Chris, Matt P and Monica with who I shared many conversations about work and also great moments of fun in the post grad centre and local pubs. I thank the workshop guys, especially Alun, who repaired some UHV pieces essential to my work.

A thank to my friends Cristina and Faye, for their loving and caring during the time of my PhD and also after, resulting in a strong friendship that will last forever.

On the family side, I give a special thank to my mother for her care and love. I add to this a big reward for her patience through the endless (cheerful or pessimistic) phone conversation about myself and my work and who has been always here to help me to go through life. A big thank also to my father for the same (but more discreet) support. A sisterly thank to Clémence and Amélie for their care and encouragements, Siegfried and Charles also for their support but also their "to nearly died laughing" joke sessions. I also thank my cousin and friend Florence for her encouragements, her aromatherapy sessions, her love and logistic support!

Finally, I will never forget the city of Cardiff, its numerous shopping sessions which left my bank account desperately slim and me so joyful; the trips to the sea side, the hiking in the Wales valley that helped to release the pressure.

A thank to Tesco and Sainsburys superstores for their everlasting supply of Lindt chocolate, double chocolate cookies and decadent chocolate puddings!

Many high barriers exist in this world - barriers between nations, races and creeds. Unfortunately, some barriers are thick and strong. But I hope, with determination, we will find a way to tunnel through these barriers easily and freely, to bring the world together...

L. Esaki

Si je considère rétrospectivement le long chemin qui a été le mien et celui de tant de collègues de mon âge ou de jeunes qui nos ont rejoints, je crois pouvoir affirmer que les facteurs essentiels de la réussite et de la satisfaction personnelle dans la recherche scientifique ne dépendent pas du degré d'intelligence ni de la capacité à exécuter et à accomplir avec précision la tâche que l'on s'est donné. Ce qui compte avant tout, dans un cas comme dans l'autre, c'est le dévouement total et la capacité de fermer les yeux devant les difficultés : C'est ainsi que nous pouvons affronter des problèmes que d'autres, plus critique et plus perspicaces, ne s'aviseraient pas d'affronter.

Rita Levi-Montalcini, *Prix Nobel de Médecine*

If I consider retrospectively the long way that was mine and the one of so many colleagues of my age or young people that joined us, I think I can affirm that the essential factors for success and personal satisfaction in the scientific research does not depend on the intelligence level nor the ability to perform and accomplish, with precision, the task undertaken. What matters before all, in a case or the other, is the complete commitment and the ability to turn a blind eye to difficulties: That is how we can face problems that others, more critical and more perspicacious, would no attempt to face.

Rita Levi-Montalcini, *Nobel price of Medicine*

Abstract

In this thesis, the structure and reactivity of palladium on titania has been studied on high surface area powdered materials and on low surface area models. Mathematical models have been established which relate the particle radius to various parameters such as particle surface area, density of particles, interparticle distance and coverage. The sintering process is studied through STM imaging and particle size distribution (PSD) calculation on two models. The technique resulting in PSD consists in the calculation of the particle density as a function of 4 parameters: perimeter, area, height and volume of the particle. This is done through the analysing of STM images using a build-in-house software. It is found that Cu followed the Ostwald ripening process while Pd followed the coalescence sintering. From the analysis of the Auger spectra, the growth mode of Cu and Pd were found to follow the Volmer –Weber mode consisting of 3D particle growth.

The structure of the Pd/TiO_2 system is investigated via STM and LEED analysis. It is shown that Pd nanoparticles supported TiO_2 reconstructed upon annealing into hexagonal, wagonwheel, star shape and zigzag superstructures. These various structures have unit cell dimensions varying from 9.5Å to 25Å and consist of mixed layer of titanium and palladium in their ground state. The possible structures are modelled and it is concluded that the Ti or Pd adatoms can be situated in atop, 2- or 3-fold sites. TPR results shows that CO uptake capacity is lost when the catalyst is reduced to high temperature. However, the CO oxidation reaction is enhanced. It is shown that encapsulation of Pd by TiO_x species is responsible for the loss of CO adsorption but also for the improvement of the CO oxidation. Weakly bound forms of CO and new active centres, as a result of the reconstruction, can improve the activity of the CO oxidation reaction.

Content

Chapter 1

Introduction

1. Introduction

This thesis focuses on heterogeneous catalysis and surface science. The correlation between the two domains is dictated by the influence of surfaces on catalytic reaction behaviour. The importance of understanding heterogeneous catalysis starts with the understanding of surface activity. Heterogeneous catalysis consists of reaction between two phases, for example liquid-solid or gas-solid. The gas-solid interface is of particular interest because catalyst particles can be deposited on a surface and are the basis of many industrial processes. Reactions take place at the surface. Surface atoms have different properties from the bulk atoms. Surface atoms cannot satisfy their bonding requirements in the same way as the bulk atoms and therefore tend to react with other or neighbouring atoms to become stable. This is where surface studies become important. Understanding the structure and evolution of particles at the surface brings important information on the behaviour of a catalyst and as a result an improvement of the catalyst activity.

In this chapter, a review of catalysis and the importance of surfaces in catalysis is first reported. A summary of surface science and UHV work is presented in the next section with a look at the advantages and disadvantages of such studies. The fourth section summarises the evolution of microscopy through time from optical microscopy to scanning probe microscopy with a highlight on scanning tunnelling microscopy which is the main instrument used during my practical work. This chapter is meant to give a background on microscopy, catalysis and surface science, looking at the kind of information we can get from microscopy studies and how can they be useful to explain catalytic reactions.

2. The importance of surfaces in heterogeneous catalysis

Recently, surface science has developed partly because scientists want to understand surface chemical reactions. The motivation of researchers arises from their desire to bring light on applications where surfaces are taking part, such as heterogeneous catalysis, corrosion, printing or dyeing. Catalysis is probably the major application so far [1]. Every reaction takes place initially on the surface atoms. The imaging of molecular structures at the surface is obviously of great interest in understanding those chemical reactions and this became possible when the Scanning Tunnelling Microscope [2] was invented and applied to imaging surfaces at the atomic scale.

2.1. Outline on catalysis

The term catalysis was first mentioned by Berzelius in 1835, giving, at the same time, an explanation to previous unexplained chemical processes [3]. It became rapidly clear that catalysis could be use to aid many chemical reactions and was also financially advantageous. The First World War was a trigger for the development of catalysis, where the production of many pure chemicals was in large demand, such as the production of explosives based upon nitric acid (Ostwald, oxidation of ammonia to nitric acid [4]). After the First World War, the demand on explosives diminished and catalysis was significantly use for FCC (Fluid catalytic cracking) process [5], allowing later the production of fuel for fighters in the Second World War. In the 1970's the trend of catalytic industry changed towards the petrochemical industry due to the vast development of the automotive market. Nowadays, catalysis is present in everyday life. Many applications involve the process of catalysis such as methanol synthesis [6], petroleum refining and processing, emission control and reduction of NO_x [7], CO and hydrocarbons. It is also involved in nearly every reaction associated with life [1]! A good example is the enzymatic catalysis where the transformation of

molecules occurs thanks to proteins called enzymes [8]. They have specific actions in the body to ease biochemical reactions and act as catalysts (figure 1).

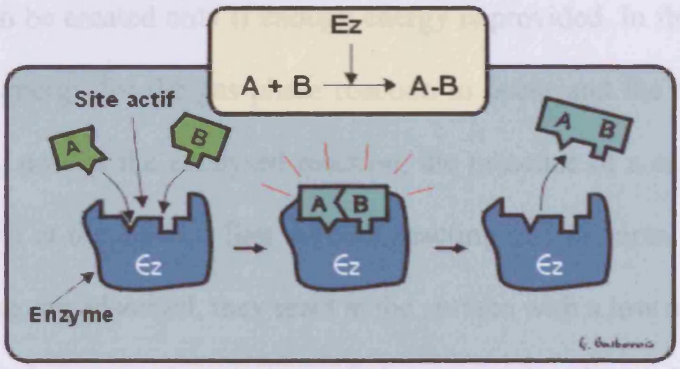

Figure 1: the above enzyme catalyses a chemical reaction where a molecule A is linked to a molecule B to form a molecule AB. One can see that both molecules have an affinity for the active site of the enzyme. They are in the right conditions to bind and form AB. At the end of the reaction, the new molecule AB detached itself from the enzyme which can then redo the same reaction many times.

Catalysis is defined as a process that accelerates a reaction by lowering the energy pathway between the reactants and the products [1]. The reaction involves the creation of intermediates that would not be created in an un-catalysed reaction (figure 2).

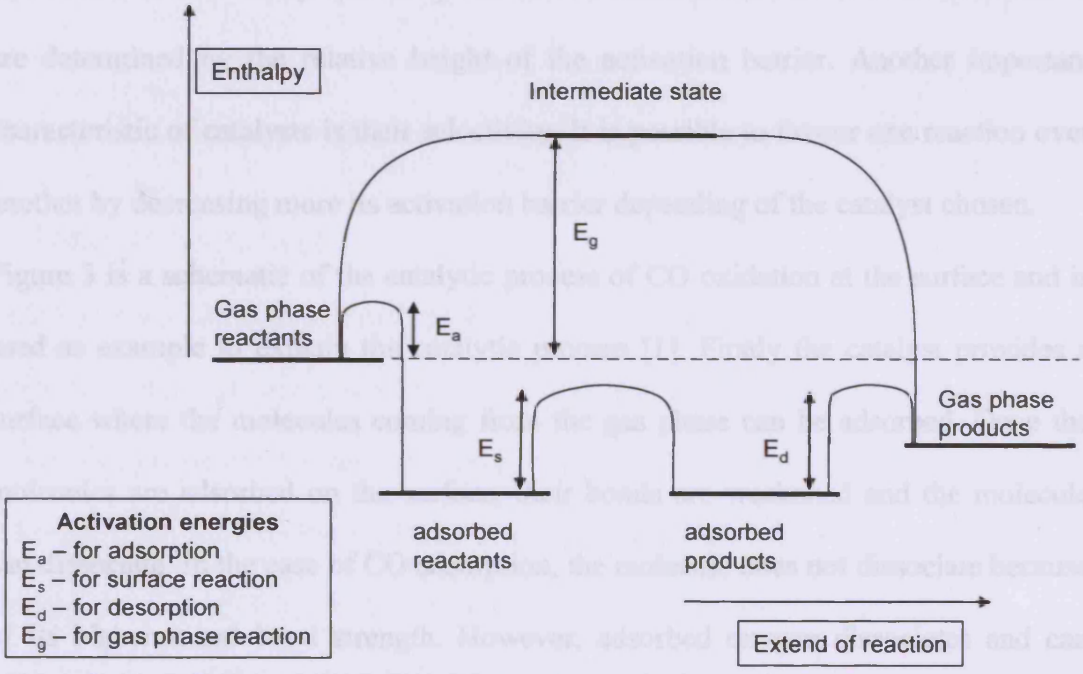

Figure 2: Simplified energetic diagram for a catalysed reaction.

Figure 2 describes the energetics involved in a catalysed and un-catalysed reaction. The un-catalysed reaction involves the creation of intermediate states. These intermediates can be created only if enough energy is provided. In this case there is a large activation energy for the gas phase reaction to occur and the reaction may not happen. Looking now at the catalysed reaction, the presence of a catalyst allows the reactant to adsorb at the surface first without reacting and requires little energy, E_a. Once the reactants are adsorbed, they react at the surface with a low activation energy, E_s compared to the activation energy of the un-catalysed reaction. Finally, the products formed at the surface desorbs into the gas phase with again a small activation energy for desorption, E_d. Those intermediates have much lower activation energy due to the stabilisation induced by the bonding at the surface. Direct un-catalysed reaction produces intermediates that have an unstable configuration in the gas phase. The reaction is accelerated by a catalyst, a chemical that takes part into the reaction without being chemically changed. The catalyst however does not change the equilibrium state; it only speeds up the rate of reaction. The kinetics of the reaction are determined by the relative height of the activation barrier. Another important characteristic of catalysts is their selectivity. It is possible to favour one reaction over another by decreasing more its activation barrier depending of the catalyst chosen.

Figure 3 is a schematic of the catalytic process of CO oxidation at the surface and is used as example to explain the catalytic process [1]. Firstly the catalyst provides a surface where the molecules coming from the gas phase can be adsorbed. Once the molecules are adsorbed on the surface, their bonds are weakened and the molecule can dissociate. In the case of CO adsorption, the molecule does not dissociate because of its high internal bond strength. However, adsorbed oxygen dissociates and can diffuse on the surface. Then, atoms and molecules at the surface react and allow new

products to be created. Those new molecules have weak bond strength with surface and so desorb into the gas phase.

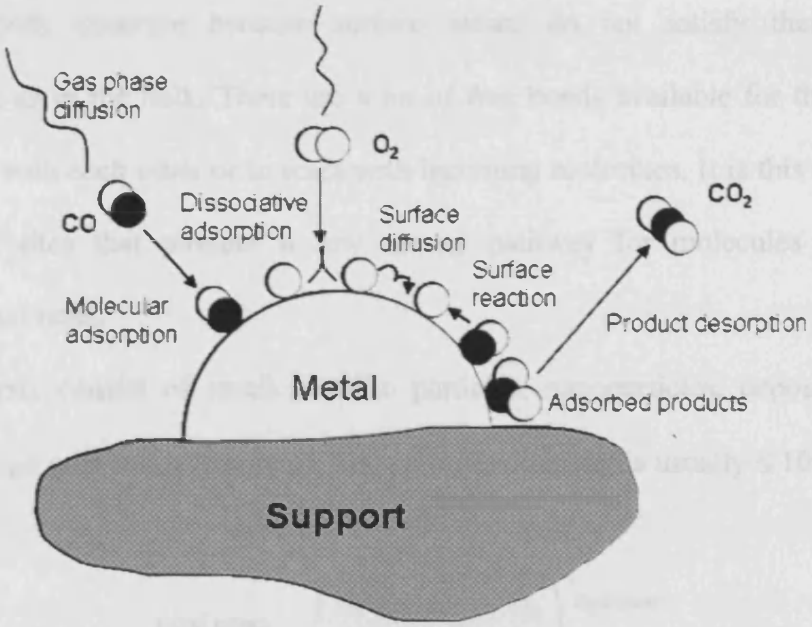

Figure 3: Molecular and atomic behaviour in the catalytic process of CO oxidation.

This succession of steps plays an important role in the limiting of the rate of reaction. In order to improve the efficiency of diverse catalysts it is essential to understand how the molecules and atoms behave at the surface during those different steps. This is where surface science becomes essential providing the right tool to gain such information. One has to understand surfaces in order to explain catalysis.

2.2 Importance of surfaces

Heterogeneous catalysis is involved in many industrial chemical reactions and has a major impact on the world economy [1]. In heterogeneous catalysis, the catalyst often consists of a solid and the reactants are in the gas or liquid phase. The reaction occurs at the interface between these phases. The nature of the surface is then very important for the activity of the catalytic reaction. The surface allows the deposition and immobilisation of the catalytic substance which would be otherwise washed away in the product gas stream or would loose its activity by sintering. It is the place where

the molecules bind, where molecular bonds may be broken and form new ones. The surface structure is on the termination of its bulk structure. However, it is different from the bulk structure because surface atoms do not satisfy their bonding requirement as in the bulk. There are a lot of free bonds available for the atoms to either react with each other or to react with incoming molecules. It is this availability of bonding sites that produce a low energy pathway for molecules to adsorb, dissociate and react.

Most catalysts consist of small metallic particles, nanoparticles, deposited at the surface of high area solids (figure 4). The particles diameter is usually ≤ 10nm.

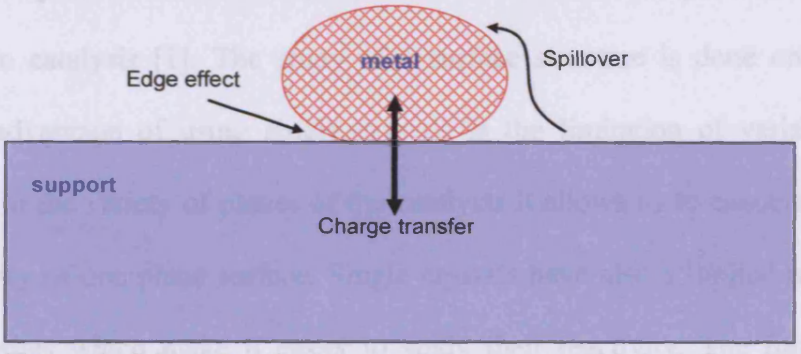

Figure 4: Schematic of a nanoparticle on a surface including the factor influencing its reactivity.

Small metal particles behave much differently from the metal itself because of the splitting of the conduction band into discrete energy levels. This has the effect of changing the surface reactivity and activation energies of the different catalytic steps. Another effect is the charge transfer that can occur between the metallic nanoparticle and the support which will depend on the nature of the metal and the support. Finally, an important site is the edge of the metallic particle where the metal atom is in contact with both the support and the gas phase. Atoms at this site can be affected by the local electronic effect of the support atoms and they will react differently with the gas phase molecules. A last effect is due to the Strong Metal Support Interaction (SMSI)

occurring when metals are in contact with partially reduced metal oxide surfaces [9]. This effect consists of diffusion of reduced support compound onto the metallic particle, influencing greatly its reactivity [10,11].

3. Surface science and Ultra High Vacuum (UHV)

3.1. Surfaces

Metallic and metal oxide surface structures are the most studied because of their application in catalysis. Surface structures are categorised in different classes. The most important ones are the body centred cubic (bcc), hexagonal closed packed (hcp) and in particularly face-centred cubic (fcc) because it concerns many metals and metal oxides used in catalysis [1]. The study of a surface structure is done on a single crystal. The advantage of using single crystals is the limitation of variables. For example, due to the variety of planes of the catalysts it allows us to concentrate only on the reactivity of one plane surface. Single crystals have also a limited number of well defined sites which make it easier to study their reactivity. The fundamental difference between real and model catalysts is the pressure, and thus, the finite residence time of species at the surface [12]. At high pressure, the surface has higher steady state coverage of adsorbed species than at lower pressure. Not only more reactions between adsorbates and oncoming molecules can occur at high pressure but also at high coverage, adsorbate may rearrange in a structure that would differ from the one at low coverages. Thus, reactions can take place that would not happen in UHV conditions. Another reason is if a reaction occurs at an active site with a very small surface density, it may not be possible to detect it by chemisorption techniques used in high pressure environments. However, in low pressure environments, a small fraction of incoming molecules reacting at the surface will be seen. Pressure gap in

the term used to define this inability to reproduce high pressure reaction in UHV conditions. The surface areas of the real and model catalyst differ also considerably. A crystal has an average surface area of less than $1cm^2$ while a real catalyst may vary from 50 to $200m^2/g$. The study of single crystal gives a restricted and optimised approach of heterogeneous catalysis. However, data gained is important in the understanding of some of the phenomenon observed on real catalyst.

Single crystals are grown from a rod of the metal of interest which is then cut and polished. This results in a plane that is assigned according to the Miller indices. Miller indices relate to the position of the atoms in the lattice. The most stables are called low index planes and consist of (110), (100) or (111) planes (figure 5). They have usually a low reactivity and thus dissociative adsorption usually occur at defects on the surface.

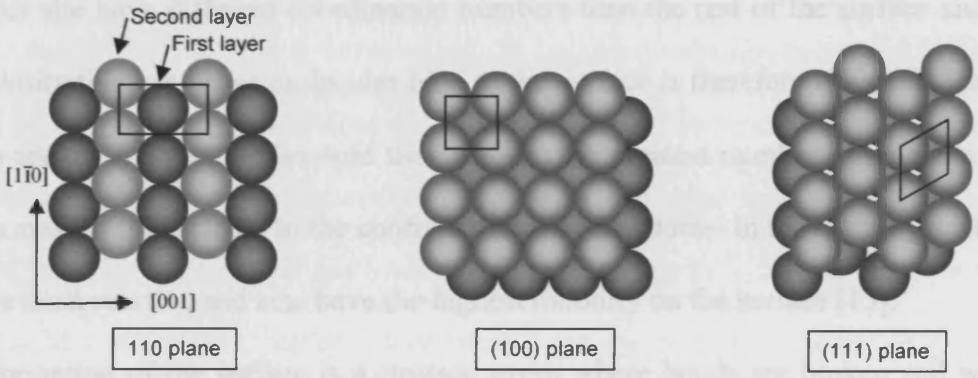

Figure 5: Hard sphere representation of the face centred cubic (fcc) low index planes. The light blue balls are the upper layer while the dark greys represent the lower layer.

As we can see on figure 5, the atoms of the planes possess different coordination number. On the (111) plane, atoms have 9 neighbouring atoms, whereas this number becomes 7 on the (110) plane and 8 on the (100) plane. This difference in coordination, thus, has an influence on the reactivity of the surface. The atoms with

lower coordination number have the highest free energy, so the highest reactivity for adsorption and the strongest binding for the adsorbed atoms.

Another particularity of surfaces is that they have distinct morphologies formed of flat terraces and defects such as steps, kinks and point defects (figure 6).

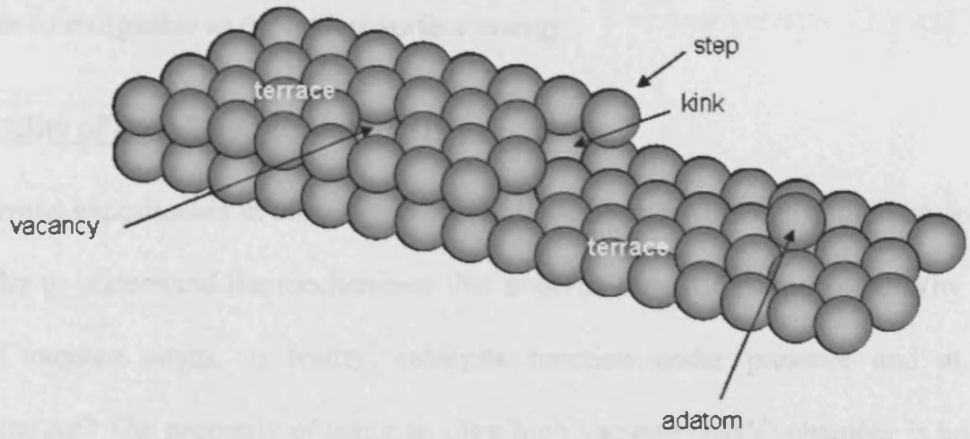

Figure 6: Schematic of atomic surface with terraces and different defects.

These defects can play an important role in the reactivity of the surface. The atoms at a defect site have different coordination numbers than the rest of the surface and the probability that gas phase molecules bind to the surface is therefore changed. Terrace atoms are the most stable because they possess the greatest number of neighbouring atoms making them closer to the configuration of bulk atoms. In the contrary adatoms are the most reactive and also have the highest mobility on the surface [13].

The formation of the surface is a stressed event where bonds are broken and which leaves the surface with a high energy. The natural tendency is a change of the atom position in order to minimise this energy. There are different ways in which atoms can accommodate. Relaxation is one of them. This consists of a movement of the atoms towards the bulk atoms. This increases the coordination of the surface atoms and reduces the bond length as well as the free energy. Sometimes surface relaxation is not enough to stabilise the surface. To minimize the surface energy, atoms reorganise

themselves into another structure that differs from the bulk one. The process is called reconstruction. Reconstruction of the surface can also be induced by adsorbed molecules. This corresponds in fact to the first step of catalytic process described in the previous section. Molecules adsorb at the surface forcing the metallic or oxide surface to reorganise to the lowest surface energy.

3.2. Utility of Ultra High Vacuum (UHV)

Numerous experiments in ultra high vacuum have been carried out in the last decades in order to understand the mechanisms that underlie catalytic phenomena. Why work under vacuum when, in reality, catalysts function under pressure and at high temperature? The necessity of using an ultra high vacuum (UHV) chamber is because of its ability to keep the surface of the crystal to analyse clean for a certain period of time. In an UHV system, the pressure is kept constant between 10^{-9} and 10^{-11} mbar. Under such pressures, the mean free path of the molecules is extremely high (order of 10^7 m) and, as a consequence, we need only to consider collisions between a molecule and a surface rather than between two molecules [14]. The average distance that a particle (atom, electron and molecule) travels in the gas phase between collisions can be determined from a simple hard-sphere collision model [15]. This quantity, known as mean free path of the particle, is denoted λ and for neutral molecules is given by the equation [14]:

$$\lambda = \frac{1}{n\sqrt{2\pi d^2}}$$

Where n is the number density, d the diameter of the molecule and the term πd^2 represents the collision cross section.

Taking $d = 3.7 \times 10^{-10} m$ for the N_2 molecule and substituting n from $p = nkT$, then:

$$\lambda = \frac{1}{\sqrt{2\pi d^2}} / \frac{p}{kT}$$

Where P is the pressure in the chamber (mbar), T the temperature (K) and k the Boltzmann constant ($1.38 \times 10^{-23} J.K^{-1}$).

$$\lambda = \frac{6.6 \times 10^{-3}}{p}$$

With sufficient accuracy, the following approximation is made:

$$\lambda = \frac{7 \times 10^{-3}}{P}$$

As one might expect, λ increases when the P decreases (and hence the number density of molecules).

The impingement rate (or flux) of molecules is given by:

$$J = \frac{P}{\sqrt{2\pi mkT}}$$

Where J is in $cm^{-2}.s^{-1}$, P the pressure in mbar and m is the mass of a molecule in kg.

Or $$N_A \times k = R$$

and $$N_A \times m = M$$

Where R is the universal gas constant of value 8.314 $J.mole^{-1}.K^{-1}$, N_A is the Avogadro constant (6.02×10^{23} molecules), M is the mass of 1 mole in kg and m is the mass of a molecule in kg. So,

$$J = \frac{PN_A}{\sqrt{2\pi MRT}}$$

Taking the example of nitrogen: M=0.028kg at 295K, then

$$J = 2.9 \times 10^{22} \times P$$

Where J is in $m^{-2}.s^{-1}$ and P in Pa

$$J = 2.9 \times 10^{20} \times P$$

Where J is in $cm^{-2}.s^{-1}$ and P in mbar

Again, with sufficient accuracy, the following approximation is made:

$$J = 3 \times 10^{20} \times P$$

Thus, under a pressure of 10^{-10}mbar, $J = 3 \times 10^{10} cm^{-2}.s^{-1}$

Considering that a monolayer contains 10^{15} atoms per cm^2 then the rate of formation for a monolayer is:

$$\frac{J}{10^{15}} = \frac{3 \times 10^{10}}{10^{15}} = 0.00003 ML.s^{-1}$$

Thus, the time t needed for one monolayer of gas molecules to form is:

$$t = \frac{1}{0.00003} = 33333.33s = 9h15\min$$

Following the same logic, under atmospheric condition, surfaces are covered with contamination in an order of 4×10^{-9} seconds. To minimise the contamination of the surface, the achievement of an ultra high vacuum pressure is necessary, thus allowing the study of its structure and reactivity.

The range of application of Ultra High Vacuum technology is quite wide. Many techniques of analysis such as Field Electron and Field Ion Microscopy, Scanning Tunnelling Microscopy, Electron Diffraction, Auger Electron Spectroscopy, and Photoelectron Spectroscopy work under ultra high vacuum and provide good measurements.

4. Microscopy from macroscopic to nanoscopic scale

It has always been in human nature to look from immensely large to incredibly small natural phenomena. From the concept "seeing is believing", the emergence of

microscopy allowed the exploration from the macroscopic to the nanoscopic (10^{-9}m) scale and the reinforcement of this concept. All those methods brought light and understanding in many research fields like chemistry, biology or biochemistry.

4.1. Optical microscopy

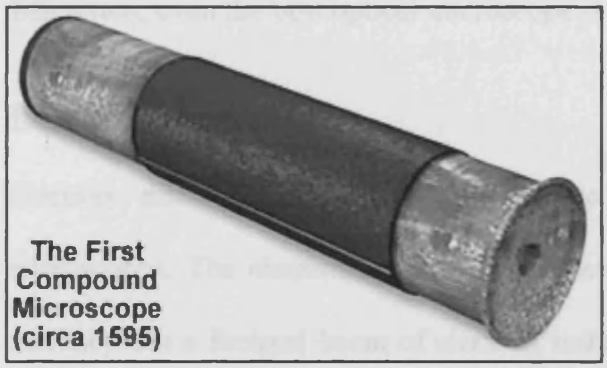

Image 1: Compound microscope taken from [16] with permission.

Most likely discovered around 1595 by Hans Janssen in Holland, the first optical microscope consisted of three brass sliding tubes with lenses inserted into the ends of the flanking tubes (image 1). The microscope could magnify images up to 10 times when completely extended [16].

In 1667, Robert Hooke published Micrographia [17], presenting experiments realised with a compound microscope (figure 7). With his microscope, he managed to visualise plant cells, a feature that had not been seen before. Modern microscopes of this kind are more complex, with multiple lens components in both objective and ocular assemblies. These multi-component lenses are designed to reduce aberrations. Chromatic and spherical aberrations were corrected in the 1730's through the work of Chester Hall. Optical microscopes are restricted in their ability to resolve features by a phenomenon called diffraction, which, based on the numerical aperture (NA) of the optical system and the

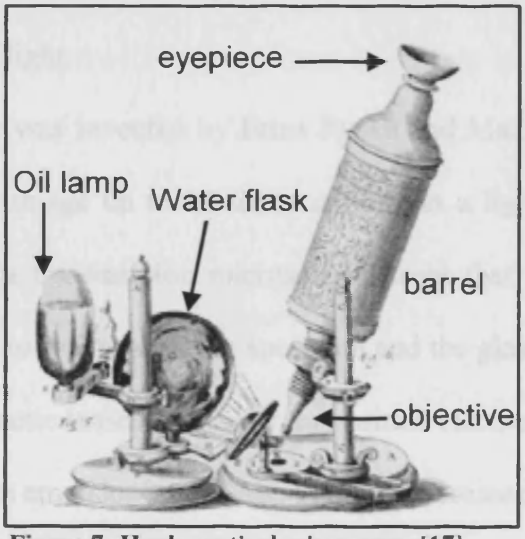

Figure 7: Hooke optical microscope [17].

wavelengths of light used (λ), sets a definite limit (d) to the optical resolution. Assuming that the optical aberrations are negligible, the resolution (d) I given by:

$$d = \frac{\lambda}{NA}$$

Assuming a λ of 400nm with the highest practical NA is 1.5 (oil as a medium), due to diffraction, even the best optical microscope is limited to a resolution of 0.2μm [18].

4.2. Electron microscopes

Electron microscopes were developed to overcome the limitation of light microscopes. The electron microscopes function exactly as the optical ones except that they use a focused beam of electron instead of light to image the specimen and gain information on its structure and composition. Electrons can behave in a wave-motion like light does (De Broglie, 1924) and have a wavelength much smaller than the one of light. By using a beam of electron instead of a light beam, it is possible to view objects smaller than the wavelength of light.

The first Transmission electron microscope was invented by Ernst Ruska and Maxx Knoll [19] in Germany in 1931 and could image up to 10 times more than a light microscope. TEM is very similar to a light transmission microscope except that a focused beam of electrons replaces the light to see through the specimen and the glass lenses are replaced by electrostatic and magnetic lenses [20] . The transmitted electron beam is then deflected to a photographic film emulsion or projected onto a fluorescent screen, generating an image at high magnification. With the progress of technology, today's TEM achieve a resolution of 0.2nm. However, the TEM has some limitations. The need to prepare very thin sample limit the examination of surfaces in 3 dimensions.

Max Knoll developed the first SEM in 1942. The electron beam which typically has an energy ranging from a few hundred eV to 50 keV, is focused by one or two condenser lenses into a beam with a very fine focal spot sized 1nm to 5nm [20]. The beam passes through pairs of scanning coils in the objective lens, which deflect the beam over a rectangular area of the sample surface. As the primary electrons strike the surface they are inelastically scattered by the atoms in the sample. Through these scattering events, the primary electron beam effectively spreads and fills a teardrop shaped volume, known as the interaction volume extending about less than 100nm to 5μm depths into the surface. Interactions in this region lead to the subsequent emission of electrons which are then detected to produce an image.

The resolution of the SEM depends on the size of the electron spot and the interaction volume. They are both very large compared to distance between atoms, so the resolution of the SEM is not high enough to image down to atomic scale. Depending on the instrument, the resolution can fall somewhere between less than 1nm and 20nm.

4.3. Scanning probe microscopes

A little more than two decades ago, an important development in the history of microscopy was the invention of the Scanning Tunnelling Microscope by Binnig and Rohrer [2] in 1981 at IBM Laboratory. The basic method consisted in moving a sharp tip very close over a solid surface and monitored the tunnelling current between the tip and the surface. The variation in the current was transformed into a topographic map of the surface. The idea of measuring surface topography gave almost a new dimension to surface research into the nanometer range. Due to this new discovery, the last decade has experienced a new aspect of science, called nanotechnology [21].

However it was in 1928 that the concept of Scanning Microscopy started with the work of Synge using near-field light [22]. By forming a microscopic aperture in an opaque screen and illuminating the backside of the screen, the light emerging from the aperture could be used to image the surface of a specimen. However, the proposal was far beyond the technical capabilities at the time. It was not until 1972 that the concept was developed by E.A. Ash and G. Nicholls [23] using microwaves passing through a probe-forming aperture.

Then, in 1972, an apparatus closely related to STM called the topografiner was developed by R. Young [24]. The metal tip was driven by a piezoelectric device that could control the tip in the 3 dimensions. The system was isolated from vibrations which were identified as an important parameter against the achievement of a good resolution. The main difference with STM was that a field emission current was used between the tip and the sample, limiting the lateral resolution to 400nm and the vertical resolution to a few nanometers. However Young suggested in his publication that using tunnelling effect (explained below) which would bring the tip closer to the surface would improve the resolution.

It took another 10 years to be put into practice with the invention of STM. By isolating the vibrations of the system, it was now possible to approach the tip very close to the sample and create a tunnelling current between the tip and the surface. The presence of a piezoelectric device to control the movement of the tip and of a single atom tip end allowed vertical resolution of 0.01Å and lateral resolution of 0.1Å to be obtained [25]. Binnig and Rohrer were the first people to publish an image of the (7×7) reconstructed Si(111) surface [26] and received the Nobel Price in 1984 for their discovery. They shared the price with Ernst Ruska who designed the first electron microscope. However the limit in STM, mainly the need for a conductive

sample, created the need for another type of microscope: the Atomic Force Microscope, AFM created by Binnig in 1986 [27]. The AFM consists of a cantilever with a sharp tip at the end. The tip is approached to the surface and the forces between the tip and the surface leads to a deflection of the cantilever. The deflection is detected by the reflection of a laser beam. The advantage of AFM over STM is that a non conductive sample can be imaged. Its disadvantage is the relatively low lateral resolution, from micro to nanometer scale.

4.4. Scanning tunnelling microscopy (STM): the details

STM was invented with the intention of resolving one of the scientist's goals: imaging the extremely small, visualising the atomic structure of materials [28]. It allowed the acquisition of surface images at the atomic scale by detecting the electron density of the surface atoms. It is considered as a powerful tool for obtaining information on the packing order of atoms on the surface.

The basic concept of STM is based on a tunnelling current between an atomically sharp tip and a conductive material resulting in an image at atomic scale of the material [29]. A small voltage (between -5V and 5V) is applied in between the tip and the sample. The tip is then approached to the surface. Once the tip is close enough (without touching), a current flows across the gap between the tip and the surface. It is called the tunnelling current.

In order to understand STM, it is also important to understand the concept of tunnelling current. The tunnelling effect is a phenomenon that can be explained by quantum mechanics [15].

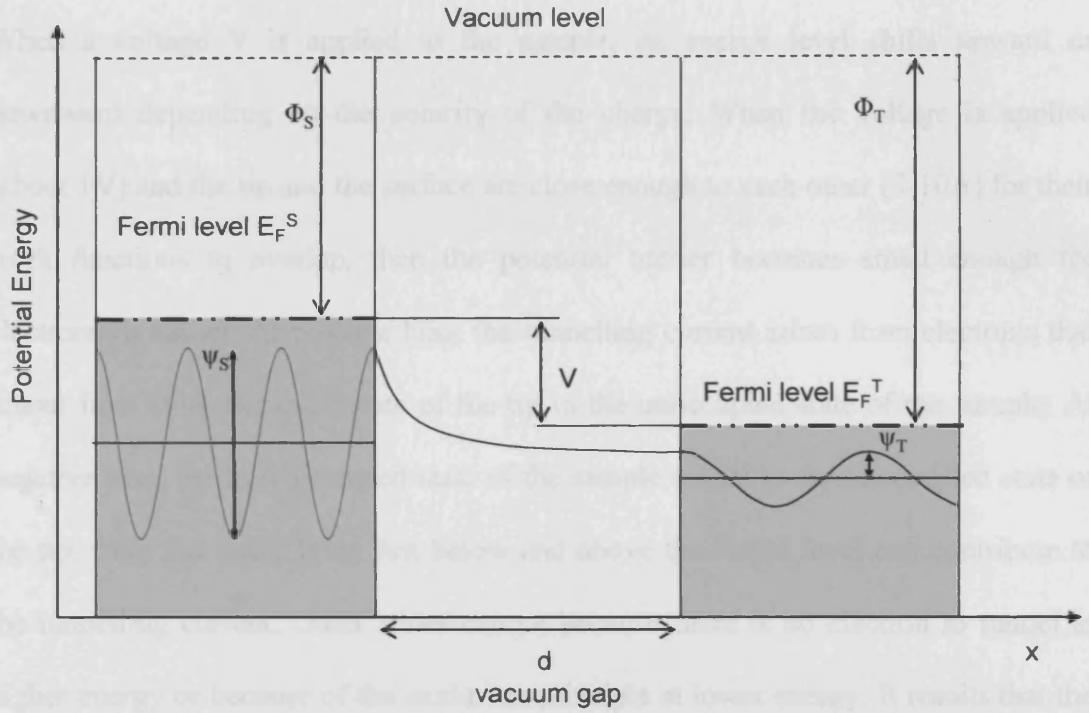

Figure 8: Energy level diagram showing the tunnelling between a tip and a surface.

In a one dimensional system, a particle (electron) with a specific wavefunction is confined within it. It cannot escape due to a potential barrier equals to its workfunction. In order to escape, the electron needs to be excited and gain enough energy to cross the vacuum level. A set, consisting of a tip and a surface, is considered. When the tip and the surface are independent, their vacuum levels are considered to be equal and their Fermi levels, E_F^T and E_F^S lie below the vacuum level by their work functions Φ_S and Φ_T (figure 8). Electrons crossing the tip-surface gap encounter the potential barrier. The wavefunctions of the electrons are periodic in their system. When the electrons try to cross the barrier, their wavefunctions decay exponentially into the vacuum region following

$$\psi = e^{\pm kx} \qquad (3)$$

$$k^2 = \frac{2m(V_B - E)}{\hbar^2} \qquad (4)$$

where m is the electron mass, ħ the Planck's constant, E the energy of the electron, k the inverse decay length and V_B the potential barrier.

When a voltage V is applied to the sample, its energy level shifts upward or downward depending on the polarity of the charge. When the voltage is applied (about 1V) and the tip and the surface are close enough to each other (5-10Å) for their work functions to overlap, then the potential barrier becomes small enough for electrons to tunnel. At positive bias, the tunnelling current arises from electrons that tunnel from fully occupied state of the tip to the unoccupied state of the sample. At negative bias, the fully occupied state of the sample tunnel to the unoccupied state of the tip. Only the states lying just below and above the Fermi level can contribute to the tunnelling current. Other states cannot because there is no electron to tunnel at higher energy or because of the exclusion principle at lower energy. It results that the probability for an electron to cross the barrier is

$$I \propto e^{-2kd} \qquad (5)$$

d is the distance of the vacuum gap.

Where k is related to the local work function by [25]:

$$k = (2m\phi/\hbar^2)^{1/2} \qquad (6)$$

Most metal work functions are around 4-5eV [29]. From equation 6, it is then possible to determine k.

$$k = (2m\phi/h^2)^{1/2} = (2\times 9.109\times 10^{-31} kg \times 4eV/(6.626\times 10^{-34})^2 J^2.s^2)^{1/2}$$

Or $1eV = 1.602\times 10^{-19} J$ and 1J=1kg.m^2.s^{-2}

So $k = 1630647799.97m^{-1} \approx 1.6$ Å^{-1}

Thus, from equation 5, for each angstrom of vacuum between the tip and the sample, the tunnelling current will drop by:

$$\exp(-4k) - \exp(-2k) = \exp(\frac{-4k}{-2k}) \approx 7$$

The control of the height of the tip above the surface is therefore a very important parameter, as well as good vibration isolation.

5. Method of fabrication of nanoparticles

5.1. Preparation of powder catalysts

There are a variety of ways to prepare catalysts. The commonly methods used are impregnation, precipitation and washcoating.

Impregnation method [1] consists in adding to a high area porous material a solution of the active phase precursor. The active phase can then be precipitated by a sudden change in the pH. The catalyst is then filtered, dried and calcined. This method is called precipitation impregnation. The drawback of this method is that much of the solution is wasted. When working with expensive precursor, incipient wetness is a more controllable method. In this case, an appropriate amount of active component is dissolved in a known volume of deionised water to give the desired concentration of metal precursor. The volume of metal solution added is sufficient to fill the pores of the support. The catalyst is finally dried and calcined in an oven.

Another common method is co-precipitation [1]. The support and active precursor are mixed together and co-precipitated at a particular pH by adding an acid, base or salt. Taking the example of a copper, zinc and alumina catalyst for methanol synthesis: a mixed nitrate solution is mixed with an aqueous solution of KOH and Na_2CO_3 and co-precipitated by rapid addition of Na_2CO_3. The precipitate produced is aged then washed and filtered to remove the Na ions responsible for the change in methanol selectivity. Finally, the catalyst is dried and calcined [30].

Washcoating [1] is a technique mostly used in industrial catalysis in car catalyst production. The catalyst is supported on a monolith structure (honeycomb-like) made

from ceramic or stainless-steel material. This support is impregnated by a washcoat. The washcoat is usually made from a highly porous alumina (containing added materials to make it resistant to sintering) dipped into the active component, a precious metal. The precious metal currently used are platinum, palladium and rhodium because they are less prone to poisoning compared to the metal oxides. The last step in washcoat preparation is drying and calcination.

5.2. Preparation of nanoparticles on model catalyst:

Model flat catalysts are usually epipolished single crystal cut in a specific plane. Crystals are solids in which the atoms are arranged regularly in a space lattice with specific geometrical symmetry elements. However, ideal surfaces do not exist in nature and the surface usually present defects such as kink, steps or vacancies. As for powder catalysts, there exist various ways to prepare nanoparticles supported on single crystal. They are classified in two major domains: chemical vapour deposition (CVD) and physical vapour deposition (PVD) [31, 32]. Chemical vapour deposition is a chemical process whereby gaseous reactants can be deposited on a surface. During this process, energy is given to the precursor gas which contains the atoms to be deposited. This energy dissociated the gaseous molecules by a series of chemical reactions in order to obtain a solid product on the substrate surface. There are different energy sources of heat for CVD process: heating of substrate, plasma, lamp and laser. The substrate temperature and system pressure are the two most important parameters in CVD since they strongly influence the growth mode. CVD covers processes such as Atmospheric Pressure Chemical Vapour Deposition (APCVD), Laser Chemical Vapour Deposition (LCVD), Metal Organic Chemical Vapour Deposition (MOCVD) or Photochemical Vapour Deposition (PCVD).

The second domain is Physical Vapour Deposition (PVD) used to deposit thin films of various materials onto various substrates by physical mean. Variants of PVD include evaporative deposition, sputtering and pulsed laser deposition. In evaporative deposition, a thermal evaporator uses an electric resistance heater to melt the material and raise its vapour pressure to a useful range. This is done in high vacuum to lower the possibility of contamination of the chamber. Another possibility is to use an electron beam evaporator that fires an electron beam from an electron gun to boil a small pot of material. Sputtering relies on an electron source to knock out material from a target a few atoms at a time which are then deposited on a substrate. The target can be kept at a relative low temperature making it a more flexible technique. It is useful for mixtures, where different component would otherwise evaporate at different rates. Pulsed laser deposition works by an ablation system. Pulses of focused laser light transform the target directly from a solid to plasma. This plasma usually reverts to gas before it reaches the substrate.

6. Aim of the thesis

In this thesis, we are looking at catalysis from both a real and modelled point of view. Chapter 2 introduces the Scanning Tunnelling Microscope (STM) design and operation. This technique is exploited extensively for this PhD work. This paragraph is followed by the description of the modelled sample preparation and deposition methods for real and model catalysts. Then, the techniques of surface analysis used are described, starting with Low Electron Energy Diffraction (LEED), followed by Auger Electron Spectroscopy (AES) and Atomic Force Microscopy (AFM). Finally, the methods used for real catalyst analysis are explained and consist in the description of the Pulsed Flow Reactor (PFR) and the theory and operation of the surface area measurement via BET system.

In chapter 3, catalyst behaviour is studied from a mathematical point of view. The chapter starts with an analysis of the geometrical aspects of monolayers and nanoparticles, and the relations between particle spacing and particle size. This is followed by the description of the different growth modes on surfaces: Volmer-Weber (VW which consists of 3D island growth), Stranski-Krastanov (SK: layer by layer followed by 3D growth) and Frank-van der Merwe (FM consisting of a layer by layer growth). Those growth modes can be differentiated by the interpretation of the AES signals at various coverages. Examples set on $Cu/TiO_2(110)$ and $Pd/TiO_2(110)$ systems are investigated to determine their growth mode and to support the models previously established. STM imaging and Auger spectroscopy are the tools used for this verification.

The reactivity of palladium metal deposited by MVD on a $TiO_2(110)$ single crystal is exploited in chapter 4. The chapter starts with an introduction on the structure of titania and of the Strong Metal Support Interaction effect (SMSI). This is followed by a paragraph on the model and real catalyst preparation. The study of the model catalyst is carried out in UHV chamber by STM, AES and LEED analysis. First, an analysis is done on the clean $TiO_2(110)$ sample. Then, the SMSI effect is studied on palladium deposited titania crystal and is followed by possible models describing the structures found. The last part of the chapter looks at the real catalyst via PFR experiments: CO uptake and CO oxidation reactions are carried out. Comparisons and relations between the two methods are described in a last paragraph.

Finally, a closing chapter (chapter 5) reminds the aim of the work, the main findings of this work regarding the mathematic models, the conclusive remarks of the model and real catalysts and the ideas on the structures imaged. The chapter ends up with subsequent work that could be carried out on the system studied.

7. Reference

1. Bowker M., *The basis and applications of heterogeneous catalysis.* Oxford University Primers, 1998.

2. Binnig G. and Rohrer H., *Scanning Tunneling Microscopy.* Surface Science, 1983. **126**(1-3): p.236-244.

3. Lindström B. and Pettersson J., *A brief History of catalysis.* Catalysis Technology, 2003. **7**(4): p.130-138.

4. Sadykov V.A., Isupova L. A., Zolotarskii I.A., Bobrova L.N., Noskov A.S., Parmon V.N., Brushtein E.V., Telyatnikova T.V., Chernyshev V.I. and Lunin V.V., *Oxide catalysts for ammonia oxidation in nitric acid production: properties and perspectives.* Applied Catalysis A: General, 2000. **204**(1): p.59-87.

5. Corma A., Melo F.V., Sauvanaud L. and Ortega F.J, *Different process schemes for converting light straight run and fluid catalytic cracking naphtha in a FCC unit for maximum propylene production.* Applied Catalysis A: General, 2004. **265**(2): p.195-206.

6. Li J-L. and Inui T., *Characterization of precursors of methanol synthesis catalysts, copper/zinc/aluminium oxides, precipitated at different pHs and temperatures*, Applied Catalysis A: General, 1996. **137**(1): p. 105-117.

7. Fridell E., Persson H., Westerberg B., Olsson L. and Skoglundh M., *The mechanism for NO_x storage.* Catalysis Letters, 2000. **66**(1-2): p. 71-74.

8. Bourbonnais G., *Les bases moléculaires et cellulaires de la vie: les molécules de la vie/les protéines*. Available from : http://ici.cegep-ste-foy.qc.ca

9. Tauster S.J., Fung S.C. and Garten R.L., *Strong metal-support interaction. Groupe 8 noble metals supported on TiO_2.* Journal of the American Chemical Society, 1978. **100**(1): p. 170-175.

10. Sadeghi H.R. and Heinrich V.E., *SMSI in Rh/TiO_2 model catalysts: Evidence for oxide migration*. Journal of Catalysis, 1984. **87**(1): p. 279-282.

11. Tauster S.J., *Strong metal-support interactions*. Account of Chemical Research, 1987. **20**(11): p. 389-394.

12. Kolasinski K.W., *Surface science: Foundations of catalysis and nanoscience*. Wiley Interscience, 2002.

13. Somorjai G.A., *Introduction to surface chemistry and catalysis*. Wiley Interscience, 1994.

14. Chambers A., Fitch R.K., and Halliday B.S., *Basic Vacuum Technology*. 2nd ed: Institute of Physics, 1998.

15. Atkins P. and De Paula J., *Atkins' physical chemistry* 7th ed: Oxford University Press, 2001.

16. Davidson M.W., *The compound microscope*.
Available from: www.micro.magnet.fsu.edu/ primer/museum/janssen.html

17. Hooke R., *Micrographia: or some Physiological Descriptions of Minute Bodies made by Magnifying Glasses with Observations and Inquiries Thereupon.* Dover publisher.

18. White G.W., *Introduction to microscopy,* Butterworth, 1966.

19. Knoll M. and Ruska M., *The Electron Microscope.* Zeitschrift fuer Physik, 1932. **78**: p. 318-339.

20. Rochow T.G. and Tucker P.A., *Introduction of microscopy by means of light, electrons, X-rays or acoustics*. 2nd ed.: Plenum Press, 1994.

21. Birdi K.S., *Scanning Probe Microscopes: applications on science and technology*. Boca Raton, Flammarion, 2003.

22. Synge E.H., *A suggested method for extending the microscopic resolution into the ultramicroscopic region.* Philosophical Magazine, 1928. **6**: p. 356-362.

23. Ash E.A. and Nichols G., *Super-resolution aperture scanning microscope.* Nature, 1972. **237**: p. 510-512.

24. Young R., Ward J. and Scire F., *The topographiner: an instrument for measuring surface microtopography.* Review of Scientific Instruments, 1972. **43**(7): p.999-1011.

25. Vickerman J.C., *Surface Analysis: The principle techniques*. Wiley ed. 2000.

26. Binnig G., Rohrer H., Gerber C. and Weibel, E., *(7×7) reconstruction on silicon(111) resolved in real space.* Surface Science, 1985. **157**(2-3): p. L373-378.

27. Binnig G., Quate C.F. and Gerber C., *Atomic force microscope.* Physical Review Letters, 1986. **56**(9): p. 930-933.

28. Bonnell D.A., *Scanning Tunneling Microscopy and Spectroscopy: Theory, Techniques and Applications*: VCH publisher, 1993.

29. Stroscio J.A. and Kaiser W.J., *Scanning Tunneling Microscopy.* Methods of Experimental Physics. Vol. 27. Academic Press, 1993.

30. Figueiredo R.T., Andrade H.M.C. and Fierro J.L.G., *The role of the coprecipitation sequence of salt precursors on the genesis of Cu-ZnO-Al_2O_3 catalysts: synthesis, characterization and activity for low temperature shift reaction.* Brazilian Journal of Chemical Engineering, 1998. **15**(2). ISSN: 0104-6632.

31. Northeast Waste Management Official's association, *Alternative methods of metal deposition.* Available from: http://www.wmrc.uiuc.edu/main_sections/ info_services/library_docs/manuals/finishing/altmeth.htm

32. Berry R.W., Hall P.M. and Harris M.T., *Thin film technology*. Van Nostrand, 1968.

Chapter 2

Experimental

1. Introduction

In this chapter the description of the equipment employed during the work is presented and the operation of the STM is explained. Then, our experimental set up is described, including all the conditions and the different parts required in the image acquirement. An account on the methods of metal deposition and cleaning processes is also reported. Finally, a description of the other surface techniques integrated on the chamber is given. These consist of Auger electron Spectroscopy (AES) and Low Electron Energy Diffraction (LEED) that bring information for the reliability of the STM images. A surface analysis technique not integrated in our system was used: the Atomic Force Microscopy (AFM) which is also described. Finally, real catalysts related to the model catalysts studied were tested in a Pulsed Flow Reactor. The reactor is described in section 8. The powder catalyst was analysed by BET measurements. This technique is described in the last section.

2. System design and operation

2.1. The chamber

The STM (image 1) is a W.A. Technology system designed to operate from ambient temperature to 1000°C. Three metal evaporators, one organic compound evaporator, a LEED/Auger analyser, a mass spectrometer, and an ion gun are attached to the chamber.

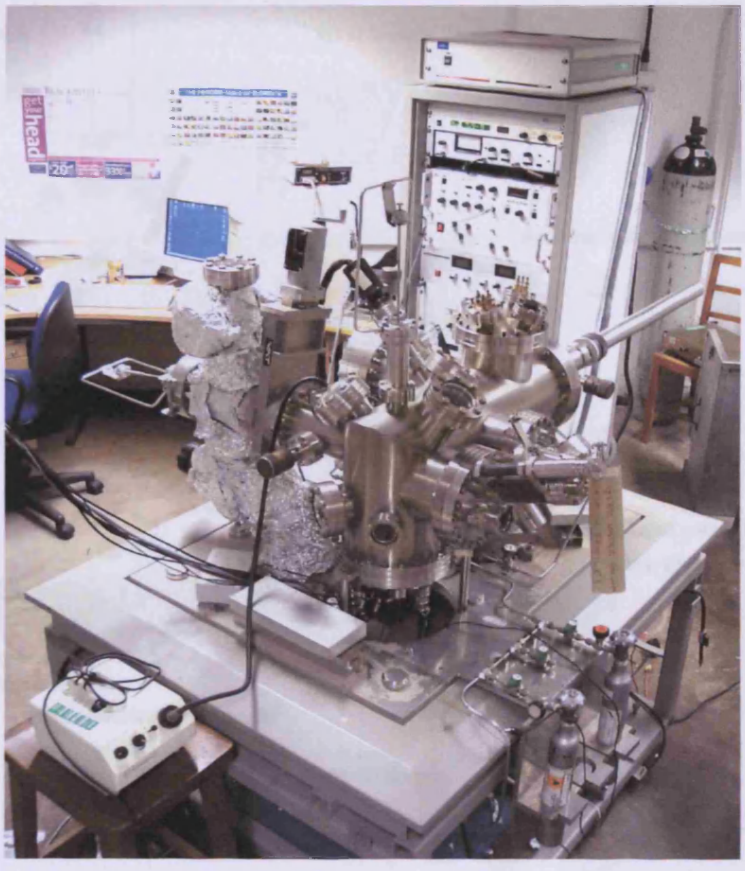

Image 1: The STM system.

The vacuum system contains a transfer mechanism that can hold two sample assemblies and two tips on a tray (these are described in details in section 2.4. and 2.5.). They can be unplugged from the head and taken out of the machine via the side chamber for repair without having to remove the STM head from UHV chamber. A schematic of the STM chamber is shown on figure 1 detailing all the parts shown on the above image [1].

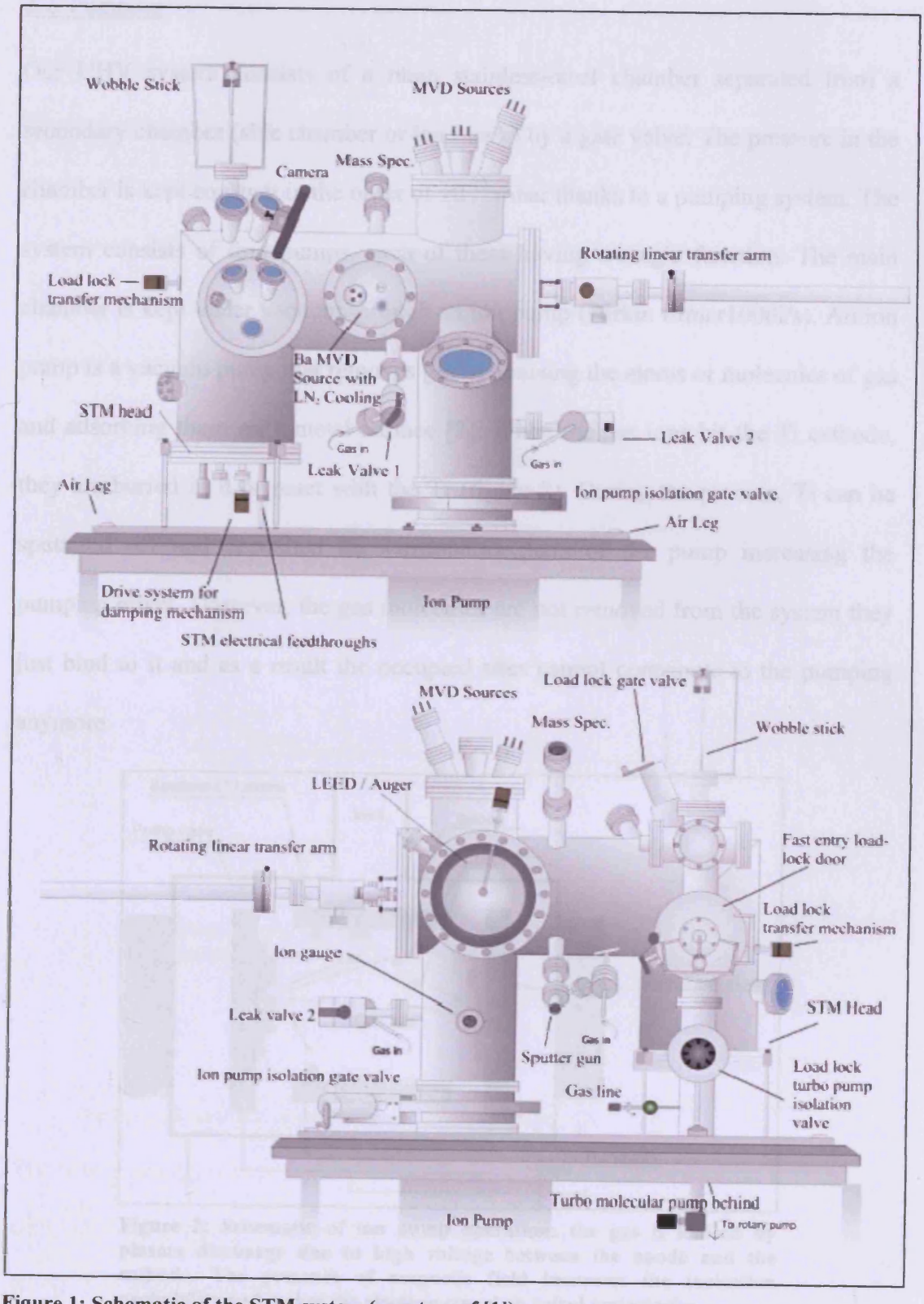

Figure 1: Schematic of the STM system (courtesy of [1]).

2.2. Pumping

Our UHV system consists of a main stainless-steel chamber separated from a secondary chamber (side chamber or load-lock) by a gate valve. The pressure in the chamber is kept constant in the order of 10^{-10} mbar thanks to a pumping system. The system consists of four pumps, each of them having a single function. The main chamber is kept under vacuum through an ion pump (Perkin Elmer1000l/s). An ion pump is a vacuum pump that removes gas by ionising the atoms or molecules of gas and adsorbing them on a metal surface [2]. When the gas ions hit the Ti cathode, they are buried in it or react with the Ti (figure 2). During the process, Ti can be sputtered off and deposited on surrounding parts of the pump increasing the pumping effect. However, the gas molecules are not removed from the system they just bind to it and as a result the occupied sites cannot contribute to the pumping anymore.

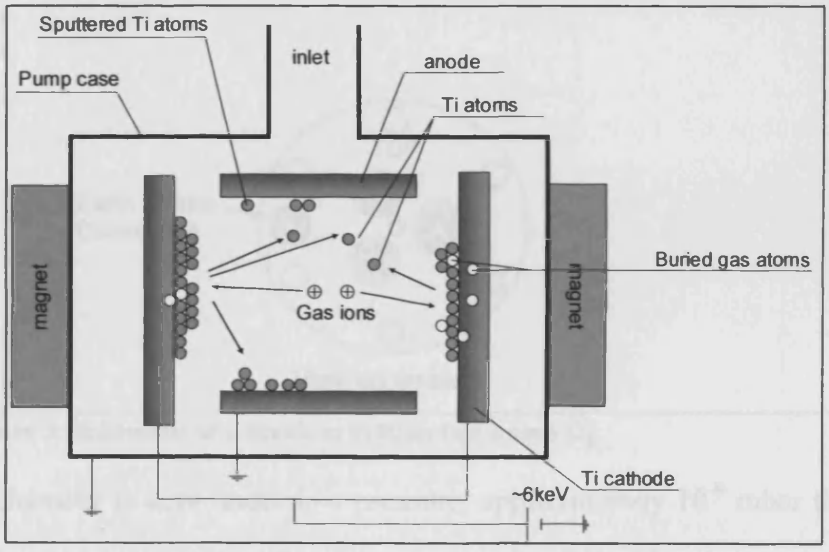

Figure 2: Schematic of ion pump operation: the gas is ionised by plasma discharge due to high voltage between the anode and the cathode. The presence of magnetic field increases the ionisation probability and makes the electron travel on spiral trajectories.

The improvement and maintenance of this very low pressure is enhanced by the presence of a titanium sublimation pump (TSP, Vacuum generators, STT22) [3].

The sublimation pump in the system consists of a chamber containing three titanium/molybdenum alloy hairpin style filaments (figure 3). When heated, the filament releases a titanium vapour that condenses on the surface around. This layer reacts with surrounding gases molecule to form stable compounds [2]. The continuous heating of the filament allows the formation of more active layers of titanium. The pump is used only for short periods (only overnight) in order to prevent the ageing of the filament.

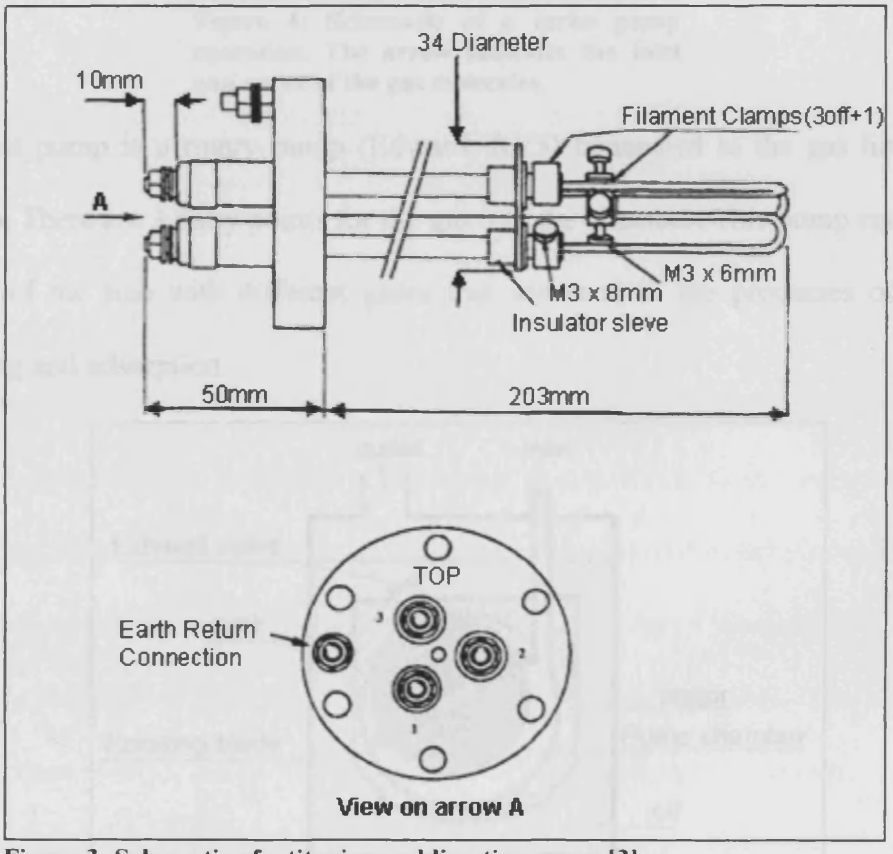

Figure 3: Schematic of a titanium sublimation pump [3].

The side chamber is kept under low pressure, approximately 10^{-9} mbar thanks to a turbo molecular pump (Varian, Turbo-V70D) attached to a rotary pump (Edwards, RV5). The basic principle of a molecular turbo pump is identical to a kinetic pump in which a momentum is given to a gas molecule by contact of the molecule to a high-speed velocity rotor (figure 4) [2]. The latter is composed of a succession of

rotor and stator discs. This has for consequence to move the molecule towards the outlet of the pump.

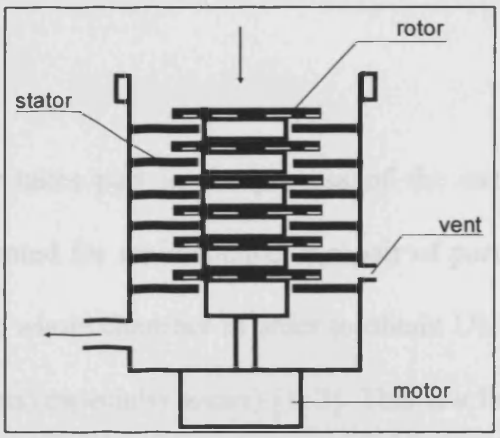

Figure 4: Schematic of a turbo pump operation. The arrow indicates the inlet and outlet of the gas molecules.

The last pump is a rotary pump (Edward, RV5) connected to the gas line of the system. There are 3 entry points for the gas into the chamber. This pump enables the filling of the line with different gases that are used in the processes of sample cleaning and adsorption.

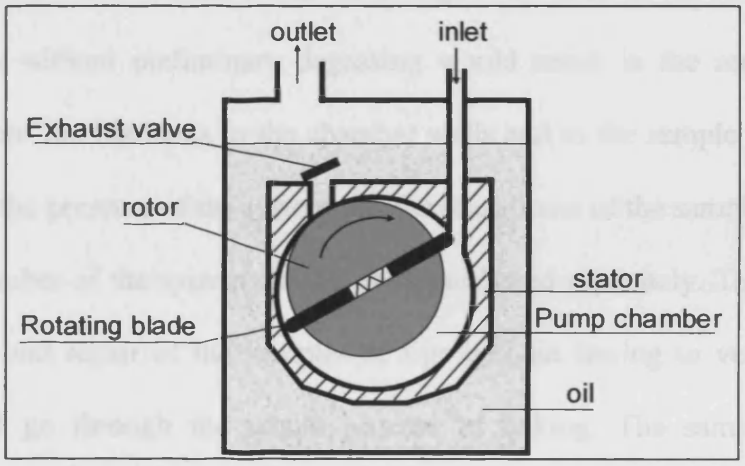

Figure 5: Schematic of a rotary pump.

A rotary pump operates by rotation of an off-centre cylinder from which movable blades turn and make contact with the side of the pump case (figure 5). First, the pump sucks air due to the depressurisation caused by the rotation of the blades. Then, the volume of air is isolated by the blades and compressed by continuous rotation of the cylinder. Finally the air is vented out through the oil. The presence of

an oil bath allows the lubrication of the moving part of the pump and also traps the air molecules.

2.3. Baking

Baking the chamber takes part in the process of the experimentation. Once the chamber has been vented for maintenance or repair of parts of the equipment, it is necessary to bake the whole chamber in order to obtain UHV conditions and get rid of all the contaminants (especially water) [1, 3]. This is a long process that takes up to 2 days to complete. The chamber is locked into a closed box made of aluminium panels and heated to approximately 120°C. Once the baking is finished and the panels removed, it is necessary to degas all the filaments. When opened to air, the inside chamber walls and the filaments of the different analysers get covered with impurities. Degassing just after baking (while the chamber is still warm) allows the removal of those contaminants without sticking to the walls of the chamber. Using the filaments without preliminary degassing would result in the removal of the impurities from the filaments to the chamber walls and to the sample surface. This would affect the pressure of the system and the cleanliness of the sample.

The side chamber of the system can be used and baked separately. This allows the maintenance and repair of the samples or tips without having to vent the whole chamber and go through the whole process of baking. The samples are first transferred to the side chamber through the gate valve using a wobble stick. Once the valve is closed, the side chamber is put under atmospheric pressure of nitrogen. The use of nitrogen reduces the contamination of the side chamber by water vapour to a minimum, and, as a result, it will take less time to get back to low pressure while baking. This procedure is much quicker since it takes only a night to get back

to the appropriate base pressure. The transfer of the sample back to the chamber is done the next day. There is then only the ion gauge filament to degas.

2.4. The sample

The sample consists of a single crystal of size 4.5mm×4.5mm×1mm, epi-polished on one side and of known orientation depending on the crystal used [4].

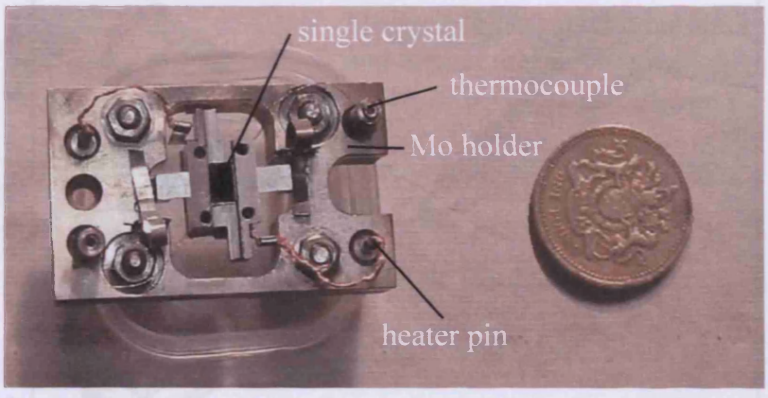

Image 2: Picture of the mounted sample in the molybdenum sample holder.

The crystal is mounted on a molybdenum holder. Molybdenum is used because of his stability to heat (melting point of 2890K) and its low expansion coefficient ($4.8\times10^{6}\,K^{-1}$) [5].

The thermocouples and heater pins are integrated in the sample holder, allowing the measurement of the true sample temperature. The sectional diagram (figure 6) shows how all the parts are held together to give the device in image 2.

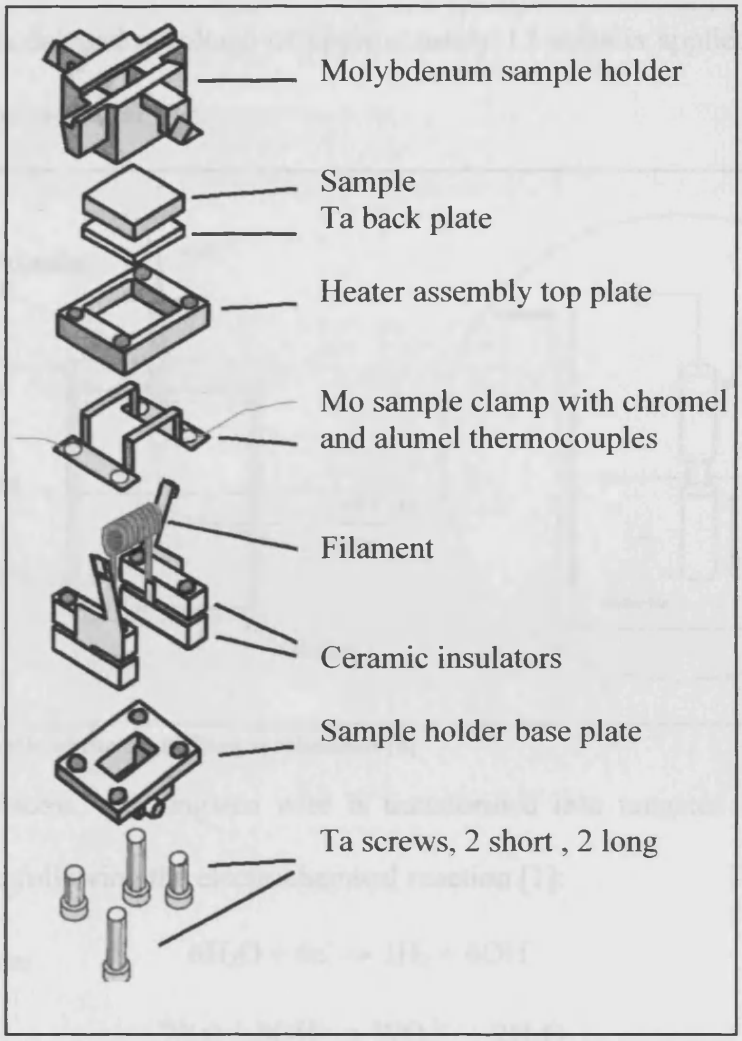

Figure 6: Exploded diagram of the sample holder: sample holder parts.

2.5. The tip

The tip is a crucial element when acquiring images. The sharpness of the tip is essential for the quality of STM imaging. Ideally, a tip should have a single atom at its end. The tips were prepared by an electrochemical etching method using 0.2mm Tungsten 97%/Rhenium 3% wire (presence of rhenium should avoid multiple tip since tungsten is quite brittle). The procedure is described below [4].

After cleaning the wire with acetone, etching takes place in a solution of 1M sodium hydroxide (Figure 7). The wire (anode), of approximately 15mm long, is suspended in the solution and the height of the wire is adjusted to obtain a tip of correct length,

usually 10mm. The tip holder is then connected to an outer plate electrode of platinum (cathode) and a voltage of approximately 12 volts is applied in order to activate the chemical reaction.

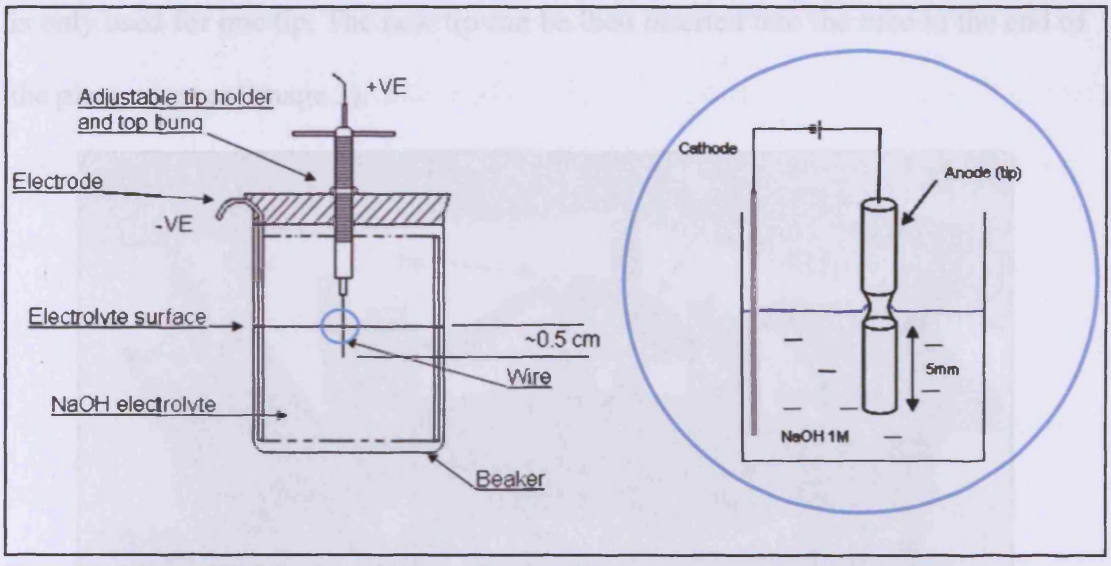

Figure 7: Schematic of the tip etching mechanism [4]

During the process, the tungsten wire is transformed into tungsten oxide at the meniscus level following the electrochemical reaction [1]:

At the cathode: $6H_2O + 6e^- \rightarrow 3H_2 + 6OH^-$

At the anode: $W(s) + 8OH^- \rightarrow WO_4^{2-} + 2H_2O$

$$W(s) + 2OH^- + 2H_2O \rightarrow WO_4^{2-} + 3H_2(g)$$

At the cathode, bubbles are released due to the formation of H_2, while the wire becomes thinner due to the dissolution of W to solute tungsten anions at the anode. The power supply displays the current flowing through the circuit and this falls during the etching process, as the wire becomes thinner. The etching ends when the wire cut into two. The weight of the submersed wire allows the elongation of the wire and ideally, a very sharp tip is created when it falls in the beaker. When this happens, it is necessary to stop the applied voltage because the end of the tip remaining in solution will keep the etching as long as a voltage is applied. In

addition, the tip is quickly rinsed with deionised water, then acetone to remove any remaining NaOH from the tip. Not doing those 2 last steps rapidly could result in a blunt tip. The OH^- ions being consumed during the reaction, the solution of NaOH is only used for one tip. The new tip can be then inserted into the tube in the end of the piezo scanner (image 3).

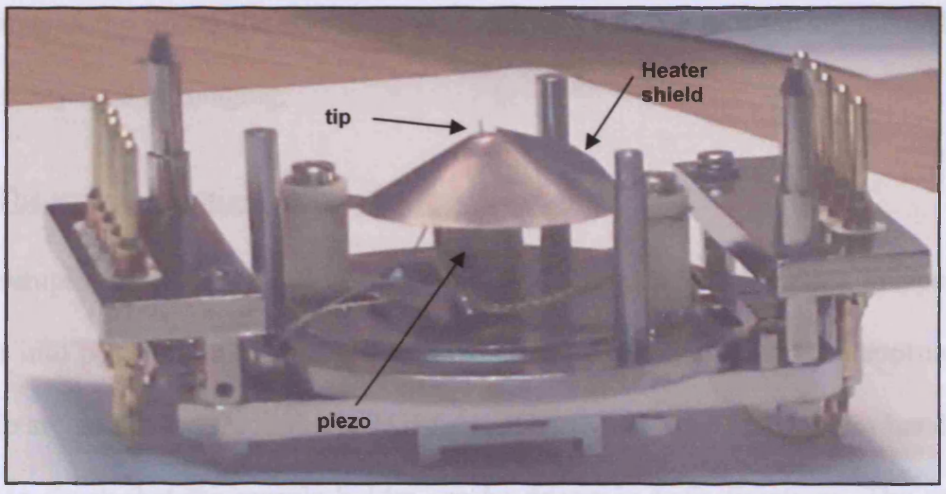

Image 3: Picture of the tip fitted in the scanner unit

2.6. Vibration isolation

The tip-sample distance must be kept constant to ~0.01Å to get good atomic resolution. Therefore it is absolutely necessary to reduce inner vibrations and to isolate the system from external vibrations.

When operating the STM, the presence of the ion pump keeps the system under vacuum and also provides vibration free running. Before any STM scanning, the side chamber is isolated from the turbo pump by a side valve and the turbo pump is switched off. The isolation of the system from vibrations is also enhanced by the presence of four air-legs at each corner of the table. In addition, the STM head is kept vibration free by a coiled spring suspension with magnetic damping [5]. For the damping mechanism, permanent magnets and copper blocks are used. This is

known as eddy current damping. The damping factor can be adjusted by varying the size of the copper block, the strength of the magnets and the distance between the two. Once the sample and tip are loaded, then the spring suspension clamp present under the STM head is released leaving the STM system on suspension. Avoiding vibrations and noise is essential while scanning. Any vibrations could lead to the collision of the tip on the crystal surface and as a result to a blunt tip incapable to obtain any type of imaging.

2.7. The approach design

The sample carrier is picked up from the tray using the wobble stick gripper and lower into position on the head. The movement of the sample and the approach of the tip are controlled through the TOPSystem hardware. The TOPSystem handset is used to check that the sample holder can be driven in both directions. The sample holder is then driven in fully reverse direction before fitting in the scanner assembly. The scanner is fitted in a similar way to the sample holder (Image 4).

Image 4: STM head loaded with the sample and the tip. The tip is held by the scanner unit and placed over the sample

Then, the spring suspension clamp is released and the system is ready for tunnelling.

The preparation tunnelling is done in two steps: manually and computer-controlled. In a first time, the sample is approached manually via two drive pins (figure 8: coarse approach drive pins [1]) placed in the STM head controlled by the drive handset. The two drive pins are located on each side below the sample holder assembly. Using the drive hand set, the pins can be driven back and forward.

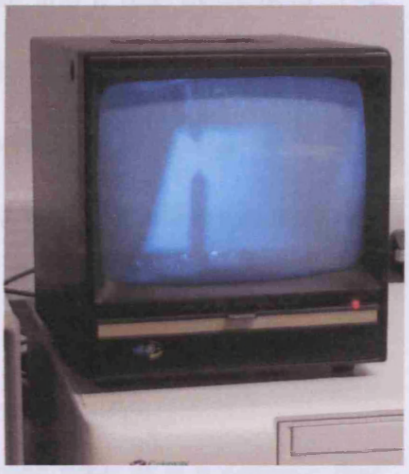

Image 5: position of the tip before coarse approach

The sample is rocked close to the tip using the forward button on the drive hand set and a video camera is used to make separation between the tip and the tip reflection on the sample visible to the naked eye (Image 5).

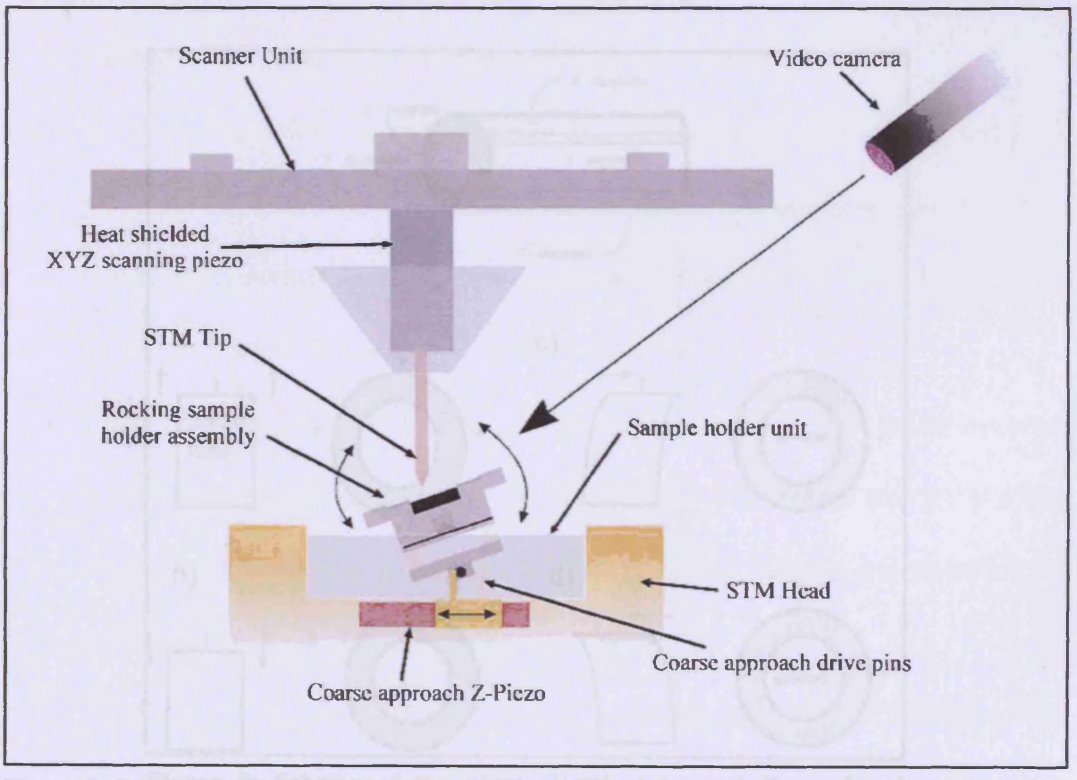

Figure 8: Schematic of the sample-tip assembly: approaching process

When the gap between the tip and its reflection becomes very small, then the gap distance is controlled by the computer approach. Two movements coexist in the automatic approach of the sample defined by a coarse and a fine movement. The computer makes the sample rock (coarse movement by moving the pins) of a very small distance at every 2 seconds. Then the tunnelling is checked by a fine movement of the tip in the z-axis. This is all controlled by the TOPSystem software after a potential of 1V has been set.

2.8. Positioning and scanning device: the piezo

The movement of the tip is controlled by a piezoelectric tube. It is a ceramic that changes its shape when a voltage is applied through it [6, 7]. It usually has four electric contacts on the outside and is grounded on the inside. By applying different voltages to the four outside contacts the tube will bend in the x, y or z direction (figure 9).

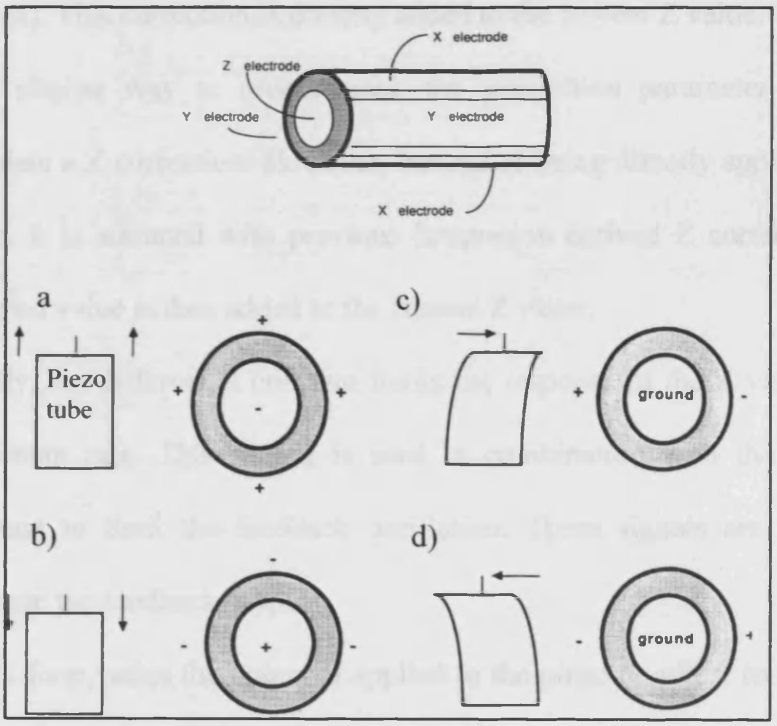

Figure 9: Scheme of the piezo electric tube and its mode of operation [6].

In order to move the tip up and down, for example, the voltage is applied to the four contacts, two contacts in the x direction and two contacts in the y direction. This makes the ceramic contract or extends in the x and y direction at the same time. In order to move the tip back and forth, the voltage on one side of the piezo is increased, while it is decreased on the opposite side (c and d). This makes one side contract while the other side is extended.

2.9. The feedback loop

The feedback loop controls the distance between the tip and the surface to stabilise the tunnelling current. Its function is to optimise the images taken in constant current mode. Also, a wide range of gains is desirable to tune the STM to a variety of operating conditions. There are three control functions that can be adjusted [8]:

- The proportional parameter is used to calculate a Z correction based on the difference between measured and required control signal (e.g. tunnel current). This correction is directly added to the current Z value.
- In a similar way to proportional, the integration parameter is used to calculate a Z correction. However, instead of being directly applied to the Z value, it is summed with previous integration derived Z corrections. This summed value is then added to the current Z value.
- Finally, the differential constant limits the response of the Z value to some maximum rate. This setting is used in combination with the integration constant to limit the feedback oscillation. These signals are summed to generate the feedback output.

The feedback loop varies the potential applied to the piezo to adjust its height. The adjustment of the gains is therefore very important. An incorrect setting could create

artefacts in the image, could crash the tip or withdraw it resulting in a loss of tunnelling current.

2.10. Operating modes

The movement of the scanner during the data acquisition is shown in figure 10 (courtesy of [9]). The direction in which the data are recorded is called Fast Scan direction. The perpendicular to it is called Slow Scan direction. The tip scans the surface in the fast scan direction and moves back, then take a step perpendicular and start a new scan and moves back again, this until the set lengths of the image are reached. At each point, the value of the tunnel current or the height between the tip and the surface is measured. This value is recorded and it defines a level of grey, which is then represented as a pixel.

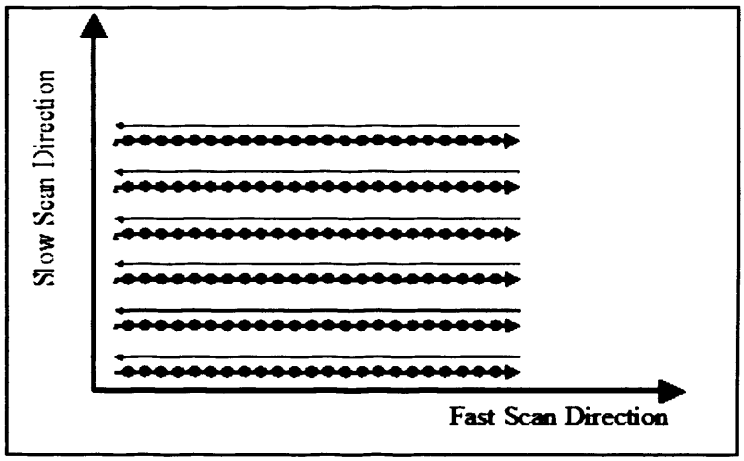

Figure 10: Schematic of the trajectory of the tip during scanning.

There are two main modes of scanning: constant height scanning and constant current scanning [10]. Constant height scanning consists in keeping the tip at a constant height in the z-axis while the variation of current is measured while the tip moves in the xy direction (figure 11). The image obtained would correspond to the variation of the tunnelling current as a function of the position on the crystal.

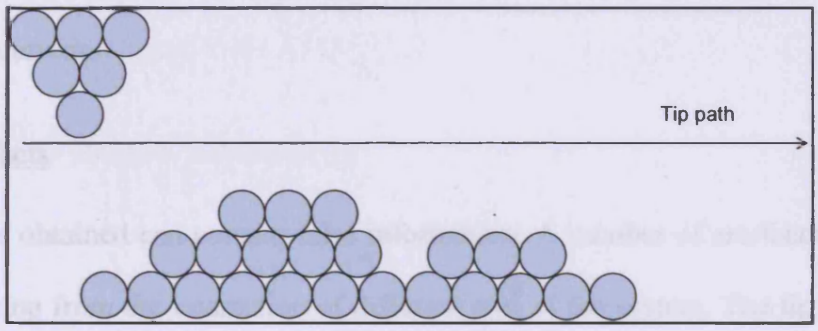

Figure 11: Schematic of scanning in constant height mode.

The constant current scanning method uses a fixed current and the variation of the tip in the z-direction is measured while scanning in the xy direction (figure 12). In this case, the image obtained would correspond to the variation of the tip height as a function of the position on the crystal. In this case, the feedback loop plays an important role. As the tip scans the surface, the feedback loop controls the separation between the tip and the surface. When a protrusion appears, corrections are done via the three functions of the feedback loop on the z-axis value keeping a constant tunnelling current The corrections are added to the current z value and results in the retraction of the piezo. Similarly, when a gap appears at the surface, the correction is done so that the piezo is extended to keep a constant current.

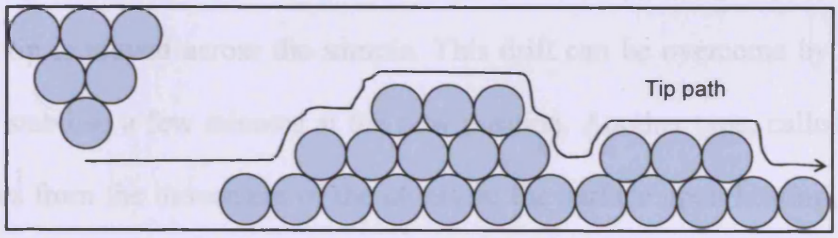

Figure 12: Schematic of scanning in constant current mode.

The latter method is usually preferred and is used in this system. The constant height method is useful when scanning very flat surfaces. For rough surfaces, presenting steps, kink, adatoms or vacancies, it is needed that the tip must have

adjustment in the z direction to prevent any tip-surface collision or loss of tunnelling current.

2.11. Artefacts

The images obtained can contain false information. A number of artefacts are well known arising from the interaction of different part of the system. The tip structure can influence the quality of an image. For example, if the tip presents a double sharp end (figure 13) the image will show the details twice and more or less equally separated (image 6).

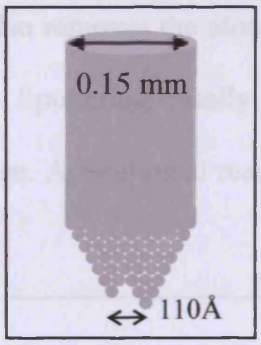

Figure 13: schematic of a double tip.

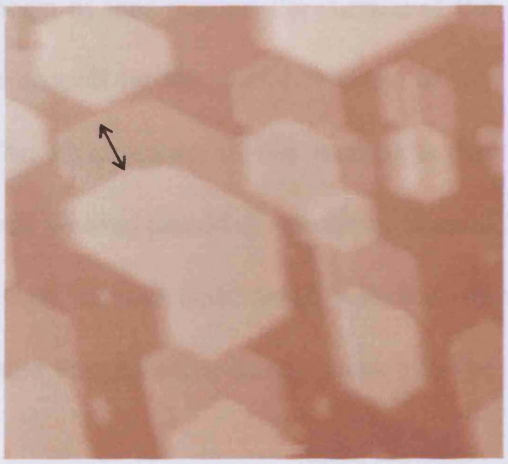

Image 6: Double tip effect. The image represents Pd particles on TiO_2. The arrow corresponds to the space difference of the double feature which is about 110Å. Image parameters: 782Å, 1V, 1nA.

Image drift can also occur as a result of a drift of the elongated piezoelectric tube when the tip is moved across the sample. This drift can be overcome by allowing the tip to stabilise a few minutes at the new position. Another type, called thermal drift, arises from the movement of the atoms on the surface upon heating. Leaving the sample to stabilise for a minimum of an hour is enough to limit the thermal drift. In addition, the pins responsible for the rocking of the sample holder can be backed off to disconnect them from the sample holder. In doing so, less current is required to keep the system at the desired temperature and can diminish the drift. The design also incorporates a thermal drift compensation [11]. The design is such that thermal

expansion is symmetric, so the only remaining drift is the unidirectional movement of the sample with respect to the holder [12].

3. Cleaning the sample: methodology

In order to obtain images of the surface, the crystal needs preliminary cleaning. Impurities are removed from the sample by sputtering. This method consists in the bombardment of the crystal using a source of argon ion (Ar^+) of energy 600eV (ion source, PSP vacuum, ISIS 3000). When the beam of ions reaches the surface of the crystal, it "kicks off" the surface atoms that deposit on the chamber walls or are pumped out from the chamber (Figure 14). The disadvantage of this method is that sputtering also removes the atoms of the crystal so long period of sputtering should not be done. Sputtering usually leaves the sample surface quite rough which is not ideal to image. Annealing at reasonably elevated temperatures usually smoothes the surface.

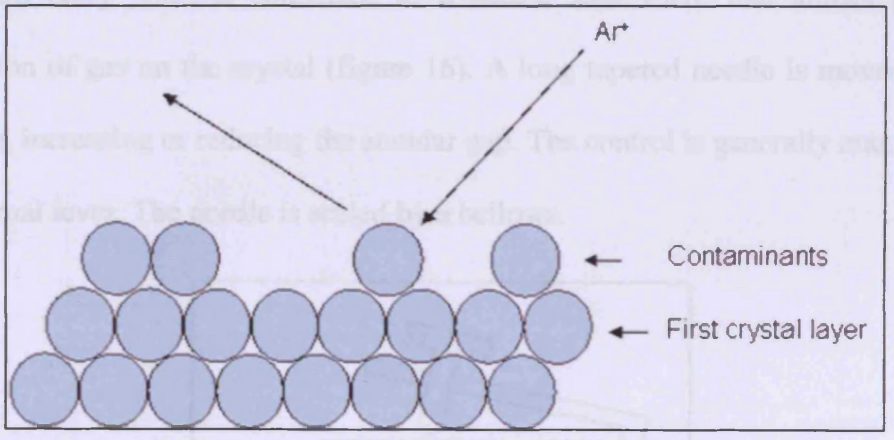

Figure 14: Schematic of sputtering concept at atomic level.

Titania crystals were cleaned following a series of sputtering and annealing cycles. Usually from 30 minutes to 2 hours sputtering at room temperature up to 400°C, followed by flashing at 850°C and annealing between 20 to 40 minutes between 700-750°C.

4. Deposition methods

A gas line is connected to the chamber through three entry points. The first entry is only used for argon and is connected to the ion gun; the second one is connected on one side of the chamber via a fine leak valve and allows the diffusion of gases in the chamber (used for oxygen) [2].

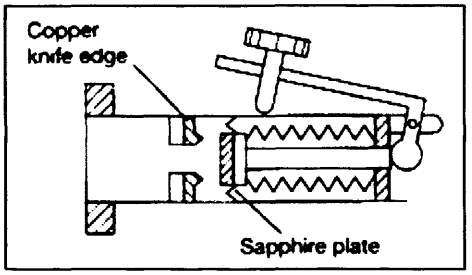

Figure 15: Schematic of an UHV fine leak valve.

This has a valve seat of copper knife edge and a valve plate of sapphire set in a flexible membrane. It can be moved by an external level giving fine adjustment of the gap (figure 15).

The third entry point is connected to a needle leak valve that allows precise deposition of gas on the crystal (figure 16). A long tapered needle is moved in an opening, increasing or reducing the annular gap. The control is generally manual, by an external lever. The needle is sealed by a bellows.

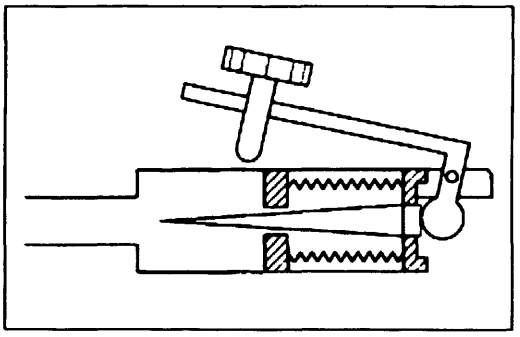

Figure 16: Schematic of a needle valve.

The line can be filled with different gases coming from compressed gas cylinder or liquid reactants. The line is pumped down via a rotary pump and the pressure is

detected using a Pirani gauge. The measurements are not accurate but we can easily check the content of the gas line by switching on the mass spectrometer and letting a small pressure of gas in the chamber. In addition to the storage of argon for sputtering process, the line was used for reaction with oxygen on a titania crystal.

Metal Vapour Deposition (MVD) consists in the deposition of a solid on a substrate by means of chemical vapour deposition. This process involves (1) the formation of reactants in the vapour state; (2) the transport of the vapours to the deposition region and; (3) the deposition of the solid from the vapour on the surface. This method possesses several advantages as it permits the preparation and use of almost any metallic materials. An evaporator for MVD consists of a coiled wire of metal attached on two filament posts that have their termination connected outside the chamber. A current is applied between the two connectors until the evaporation current is reached (figure 17). Particular care is required when setting up the power supply since the connectors include ceramics in the feedthroughs and they are extremely fragile.

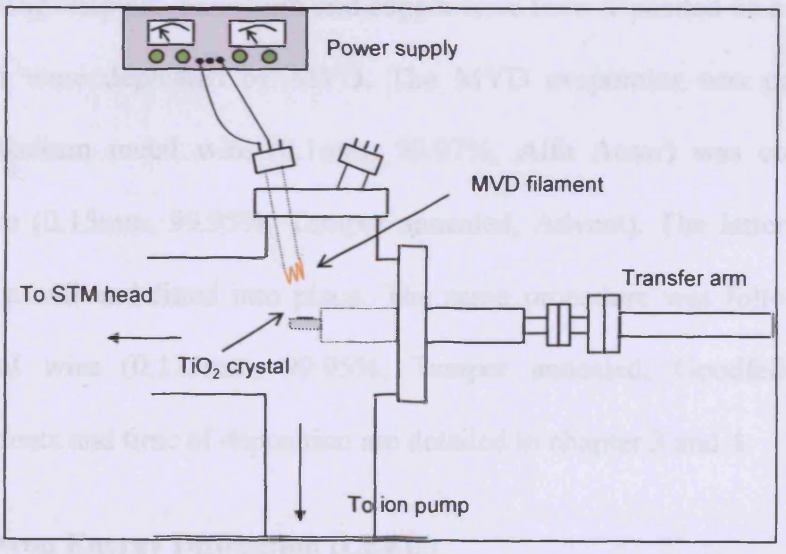

Figure 17: Schematic of metal vapour deposition (MVD) device.

Metal Organic Chemical Vapour Deposition (MOCVD) has the same aim as MVD but instead of evaporation from a metal wire, a metallic organic compound contained within a glass tube linked to the UHV chamber is evaporated onto the crystal surface (figure 18). The valve is first open to a maximum.

Then, the glass tube is heated with a heater gun until the pressure increases in the chamber (~10^{-8} mbar).

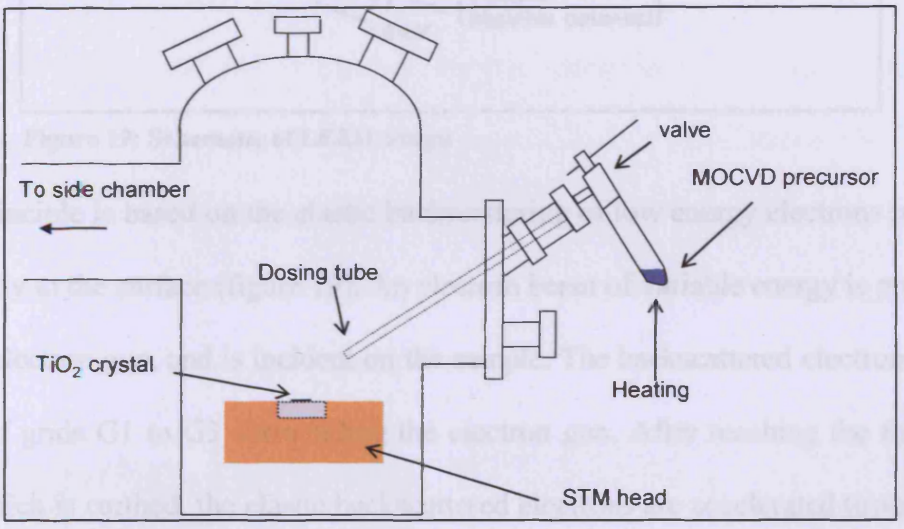

Figure 18: Schematic of the metal organic chemical vapour deposition (MOCVD) device.

In the following chapters, palladium and copper have been deposited on a surface of titania. Both were deposited by MVD. The MVD evaporator was prepared as follows. Palladium metal wire (0.1mm, 99.97%, Alfa Aesar) was coiled on a tungsten wire (0.15mm, 99.95%, Temper annealed, Advent). The latter was then shaped into a coil and fitted into place. The same procedure was followed for a copper metal wire (0,125mm, 99.95%, Temper annealed, Goodfellow). The different currents and time of deposition are detailed in chapter 3 and 4.

5. Low Electron Energy Diffraction (LEED)

LEED is one of the most suitable methods to determine the arrangement of the atoms present on the surface [10, 13].

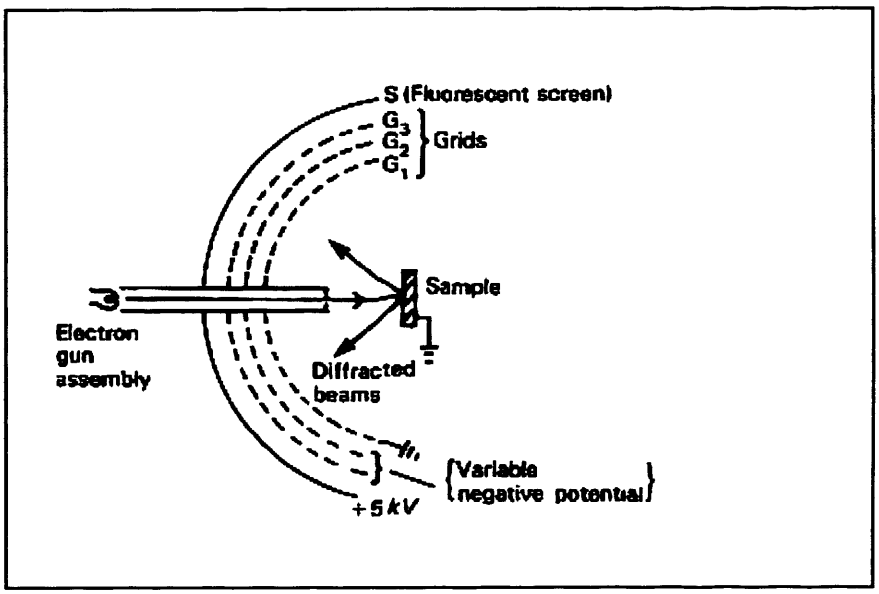

Figure 19: Schematic of LEED design

The principle is based on the elastic backscattering of low energy electrons incident normally to the surface (figure 19). An electron beam of variable energy is produced by an electron gun, and is incident on the sample. The backscattered electrons reach a set of grids G1 to G3 surrounding the electron gun. After reaching the first grid G1, which is earthed, the elastic backscattered electrons are accelerated towards the fluorescent screen that carries a voltage of 5keV. This gives enough energy to the electron of the diffracted beams to create fluorescence on the screen S and to obtain a bright LEED pattern. The other pair of grids G2 and G3 is present to stop the inelastic scattered electrons. They would, otherwise, lead to a bright and diffuse background on the fluorescent screen. The grid is held to a negative potential that can be adjusted to minimise the diffuse background of the LEED pattern.

LEED is used here to observe the state of the crystal surface. Mainly used to check the cleanliness state of the crystal, it also brought information on the surface reconstruction after annealing, deposition of nanoparticles and gives us an idea of what to expect on STM images. Because of the sensitivity of LEED to surface contamination and surface roughness, the appearance of a LEED with bright, sharp

spots can be seen as some evidence of clean and ordered surface. However, it appears that surfaces which show sharp LEED patterns can sometimes give a very blurry image on STM.

From the analysis of the spots position on a LEED pattern, it is possible to determine the geometry at the surface. It can also be used to determine whether any molecules deposited at the surface are adsorbed in an ordered way. If an overlayer is ordered, its surface unit size can be measured and its orientation relative to the underlayer determined. A LEED image gives a pattern in the reciprocal space. The distance between the points is inversely proportional to the distance between the points on the real surface. Taking the example of the (1×1) surface of TiO_2 (110) crystal, the distance between the rows of atoms is 6.5Å in the [1$\bar{1}$ 0] direction and 2.95Å in the [001] direction (figure 20).

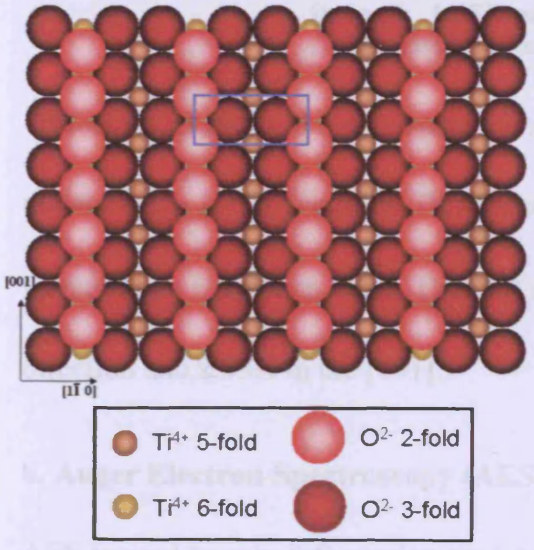

Figure 20: Model of (1×1) surface of TiO_2 (110) single crystal.

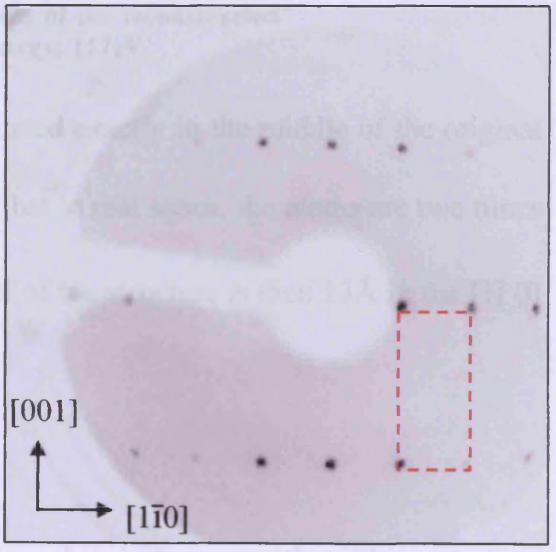

Image 7: LEED pattern of the (1×1) surface corresponding to the bulk termination. Beam energy: 122eV.

In reciprocal space the distance between the spots is proportional to $\frac{1}{6.5}$ and $\frac{1}{2.95}$.

At a given energy for two LEED patterns showing both the original (1×1) structure,

it is then possible to determine the distance of the added spots. Looking at image 7 and 8, the red rectangle corresponds to the (1×1) unit cell and the (1×2) unit cell is represented by the blue rectangle. The surface has reconstructed in figure 8 and extra spots have appeared on the LEED diffraction pattern due to the presence of a unit cell of the reconstructed surface unit which is doubled in size.

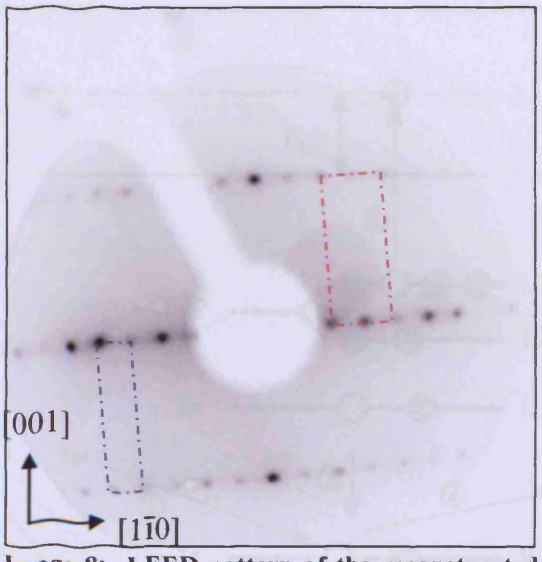

Image 8: LEED pattern of the reconstructed (1×2) surface. Beam energy: 117eV

In reciprocal space, the new spots are situated exactly in the middle of the original pattern in the [1$\bar{1}$ 0] direction. This means that in real space, the atoms are two times further apart from each other. The unit cell of the structure is then 13Å in the [1$\bar{1}$ 0] direction and 2.95Å in the [001].

6. Auger Electron Spectroscopy (AES)

AES is used to gain information on a surface chemical composition. This technique was discovered by Pierre Auger in 1925 [13, 14].

A beam of electrons is directed to the surface of a crystal. An incident electron of the beam causes the ejection of a core electron from a surface atom (figure 21: steps 1and 2). The electron vacancy creates instability, which can be balanced by the

transition of an electron of lower binding energy (figure 21: step 3). The difference in binding energy ΔE between the vacancy and the transition electron can be emitted as a photon or can be transferred to a third electron, the Auger electron. This electron can then escape into the vacuum with a specific kinetic energy, E_k (figure 21: step 4). E_k is independent of the energy of the incident radiation.

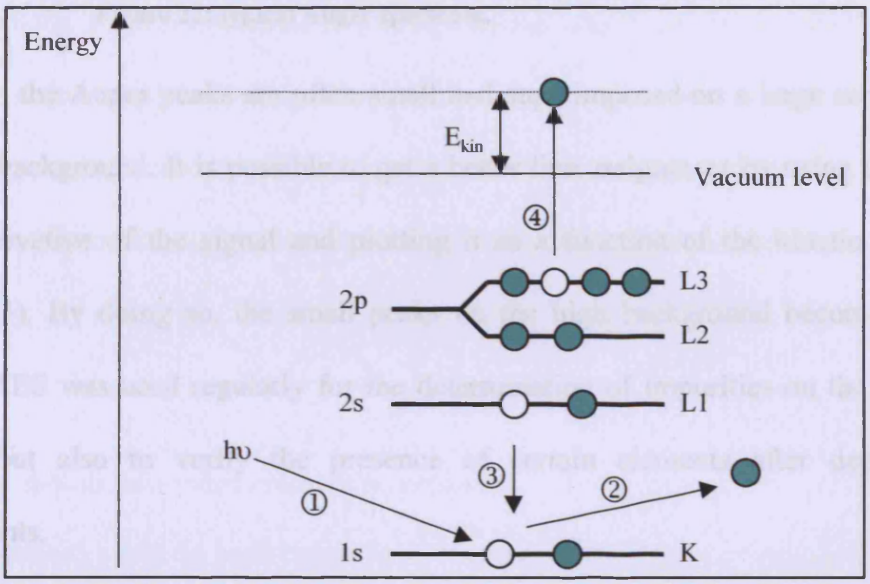

Figure 21: Schematic of the energy diagram taking place during the Auger process.

The kinetic energy gained by the third electron is related to the binding energy of the electron within the atom and is specific to that atom. So the Auger electron can be used to identify surface elements.

Auger spectroscopy is based upon the measurement of the kinetic energies of the emitted atoms. An AES spectrum plots the number of electron detected as a function of the kinetic energy (eV). The position of the peaks gives information on the element while their intensity is related to their concentration on the surface. For one element, several lines of Auger emission can be seen at different kinetic energies (figure 22).

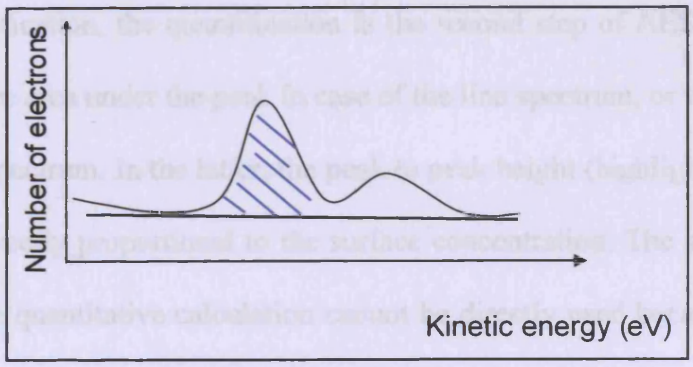

Figure 22: typical Auger spectrum.

However, the Auger peaks are often small and superimposed on a large secondary electron background. It is possible to get a better line assignment by using the first order derivative of the signal and plotting it as a function of the kinetic energy (figure 23). By doing so, the small peaks on the high background become more visible. AES was used regularly for the determination of impurities on the crystal surface but also to verify the presence of certain elements after deposition experiments.

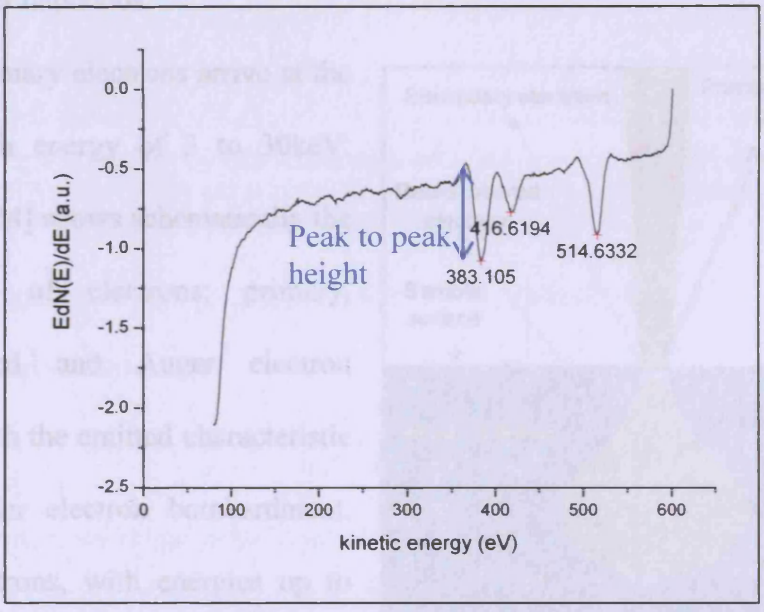

Figure 23: first derivative of Auger spectrum of clean TiO_2. Peaks at 383eV and 416eV are of Ti and the peak at 514eV is oxygen.

After the identification, the quantification is the second step of AES. This is done using the surface area under the peak in case of the line spectrum, or the intensity of the derivative spectrum. In the latter, the peak to peak height (highlighted in blue on figure 23) is directly proportional to the surface concentration. The surface area or intensity for the quantitative calculation cannot be directly used because of various electron/matter phenomena such as electron escape depth and backscatter factors, chemical effects on peak shapes and intensities, and surface roughness. It is necessary to include matrix effect and cross sections in those calculations. However, the composition of a sample of n elements can be calculated semi-quantitatively by

$$x_A = \frac{I_A/S_A}{\sum_i^n I_i/S_i} \qquad (1)$$

Where the matrix correction factors are neglected.

I is the intensity (peak to peak height) and S the sensitivity factor that can be found in any Auger handbook.

In AES, primary electrons arrive at the surface with energy of 3 to 30keV. Figure 24 [14] shows schematically the distribution of electrons: primary, backscattered and Auger electron together with the emitted characteristic X-rays under electron bombardment. Auger electrons, with energies up to 2000eV have a high probability to escape only from the first few monolayers because of their restricted kinetic energy [13].

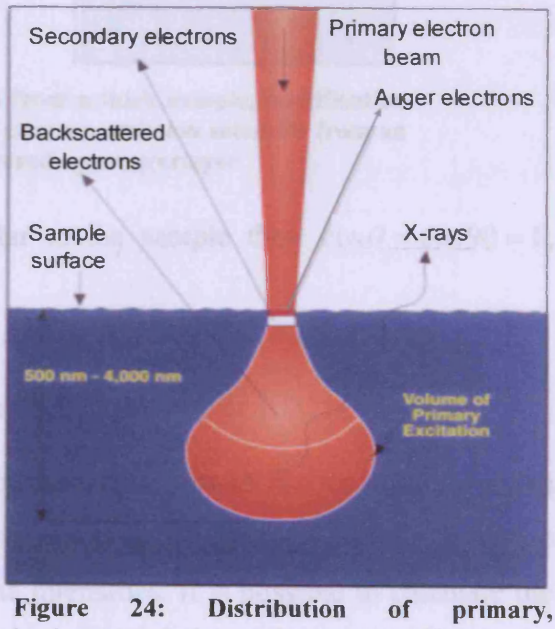

Figure 24: Distribution of primary, backscattered, Auger electrons and X-rays

During their trajectory, these electrons lose a certain amount of energy, change their direction and are also backscattered. They may create secondary electrons, Auger electrons and photons. Some of the backscattered electrons can in turn produce themselves into Auger electrons if they have sufficient energy. This way, the backscattered electrons contribute to the total Auger current. If the secondary electrons have a low energy, they will contribute to the background of the Auger spectrum. The distance travelled by an electron between two inelastic scattered collisions is called the mean free path and is noted λ. The thickness of the matter through which the electrons travel is expressed (following the Beer's law) as:

$$I_k = I_0 \exp^{-d/\lambda \cos\theta} \qquad (2)$$

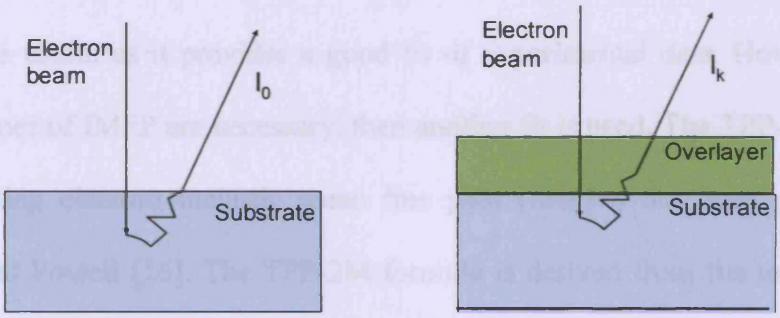

Figure 25: For electron emission from a thick sample, modification of the Beer's law can explain the electron emission intensity from an overlayer or from a substrate covered by an overlayer

When the electron beam is perpendicular to the sample then $\cos\theta = \cos 90 = 1$, therefore equation becomes:

$$I_t = I_0 \exp^{-d/\lambda} \qquad (3)$$

This equation is valid assuming that each unit thickness of matter through which electrons travel is adsorbing the same fraction of energy. Thus, from the measurements on the Auger spectra of the intensities, it is possible to calculate the thickness of a deposited layer of material. The values of the IMFP of electrons through matter are function of the energy of the electron and nature of the sample which they traverse. The equation that relates the IMFP with the kinetic energy of

the electrons and the type of material has been developed by Seah and Dench [15] who produced the plot showed on figure 26.

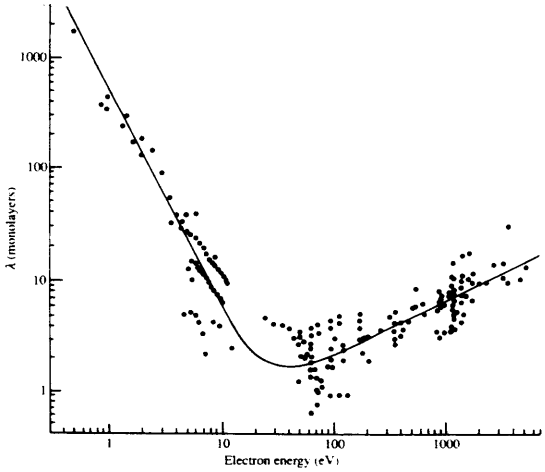

Figure 26: Dependence of IMFP, λ, on kinetic energy of the electron. The points represent the experimental data. The line is the model derived from them.

This plot is useful as it provides a good fit of experimental data. However, when precise values of IMFP are necessary, then another fit is used. The TPP-2M formula for estimating electron inelastic mean free path (IMFPs) has been proposed by Tanuma and Powell [16]. The TPP-2M formula is derived from fits to IMFPs that were calculated for many solids from optical data. The formula can thus be used to estimate more precise IMFPs for any solids material which certain physical parameters are known or can be reasonably estimated [17]. The main parameters in the formula are:

- ρ, the solid density in $g.cm^{-3}$
- N_v, number of valence electrons per atoms
- E_P, the plasmon frequency in eV which can be determined from the molecular weight (AW) of an element: $E_p = 28.8\sqrt{\frac{\rho N_v}{AW}}$
- E_g, the energy gap in eV.

The relative accuracy of this model ranges from 20% at 50eV to 15% at 100eV and 14% at 2000eV [17].

7. Atomic Force Microscopy (AFM)

AFM was invented shortly after STM. Based on almost the same principle as for STM, the AFM was developed for non conducting surfaces as well as conducting surfaces. Its operating principle is based on the deflection of a laser beam which is reflected from a mirror mounted on the back of the cantilever tip. While STM information is obtained from tunnelling current, AFM data come from the measurement of the forces between two separated bodies at close approach [13, 18]. A tip (usually silicon nitride), mounted at the extremity of a flexible cantilever, is positioned on the surface. In order to obtain a 3D image, the sample is placed on a piezoelectric tube that can moves in the x,y and z directions. The forces are detected by the deflection of the cantilever as the scanning takes place. The deflection of the cantilever is proportional to the force applied. A laser beam, directed onto the cantilever, is reflected when deflection occurs.

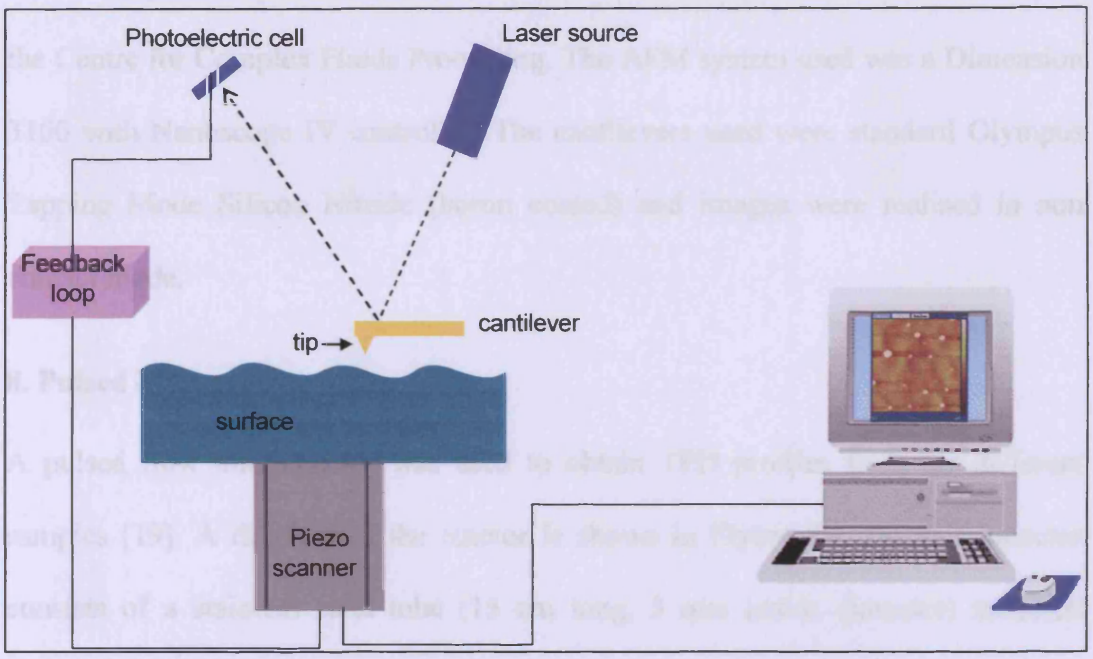

Figure 27: Schematic of AFM design and operation

The reflection is collected on a photodetector constituted of four photoelectric cells. The photodetector measures the difference in light intensities between the upper and lower cell and uses this data to build up a image point by point (figure 27).

There are three main modes of AFM operation that are currently in use: contact, non-contact and tapping modes. Contact mode consists in bringing the tip in close contact with the sample so that the repulsive Van der Waals forces dominate. The non contact AFM principle is based on detection of the attractive Van der Waals forces. Those forces being very weak, the cantilever is first given a little oscillation. The forces are detected by the changes in amplitude, phase or frequency of the oscillations. In tapping mode, the tip is given a high oscillation and is constantly touching and lifting off the surface. When the tip is touching the surface, it encounters both repulsive and attractive Van der Waals forces that reduce the amplitude of oscillation due to the contact. This loss of amplitude is measured and used to build up an image of the surface.

The AFM pictures present in this thesis have been taken at Swansea University in the Centre for Complex Fluids Processing. The AFM system used was a Dimension 3100 with Nanoscope IV controller. The cantilevers used were standard Olympus Tapping Mode Silicon Nitride (boron coated) and images were realised in non contact mode.

8. Pulsed Flow reactor set up

A pulsed flow microreactor was used to obtain TPD profiles from the different samples [19]. A diagram of the reactor is shown in Figure 28. The microreactor consists of a stainless steel tube (15 cm long, 3 mm inside diameter) mounted horizontally in a tube furnace (Carbolite MTF10/15/130), which can be maintained at constant temperature or ramped between two temperatures at a constant rate. Two gases can be passed continuously through $1/8^{th}$ inch stainless steel tubing and over the sample bed (comprising of 0.5 g of sample held in place by quartz wool plugs), whilst a third gas may be introduced in 0.36 cm^3 pulses. The gas was introduced in the tube via a Taylor Sevromex six-port sampling valve. The pneumatic sampling valve moves by compressed air (60 psi) and is computer controlled. Mass flow controllers were used to set the gas flow. Manual injections were also possible through a PTFE septum assembly and under continuous flow conditions. The gas was injected by means of a Razel A-99 syringe. A ramp rate of 10 $K.min^{-1}$ was employed during the TPD experiments and a thermocouple (Eurotherm 2416 CG controller thermocouple) was inserted axially into the catalyst bed to accurately measure the temperature. Products resulting from the reactions were carried by a helium flow into a quadrupole mass spectrometer and the results were recorded in real time using a computer.

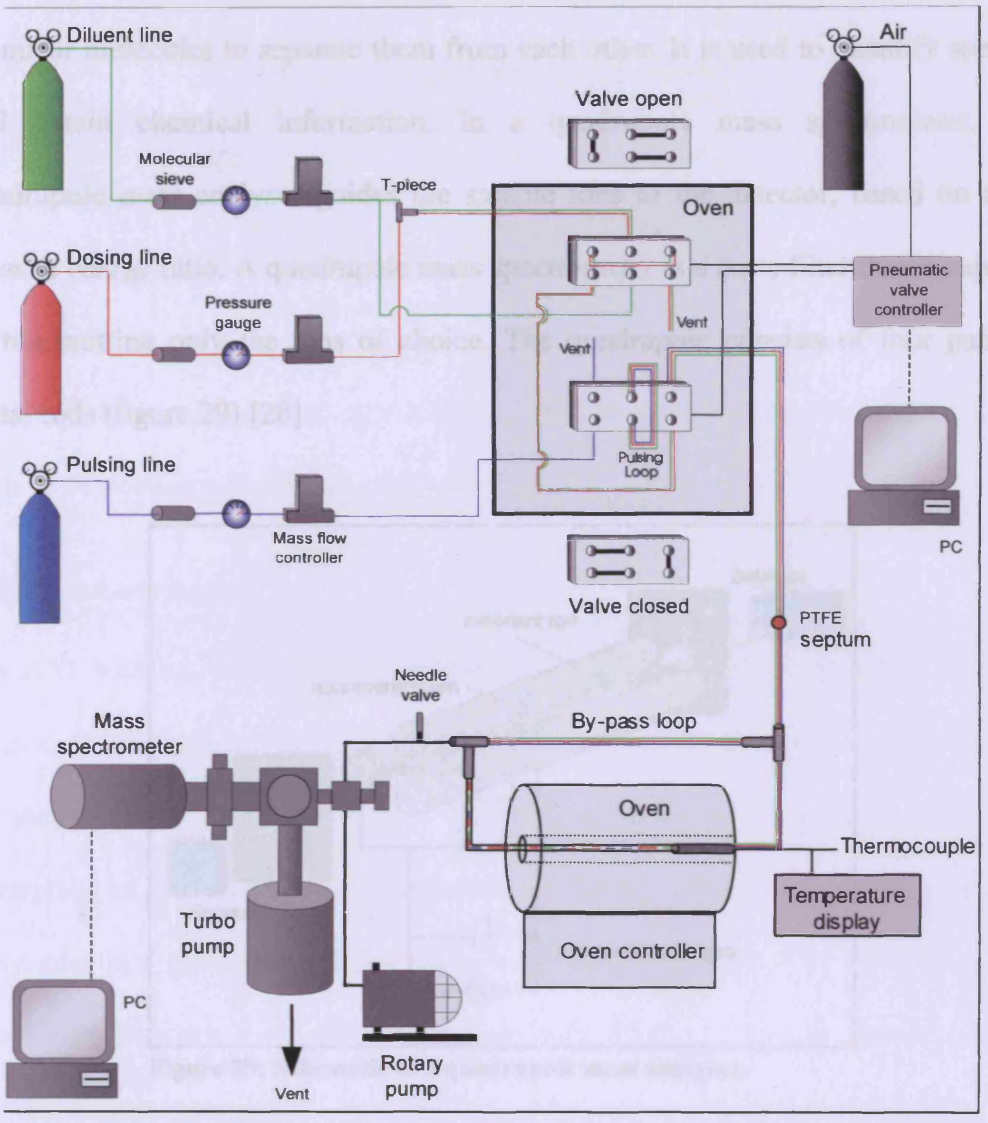

Figure 28: Schematic of the pulsed flow microreactor

Various products were followed by the mass spectrometer as the temperature of the system was increased. The masses of the species followed were H_2 (2g.mol^{-1}), H_2O (18g.mol^{-1}), NH_3 (17g.mol^{-1}), O (16g.mol^{-1}), N (14g.mol^{-1}), CO (28g.mol^{-1}), O_2 (32g.mol^{-1}), HCl (36.5g.mol^{-1}) and CO_2 (44g.mol^{-1}).

The mass spectrometer (Hidden Analytical quadrupole Hal 201) is kept under high vacuum via a turbo pump attached to a rotary pump. The principle of those pumps is described in paragraph 2.2.

Mass spectrometry uses the difference in mass to charge ratio (m/z) of ionised atoms or molecules to separate them from each other. It is used to quantify species and obtain chemical information. In a quadrupole mass spectrometer, the quadrupole mass analyser guides the sample ions to the detector, based on their mass to charge ratio. A quadrupole mass spectrometer is a mass filter that is capable of transmitting only the ions of choice. The quadrupole consists of four parallel metal rods (figure 29) [20].

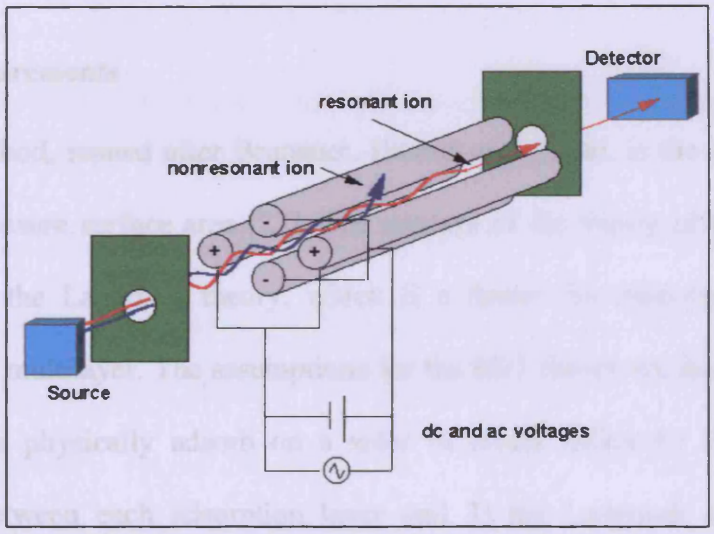

Figure 29: Schematic of a quadrupole mass analyser.

Each pair of rods is connected to a variable DC voltage source [21]. A 180° out of phase AC voltage source is superimposed on the DC voltage. As a voltage is applied to the rods, the ions travel through the quadrupole between the rods. Both AC and DC voltages are scanned, causing all but single m/z ratio at any given time to strike a rod, converting it to a neutral. Ions travel in a helical fashion (figure 30). There are two possibilities for the ions trajectory: 1) the ions have a stable trajectory where the oscillations are finite; 2) the oscillations grow exponentially and approach infinity, leading to the collision of the ions with the rod.

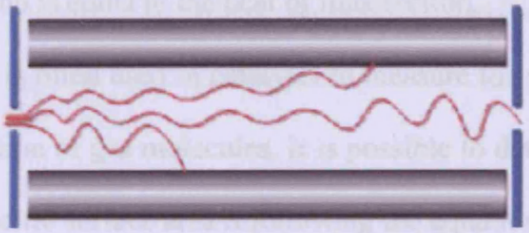

Figure 30: ion trajectory between the rods

A mass spectrum is obtained by monitoring the ions passing through the quadrupole filter as the voltages on the rods are varied.

9. BET measurements

The BET method, named after Brunauer, Emmet and Teller, is the most common method to measure surface area [22]. The concept of the theory of the BET is an expansion of the Langmuir theory, which is a theory for monolayer molecular adsorption, to multilayer. The assumptions for the BET theory are the following: 1) gas molecules physically adsorb on a solid in layers infinitely; 2) there is no interaction between each adsorption layer and 3) the Langmuir theory can be applied to each layer.

The resulting BET equation is:

$$\frac{1}{v[(P_0/P)-1]} = \frac{1}{v_m c}\left(\frac{P}{P_0}\right) + \frac{1}{v_m}$$

Where P and P_0 are the equilibrium and the saturated pressure of adsorbates at the temperature of adsorption, v the adsorbed gas quantity (for example in volume units) and v_m the monolayer adsorbed gas quantity; c is the BET constant which equals:

$$c = \exp\left(\frac{E_1 - E_L}{RT}\right)$$

Where E_1 is the heat of adsorption for the first layer and E_L is that for the second and higher layers and is equal to the heat of liquefaction.

The BET isotherm is often used in catalysis to measure the surface area of catalysts by physical adsorption of gas molecules. It is possible to determine the total surface area S_{total} and a specific surface area S following the equations:

$$S_{total} = \frac{v_m N s}{M}$$

$$S = \frac{S_{total}}{a}$$

Where N is the Avogadro constant in mol^{-1}, s is the adsorption cross section in m, M the molecular weight of adsorbate in $mol.g^{-1}$ and a the weight of the sample in g.

BET measurement is based on the isothermal physisorption of N_2 at the surface of a material. N_2 molecules tend to form at low temperature a monolayer which depends only on the size of the N_2 molecule (which is known) and not of the material to analyse. In a first time, the sample is heated up to remove the contamination, water, from the sample that brings error of the measurement of the surface area. Then the sample is cooling down in liquid nitrogen and the adsorption of N_2 takes place at 77K. The pressure on nitrogen is increased to ensure the maximum adsorption of N_2 at the surface. Finally, the sample is heated up until room temperature and the desorption of nitrogen is measured.

The surface area is measured with a QSurfM1 surface area analyser that is a continuous flow BET and employs the multipoint BET method. Variable N_2/He mixture was used with a range of values, six points in all. Every gas injection within the machine was pre-calibrated by a loop valve injection.

10. References

1. Smith R.D., *Scanning Tunnelling Microscopy Studies of the Structure and Reactivity of Model Oxide-Supported Catalysts*, PhD thesis, Reading University, 2003.
2. Chambers A., Fitch R.K. and Halliday B.S., *Basic Vacuum Technology*. Second Edition: Institute of Physics.
3. *ST22 Titanium sublimation pump cartridge – Operating instructions*, Fisons Instrument Vacuum Generators, 1994.
4. *VTSTM MkII – Variable Temperature STM in surface Lab – Operator's handbook*, Oxford Instrument, 1997.
5. Personal communication: Stone P., *Scanning Tunnelling Microscopy*, Report, Reading University, 1996.
6. Woodruff D.P., Delchar T.A., *Modern techniques of surface science*. 2nd edition: Cambridge University Press, 1994.
7. Bonnell D.A., *Scanning Tunneling Microscopy and Spectroscopy: theory, Techniques and Applications*: VCH publisher, 1993.
8. TOPSystem 3 Advanced SPM controller, Operator's handbook, Oxford Instrument, 1997.
9. Strappazzon, A., *Etude par microscopie à effet tunnel de monocouche auto-assemblée*. 2002, Dissertation, Facultés Universitaires Notre Dame de la Paix: Namur.
10. Attard, G. and C. Barnes, *Surfaces*. Vol. 59: Oxford Chemistry Primers, 1998.
11. *Scanning Probe Microscopy system instrumentation for surface science,* WA Technology, 1997.

12. Drybanski, A., *Variable Temperature STM.* 1996, topac Inc. Available from: http://www.topac.com/to3012.html
13. Vickerman, J.C., *Surface Analysis: The principle techniques.* Wiley, 2000.
14. Childs K.D., Carlson B.A., LaVanier L.A., Moulder J.F., Paul D.F., Stickle W.F. and Watson D.G., *Handbook of Auger Electron Spectroscopy.* Physical Electronics, Inc., 1995.
15. Seah M.P. and Dench WA, *Quantitative electron spectroscopy of surfaces: a standard data base for electron inelastic mean free paths in solids.* Surface Interface Analysis, 1979. **1**: p. 2.
16. Tanuma S., Powell C.J. and Penn D.R., Surface and Interface Analysis, 1993. **21**: p. 165.
17. Tanuma S., Powell C.J. and Penn D.R., *Electron inelastic mean free paths in solids at low energies.* Journal of Electron Spectroscopy and Related Phenomena, 1990. **52**: p. 285.
18. Birdi K.S., *Scanning Probe Microscopes: applications on science and technology.* Flammarion, 2003.
19. M^{c}Cormack E., *NO_x storage -reduction catalysis.* 2004, MChem Report, Cardiff University.
20. *Quadrupole mass analyser*, www.wikipedia.org.
21. Petrovic S., *Chapter 11 and 20 - Mass spectrometry.* 2003, Southern Oregon University Available from: http://www.sou.edu/chem/ch425/MassSpec-Chapter20/index.htm
22. Brunauer S., Emmett P.H. and Teller E., *Adsorption of gases in multimolecular layers*, 1938. **60**: p.309-319.

Chapter 3

Physical properties of nanoparticles

1. Introduction

STM has been the main method to analyse the formation of particles and their behaviour depending on the surface treatment in the work to be reported in chapter 4. In this chapter, some of the fundamental properties of nanoparticles are examined from a mathematical point of view. In a first part, the volume of adsorbate and the number of atoms dependence on coverage will be determined. In the second part, the basic properties of nanoparticles will be described; defining surface area-size relationship. This is then compared to the results from STM imaging and Auger analysis. The third part will describe the different modes of particle growth and how they can be related to AES data. The fourth part will focus on the deposition and sintering process, on the structural changes involved and the relation to thermodynamic and kinetic for the nanoparticle evolution. Finally, the last part will relate to the relevance of this information to catalysis. Knowing how an adsorbate on a surface can help to understand PFR spectra and the catalytic reaction taking place. The aim of this chapter is to bring information on the behaviour of nanoparticles at the surface when subjected to variations in the coverage and temperature.

2. Properties of monolayers

Considering the deposition (MVD) and formation of 1 monolayer of Cu, i. e. a single layer of chemisorbed metallic atoms: Cu has a fcc structure with $a = 3.6149\,\text{Å}$ [1] and deposits in the (111) plane on a TiO_2 crystal support.

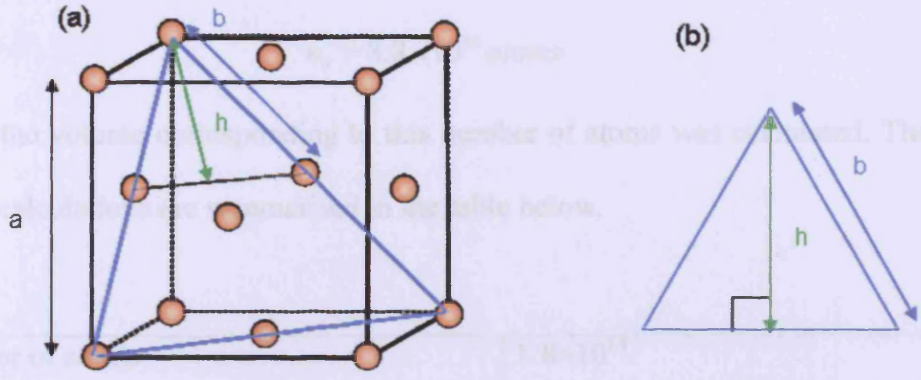

Figure 1: (a) fcc (cubic close-packed) crystal structure. h is half the length across the unit cell of the (111) plane. b is the interatomic distance in the (111) plane. (b) 1D schematic of the triangle in (a). From b, it is possible to calculate h.

Figure 1 shows the structure of the unit cell of copper. In reality, some of the atoms are touching each other within the unit cell (closed packed). The number of atoms on 1cm^2 surface (A), for 1 monolayer coverage can be calculated. First the radius of the Cu particle is determined by calculating the distance between 2 atoms in the (111) plane.

$$b = a\frac{\sqrt{2}}{2} \qquad (1)$$

$$b = 2r_{Cu} = 2.556\,\text{Å}$$

When atoms are hexagonally packed, they block an area of ABCD (figure 2).

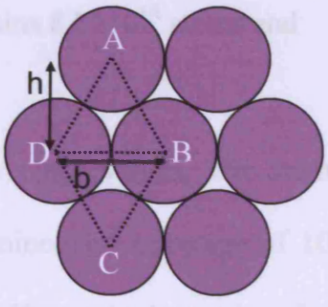

Figure 2: model for the space occupied by 1 atom on a support. The dashed shape correspond to the unit cell of a (111) plane. h is the height of a dashed triangle, b is the base length. A triangle contains 3/6th part of one atom. The contact area of an atom is then equals to 2 times the area of the triangle.

From figure 1, using Pythagoras theorem,

$$h = b\frac{\sqrt{3}}{2} \qquad (2)$$

Thus, $S_0 = 2bh = b^2\sqrt{3}$ (3)

Where S_0 is the total amount of surface occupied by one atom.

The number of atoms, n_0 is given by

$$n_0 = \frac{A}{S_0} = \frac{A}{b^2\sqrt{3}} \quad (4)$$

So $n_0 = 8.8\times10^{14}\,atoms$

Then, the volume corresponding to this number of atoms was calculated. The details of the calculations are summarised in the table below.

Number of atoms	8.8×10^{14}
Number of moles With $A = 6.023\times10^{23}$ = Avogadro constant	$\frac{8.8\times10^{14}}{A} = 1.47\times10^{-9}$ moles
Weight in g with $M = 63.546 g.mol^{-1}$	9.3×10^{-8} g
Volume in cm^3 with $\rho = 7.11 g.cm^{-3}$	$1.31\times10^{-8} cm^3$

Table 1: Determination of the volume of $1.76x10^{15}$ atoms of copper by calculation of the number of moles, followed by the weight using the molecular weight of one copper atom and finally the volume using the density of copper.

One monolayer of adsorbate deposited over 1 cm^2 area contains 8.8×10^{14} atoms and represents a volume of $1.31\times10^{-8}cm^3$.

The same calculations were carried out using different coverage values. The atom number and total volume of material deposited was determined for coverage of 10 monolayers and 0.1monolayer and is summarized in table 2. The equivalent values for Pd are summarized in table 3. It is assumed that the number of atoms is proportional to the coverage: $n_\theta = n_0 \times \theta$.

Coverage, θ	Number of atoms, n_0	Volume, V_T /cm^3
10	8.8×10^{15}	1.31×10^{-7}
1	8.8×10^{14}	1.31×10^{-8}
0.1	8.8×10^{13}	1.31×10^{-9}

Table 2: Number of atoms and total volume of copper at different coverages.

Coverage, θ	Number of atoms, n_0	Volume, V_T /cm^3
10	7.6×10^{15}	1.12×10^{-7}
1	7.6×10^{14}	1.12×10^{-8}
0.1	7.6×10^{13}	1.12×10^{-9}

Table 3: Number of atoms and total volume of palladium at different coverages. With ρ=12.023g.cm^{-3} and M= 106.42g.mol^{-1}.

3. Properties of nanoparticles

3.1. Basic properties: perimeter, area and volume

Assuming that the particles are hemispherical, then the following equations can be used to determine the perimeter, P, the exposed surface area, S and volume, V of one hemisphere [2]:

$$P = 2\pi r \qquad (5)$$

$$S = 2\pi r^2 \qquad (6)$$

$$V = \frac{2}{3}\pi r^3 \qquad (7)$$

Where r is the radius of a particle.

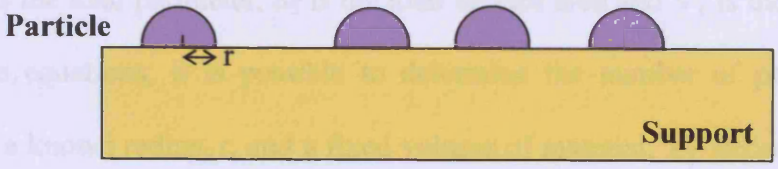

Figure 3: schematic of ideal particles deposited on a surface

Three curves can be derived from those equations and superimposed on the same graph. The aim of those curves is to give an idea of the trend of the volume, area and perimeter change as a function of the radius of the particles.

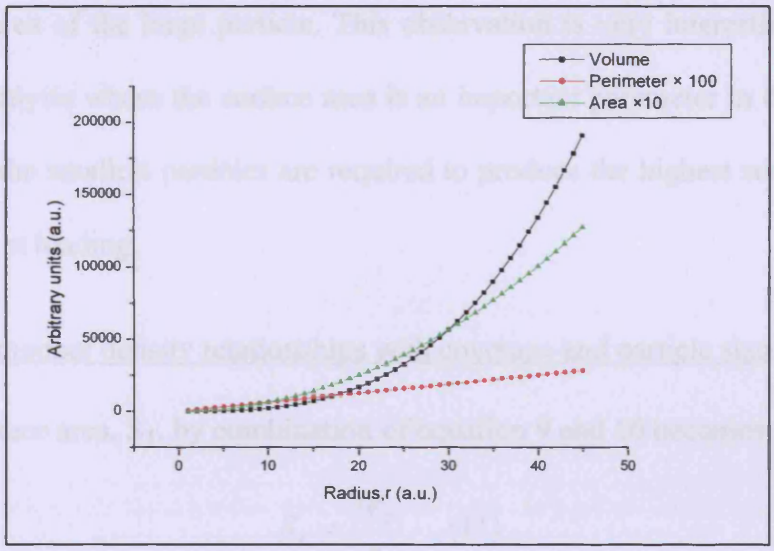

Figure 4: graphical form of equations 1, 2 and 3

As the radius of the particles increases, the perimeter follows a linear increase, the area increases by a power of 2 and the volume by a power of 3.

When considering a complete system, composed of a multitude of nanoparticles, then a new variable is added: n, the number of particles. Those equations become then dependant on n when more than one particle is involved. They are then expressed as follows, in the limit that particles are not touching:

$$P_T = n2\pi r \qquad (8)$$

$$S_T = n2\pi r^2 \qquad (9)$$

$$V_T = n\frac{2}{3}\pi r^3 \qquad (10)$$

Where P_T is the total perimeter, S_T is the total surface area and V_T is the total volume. From those equations, it is possible to determine the number of particles on the surface for a known radius, r, and a fixed volume of material, V_T, deposited. It is also possible to determine the surface area of 1 particle and compare it to the area of a

group of particles. For example, a particle of radius 8nm has the same volume as 512 particles of radius 1nm (equation 10) and has a surface area 64 times larger than the area of one particle of 1nm (equation 9). However, 512 particles of 1nm have 8 times the surface area of the large particle. This observation is very interesting when it is related to catalysis where the surface area is an important parameter in the activity of the catalyst; the smallest particles are required to produce the highest surface area for a fixed catalyst loading.

3.2. Particle number density relationships with coverage and particle size

The total surface area, S_T, by combination of equation 9 and 10 becomes:

$$S_T = \frac{3V_T}{r} \qquad (11)$$

Thus, for a fixed volume of material deposited, the total surface area of the particles will decrease as the radius of the particles increase despite the fact that the surface area of one particle will increase with its radius (equation 6). This is due to the big decrease in n, as shown in equation 14 (below). In order to appreciate the importance of this equation, an example is described below.

The surface area can be also represented as follows:

$$S_T = \frac{3W}{\rho r} \qquad (12)$$

or as

$$S_p = \frac{3}{\rho r} \qquad (13)$$

Where S_p is the specific surface area, W is the total weight of nanoparticles and ρ their density. The graph displayed on figure 5 corresponds to the total surface area for 0.05g of Cu (density 7.11 $g.cm^{-3}$) and 0.05g of Pd (density 12.02 $g.cm^{-3}$) deposited on a substrate as a function of particle radius.

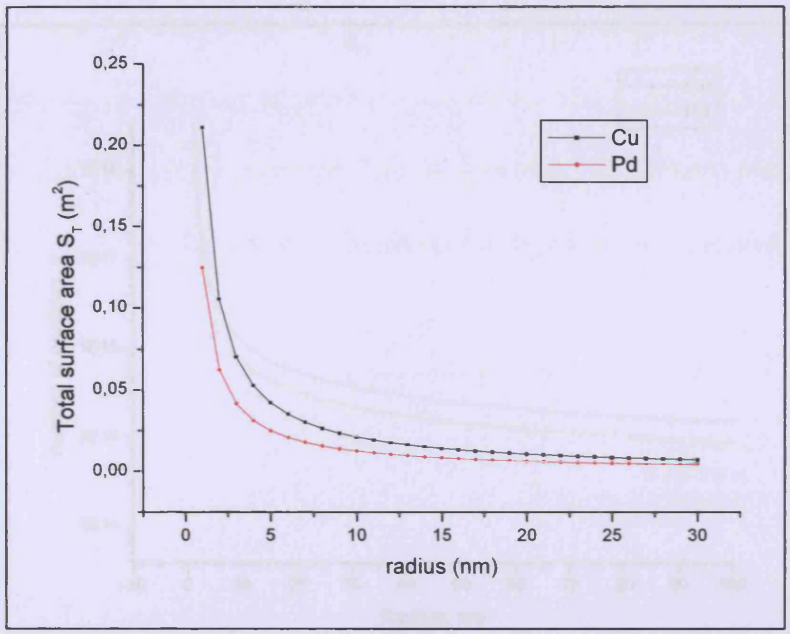

Figure 5: Total surface area variation with the particle radius for a fixed volume of material of copper and palladium. The y-axis is in logarithmic scale for clarity.

For the same radius of particle, there is a significant variation in surface area with atomic number, since there are fewer particles for heavier metals of the same total weight (figure 6).

Equation 10 can be rearranged into:

$$n = \frac{3V_T}{2\pi r^3} \qquad (14)$$

Figure 6 represents the graph of equation 14 for the example of copper and palladium. At a constant volume of metal, an increase in the radius of the particle will lead to a decrease in their number.

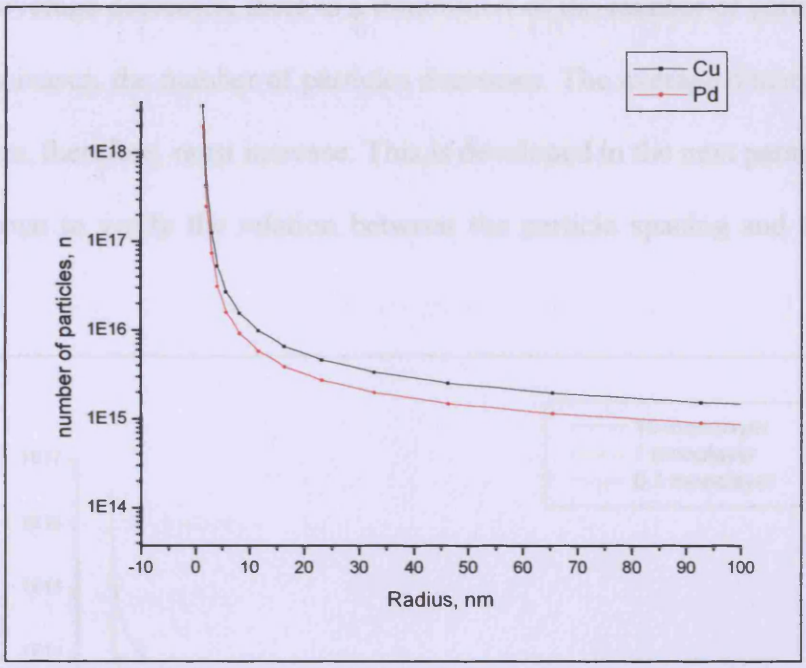

Figure 6: Particle density variation with radius of the nanoparticles. The particle density is proportional to $1/r^3$. The y-axis is in a logarithmic scale for clarity.

The first part of the plot shows a considerable decrease in the number of particles as the radius increases (until ~25-30nm). The curve follows a smaller decrease at longer radius. This is explained by using basic mathematical limits.

$$\lim_{r\to\infty}\frac{1}{r}\approx 0 \quad \text{so} \quad \lim_{r\to\infty} n \approx 0$$

$$\lim_{r\to 0}\frac{1}{r}=\infty \quad \text{so} \quad \lim_{r\to 0} n \approx \infty$$

The limit of $\frac{1}{r}$, when r tends to the infinite (∞), tends to zero whereas when r tends to zero, the limit tends to infinity. Equation 14 is in function of $\frac{1}{r^3}$, thus the number of particles is affected by a power of 3. As r becomes smaller, n tends to infinite as seen on the first part of the curve. While n tends to 0 as the radius increases.

Looking then at the variation of particle density with coverage (figure 7), one can see that as the coverage decreases, there is a diminution of the number of particles and as the radius increases, the number of particles decreases. The average distance between those particles, therefore, must increase. This is developed in the next paragraph and a model is drawn to verify the relation between the particle spacing and the particle size.

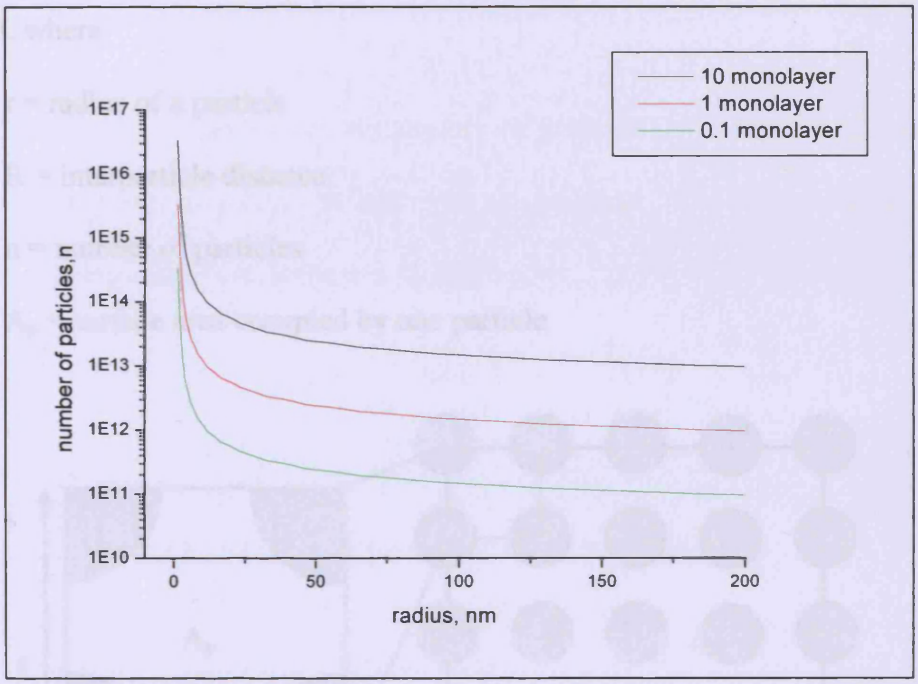

Figure 7: Copper particle frequency dependence on radius at different coverages. The assumptions are that the volume remains constant and the particles are hemispherical at all times. The y-axis is in the logarithm scale for clarity.

4. Relation between particle spacing and particle size

In order to follow the evolution of the particle size and position, particularly important during growth or sintering, a model is set up in order to correlate the particles sizes and their distances from each other at different coverages. In order to build up the model it is assumed that all the particles are 3D hemispheres with the same size and same separation and, for simplicity, they are in a square arrangement, as illustrated in figure 8, where

r = radius of a particle

R = interparticle distance

n = number of particles

A_p = surface area occupied by one particle

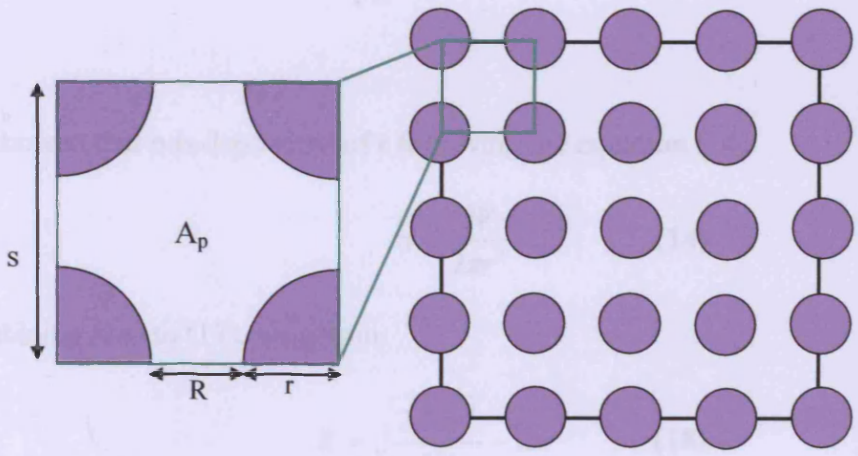

Figure 8: Ideal model of particle dispersion on a surface of constant area, A

The fixed parameter of the model is a constant volume of material deposited, V_T, and a constant total surface area, A while the variables are r, R and n for a given volume with n depending of r and R.

First, the relationship between the surface area and the particle size is determined. Considering the case of 1 particle, the area at the surface which the particle occupies is highlighted in green in figure 8 and can be expressed as:

$$A_p = s^2 = (R+2r)^2 \qquad (15)$$

Thus,

$$A = nA_p = n(R+2r)^2 \qquad (16)$$

Then as the radius (r) increases, the number of particles (n) decreases as seen in the previous paragraph in order to maintain A constant. The interparticle distance (particle spacing) therefore, increases as follows:

$$R = \sqrt{\frac{A}{n}} - 2r \qquad (17)$$

Or we showed that n is dependent of r following the equation (14):

$$n = \frac{3V}{2\pi r^3} \qquad (14)$$

By combining (14) to (17), we obtain:

$$R = \sqrt{\frac{2A\pi r^3}{3V}} - 2r \qquad (18)$$

Where A and V are constant.

Using equation (18), it is then possible to obtain the interparticle distance as a function of the radius of the particles. In addition, it is possible to plot the variation of the interparticle distance with the radius at different coverages.

From the calculation in section 2, table 1, the relationship between the coverage and the volume of material deposited on $1cm^2$ is:

$$V = \frac{n_0 M\theta}{A_v \rho} \qquad (19)$$

where n_0 is the initial number of atoms, M is the molecular weight, θ is the coverage, A_v is the Avogadro constant and ρ is the density.

By combining (18) and (19) the interparticle distance is expressed as:

$$R = r\sqrt{\frac{2A\pi\rho A_v}{3n_0 M\theta}} - 2r \qquad (20)$$

And, thus, the minimum radius for the particle can be calculated from the equation 20:

$$r_{\min} = \frac{6n_0 M\theta}{A\pi N_A \rho}$$

Where n_0 is the initial number of atoms, M the molecular weight, Θ the coverage, A the area of the sample, N_A the Avogadro constant and ρ the density of the material deposited.

Figure 9 displays a plot of the evolution of the interparticle distance of the nanoparticles as a function of the coverage and radius.

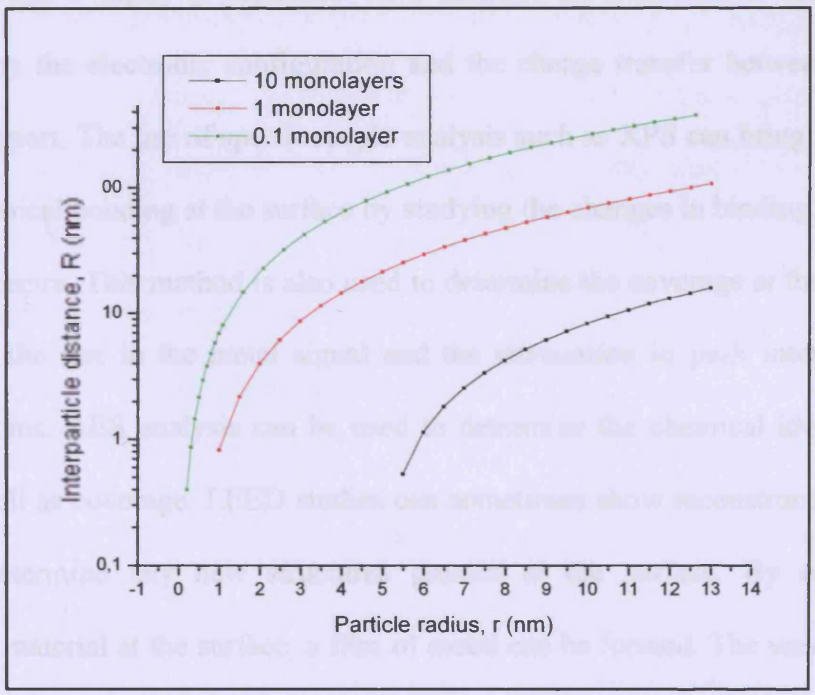

Figure 9: Plot of the interatomic distance as a function of the radius of Cu particles for different coverages. The y-axis is represented in a logarithmic scale for clarity.

The interatomic distance, R, increases when the particle size, r, increases. At $\theta < 1$ then R>0 when r equals the radius of one atom. For coverage higher than 1, the particles need to have a radius $\geq$ 5.5nm in order to be separated from each other. For particles of the same size, the interparticle distance R is larger as the coverage decreases, which is what expected. We showed earlier that, for a constant volume of material deposited, the increase of the particle size, r, lead to a decrease of the total surface area, S_T, due to a decrease of the number of particle, n, while the surface area, A_p of one particle increased. The model provided here is tested in the next section below by analyzing Cu and Pd distribution on TiO_2 from STM images and Auger spectra.

5. Particle growth at the surface

5.1. The growth mode of nanoparticles

There are a number of ways of varying complexity in which a metal interacts with a surface. When a metal is deposited on a surface, the structure at the surface is governed by the electronic configuration and the charge transfer between the metal and the support. The use of spectroscopic analysis such as XPS can bring information on the chemical bonding at the surface by studying the changes in binding energies on the XPS spectra. This method is also used to determine the coverage at the surface by measuring the rise in the metal signal and the attenuation in peak intensity of the support atoms. AES analysis can be used to determine the chemical identity of the layer as well as coverage. LEED studies can sometimes show reconstruction and can help to determine any new structures present at the surface. By continuously depositing material at the surface, a film of metal can be formed. The way these peak intensities change can give information on the way the film grows on the surface.

There are three main ways in which a film can grow on the surface. These can be formulated in terms of surface free energy criteria [3].

Considering the adsorbate surface free energy γ_A, the substrate surface free energy γ_S and the interface surface free energy γ_I, then the morphology of growth of the metal on the substrate will depend on the balance of those surface energies.

If $\gamma_A+\gamma_I<\gamma_S$, the adsorbate will have the tendency to spread over the surface in order to reduce the free energy of the substrate leading to a monolayer growth. When deposited, the atoms are bound more strongly to the substrate than they are to each other. They aggregate to form monolayer islands of deposit which enlarge as deposition continues until a complete monolayer has formed. This is due to the additional benefit of adatom-adatom binding. The surface energy of the substrate is then reduced by the first monolayer and the subsequent adsorbate does not experience the same interface energy. The adsorbate also has to adapt to the strain energy created by the first monolayer which increases with the film thickness. Thus, there are 2 possible ways for the adsorbate to grow. First possibility, fresh monolayer islands form on the first monolayer which results in the formation of a second monolayer. This growth mode is called Frank-Van der Merwe mode. The second possibility consists in nucleation following the monolayer formation. It involves the formation of one monolayer, or a small number of monolayers, followed by subsequent nucleation of 3-D islands on top of these monolayers. This growth mode is called Stranski-Krastanov mode.

If $\gamma_A+\gamma_I>\gamma_S$, the initial deposit atoms aggregate as small 3-D islands and leave the low energy substrate exposed. These islands increase in size as the deposition continues until they touch and grow to form a grainy film. This growth mode is

known as Volmer-Weber mode. Figure 10 displays a schematic of those growth modes.

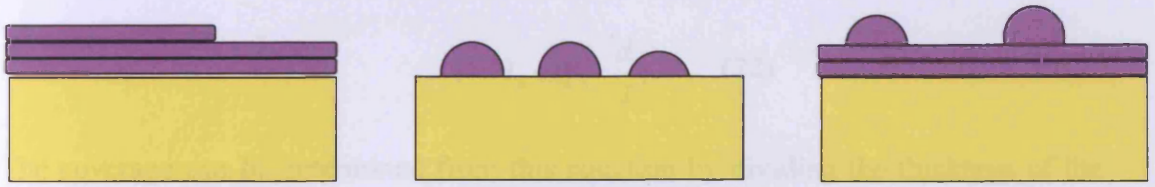

Layer by layer (Frank-Van der Merwe) | 3D islands (Volmer-Weber) | Layer by layer followed by 3D islands (Stranski-Krastanov)

Figure 10: Three most basic growth modes of thin film growth by vapour deposition

5.2. Distinguishing growth mode by AES

The Auger Electron Spectroscopy technique allows qualitative and quantitative determination of the material analysed [3]. As we have seen in the experimental chapter, AES gives a fingerprint of the chemical composition of the material surface. It is also possible to measure the concentration of elements present using the peak intensities shown on the spectrum. The deposition of adsorbate affects the signal of the substrate. The signal of the substrate decreases as the signal of adsorbate increases. Hence, it is possible to determine the coverage as long as a point of reference, of known coverage, is available. The relation between the thickness of the adsorbate with the surface peak intensity is given by [4]:

$$I = I_0 \exp(-\frac{d}{\lambda \sin\theta}) \qquad (21)$$

Where I is the integrated intensity of the surface peak, I_0 is the integrated intensity of surface peak at 0 coverage, λ is the inelastic mean free path (IMFP), d is the thickness of material deposited and θ is the emission angle of the electrons relative to the surface normal.

In the case of our experiments, the crystal is perpendicular to the electron beam so $\theta = 90°$

Knowing that $\sin 90 = 1$, the relation becomes

$$I = I_0 \exp(-\frac{d}{\lambda}) \qquad (22)$$

The coverage can be determined from this equation by dividing the thickness of the film by the height difference between 2 layers or by the thickness of 1 monolayer. As we have seen earlier, there are 3 basic modes for an adsorbate to grow on a surface. Taking the Volmer-Weber growth [5, 6], which consists in 3D islands growth, as more adsorbate is deposited, the islands grow in size and height and the substrate is still visible (figure 11 and 12).

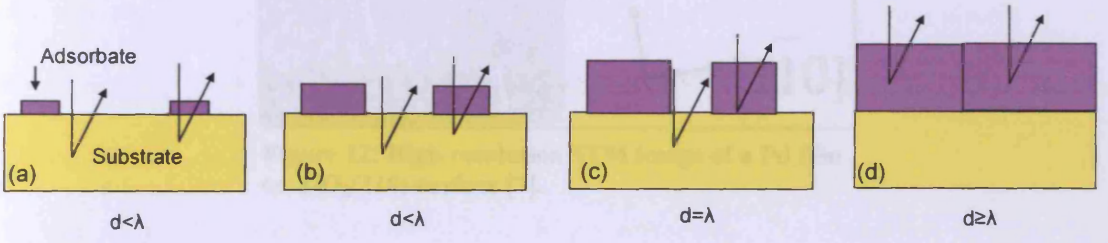

Figure 11: schematic of the particle evolution of the Volmer-Weber growth. The arrows represent the electron beam.

Looking at figure 11, in the cases (a) and (b), the coverage measurement is an average one. The Auger signal for the substrate, I, is an average between the covered and uncovered section. Figure 12 shows an STM image of an annealed Pd film on a $TiO_2(110)$ surface [7]. It is a good example of what happens in case of figure 11(b and c), where the substrate is still visible. The risk encountered here is to get a particle height bigger than the IMFP of the electrons (Figure 11 (c)). In this case, some substrate would still be uncovered and the signal from this part would be used to calculate the thickness. Thus, the coverage measurements would be not accurate without a good knowledge of the morphology of the film beforehand. When reaching case (d) then the substrate signal disappears while the adsorbate signal stays constant.

At that stage, coverage measurements may not be possible due to the loss of the substrate peak.

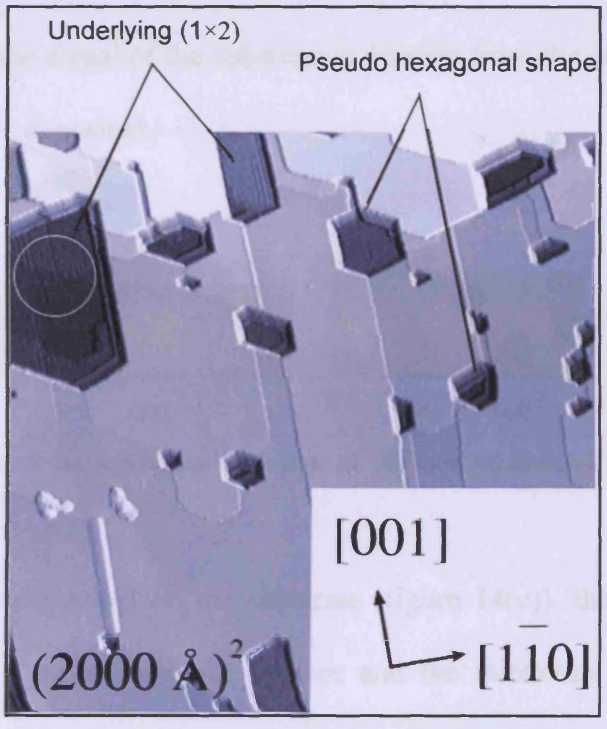

Figure 12: High resolution STM image of a Pd film on TiO_2(110) surface [7].

The plot of the Auger signal as a function of deposition time for such a growth mode is displayed in figure 13. AES is not well suited for examining the VW growth mode since the signal would vary slowly with deposited quantity and there is no monolayer break that can be used as a reference [3].

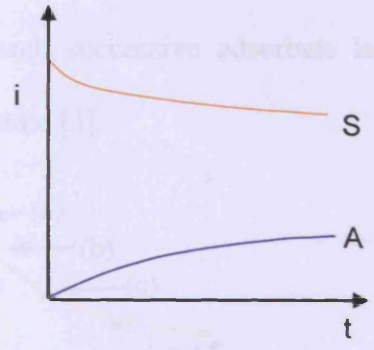

Figure 13: theoretical AS-t plot for the variation of the substrate (S) and adsorbate (A) signal (i) during the VW growth mode.

In the case of Frank-Van der Merwe mode [5, 6] the adsorbate is deposited monolayer by monolayer. Looking at figure 13(b), the substrate signal, in theory, decreases constantly as a monolayer is formed. Thus the calculation of the thickness is then more precise since the signal of the substrate is coming from the covered surface only when 1 monolayer is deposited.

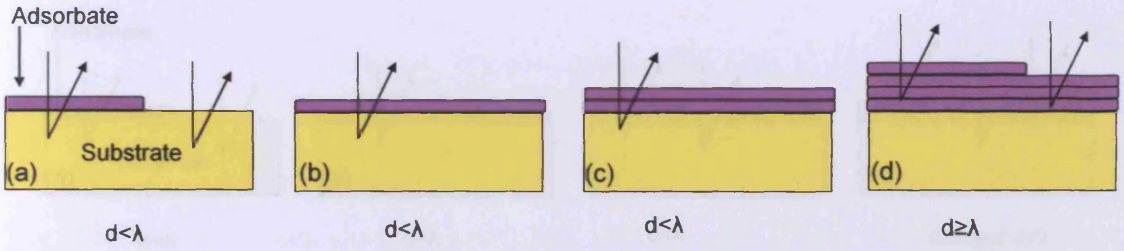

Figure 14: Schematic of the adsorbate evolution in the case of Frank-Van der Merwe growth mode.

As another layer is deposited on the substrate (figure 14(c)), the attenuation of the substrate signal is identical over the surface and the thickness of the film can be calculated.

Figure 15 displays the AS-t plot of the FM growth mode. The evolution of the signal with time is characterised by a series of linear segments of differing gradients. As one layer is built, the substrate signal decreases. Changes occur after completion of each monolayer by a kink or break in the plot. As another layer starts forming on the first layer, the signal decreases again but with a different slope. This is due to the effect of the each successive adsorbate layer that attenuates the signal generated from the substrate [3].

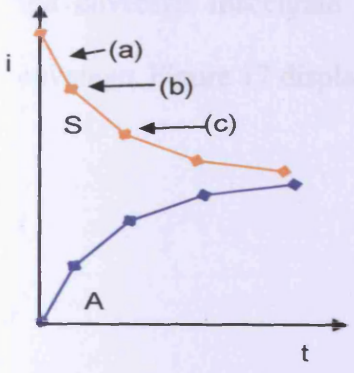

Figure 15: Theoretical AS-t plot for the variation of the substrate (S) and adsorbate (A) signal (i) during the Frank Van der Merwe growth mode.

In the Stranski Krastanov mode (SK), the adsorbate builds first as a monolayer and follows the same signal as observed for the FM growth. Beyond the monolayer coverage, the adsorbate starts to form 3D islands (Figure 16). The surface free energy is lowered once one monolayer is built. Depending on the surface free energy at the top of the first layer, either monolayer (FM mode) or 3D-islands will grow.

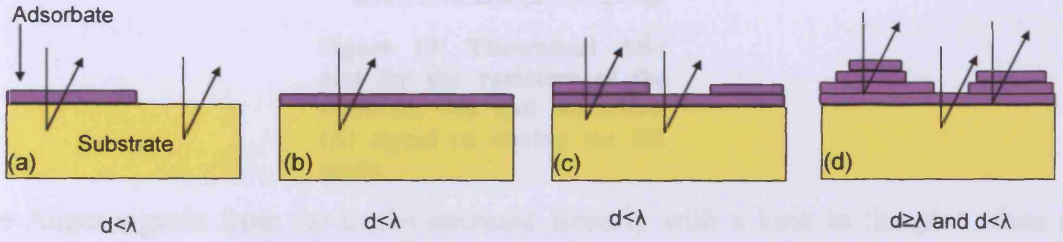

Figure 16: Schematic of the evolution of adsorbate for the Stranski Krastanov growth mode.

In the case of SK growth, the substrate signal is attenuated linearly until one monolayer is built (Figure 16 (a) to (b)). As more adsorbate is deposited (Figure 16 (c)), the substrate signal decreases, less than if the material was deposited in monolayers. The fraction of surface not covered by the 3D-islands can dominate in the emission of the substrate signal even up to very high coverages. This bring imprecision in the calculation of the thickness of the adsorbate. The risk of this method is the same as for the VW growth mode. When the island height is greater than the IMFP, significant substrate signal can still be detected (Figure 16(d)). Therefore the signal of the substrate slowly decreases as more material is deposited while the signal of the adsorbate slowly increases. This makes the measurements of the coverage inaccurate because the signal detected corresponds to an average coverage. Figure 17 displays the schematic AS-t plot of the SK growth mode.

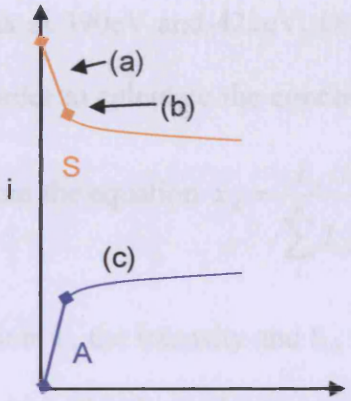

Figure 17: Theoretical AS-t plot for the variation of the substrate (S) and adsorbate (A) signal (i) during the SK mode.

The Auger signals from (a) to (b) decrease linearly with a kink in the plot when a monolayer is complete. This behaviour is identical to the early FM growth mode. Then after one monolayer completion, the plot is similar to the VM growth plot, where the substrate and adsorbate signal vary much more slowly [3].

5.3. Particular case of Cu and Pd

As an example, the growth curve for palladium and copper was determined using Auger analysis. The crystal of titania was first cleaned by successive cycles of sputtering and annealing until a clean Auger spectrum was obtained. Then, the deposition of palladium was carried out using the same evaporation current at various times.

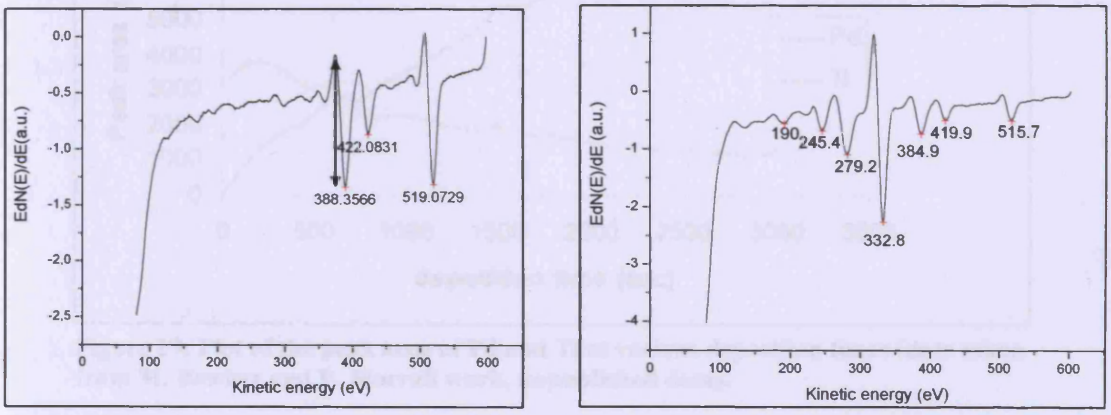

Figure 18: Auger spectra for (a) clean TiO_2 and (b) after a large amount of palladium deposition.

The intensity of the Ti peak at 390eV and 421eV, O at 510eV and Pd at 275eV and 333eV were measured in order to calculate the concentration in percentage of Ti and Pd species at the surface from the equation $x_A = \frac{I_A/S_A}{\sum_i^n I_i/S_i}$

Where x_A is the concentration, I_A the intensity and S_A the sensitivity factor of species. The different sensitivity factors of each species are summarised in the table below [9].

Element and energy (eV)	Sensitivity factor
Pd (283eV)	0.5673
Pd(333eV)	3.2842
Cu (66eV)	1.3451
Ti (390eV)	1.2155
Ti(421eV)	1.9280
O (510eV)	1.2571

Table 4: Auger sensitivity factors of the different elements present at the surface.

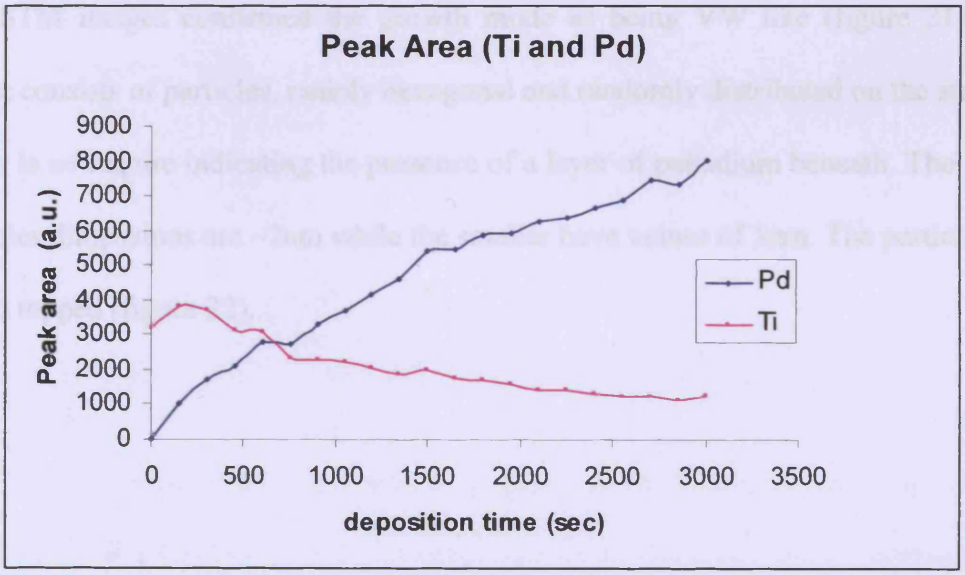

Figure 19: Plot of the peak area of Pd and Ti at various deposition times (data taken from M. Bowker and P. Morrall work, unpublished data).

By plotting the concentration of the species as a function of the deposition time, the graph on figure 19 was obtained. From the trend of the plot, the growth could be Stranski Krastanov (characterised by a linear then an exponential trend) or Volmer-Weber mode (the palladium plot follows an exponential growth). At 50mins, 2.5 monolayers of Pd were deposited.

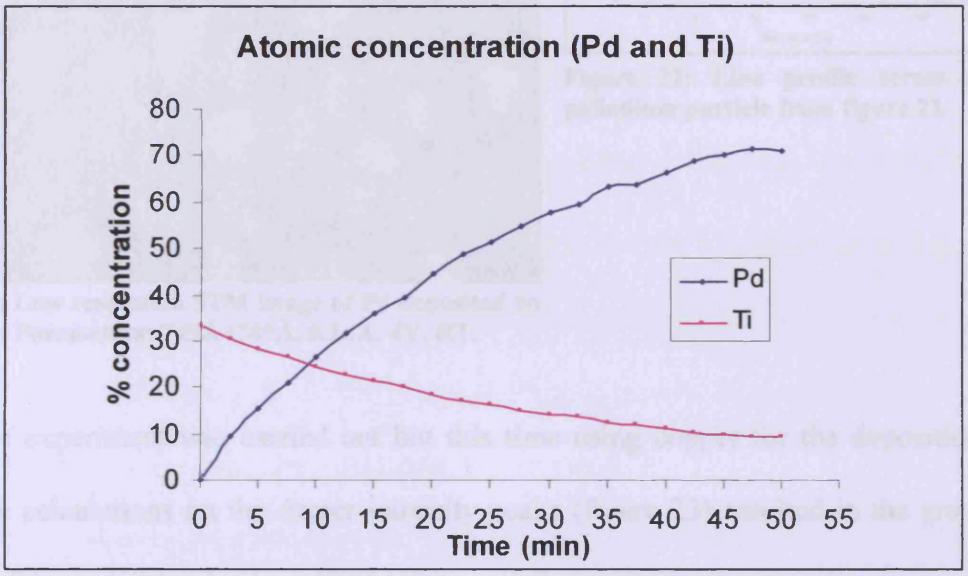

Figure 20: Atomic concentration of Pd on TiO_2 after successive deposition by MVD at RT (data taken from M. Bowker and P. Morrall work, unpublished data).

The STM images confirmed the growth mode as being VW like (figure 21). The image consists of particles, mainly hexagonal and randomly distributed on the surface. There is no feature indicating the presence of a layer of palladium beneath. The larger particles dimensions are ~7nm while the smaller have values of 5nm. The particles are round topped (figure 22).

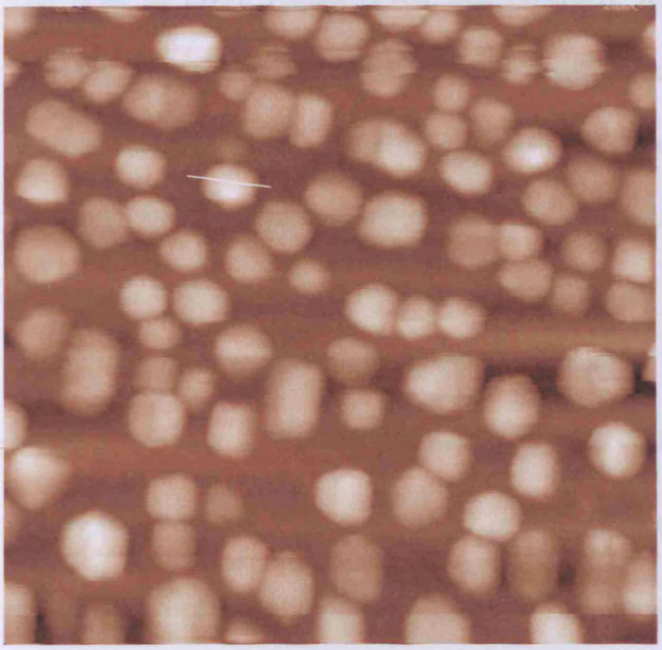

Figure 21: Low resolution STM image of Pd deposited on TiO_2(110). Parameters: 749Å×749Å, 0.1nA, 4V, RT.

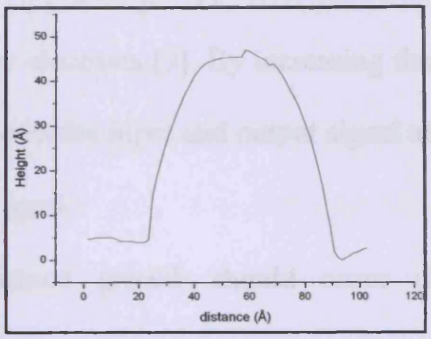

Figure 22: Line profile across a palladium particle from figure 21.

The same experiment was carried out but this time using copper for the deposition. The same calculations on the Auger intensity peaks (figure 23) resulted in the graph on figure 24.

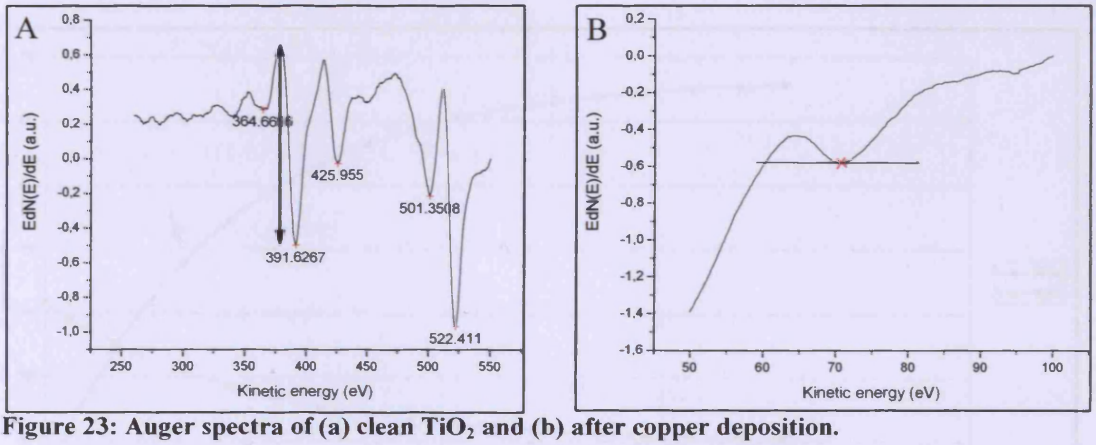

Figure 23: Auger spectra of (a) clean TiO_2 and (b) after copper deposition.

The Auger spectrum of copper results in peaks at 66eV and 922eV. The peak at 922eV was not taken into consideration because of the detection limits [8]. Peaks with higher kinetic energy have a larger width (FWHM: full width at half maximum is typically 3to 10eV) and therefore, at low coverages, it is difficult to resolve a peak.

The peak at 66eV (figure 23b) was detected by increasing the sensitivity of the analyser. The surface sensitivity of the Auger Electron Spectroscopy arises from the relatively short inelastic mean free path of for Auger electrons [9]. By increasing the sensitivity of the amplifier, it increases the gain between the input and output signal at any energy and thus it increases the intensity of the signal.

Based on thermodynamics, three dimensional island growth should occur if $\gamma_{TiO_2} < \gamma_{Cu} + \gamma_{Cu/TiO_2}$ where γ_{TiO_2} and γ_{Cu} are the surface free energies of the titania and the copper, respectively, and γ_{Cu/TiO_2} is the interfacial energy between the metal and the titania. Since the surface free energy of titania (~0.7J/m^2) is lower than that of copper (~1.3J/m^2), the islands should grow three-dimensionally unless a strong metal-oxide interface is formed [10]. For Cu, metal-TiO_2 is known to be relatively weak [11] and therefore 3-D island growth should be observed.

The plot of the species concentration obtained for the Cu deposition showed a similar trend line to the Pd plot described above.

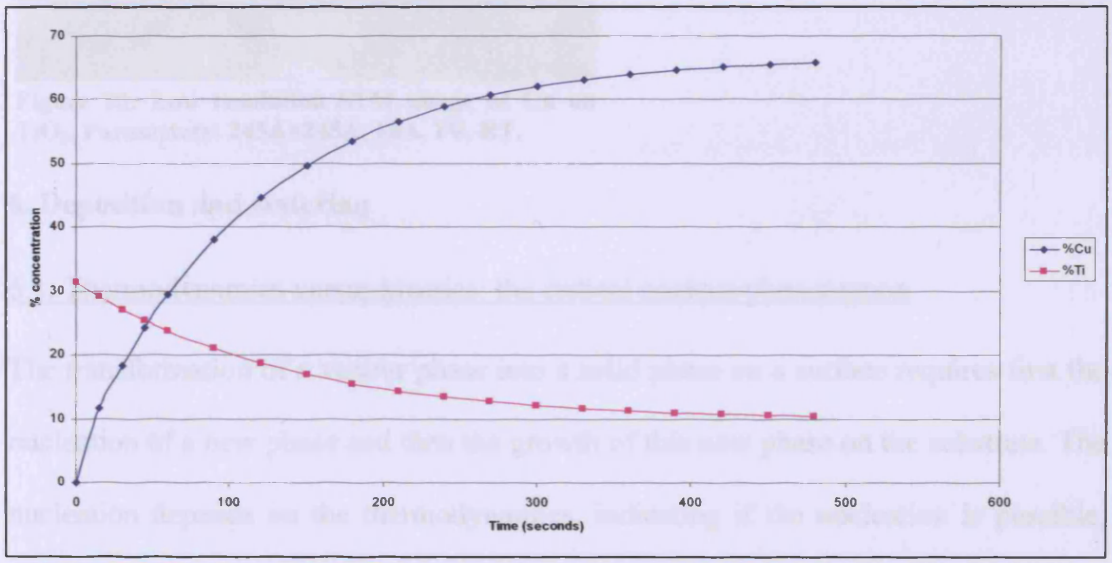

Figure 24: Atomic concentration of Cu on TiO_2 after successive deposition by MVD at RT.

As for Pd, the Cu plot follows an exponential growth indicating a VW growth mode in agreement with other studies [11]. The STM images taken after deposition confirm also the growth mode of the Cu metal on the surface (figure 25). Particles are distributed randomly at the surface with similar sizes and they appear to be of rounded shape. From the Auger peak intensities, the average coverage is 4 monolayers. The film of copper at the surface consists of numerous particles touching each other which is consistent with the Volmer-Weber growth mode.

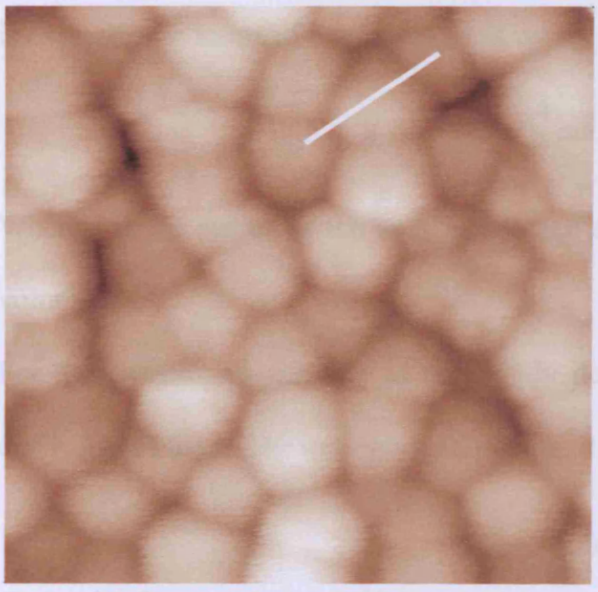

Figure 25: Low resolution STM image of Cu on TiO_2. Parameters: 245Å×245Å, 1nA, 1V, RT.

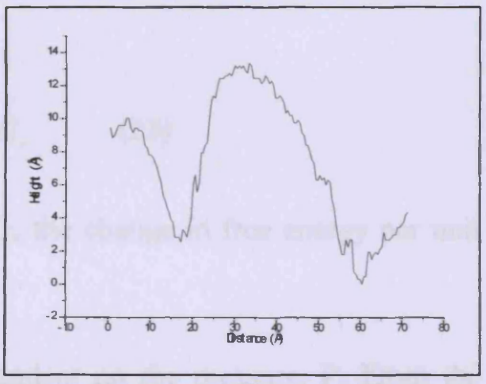

Figure 26: Line profile across the image on figure 25.

6. Deposition and sintering

6.1. Thermodynamics versus kinetics: the critical nucleus phenomenon

The transformation of a vapour phase into a solid phase on a surface requires first the nucleation of a new phase and then the growth of this new phase on the substrate. The nucleation depends on the thermodynamics, indicating if the nucleation is possible, and kinetics involving the nucleation rate, or how fast the reaction will happen. In order to reach equilibrium, the system must minimise its Gibbs free energy which involves two terms: first the volume transition from vapour to solid and then the

surface formation [12]. The rate of homogeneous nucleation is determined by the rate of formation of nuclei which maximise the free energy with respect to a property such as the radius. After the nucleus reaches this point, further growth becomes energetically favourable. This maximum in free energy arises from the contributions from the surface and from the bulk. As more of the system converts to the thermodynamically stable phase, the energy associated with the surface of the nucleus increases in proportion to the radius squared, but the energy of the bulk decreases proportionally to the radius cubed. Assuming spherical particles, the volume transition is expressed in terms of free energy following:

$$\Delta G = \frac{4}{3}\pi r^3 \Delta G_v \qquad (23)$$

Where r is the radius of the solid phase and ΔG_v the change in free energy per unit volume.

For this system, the activity is essentially dependent on the pressure, P. From the derivative of the Gibbs free energy equation, it can be deduced that:

$$\Delta G_v = \frac{kT}{\Omega} \ln \frac{P_s}{P_v}$$

Where Ω is the atomic volume, P_s is the pressure around the solid and P_v is the pressure of the vapour. It is necessary to have $P_v > P_s$ so that ΔG is negative (the reaction is then allowed). As a result, supersaturation provides the driving force for the nucleation of the solid phase.

The surface formation involves the free energy of a surface following:

$$\Delta G_{surf} = 4\pi r^2 \gamma \qquad (24)$$

Where γ is the surface energy per unit area.

From equations 23 and 24, the total energy change equals:

$$\Delta G_{total} = \frac{4}{3}\pi r^3 \Delta G_v + 4\pi r^2 \gamma \qquad (25)$$

By plotting ΔG as a function of r, the graph on figure 27 is obtained.

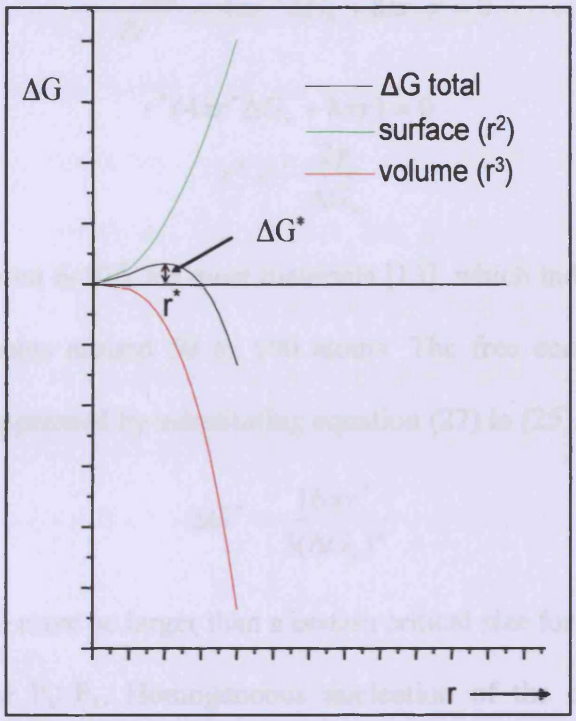

Figure 27: total free energy change, ΔG_{total}, of a particle as a function of its radius r and the change of its surface and volume free energy as a function of r.

Initially when the condensed particle is very small, the surface free energy term must be the larger of the two terms on the right hand side of equation 25, and so ΔG increases with r^2. In this range of sizes the particles are unstable. If $r<r^*$, then the nuclei shrink to lower ΔG until they disappear (desorption of the atoms). Above the critical nucleus size, however, the volumetric term becomes larger and dominates, since it decreases as r^3 while the surface free energy term increases only with r^2. Hence a particle of that size or larger grows spontaneously ($P_S>P_v$). Sintering of the particles will occur above this critical size in order to decrease the total energy, ΔG_{total}. This leads to a loss of the total surface area and in the case of catalysts to a

loss of the activity. When ΔG is at a maximum, that is $\frac{\partial \Delta G_{total}}{\partial r} = 0$, the particle reaches the critical size it must have for spontaneous growth to begin.

$$\frac{\partial \Delta G_{total}}{\partial r} = 4\pi r^{*2} \Delta G_v + 8\pi r^* \gamma = 0 \qquad (26)$$

$$r^* (4\pi r^* \Delta G_v + 8\pi\gamma) = 0$$

Then,
$$r^* = -\frac{2\gamma}{\Delta G_v} \qquad (27)$$

The value of r^* is about 6-10Å for most materials [13], which indicates that a particle of critical size contains around 50 to 100 atoms. The free energy of a particle of critical size can be expressed by substituting equation (27) in (25).

$$\Delta G^* = \frac{16\pi\gamma^3}{3(\Delta G_v)^2} \qquad (28)$$

A condensed particle must be larger than a certain critical size for spontaneous growth to occur at pressure $P_s > P_v$. Homogeneous nucleation of the condensed phase by simultaneous clustering of many vapour atoms to reach this critical size is, however, very improbable. This is why supersaturated vapour is needed. Ambient conditions in which vapour pressure are larger than the equilibrium vapour pressure ($P_s > P_v$) of a condensable substance can be established without the formation of the condensed phase. Precipitation in the absence of nuclei is very difficult, and larger pressures, much higher than he equilibrium vapour pressure ($P_s >>> P_v$) must be established before condensation can occur within reasonable experimental time. Because of the difficulty of homogeneous nucleation, growth of condensed phases generally occurs on solid surfaces already present. The introduction of solid crystallites to induce the formation and growth of the condensed phase is frequently called heterogeneous nucleation.

6.2. Modes of sintering

In the semiconductor industry, metallization of oxides requires the growth of uniform smooth films [14]. In heterogeneous catalysis small particles are required with a large surface area. This is why it is important to examine the changes in particle size at elevated temperatures. The performance of a catalyst can clearly be influenced by such changes. In the formation of clusters at the surface, three main steps are involved. During the deposition, the clusters first nucleate, then grow due to the imposed supersaturation. Finally, this supersaturation disappears when the deposition is stopped. In this final stage clusters continue to grow due to sintering. Sintering is a process whereby clusters increase their sizes and reduce their number. Two main mechanisms are a) coalescence and b) Ostwald ripening sintering (figure 28).

In a publication on sintering, M. Bowker explained [15]: "Coalescence sintering occurs when two clusters touch or collide and merge to form one bigger cluster. In contrast, Ostwald ripening sintering occurs when atoms leave small islands more readily than large islands to then transfer to another. Both clusters exchange atoms, but the rate of loss for the smaller is higher because of the lower average coordination of atoms at the surface and their relative ease of removal. Thus big clusters get bigger at the expense of smaller clusters that shrink and eventually disappear. The latter process is the usual form of sintering for metal clusters on a supported surface that are well spaced apart, although coalescence can occur for a higher density of clusters."

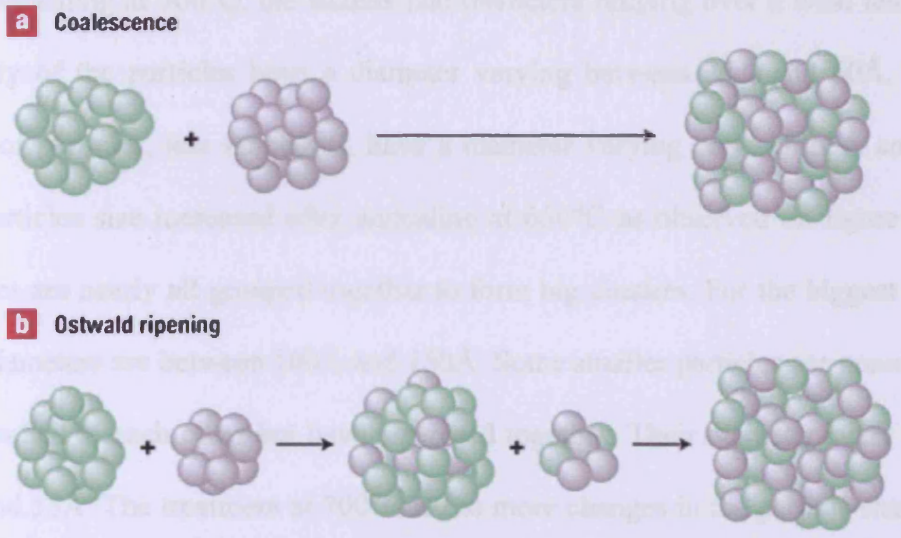

Figure 28: the two modes of sintering process at the surface. [15]

Usually the growth of the average particle size can be described by a power law that describes the radius as a function of time [14]:

$$r = r_0 + kt^{1/m}$$

Conclusions about the growth mechanism are often drawn directly from the value of m. For Ostwald ripening m=3 or m=4 is expected but in practice much higher values for m (5-11) are often found. Moreover, the value of m often decreases with the increase of temperature. The higher values of m are usually ascribed to particle growth due to coalescence. However, in spite of the many studies of the subject, there is still no satisfactory understanding of this ageing behaviour [14].

6.3. Application to Cu and Pd

After dosing Cu on the surface, sintering experiments were carried out. The STM images after each annealing sequence are shown on figure 29. The copper particles had an initial average diameter of 30Å. After annealing at 200°C, changes were observed in the location of the particle. They start assembling themselves into clusters and the particles had more or less the same sizes as before.

After annealing at 500°C, the islands had diameters ranging over a wide length. The majority of the particles have a diameter varying between 25Å and 60Å. Another group of particles, less numerous, have a diameter varying between 65Å and 120Å. The particles size increased after annealing at 650°C as observed on figure 29. The particles are nearly all grouped together to form big clusters. For the biggest clusters, their diameters are between 100Å and 150Å. Some smaller particles are present. They are attached to each other but have not fused together. Their diameters vary between 30Å and 55Å. The treatment at 700°C led to more changes in the particle shapes. The groups of smaller particles seen on the previous image have fused and large clusters are present at the surface with diameters ranging from 50Å to 100Å. Some small particles are still present between the large clusters. Finally, annealing at 750°C led to further sintering. It was difficult to scan, probably because of the height of the particles whose diameter was ranging from 200 to 300Å.

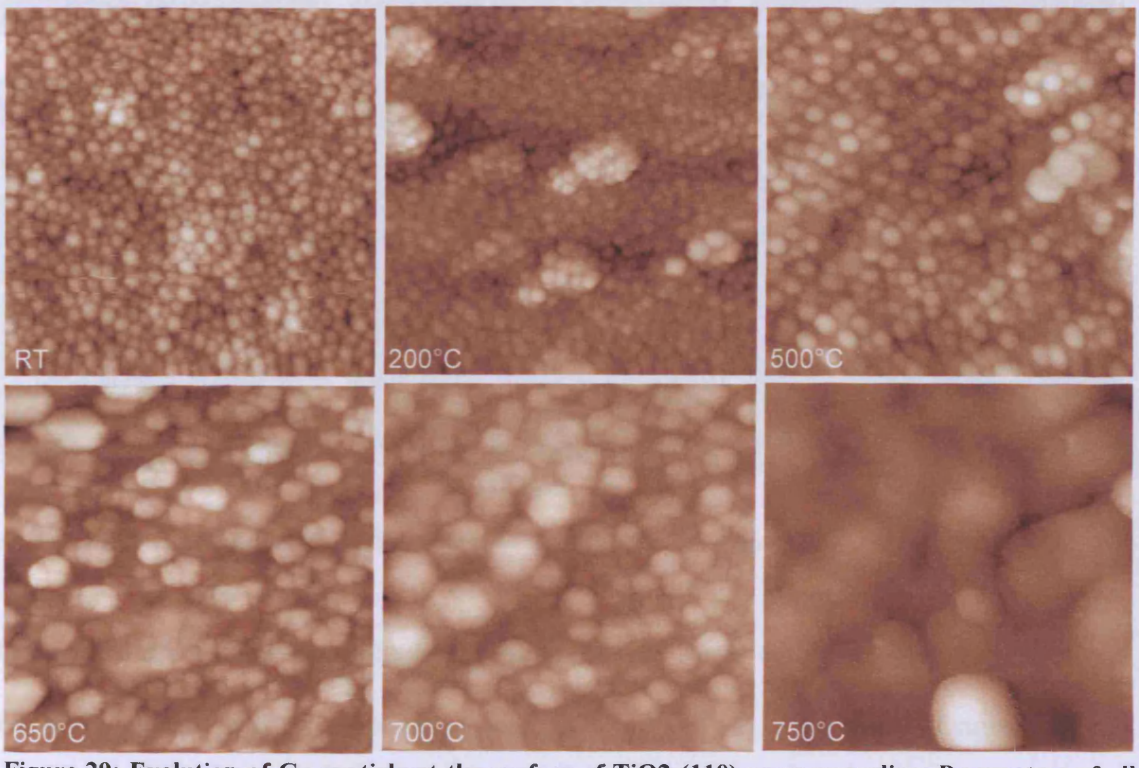

Figure 29: Evolution of Cu particle at the surface of TiO2 (110) upon annealing. Parameters of all the images: 998Å^2, 1nA, 1.5V.

Particle size distribution measurement was carried out on each image and are summarised in the following section.

The same experiments were carried out with palladium deposited on TiO_2(110). The data were collected in collaboration with Rupert Smith at Reading University. At room temperature, the particles covered the surface with not obvious preferential nucleation sites. The average diameter for the particle was ~15Å. As the annealing temperature was increased, the average diameter of the particles increased too. Between A and F, there is a discernable growth in the size of the particles.

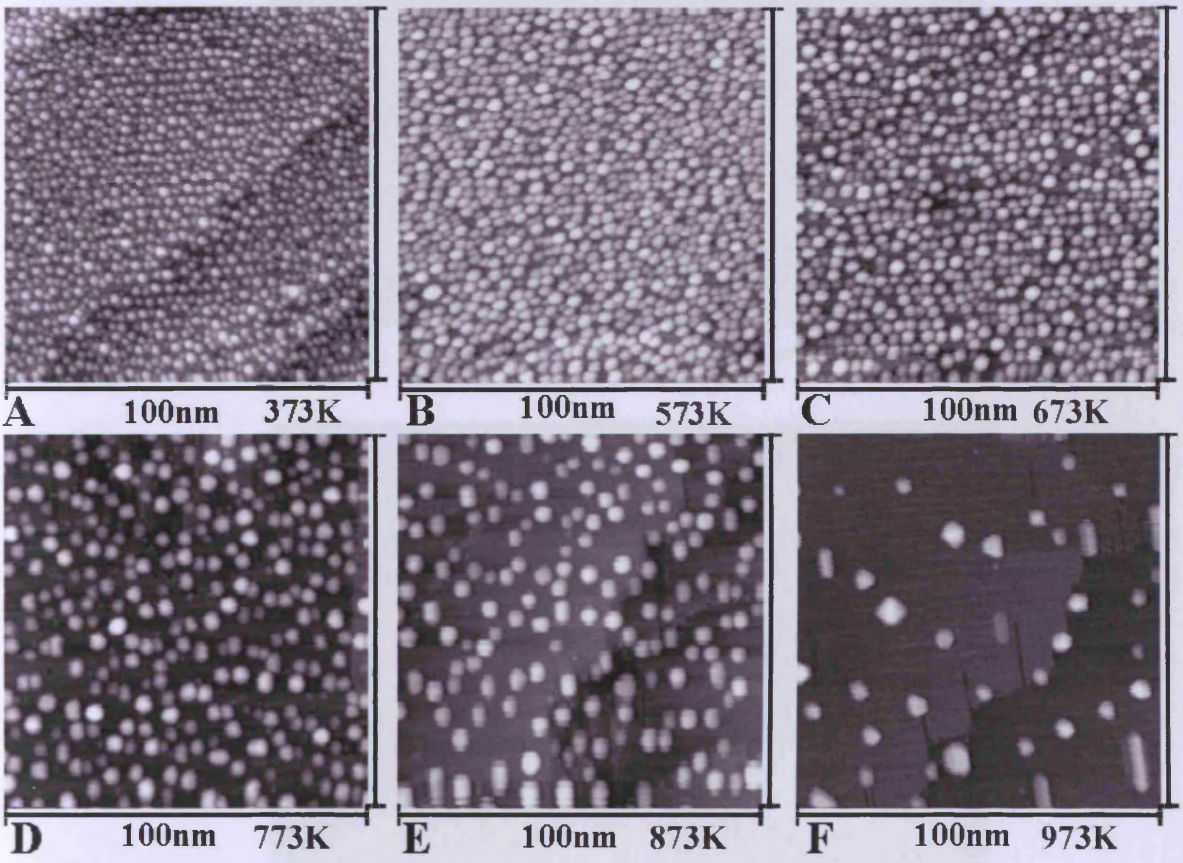

Figure 30: Evolution of Pd particle at the surface of TiO_2 (110) upon annealing.

After annealing at higher temperature, AFM images were collected. The particles were so big that it was not possible to image them by STM. Two AFM images are shown on figure 30 and 31 that were collected at Swansea University. The particle

diameters vary between ~500Å and ~1600Å. Those images were obtained after the sample was annealed at 1000°C.

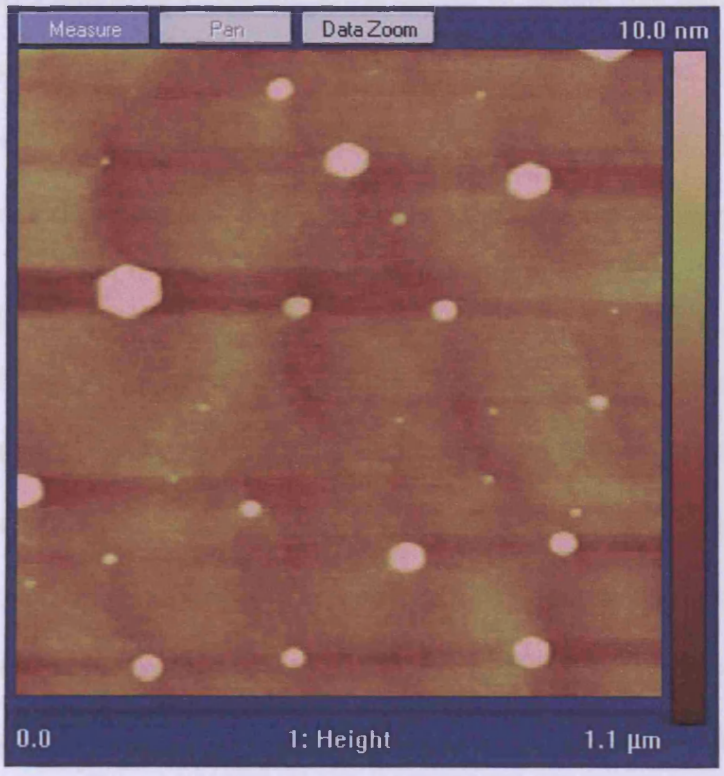

Figure 31: AFM image of Pd on TiO_2(110) after annealing at 1000°C.

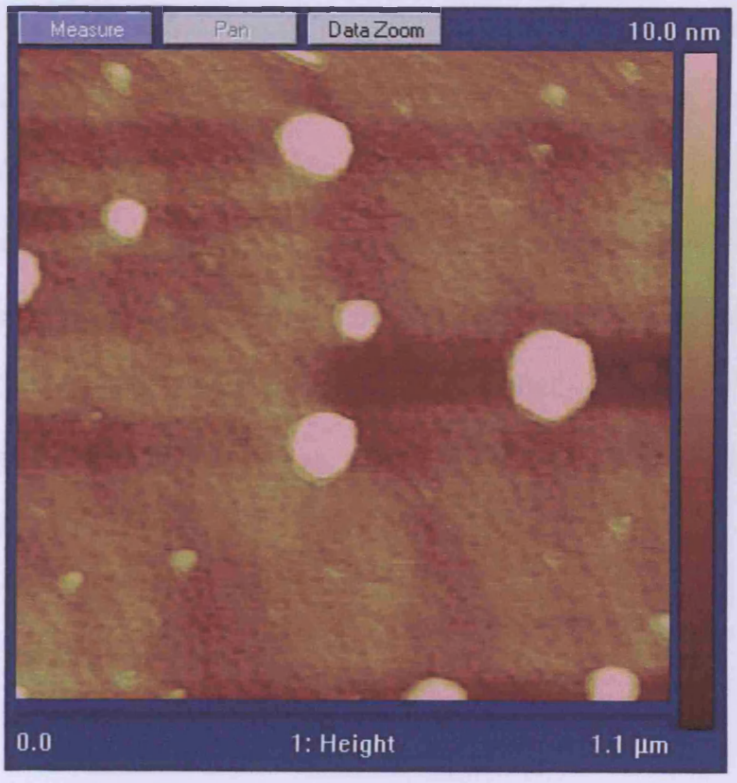

Figure 32: AFM image of Pd on TiO_2(110) after annealing at 1000°C.

The particles present at the surface are far apart from each other. They have a hexagonal shape for the biggest ones. When comparing those images with the models described in section 3 and 4, they confirm the equation 16 stating that the number of particles decreases as the radius increases. Equation 22 states that the interparticle distance increases with the particle radius which is also seen on figure 28. Particle size distribution measurements explained how the images were conform to the equations.

6.4. Particle size distribution

The particle size distribution (PSD) was determined for each of the images and the volume, height perimeter and area of each particle was obtained from the analysis. The PSD was done using in-house software. First a map of the image was produced showing the dispersion of the particles on the surface. This map was based on the rate of change of height within each scan line. This resulted in a black and white image, with the white areas consisting of the particles and the black area, the substrate. Thus the importance to use images showing particles on flat surface for the analysis. The area and perimeter were calculated directly from the shape of the particles on the map. The volume and height distributions were obtained from their apparent height. This parameter may be influenced by electronic effects. Annealing results in significant changes in Cu islands growth. On figure 33, the area of the majority of the particles is below 2000Å^2 before annealing, whereas the area increases considerably after annealing to 650°C, with some having areas greater than 4000Å^2. However, there are still particles with small area after annealing. The apparent height of the particles also varies with annealing.

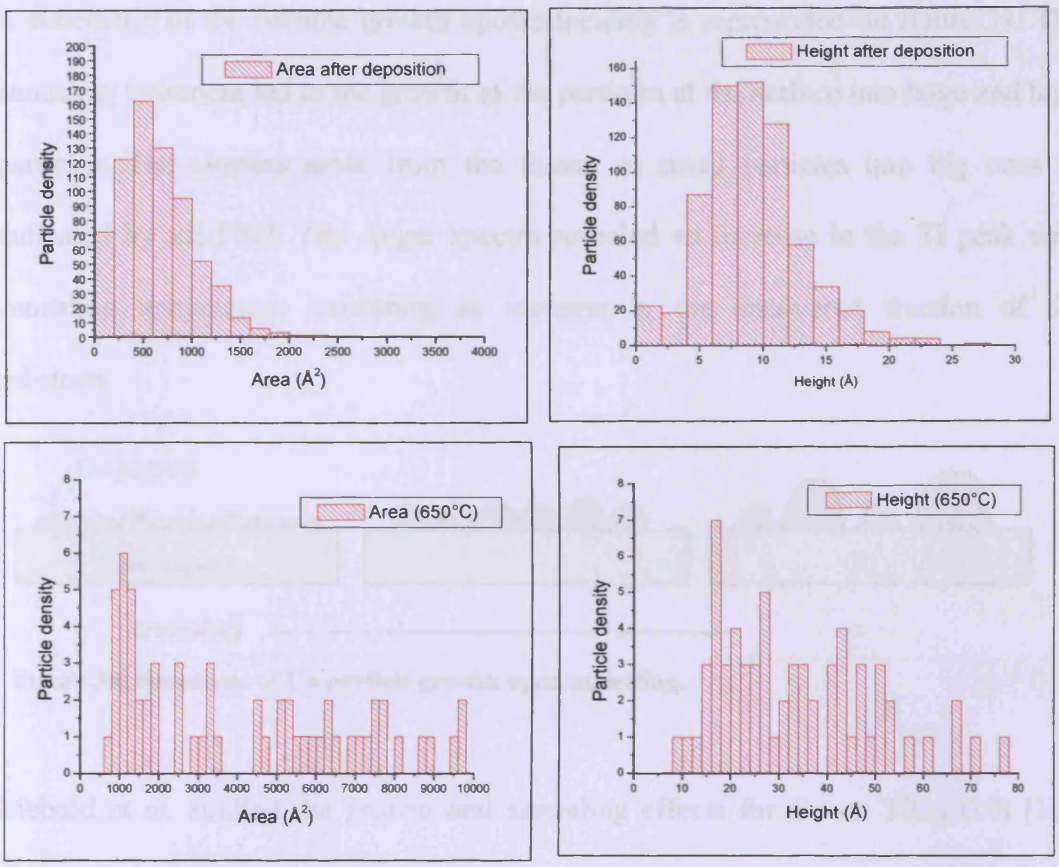

Figure 33: Particle Size Distribution of Cu particles on Titania at room temperature and after annealing at 650°C.

While the particles have height comprised between 1 and 30Å at room temperature with the largest frequency between 6 and 14Å, the height of particles varies between 9 and 80Å after annealing presenting a much broader distribution. The histogram shows a growth of the largest particles and a reduction of the smaller ones upon annealing which is in agreement with the coalescence process.

After annealing at 700°C, the island height was between 1 and 80Å with a maximum at 35Å and the diameter between 50-100Å. Significantly larger islands were formed by annealing to 750°C which were between 1-120Å in height and 200-400Å in diameter. From the calculations of the volume, it shows that there was no loss of the amount of copper on the surface after annealing.

A schematic of the particle growth upon annealing is represented on figure 34. The annealing treatment led to the growth of the particles at the surface into large and high particles. The clusters arose from the fusion of small particles into big ones as indicated by the PSD. The Auger spectra revealed an increase in the Ti peak with annealing temperature indicating an increase in the uncovered fraction of the substrate.

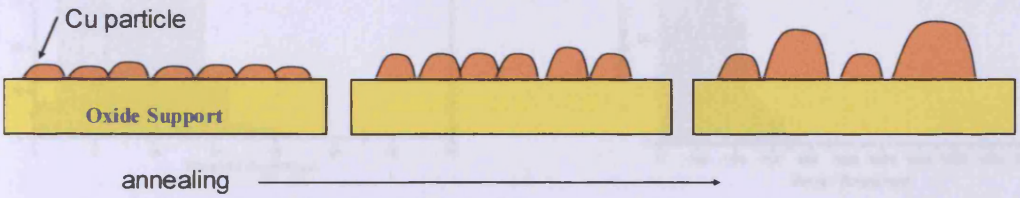

Figure 34: Schematic of Cu particle growth upon annealing.

Diebold et *al.* studied the growth and annealing effects for Cu on TiO_2(110) [11]. They observed, during annealing at high temperature, a change in morphology of the Cu film. An increase in cluster size and an increase in the uncovered fraction of the substrate were observed. Based on their experimental data, they supposed that single Cu atoms dispersed on the surface migrated towards the clusters and subsequently are incorporated into them. Bigger clusters could be formed out of smaller ones, Ostwald ripening, either if the small clusters are mobile enough to merge together or if single atoms break away and moves toward bigger clusters. However, no STM images supported their work. Chen et *al.* [16] confirmed the Ostwald ripening sintering process (at low coverage) with their observation of small clusters in addition to big clusters after annealing at 700K. However, they reported that at higher coverages the percentage of those small clusters is reduced (13% at 0.14ML and 2% at 0.051ML) and thus the coalescence process may occur.

Looking at the evolution of the height and area of Pd nanoparticles (figure 35) definite changes were observed after annealing at 400°C and 800°C. The height and area ranges after annealing at 400°C were 5-15Å and 100-400Å^2 respectively.

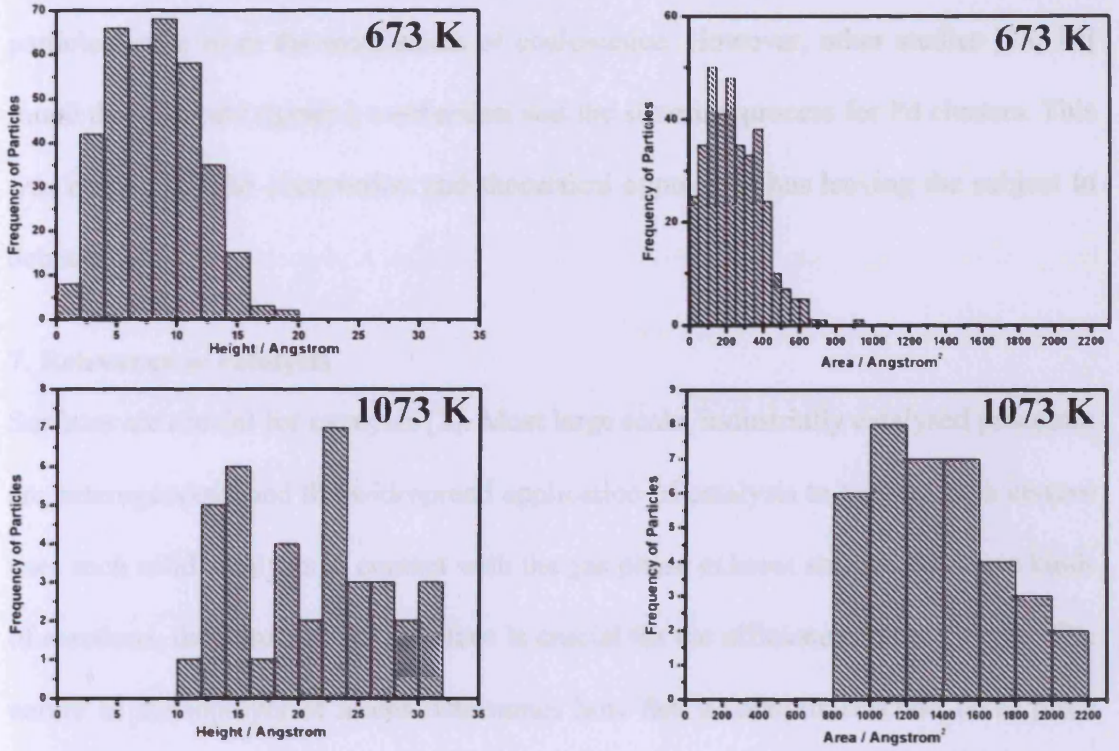

Figure 35: Particle Size Distribution of Pd particles on Titania after annealing at 400°C and 800°C. The area and height PSD are shown for each temperature.

After annealing at 800°C, the height frequency was dispersed along a range of value from 10 to 32Å. The frequency for the area was between 800-2200Å^2. The amount of palladium deposited remained constant after the annealing treatment. If Ostwald ripening sintering was occurring as for Cu particles, one would expect a histogram of big clusters and smaller ones after annealing. However, after annealing to 800°C, the area and height of particles have shifted to higher values and no small particles are present at the surface (figure 35). The histograms show only particles with large surface area and height. This is consistent with the coalescence sintering that consists in fusion of clusters to form a bigger one. No groups of particles are present at smaller

area indicating that the surface is covered only with big clusters. Jak et *al.* [14] found that, based on their particle size distribution, cluster diffusion and coalescence formed the dominant growth mechanism for palladium cluster on $TiO_2(110)$. Bowker et *al.* [17], based on their STM observation and PSD, concluded also that the sintering of Pd particles arose from the mechanism of coalescence. However, other studies [18, 19] found that Ostwald ripening mechanism was the sintering process for Pd clusters. This was based on STM observation and theoretical approach, thus leaving the subject to debate.

7. Relevance to catalysis

Surfaces are crucial for catalysis [2]. Most large scale, industrially catalysed processes are heterogeneous and the widespread application of catalysis to car emission control uses such solid catalysts in contact with the gas phase exhaust stream. For these kinds of reactions, the nature of the interface is crucial for the efficiency of the process. The nature of the toplayer of atoms determines how fast a catalytic reaction takes place and small amount of additives can reduce or enhance the reaction.

A catalyst usually consists of a metal supported on a highly porous material (e.g. alumina). The support material is there in order to maintain the integrity of the metal phase, where the selective reaction takes place. Without the support, the metal would undergo sintering very rapidly and would therefore lose activity. It is therefore very important to produce a catalyst with high surface area and which remain stable under the extreme conditions of the car exhaust (high pressure and temperature). Understanding the growth mode of active particles and their stability toward annealing are very important factors in the activity of the catalyst. The longer the particles remain small and dispersed on the support, the longer the catalyst will remain active.

It is possible to manipulate the behaviour of a catalyst for a reaction by any method that alters the properties of its surface. In thermodynamics terms, the surface free energy may be increased or decreased, in microscopic terms the individual sites responsible for giving the desired products may be altered. For example, sintering may lead to a loss of activity but can also change the selectivity of a reaction due to the changed site type ratio. This could be advantageous for some more selective reactions. Promotion is another possible treatment that could lead to the increase of the activity. This is achieved by addition of alkali salts (e.g. ammonia synthesis where K is added to the Fe catalyst and act as a promoter). It was stated that a promoter improves the properties of a catalyst for the reaction but in several ways [2]:

- activity enhancement: an alkali can directly increase the rate of synthesis
- selectivity enhancement: a promoter may change the pathway of a reaction to enhance the rate of formation of the selective product
- lifetime enhancement: sometimes a promoter may have little effect on a catalyst but can keep it operating longer. This is often due to a decrease of sintering rate or decrease of poisoning of surface with time.

The support can also be used as a way of tailoring the performance of a catalyst, particularly if the active phase consists of small particles. The area of the support affects the dispersion of the active phase. Some supports are reducible in reducing gases (e.g. TiO_2) and the reduced form of the support is often labile and can diffuse on the metal, giving marked effect on the catalyst activity –the strong metal support interaction effect (SMSI) [20]. This effect reduces the sorption of CO and H_2 on the catalyst but can improve the selectivity of hydrogenation reaction (e.g. acetylene hydrogenation) [21, 22]. The nature of the active phase is also a determinant in the activity of a reaction.

Supported metal clusters on single crystal metal oxide surfaces have been shown to exhibit extraordinary catalytic activity which correlates with their size and atomic like structure [15]. It is therefore very important to closely examine island nucleation and growth on oxide support and to characterise the resulting island distribution for a range of deposition conditions. For example, gold in bulk is chemically inert and is poorly active as a catalyst. However, when gold is small enough (with particle diameters below 10 nm) it turns out to be active for many reactions, such as CO oxidation and propylene epoxidation. The catalytic performance of Au is defined by three major factors: contact structure, support selection, and particle size, the first of which being the most important because the perimeter interfaces around Au particles act as the sites for reaction [23].

Metallic iron particles in solution have interesting and potentially useful chemical properties, including an ability to reduce chlorinated hydrocarbons in geochemical environments [24]. Some studies indicate that the dechlorination pathway may be altered if the particles are nanoparticles, thus the necessity to gain information on size, size distribution, density and shapes that are not always easily obtained.

Another publication [25] indicated that the catalytic activity for chlorohydrocarbon conversion was considerably enhanced by Cu and Ni particles. An important feature for the catalytic behaviour was that their activity depended strongly on the average distance between the nanoparticles or on the nanoparticle density on a support. The maximum of activity corresponded to the one-layer film consisting of closely packed ensembles of nanoparticles.

All those examples confirm the importance of studying properties of nanoparticles at the surface. Establishing knowledge on the behaviour of the different systems would allow the optimisation of the catalyst activity.

8. Conclusion

A mathematical description has been given of the properties of monolayers and nanoparticles. How many particles are comprised in a monolayer, the evolution of the particles size (volume and area) as well as the particle density as a function of the coverage were areas of study in this chapter. First, graphs displaying the variation of volume, perimeter and area as a function of the radius were described. This was followed by the particle density variation as a function of their size and of the surface coverage. It was found that the total surface area of deposited material decreases with increasing the particle radius despite the fact that the surface area of each individual particle increased with its radius. The particle density also decreased with the increase of the radius. STM images support these statements, especially in the case of palladium were the particle evolution was clearly visible. Then a model was drawn from the various equations stating a relationship between the interparticle distances as a function of the radius of the particles and the surface coverage. It was demonstrated that the interparticle distance increased with the increase of the particle radius and with the decrease of the particle density for a constant volume of material deposited (constant coverage). STM images of Pd on TiO_2 showed clearly this phenomenon during the annealing treatment and there was no loss of the metal. Finally a short review on the relevance of this work to catalysis was given. It was proven from various studies that parameters such as the size, size distribution, shape, particle density, interparticle distances were important factors contributing to the activity of a catalyst. Understanding the basic properties of nanoparticles is very important for studying and optimising the properties of catalysts.

9. References

1. Available from: http://www.webelements.com/webelements/elements/text/Cu/radii.htm
2. Bowker M., *The basis and applications of heterogeneous catalysis*. 1998: Oxford Chemistry Primers.
3. Argile C. and Rhead G.E., *Adsorbed layer and thin film growth modes monitored by auger electron spectroscopy.* Surface Science Reports, 1989. **10**(6/7): p. 277-356.
4. Attard G. and Barnes C., *Surfaces*. Vol. 59. 1998: Oxford Chemistry Primers.
5. Diebold U., *The surface science of titanium dioxide.* Surface Science Reports, 2003. **48**: p. 53-229
6. Kolasinski K.W., *Surface science: Foundations of catalysis and nanoscience*. 2002: Wiley Interscience.
7. Bennett R.A., Ppang C.L., Perkins N., Smith R.D., Morrall P., Kvon R.I. and Bowker M., *Surface structure in the SMSI state; Pd on (1×2) reconstructed $TiO_2(110)$,* The journal of Physical Chemistry B, 2002, **106**:p.4688-4696.
8. Vickerman J.C., *Surface Analysis: The principle techniques*. Wiley ed. 2000.
9. Childs K.D., Carlson B.A., LaVanier L.A, Moulder J.F., Paul D.F., Sticklen W.F. and Watson, D.G., *Handbook of Auger Electron Spectroscopy*. 1995: Physical Electronics, Inc.
10. Zhou J., Kang Y.C. and Chen D.A., *Controlling island size distributions: a comparison of nickel and copper growth on $TiO_2(110)$.* Surface Science, 2003. **537**(1-3): p. L429-L434.
11. Diebold U., J.-M. Pan and Madey T.E., *Growth mode of ultrathin copper overlayers on $TiO_2(110)$.* Physical Review B, 1993. **47**(7): p. 3868-3876.

12. Ohring, *Physics of thin films*. Available from: http://www.uccs.edu/~tchriste/courses/PHYS549/549lectures/index.html
13. Somorjai G.A., *Introduction to surface chemistry and catalysis*. 1994: Wiley Interscience.
14. Jak M.J.J., Konstapel C., van Kreuningen A, Verhoeve J. and Frenken J. W. M, *Scanning tunnelling microscopy study of the growth of small palladium particles on TiO2(110)*. Surface Science, 2000. **457**: p. 295-310.
15. Bowker M., *The going rate for catalysts*. Nature Materials, 2002. **1**: p. 205.
16. Reddic J.E., Zhou J. and Chen D.A., *Scanning tunnelling microscopy of the growth of Cu clusters on a reconstructed $TiO_2(110)$-(1×2) surface*. Surface Science, 2001. **494**: p. 767-772.
17. Stone P., Poulston S., Bennett R. A. and Bowker M. , *Scanning tunnelling microscopy investigation of sintering in a model supported catalyst: nanoscale Pd on $TiO_2(110)$*. Chemical Communication, 1998: p. 1369-1370.
18. Bennett R.A., Tarr D.M. and Mulheran P.A., *Ripening processes and pinned nanoclusters-experiment, simulation and theory*. Journal of Physics: Condensed Matter, 2003. **15**: p. S3139-S3152.
19. Howard A., Mitchell C.E.J. and Edgell R.G., *Real time STM observation of Ostwald ripening of Pd nanoparticles on $TiO_2(110)$ at elevated temperature*. Surface Science Letters, 2002. **515**: p. L504-L508.
20. Tauster S.j., Fung S.C. and Garten R.L., *Strong metal-support interaction. Group 8 noble metals supported on TiO_2*. Journal of the American Chemical Society, 1978. **100**(1): p. 170-175.

21. Kang J.H., Shin E.W., Kim W.J., Park J.D. and Moon S.H., *Selective hydrogenation of acetylene on TiO_2-added Pd catalysts.* Journal of Catalysis, 2002. **208**: p. 310-320.

22. Kim W.J., Kang J.H., Ahn I.Y. and Moon S.H., *Deactivation behaviour of a TiO_2-added Pd catalyst in acetylene hydrogenation.* Journal of Catalysis, 2004. **226**: p. 226-229.

23. Haruta M., *Catalysis of gold nanoparticles deposited on metal oxides.* Cattech, 2002. **6**(3): p. 102-115.

24. Busca G., Baldi M., Pistarino C., Gallardo Amores J.M., Sanchez Escribano V., Finocchio E., Romezzano G., Bregani F. and Toledo G.P., *Evaluation of V_2O_5-WO_3-TiO_2 and alternative SCR catalysts in the abatement of VOCs.* Catalysis Today, 1999. **53**(4): p. 525-533.

25. Rostovshchikova T.N., Smirnov V.V., Gurevich S.A., Kozhevin V.M., Yavsin A., Nevskaya S.M. and Nikolaev S.A., Lokteva,E.S, *Nanostructured metal films: Fabrication and catalytic properties.* Catalysis Today, 2005. **105**(3-4): p. 344-349.

Chapter 4

The SMSI process on Pd nanoparticles

1. Introduction

Metallic layers on oxide surfaces form a relevant area of research presenting many applications. The support is usually inert and the metal is dispersed to obtain a maximum exposed surface area. Metal atoms can interact with metal oxide in varied and complex ways [1]. The initials stages of metal deposition involve structure and the degree of charge transfer between the metal and the surface. Given a certain degree of charge transfer, the bonding with the surface is expected to have a strong ionic component dominated by metal-oxygen interactions [1]. Transition metals can adopt complex structures. There can be some direct overlap of the d-orbital of the metal with the d-orbital of the metal oxide creating some sort of metal-metal bonding [1]. However, interaction by electron transfer and bonding to the surface is a too simplistic model to be considered. Bonding of metals on transition metal oxides substrate can lead to reconstruction of the surface, with a considerable rearrangement of the oxygen and metal ions. In this chapter, the work is focused on palladium metal and its behaviour when deposited on a single crystal of titania and on powder catalyst. The growth of metals on TiO_2 has been extensively studied for a large range of metals [2]. The effect of the interaction between metal particles and metal oxide on the chemical properties of the metal oxide was the subject of much investigation. The interest for the Pd/TiO_2 system is coming from the discovery of the SMSI (Strong Metal Support Interaction) effect observed on the reduced catalyst and more recently, the same effect on single crystal model catalyst [3-5]. This effect consists of the migration of the support atoms onto the metal nanoparticles, thus affecting the reactivity of the catalyst. Many studies have been carried out on $TiO_2(110)$ crystals [5-11] and a review of the findings is reported in the first part of this chapter. The second part is related to catalytic work previously done on Palladium supported TiO_2.

Then, the reconstruction process brought about by the reduction of the $Pd/TiO_2(110)$ system is reported. In the third part of the chapter, my studies, carried out by STM imaging, are described with the observed structure characterised and identified by Auger spectroscopy and LEED analysis. Re-oxidation is then carried out and more images of the surface are analysed. The last part of the chapter is dedicated to the study of a Pd/TiO_2 powdered catalyst. The reactivity of the catalyst is tested by Pulsed Flow reactor (PFR) experiments of CO uptake and CO oxidation reactions. BET analysis is also reported.

The aim of the following experiments is to bring some more understanding to the interaction of small metal particles with reducible metal oxides, in particular Pd on TiO_2. This system is favourably studied because of the large TiO_2 effect on metal catalysis. A complete knowledge of the behaviour of TiO_2 metal oxide would provide a basis to search for similar but more subtle effect on more inert oxide supports [12].

1.1. The structure of titania

Titania has been widely investigated mainly because of its large range of applications [1, 2]. The importance of titania arises predominantly from its uses in white pigment in paint and cosmetic due to a high refractive index in the visible region of the spectrum. It is also a support for photocatalysts: Titania acts as a photosensitiser for photovoltaic cells, and when used as an electrode coating in photoelectrolysis cells it can enhance the efficiency of electrolytic splitting of water into hydrogen and oxygen. Another feature of titania is as an antimicrobial coating. The photocatalytic activity of titania results in thin coatings of the material exhibiting self cleaning and disinfecting properties under exposure to UV radiation. These properties make the material a candidate for applications such as medical devices and food preparation surfaces.

1.1.1. Bulk structure and defects

Titania exists in 3 forms, rutile, anatase and brookite. Rutile and anatase are common forms while brookite is rare. Rutile is the most common form in nature and produced commercially. When heated, anatase and brookite transform into rutile [13].

Rutile titania has the tetragonal structure with $a = b = 4.587$ Å and $c = 2.953$ Å. Its unit cell consists of 8 titanium atoms at each corner and one at the centre of the cell. The central titanium is surrounded by 6 oxygen atoms in a slightly distorted octahedral structure (figure 1A).

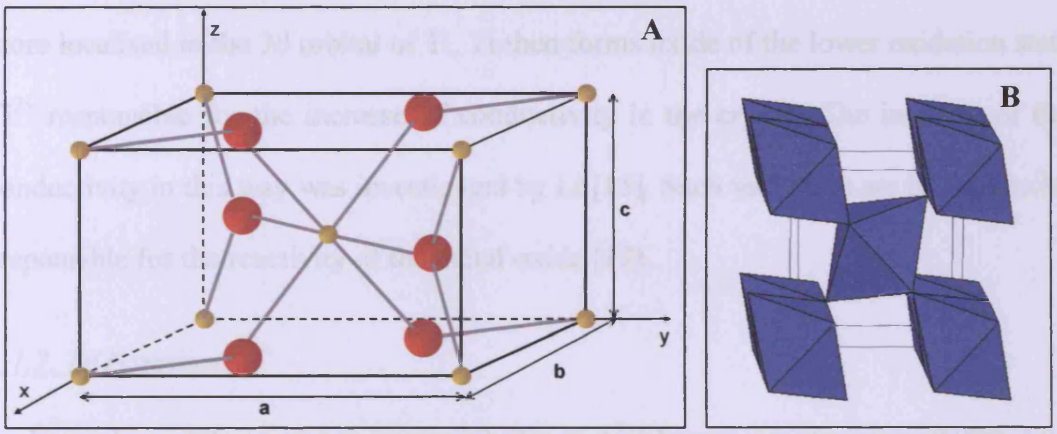

Figure 1: A) Schematic representation of TiO_2 rutile unit cell. The yellow and red spheres represent titanium and oxygen respectively. B) The crystal structure of rutile. Each octahedron corresponds to TiO_6.

Viewing the structure as a chain of octahedra, each octahedron shares a pair of opposite edges. The chains are attached to each other at their corner (figure 1B) [14].

TiO_2 is a transition metal oxide with a poor conductivity. However, it transforms to an n-type semiconductor with a band gap at ~3.1eV when reduced or when various defects are introduced, making it a suitable support for surface science studies [1]. Initially transparent, the colour of the titania crystal changes upon reduction. It becomes light blue, then dark blue to ends up nearly black as defects are created in the crystal [1].

Bulk reduction occurs when sputtering and/or annealing the surface. Sputtering techniques, employed to clean the surface from contaminants, also removes atoms from the TiO_2 surface. Considering the TiO_2(110) crystal, two kind of oxygen atoms (detailed below) are present at the surface: 2-fold coordinated oxygens (called bridging oxygens) and 3-fold coordinated oxygens. Because of the coordinative insaturation of the bridging oxygens, those atoms are thought to be preferentially removed during annealing or sputtering process [1]. Oxygen leaves the surface in an ionic state, O^{2-}, two Ti ions are left with one delocalised electron each thus creating oxygen vacancies at the surface. Those electrons must then occupy states that are more localised in the 3d orbital of Ti. Ti then forms oxide of the lower oxidation state Ti^{3+} responsible for the increase of conductivity in the crystal. The increase of the conductivity in this way was investigated by Li [15]. Such vacancies are thought to be responsible for the reactivity of the metal oxide [12].

1.1.2. TiO_2 surfaces

Early work on TiO_2 surfaces employed ultraviolet electron spectroscopy (UPS), low energy electron diffraction (LEED) and Auger electron spectroscopy (AES) techniques to investigate the stability of the surfaces. The (100), (110) and (001) surfaces were studied [16] as well as (011) [17]. The (110) surface was found to be stable with no reconstruction after annealing at 600-800°C, which later was proven to be incorrect [18]. The (100) surface, in contrast, showed three different structures upon heating. A (1×3), (1×5) and (1×7) reconstruction were obtained after annealing at 500°C, 800°C and ~1200°C respectively [16]. Finally the (001) surface reconstructed to give (110) and (100) facets.

Later work by Ramamoorthy and Vanderbilt [17] on the calculation of the energetics of TiO_2 surfaces indicated that the (110) surface had much lower surface energy than

the (001) surface. The (100) and (011) had surface energies lying between those two extremes. They also indicated that the TiO_2 (110) surface showed a (1×2) reconstruction after annealing at 600°C. This latter finding is described in many publications [18-23]. Having the lowest surface energy [17], being cheap and readily available are some of the reasons why TiO_2 (110) is used as a support in this work. Image 1 is an example of a clean TiO_2 surface imaged by STM at Cardiff University. The image shows rows of ordered dark and bright lines running along the [001] direction. A line profile (figure 2) across the terrace shows an interatomic separation of 6.05Å. This dimension is very close to that of the bulk termination. The step height measured ~3.4Å (the theoretical step separation is 3.24Å for an ideal bulk termination).

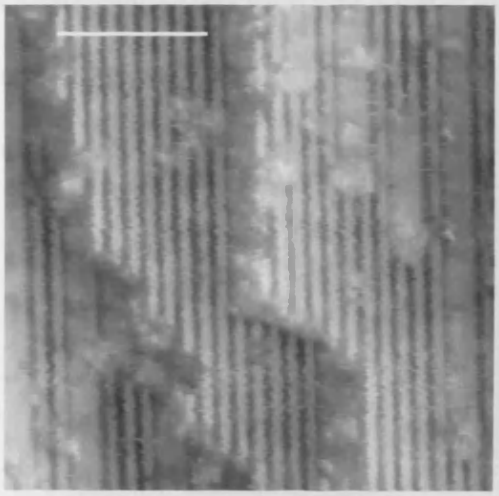

Image 1: High resolution STM image of TiO_2 (110) (1×1) parameters: 171Å×171Å, 1.5nA, 1V

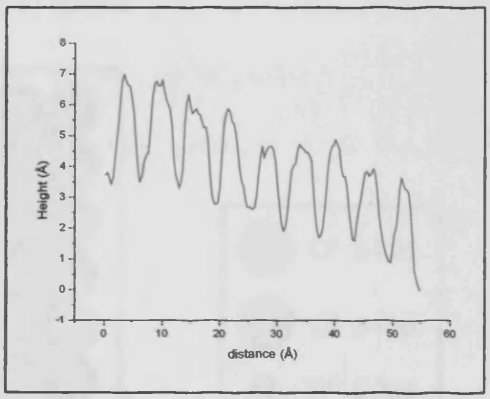

Figure 2: line profile showing an interatomic distance of 6.05Å

When TiO_2 was first imaged, it was not apparent if these bright rows corresponded to bridging O^{2-} anions or 5-fold Ti^{4+} cations. Onishi and Iwasawa [24] observed that formate ions deposited on the surface were sitting on top of the bright rows. Since formates are expected to adsorb on Ti sites, this observation allowed them to deduce

that the bright rows consisted of 5-fold coordinated Ti atoms. This was confirmed by the work of Diebold using different adsorbates and obtaining similar results [25].

If the STM images were dependent only on the geometry of the surface, then we could deduce that the features seen in the image are coming from bridging oxygen atoms since they sit at 1.5Å higher than the Ti cations. However, the tunnelling current does not depend only on the geometry but also on the electronic states available, especially the local density of state (LDOS). Pseudopotential calculations of the LDOS were carried out at the surface of the (110) plane [26] and the charge density of the conduction band was found to be 2eV above the Fermi level. In addition, the charge density contour around the Ti atoms was bigger than that around the oxygen atoms, despite their protrusion above the surface. This confirmed the experimental observation that STM is imaging Ti atoms.

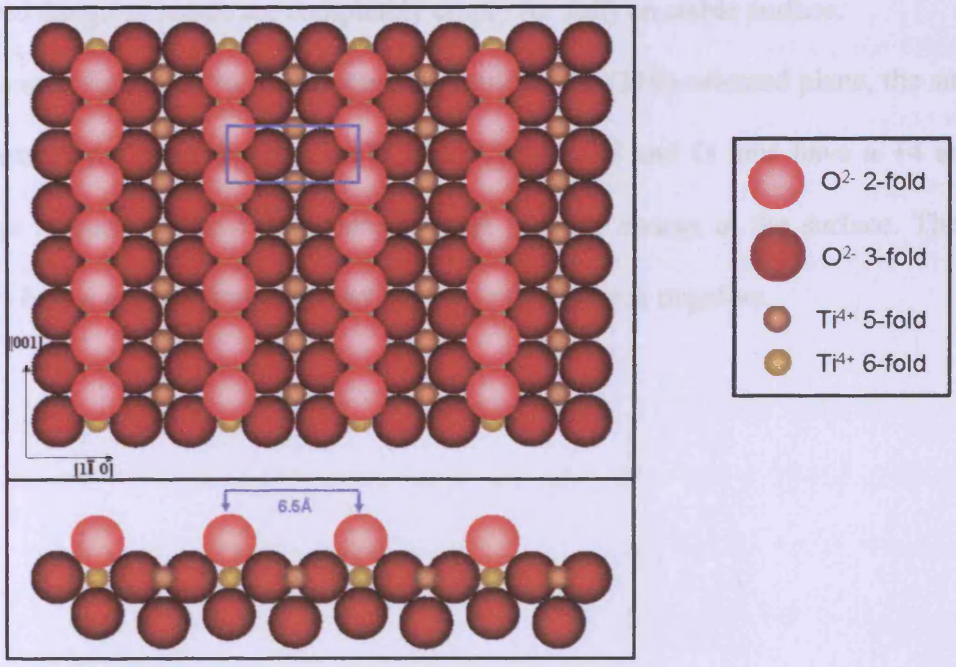

Figure 3: Model of the (1×1) surface structure.

A schematic representation of TiO_2 (110)-(1×1) surface is given in figure 3. The (1×1) surface is stable. Two concepts have been proposed to predict the stability of a

surface. In the first one, the stability is based on pure electrostatic considerations [27]. This concept proposed by Tasker indicates that the dipole moment of a repeat unit perpendicular to the surface must be zero in order for the surface energy to go to a minimum. From this concept, he introduced three categories for ionic structures. Type 1, which has equal number of anions and cations on each plane parallel to the surface, is stable. Type 2 is also stable and consists of charged planes but with no dipole moments because of a symmetrical stacking sequence. Finally, type 3 surfaces are usually not stable because they are charged planes with a dipole moment in the repeat unit perpendicular to the surface.

The second proposal introduces the concept of autocompensation on metal oxides by LaFemina [28] stating that the excess charge of cation derived dangling bonds compensates the anion derived dangling bonds. It results that the cation- (or anion-) derived dangling bonds are completely empty (or full) on stable surface.

Looking at figure 4a, that represents the rutile in the (110)-oriented plane, the surface consists of the same number of Ti and O atoms. Ti and O ions have a +4 and -2 charge respectively and thus there is a net positive charge at the surface. The two layers below are oxygens only and the total net charge is negative.

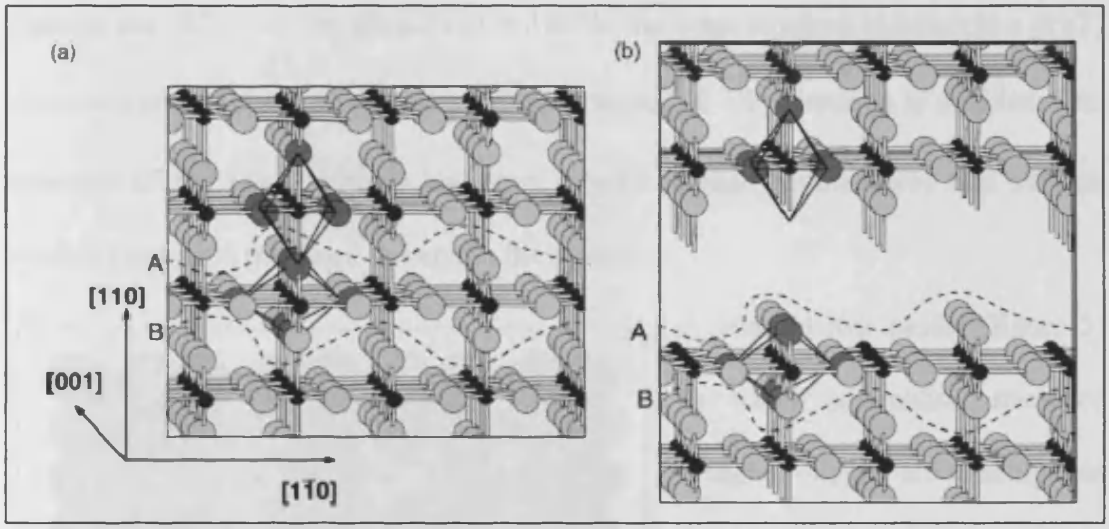

Figure 4: Stick and ball representation of the rutile crystal in the (110)-oriented plane. (a) Two octahedra units are indicated. The dashed lines A and B enclose a charge neutral repeat unit without a dipole moment perpendicular to the (110) direction (a type 1 crystal according to Tasker [27]. (b) The crystal is cut along the line A. The same number of Ti-O and O-Ti bonds are broken and the surface is autocompensated [2, 28]

According to Tasker concept [27], the dashed lines A and B outline a type 2 repeat units. It consists of a mixed layer of Ti and O sandwiched between two layers of oxygen atoms. The total unit cell does not have a dipole moment and looking at the charges of the layer, it turns out to be also neutral [1]. So, by cutting the crystal in order to expose the (110) plane along the line A or B, the crystal will terminate with a corrugated surface because one layer of oxygen atoms is left behind (figure 4b). It is thus evident from figure 4a and 4b that the (1×1) surface corresponds to the bulk termination.

The top layer consists of 2 types of titanium atoms as well as 2 types of oxygen atoms. In the [1$\bar{1}$0] direction, alternating rows of 6-fold and 5-fold coordinated Ti atoms are separated by 3-fold coordinated oxygen atoms. On the [001] direction, the 6-folds Ti atoms are linked to each other by 2-fold oxygen atoms, bridging atoms. The unit cell, represented in the model (figure 5) by the blue rectangle, has the dimensions of 6.48Å by 2.95Å.

Heating the TiO_2 (1×1) in vacuum over 1000K has been reported to result in a (1×2) reconstruction [21] where the periodicity along the [1 $\bar{1}$ 0] direction is doubled. The structure of the (1×2) surface has been subject to many controversy and various models have been proposed to explain the structure.

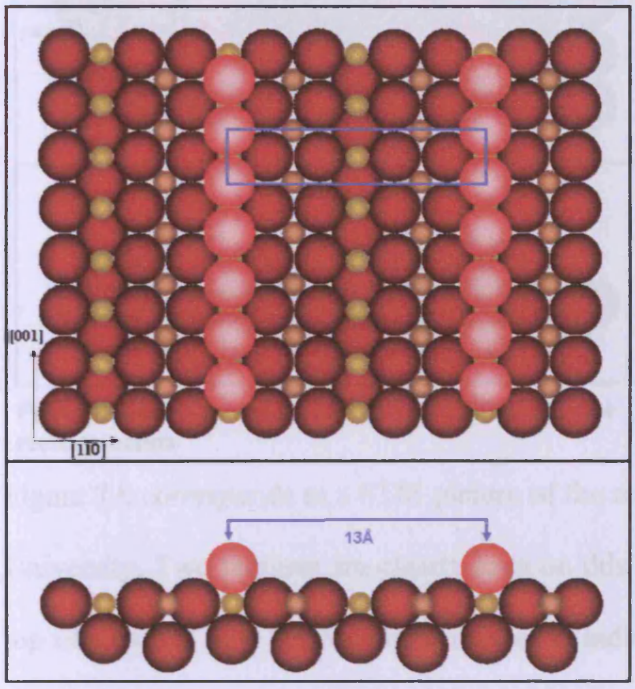

Figure 5: Missing row model of the (1×2) TiO_2 reconstructed surface

A missing row model (figure 5) in which alternative rows of bridging oxygen are missing was first proposed by Møller and Wu [29]. Their conclusions were based on the (1×2) LEED pattern and AES observations. The elimination of the bridging rows lead to a doubled unit cell dimension of 13Å in the [1 $\bar{1}$ 0] direction. This model was confirmed by Engel [20, 30] with the support of STM images. He proposed also a (1×2) structure described as a distorted missing row model with the coexistence of a cross-linked structure. This model was also confirmed by Murray [31].

However, diverse publications [32-33] differ with those results and the missing row model was later rejected. Two other models were proposed. The first one was by Onishi and Iwasawa [33] who observed, in STM images, long strings composed of two ridges separated by 3.5Å and lying above the (1×1) surface. They then based their model on a partially reduced oxide, Ti_2O_3, and not on the stochiometric truncation of oxygen which did not fit his observations. This model is represented in figure 6. It consists of double rows of Ti cations that run along the [001] direction and

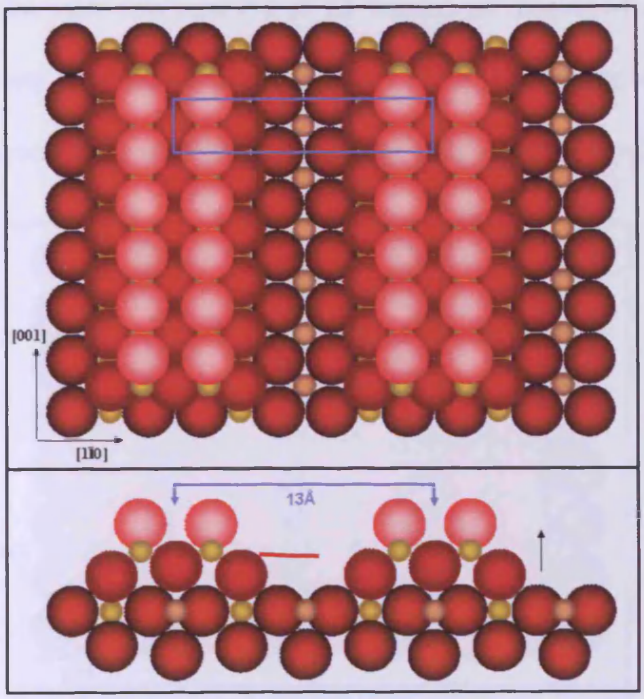

Figure 6: added row model for the (1×2) TiO_2 surface reconstruction

reside in position similar to interstitial sites in the rutile lattice whereas oxygen atoms sits on their original position. The height of a (1×2) row lies lower than a complete single step with an apparent height of ~1.3Å. In addition, the Ti cations sit closer to each other than on the (1×1) surface.

Figure 7A corresponds to a STM picture of the reconstructed surface taken at Cardiff University. Two features are clearly seen on this image, bright clusters sitting on the top of rows. A step between two terraces is indicated by the white arrow and has a height of ~2.3Å. This is smaller than the distance of 3.24Å between 2 (1×1) planes.

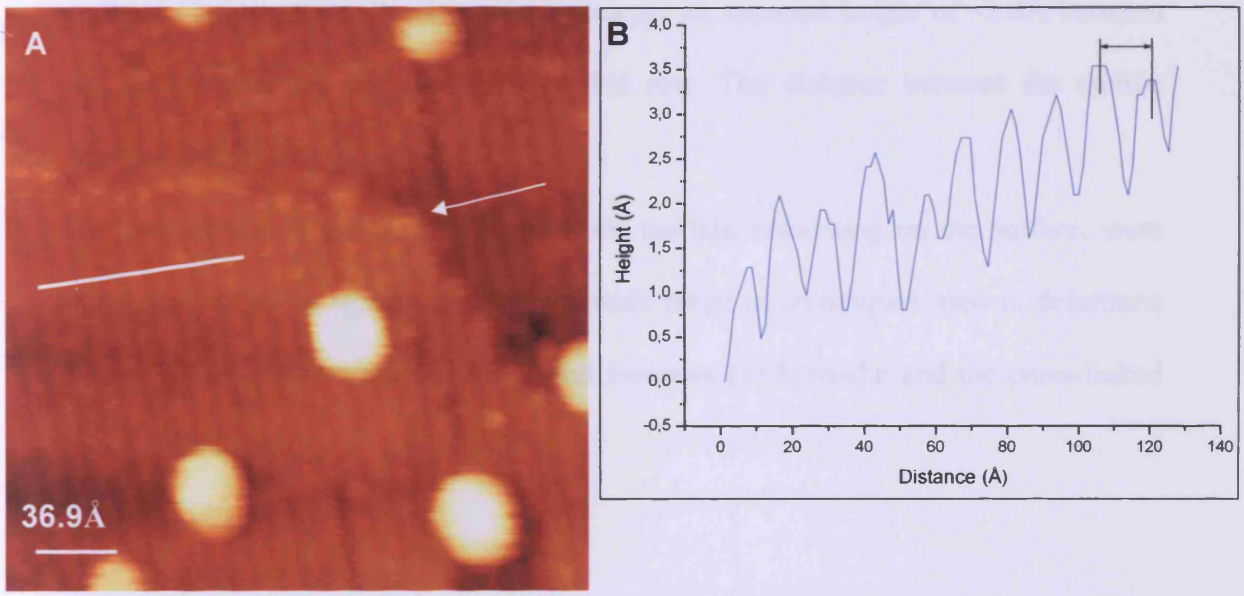

Figure 7: A) High resolution STM image of the TiO_2 (110). The few bright rows are coming from (1×2) reconstruction. Parameters: 349Å×349Å, 1nA, 1.5V. B) Line profile across 7A. The width of the (1×2) row is twice the one of the (1×1).

The inter row spacing is 12.4±0.1Å as measured on the line profile figure 7B. It is clear that the surface consist of a (1×1) substrate with (1×2) added rows which is in accordance with Iwasawa model [33] of added (1×2) rows.

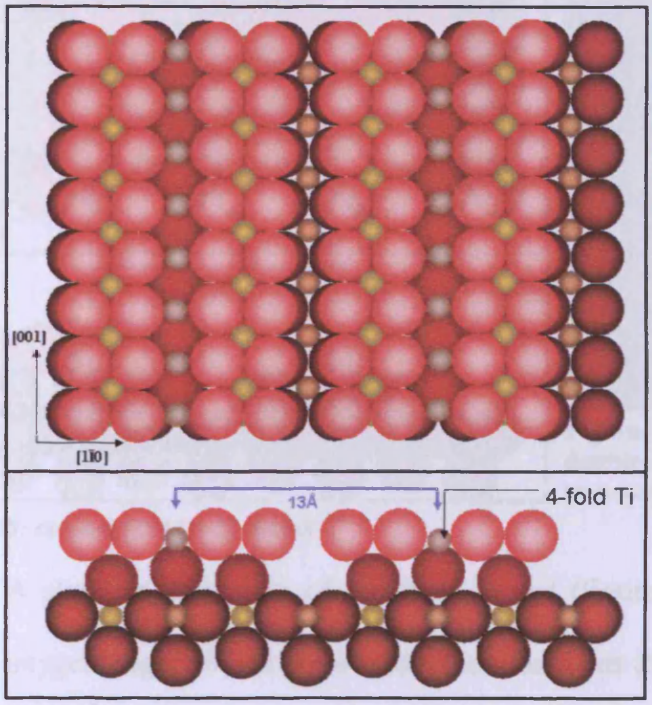

Figure 8: added unit model for (1×2) surface reconstruction

More recently, after the Onishi and Iwasawa work [33], a new model (figure 8) for (1×2) reconstruction was proposed by Pang et al. [23] based on STM images and theoretical calculations, bringing light on the different structures of the reconstructed (1×2) surface. They proposed that the model for the (1×2) structure consisted in added rows along the [001] direction, in which the termination was of completely reduced (1×1) surface. Such structure presents an apparent height of ~2.8Å between the (1×1) layer and the top of the added row. The distance between the atomic features in the [1$\bar{1}$0] direction is 5.5Å.

However, from all those models, only two models, coexisting on the surface, were considered to be in agreement with the wide range of techniques used to determine the TiO_2 (1×2) structure: the Onishi and Iwasawa (1×2) model and the cross-linked (1×2) model [22].

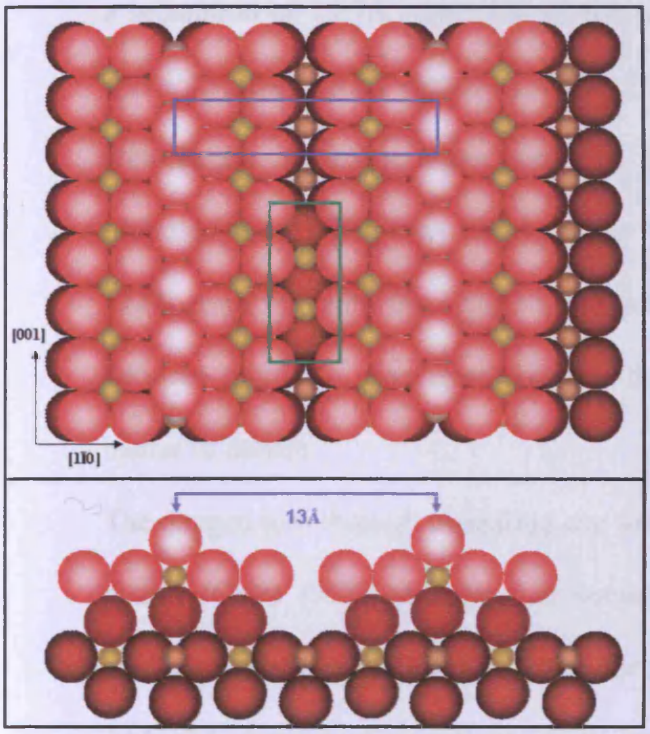

Figure 10: cross-linked (1×2) model

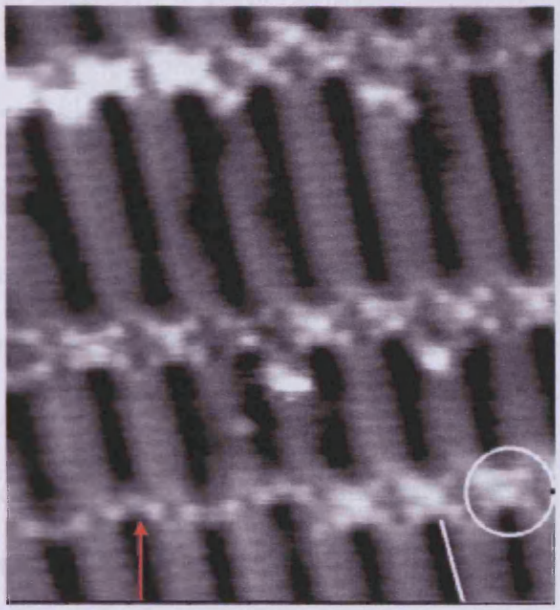

Figure 9: High resolution STM image of the double (white circle) and single cross-linked structure (red arrow) (courtesy of [22]).

A slight modification of the Pang model (figure 8), by adding a row of bridging oxygen (figure 9) on the 4-fold Ti ion, explains the cross linking feature observed in STM [22]. The apparent height of the added row appeared to be higher (~2.8Å). It was also observed that the cross-links show chains of single links and double links as shown on figure 10. The bright green rectangle on figure 9 highlights a double cross-linked structure.

The differences in the apparent height of the row structure helped to distinguish both (1×2) structures. The apparent height between the (1×2) rows of the cross linked structure (figure 9) and the (1×1) terrace is 2.8Å which is smaller than the height between two (1×1) TiO_2 steps (~3.2Å). The model proposed by Iwasawa and consisting of the added row of Ti_2O_3 (detailed above) shows an apparent height of ~1.8Å.

Another reconstruction after annealing was observed as being (1×3) feature [19, 23, 34]. Pang [23] reported the imaging of (1×3) phase consisting of thicker rows having

a separation of 19.7Å consistent with a tripling of the bulk unit cell. This structure was interpreted as an extension of the (1×2) phase along the [0-11] direction. The features in the image were attributed to 5-fold coordinated Ti atoms. Another proposed model [19] was based on the Ti_2O_3 added row. The model consisted of Ti_2O_3 rows but with the bridging oxygen rows along the 5-fold Ti atoms existing between the Ti_2O_3 unit rows. Despite those observations, the structure is still the matter of debate.

The oxygen loss through annealing can lead to the formation of crystallographic shear planes (CSP) [35]. Annealing in vacuum preferentially removes oxygen atoms, creating oxygen vacancies that can be accommodated by the creation of point defects. At higher degrees of reductions, TiO_{2-x} with $x<1.90$, interstitials are produced along with the point defects. Those defects can be eliminated at high temperature by the creation of CSP. Their formation can be visualised as a change of the octahedral rearrangement. In a normal configuration each octahedron shares a pair of opposite edges. These chains are attached to each other at their corners by their oxygen atoms. In the CSP, octahedrons are in a face sharing arrangement [36]. In addition, The step measurement between 2 CSP revealed a height of 1.6Å, half the value of a normal step height of TiO_2(110). As the concentration of CS planes increases, new crystallographic phases are created known as Magnéli phases. Those new phases consist of bulk like rutile structure joined to each other by CSP (figure 11).

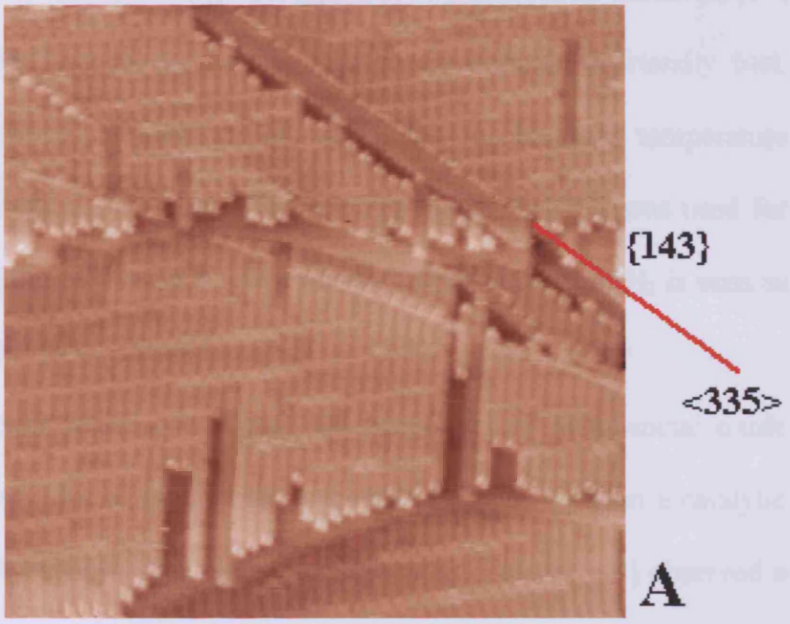

Figure 11: STM image (400 × 400 Å, 0.2 nA, 1 V, 773 K) showing a CSP pair running in the <335> direction across the reconstructed terraces. Note the differing level of attachment of the (1 × 2) terrace to the raised central slab of (1 × 1) surface between the CSPs. Also visible is a change of the cross-links of the terraces from a full cross to a single link in the proximity of the CSPs. This may be related to long range strain fields produced by the CSPs.

1.2. The SMSI effect

One of the problems encountered in metal-metal oxide catalysis is the loss of activity upon heating. The number of small metal particles decreases upon heating and the average size of particles increases. This corresponds to a decrease in the surface area of the catalyst. A small particle possesses different chemical and physical properties compared to bigger ones. This, therefore, influences the performance of the catalyst. A real catalyst is often made of a porous and inert metal oxide with metal nanoparticles dispersed at its surface. Due to its complex geometry, it is difficult to understand the metal behaviour at the surface. A model catalyst thus represents a simpler surface to study catalysis. The following paragraph reviews the findings published on metal/metal oxide systems on real and model catalysts. Both catalysts have been studied in close relation; the crystal surface findings helping to understand the real catalyst behaviour.

Palladium supported TiO_2 has been widely investigated for catalytic reactions. Such reactions include nitrite reduction in drinking water [37] or acetylene hydrogenation

[38]. This catalyst has also been studied as a support for methane total oxidation [39, 40] which is an effective way to use methane as an environmental friendly fuel. Related to emission control, Pd has an excellent activity for low temperature oxidation of CO, hydrocarbons [41] and NO_x reduction [42]. Pd/TiO_2 was used for the photocatalytic reforming of methanol. This method of production of H_2 is seen as an alternative for hydrogen production [43].

A particular discovery was made concerning the properties of metal-metal oxide catalysis and has attracted a lot of interest from scientists especially from a catalytic and surface science point of view. The pioneer of this work, Tauster [44] observed a great reduction in the CO and H_2 chemisorption on metals supported on TiO_2 which were reduced at 773K. They suggested that this decrease was a result of bonding between metal particles and Ti of the support and used the term "Strong Metal Support Interaction" to name this effect. More studies were undertaken to bring light on this SMSI effect which suggested a migration of the support metal atoms on the metallic particles during reduction [45, 46]. In 1987, an account was published by Tauster [47] giving a direct evidence of the bonding and what had been learned on its fundamental nature. Simoens and co workers [45] used HRTEM and ferromagnetic resonance studies to describe the morphology and state of Ni on TiO_2. They showed that not only electron transfer [48] was at the origin of the SMSI but involved also a decoration model which consisted in the formation of TiO_2 species on the surface of the metal. This was also suggested by Sadeghi and Heinrich [46] who stated that the transport of suboxides of Ti over Rh particles was responsible for the suppression of CO chemisorption on Rh on a TiO_2 single crystal in the SMSI state. Work by Baker on metal on TiO_2 showed that reduction of TiO_2 to Ti_4O_7 appeared to correlate with the SMSI behaviour [49]. The mechanism of such migration was, however, not well

understood. It appeared to occur via the grain boundaries since it was too rapid to come from the diffusion of Ti through the metal [50]. Once the Ti atoms from the support had migrated on the surface, TiO_x spreading on metal and metal on TiO_x was considered. The presence of an interaction between Ti and a metal might allow the spread of the adlayer instead of the agglomeration into three dimensional islands. This appeared to be true for some metals e.g. Pt [49] but Pd did not show such evolution and the migration lead to decoration and eventually to complete encapsulation of the metal particles. Reducing the catalyst at higher temperature led to sintering (above 500°C) by an atomic migration mode, in which large particles increased in size at the expense of smaller particles.

Tauster, in his account on SMSI [47], emphasized that a reduced titanium ion, e.g. Ti^{3+}, was required to observe strong metal support interaction effect with a metal atom. This bond could only exist at the interface because of the incompatibility of metal atoms and cations within a solid lattice. Thus, the contact perimeter of the metal-TiO_x might be important in some systems. The bond created from the SMSI effect appeared to be partially ionic with a net electron transfer from Ti^{3+} to the metal. Herrmann [48] reported that any electron transfer from an oxide to a metal can occur when they are put into contact by the spontaneous alignment of their Fermi levels, provided the work function of the metal (ϕ_n) is greater than that of the oxide (ϕ_{ox}). The latter will depend upon the reduction state of the oxide. The more reduced the oxide, the smaller ϕ_{ox} and the stronger the electron migration to the metal. He concluded that the existence of the SMSI state of M/TiO_2 catalysts corresponds to a strong electron excess within the metal. Using EXAFS and TEM studies, the Pavlova group investigated the morphology of Pd clusters on different surfaces including TiO_2 (anatase) [51]. TEM data revealed a uniform dispersion of Pd on TiO_2 with flattened

clusters developed on the (110) plane of TiO_2. EXAFS studies showed a complete metallic character after the samples were reduced in H_2 at 470°C. Van de Loosdrecht [52] observed a higher production of high hydrocarbons in his study of the Fisher Tropsch reaction on Ni/TiO_2 catalysts. He suggested the presence of an interaction between Ni and TiO_x ($x<2$) species, which can cover parts of the Ni particles and be responsible for changes in dissociation properties and thus in product selectivity.

Later, STM was the main method used to determine the geometric structure of TiO_2 and study the structure and nucleation behaviour of metal nanoparticles at the surface. Ni/TiO_2 [45], Rh/TiO_2 [46], Pd/TiO_2 and Pd/Al_2O_3 [49], Pt/TiO_2 [53], $TiO_2/Pt(111)$ [54, 55] systems are some examples of studied model catalysts. In 1995, Boffa [54] looked at the growth of titanium oxide films on Pt(111) and found that titanium oxide formed disordered and ordered structures on Pt(111). They reported the formation of a stochiometric TiO_2 layer with $(\sqrt{43}\times\sqrt{43})-R7.6°$ superstructure with a (18.2Å×18.2Å) unit cell. It was proposed that this superstructure could be derived from the $TiO_2(111)$ surface although a significant expansion of the O-O distance would be required to match the Pt(111). However, they did not suggest other possible structures. Sedona et *al.* [55] reported, in a later publication, the same structure and concluded that the ultrathin TiO_2 film showed a high degree of long range order with a predominance for the $TiO_2(110)$ surface. Looking at Au, Pd and Ag clusters, Lai et *al.* [56] found that at high coverages, the clusters grew in three dimensional, 3D, (Volmer- Weber) fashion on TiO_2 while at low coverages, quasi 2D Au and Pd clusters were observed (one to two atomic layers). A preferential nucleation at step edges was observed for Pd. The growth mode for Au and Pd was dominated by nucleation at low coverages and clusters growth at high coverages. Au and Pd clusters sintered upon annealing at high temperature forming large micro crystals with well

defined hexagonal shapes. Studies by Suzuki brought some more information on the Pd/TiO_2 system [3]. The initial adsorption site for the palladium was the 5-fold Ti atoms. During re-oxidation, oxygen adsorbed dissociatively on Pd. Pd then became a source of oxygen atoms that spill over from the particle to the support. In a later paper, Bowker and co-workers [7] investigated the re-oxidation and thermal treatment on Pd particles on $TiO_2(110)$ by STM imaging. They showed that non-stochiometry in TiO_{2-x} is accommodated by the diffusion of Ti interstitial into the bulk of the rutile structure. During re-oxidation these ions are diffusing back to the surface where they grow in their normal crystallographic structure. Looking then at the reaction with metallic nanoparticles [5, 7], they studied the "spillover" phenomenon (figure 12) and they observed the same phenomenon as Suzuki.

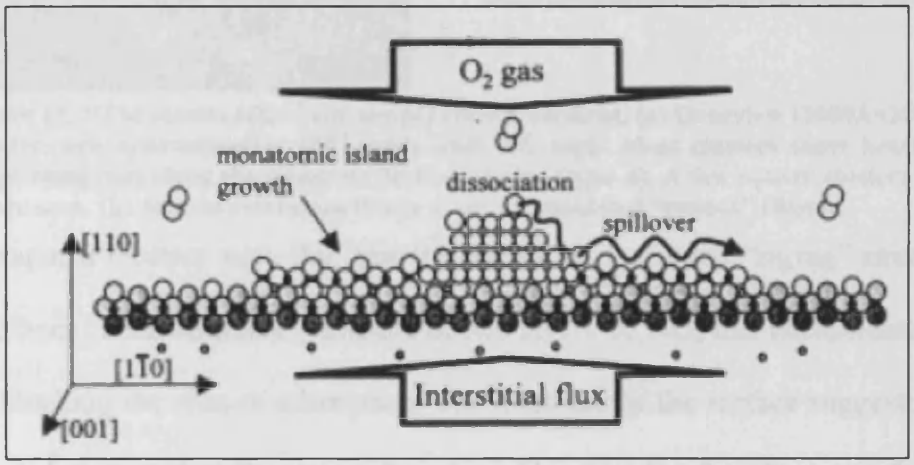

Figure 12: Schematic showing the mechanism of re-oxidation. Ti^{n+} interstitials constantly diffuse into and out of the surface region from the bulk of the crystal. Oxygen adsorbs onto the Pd nanoparticle and spills over onto the TiO_2 support, where it capture Ti^{n+} and adds to the (1×1) island periphery [5].

The TiO_2 grows out from the particle in its stochiometric (1×1) termination due to the abundance of oxygen around the particle. The Ti^{n+} needed are removed from their interstitial position in the bulk and this mechanism occurs 16 times faster than for a clean surface. The extend of spillover was found to be temperature dependent and was controlled by adsorption/desorption from Pd nanoparticles. Finally it was noted

that the nanoparticles were buried into the new TiO_2 layer and thus "removed" from the surface and was defined as a new kind of SMSI [5]. It seems that in these papers, encapsulation is an effect in SMSI.

The Diebold group [57] examined Pt on TiO_2(110) in the SMSI state confirming the encapsulation of Pt clusters after annealing in UHV at high temperature. They observed square and hexagonal shaped clusters (figure 13).

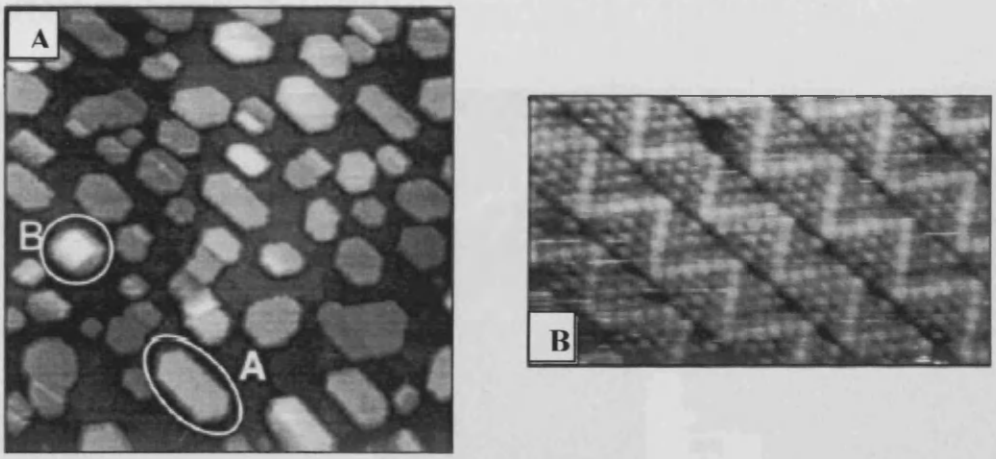

Figure 13: STM results after high-temperature treatment. (a) Overview (2000Å×2000Å). Clusters are approximately 200Å wide and 40Å high. Most clusters show hexagonal shape elongated along the substrate [001] direction (type *A*). A few square clusters (type *B*) are seen. (b) Atomic-resolution image of an encapsulated "type-*A*" cluster.

The hexagonal clusters were flat, smooth and showed stripped "zigzag" structures at their surfaces. Their structure consisted of two layers of TiO_2 that encapsulated the Pt atoms, blocking the sites to adsorption. The inertness of the surface suggested either an oxygen terminated surface or a saturation of bonds of surface Ti atoms. Reactions (such as hydrogenation reactions) that saw their activity enhanced is explained by local effects. Special Ti^{3+} sites at the modified Pt catalyst or Pt sites next to the reduced TiO_x layer are thought to be responsible for this enhancement. In a computational study, the same group found a similar structure with the above experimental STM observations and the energetics of a TiO film on Pt(111) determined from theory [57]. Looking back at the growth of Pd on TiO_2(110) surface, it was found that the growth rate is influenced by the level of substrate defects such as

oxygen vacancies and added rows (arising from the reduction of the oxide at high temperature). Both defects and steps delay diffusion and thus slow down particle growth [58]. Pd nanoparticle also formed on the cross links in the case of the cross linked (1×2)-TiO_2(110). The deposited clusters sintered to form particles upon annealing and arranged along the cross links [6]. The Bowker group [4] showed the formation of two coexisting SMSI states by heating Pd supported on the (1×2)-TiO_2(110), as shown in figure 14.

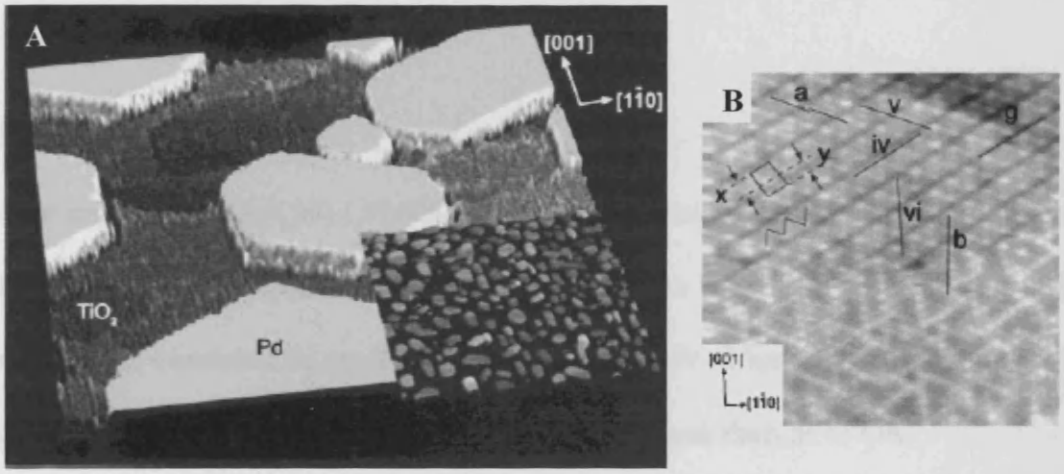

Figure 14 : A) 3D representation of a 1630Å ×1630Å STM image of Pd/TiO2(110)-(1×2) following annealing at 573K for 25min, 773K for 20min, and 973K for 20min. The inset is a 13770Å×13770Å STM image of the same surface. B) A 101Å×101Å STM image of an area showing the pinwheel structure (bottom) and the zigzag structure (top). The unit cell marked that of the zigzag structure. *a* marks two lines drawn along the zigzag diagonals; these indicate the phase shift as one goes across the troughs. *g* marks a glide-plane. *b* marks the rotation as one goes from the spokes of the pinwheel to the diagonal of the zigzag. The lines, iv, v, and vi indicate line profiles not shown here.

A complicated "pinwheel" structure showing a similar geometry as the surface alloy observed by Zhang et *al.* Cr/Pt(111) [59] the other consisting of rows of zigzag similar to titania encapsulated Pt support on TiO_2(110)-(1×1) [57] and to the thin film of TiO_2 grown on Pt(111) [54].

A recent publication on the model system Pd/TiO_2 via XPS, AES and Rutherford Backscattering Spectroscopy (RBS) showed that encapsulation depended on the electronic structure of TiO_2 [60]. They concluded that a number of events were

necessary for encapsulation of metal clusters on oxide supports: 1) The energy at the Fermi level of the oxide, E_F(oxide), must be greater than the one of the metal. 2) Reduced or n-type doped oxides with small surface energies (e.g.TiO_2) are required as well as 3) metals with large work functions and large surface energies such as Pt, Pd and Ru. 4) Sufficiently high temperature to activate transport processes. This enabled them to control the encapsulation reaction or SMSI in many metal oxide catalytic processes.

2. Experimental

2.1. Crystal preparation

A new crystal of TiO_2(110) (PI KEM, UK) was placed in the STM. The crystal was subject to cleaning cycles until a decent LEED pattern was observed (1×1 then 1×2). The cleaning consisted in cycles of sputtering (0.6keV, 15mins to 30mins) at room temperature followed by 15mins annealing at 1023K and flash at 1173K.

Palladium was then deposited on the crystal by MVD (metal vapour deposition). A current was passed through the metallic filament and left to degas for 30 seconds. The crystal was then moved and placed beneath the source filament (~5cm below). To obtain a consistent deposition, the best position was set when the glowing filament reflection was seen on the surface of the crystal.

2.2. Catalyst preparation and experiments

The catalyst was prepared by incipient wetness using TiO_2 (Degussa P25) and palladium (II) chloride (Alfa Aesar, 99.999% purity, 59.97% assay). The volume required to reach incipient wetness was determined using de-ionised water and different batches of 1g of TiO_2. The water was added drop wise until the pores of the powder were filled (paste like mixture). The volume of deionised water determined

was 0.656± 0.003cm^3/g of catalyst. The sample was prepared to obtain a 5% Pd loading on TiO_2.The appropriate amount of $PdCl_2$ was dissolved in a known volume of deionised water (0.656cm^3) to give the desired concentration of metal precursor. The volume of metal solution added was sufficient to fill the pores of the TiO_2 support. The impregnated compound was then dried at 120°C for 12 hours and calcined in air at 500°C overnight. The sample was pressed to 9 tonnes and sieved to produce granules between 600 and 850μm in diameter. Approximately 0.5g (0.50021g) of catalyst was loaded in the tube which was then fitted in the oven.

The catalyst was reduced at 200°C, 400°C, 500°C and 550°C by pulsing H_2 every 30 seconds in a carrier gas flow of He running at 30cm^{-3}.min^{-1}. Between each reduction, CO uptake and CO oxidation experiments were carried out. CO uptake was realised by pulsing CO in the He carrier gas. The catalyst was kept at room temperature. For the CO oxidation reaction, a CO was pulsed in the carrier flow gas consisting of 10%O_2/He. The catalyst was first kept at room temperature and then the temperature was ramped to 500°C with a rate of 10°C.min^{-1}.

Additional reduction/oxidation experiments were carried out on the catalyst reduced at 200°C. Before being reduced at 200°C, the catalyst was reoxidised by manually pulsing oxygen with a VICI GC syringe via a septum placed on the gas line. Reduction was done as before by pulsing hydrogen every 30 seconds in a carrier gas of He running at 30cm^3.min^{-1}.

3. Results and discussion

3.1. The preparation of model $Pd/TiO_2(110)$ catalysts

3.1.1. Clean TiO_2

After the cleaning treatment, the surface presents little contamination. The Auger spectrum of the crystal, displayed on figure 15, shows a peak of calcium (6%) at ~295eV and no carbon. Peaks at lower energies, 190eV and 225eV, correspond to molybdenum coming from the block holding the crystal.

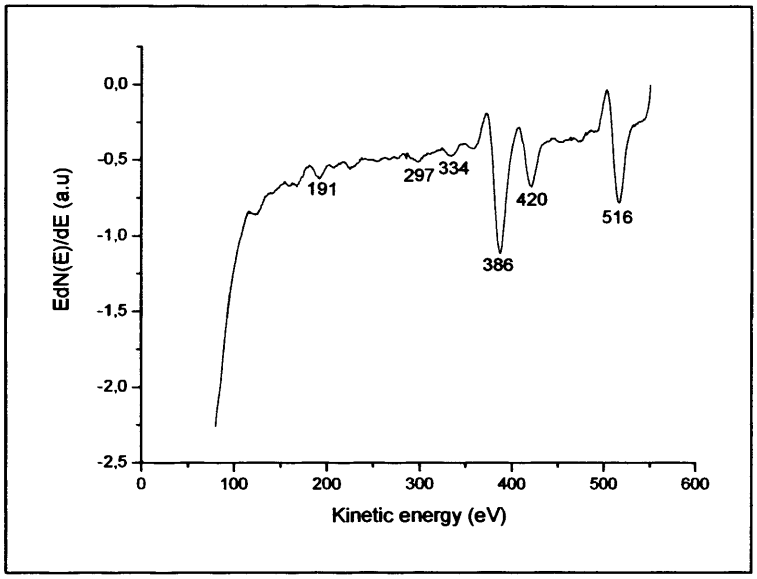

Figure 15: Auger spectrum

The LEED pattern observed after the cleaning cycles showed a (1×2) surface reconstruction. The LEED patterns of (1×1) and (1×2) surface structures are displayed on figure 16.

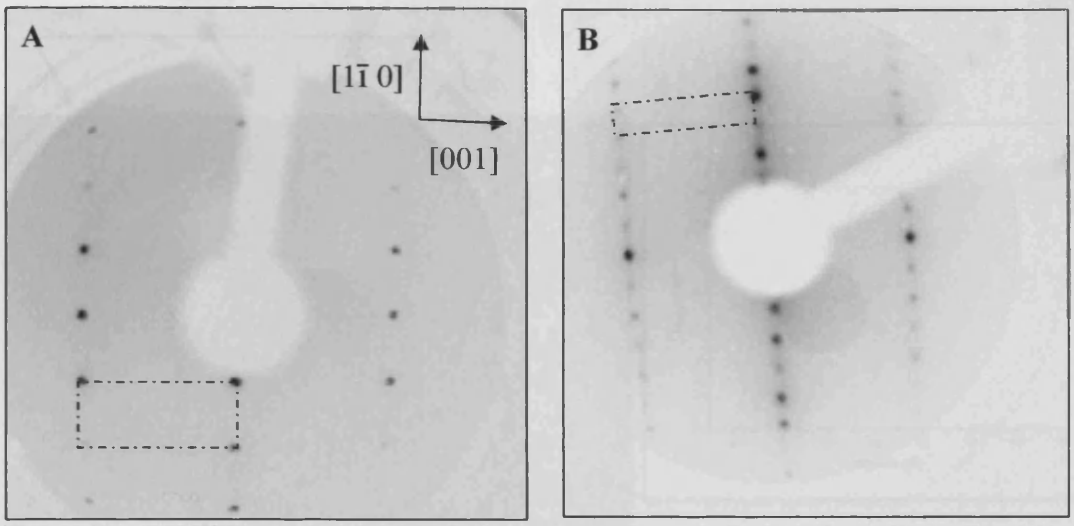

Figure 16: A) LEED pattern of the (1×1) surface corresponding to the bulk termination. Beam energy: 122eV. B) LEED pattern of the reconstructed (1×2) surface. Beam energy: 117eV.

The unit cells are represented by the dashed black squares. The (1×1) pattern is observed after the few first cleaning cycles. Continuous cycles induced a (1×2) pattern. This (1×2) reconstruction arises from the reduction of the surface due to sputtering. As we have seen previously, sputtering preferentially removes oxygen atoms, leaving a disordered reduced surface that reconstruct upon annealing.

The unit cells of the (1×1) TiO_2 and the (1×2) TiO_2 are ~2.95Å by ~6.5Å and ~2.95Å by ~13Å respectively. In the LEED reciprocal space, one can see that the size of the unit cell along the [001] direction is the same for both structure while the size along the [1$\bar{1}$ 0] is half the distance. In real space, this distance is then doubled, which is in accordance with the (1×2) unit cell.

High resolution images of TiO_2 surface were recorded and are presented on figure 17, 18 and 19. Four breaks are visible into the surface that splits it into terraces. A line profile across a break (figure 17, white line) shows a step height of 3.31±0.07Å. This is in agreement with the vertical spacing between two TiO_2 (110) planes (3.24Å). Another notable feature consists in long bright rows in the [001] direction. Their terminations often appeared brighter.

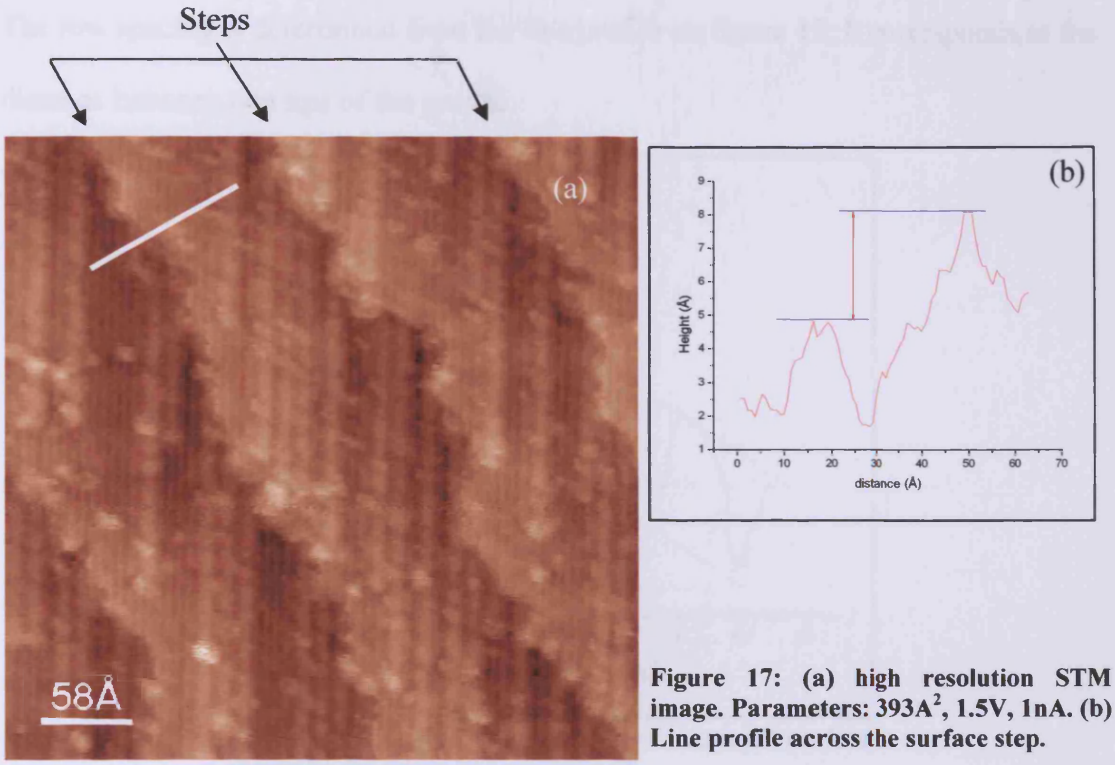

Figure 17: (a) high resolution STM image. Parameters: 393A^2, 1.5V, 1nA. (b) Line profile across the surface step.

This is interpreted as an increased density of empty states due to a different composition to the rest of the row. The main feature on figure 18 consists of large bright rows with a spacing of 12.55±0.4Å (figure 19).

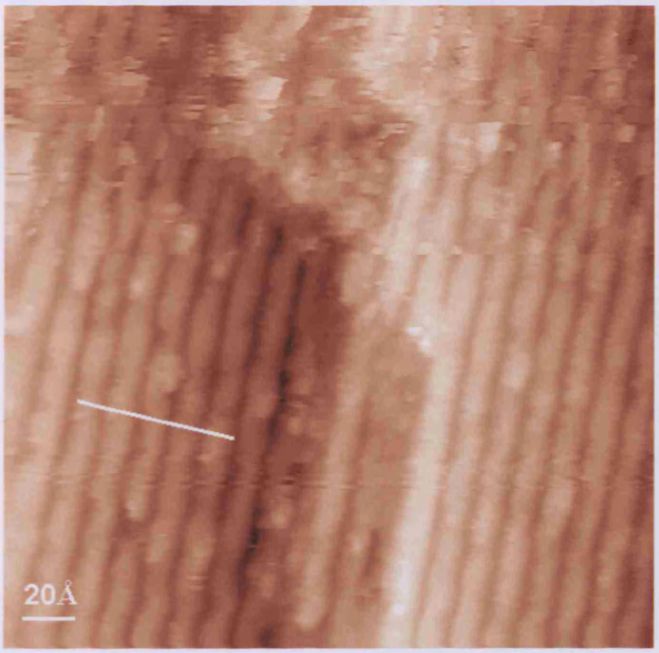

Figure 18: High resolution STM image. Parameters: 248Å^2, 1V, 1nA.

The row spacing is determined from the line profile on figure 19. It corresponds to the distance between two tips of the profile.

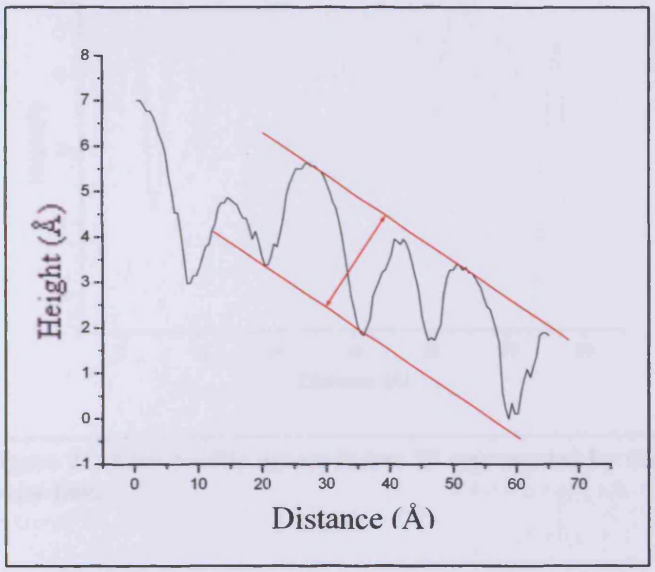

Figure 19: Line profile across the reconstructed surface shown by the white line on figure 18.

The rows are sitting at 2.5±0.2Å from the (1× 1) surface and corresponds to the distance represented by the red arrow on the line profile. This is smaller than the distance of 3.24Å between two (1×1) planes. From the above measurements, it is clear that the surface consists of a (1×1) substrate with (1×2) added rows.

On the high resolution image (figure 20), the structure is (1×1)TiO_2.

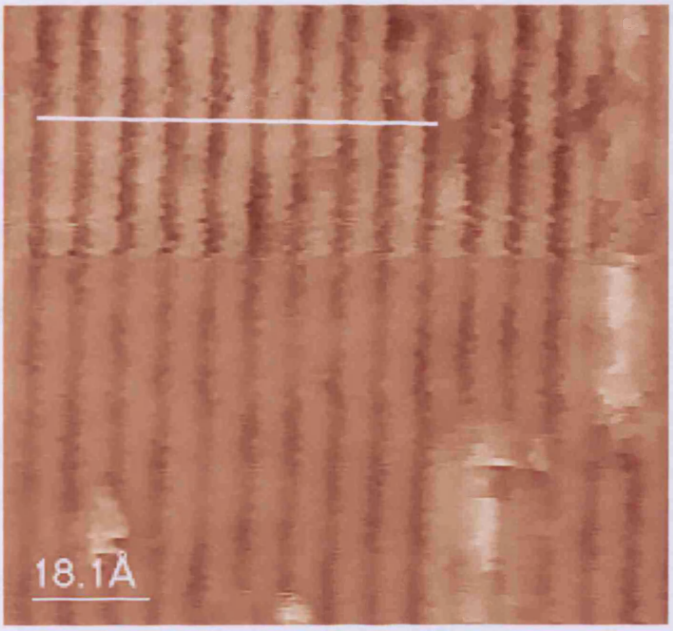

Figure 20: (a) High resolution STM image of (1×1) surface. Parameters: 91.1Å^2, 1.5V, 1.5nA.

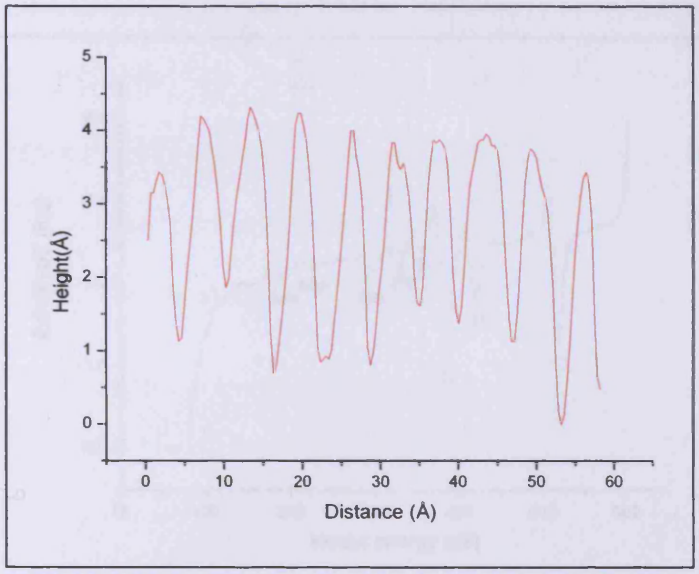

Figure 21: Line profile across figure 20 represented by the white line.

The line spacing is 6± 0.1Å which is close to the theoretical (1×1) line spacing of 6.48Å. A few brighter spots and start of a strand are also present and probably correspond to nucleation sites of the (1×2) strands.

Calcium contamination is a common impurity in single crystal of TiO_2. It tends to segregate at the surface upon high-temperature annealing [61-63]. This contamination started during the study of Pd/TiO_2 surface when sputtering and annealing treatments were carried out. The cleaning treatment of the crystal consisted more sputtering and high temperature flashes (1173K) to remove the Pd layer followed by long annealing (30mins to 45mins) to smooth the surface. This treatment resulted in the decrease and near loss of the Pd peak but in the appearance of the Ca peak. The Auger spectrum is shown in figure 22.

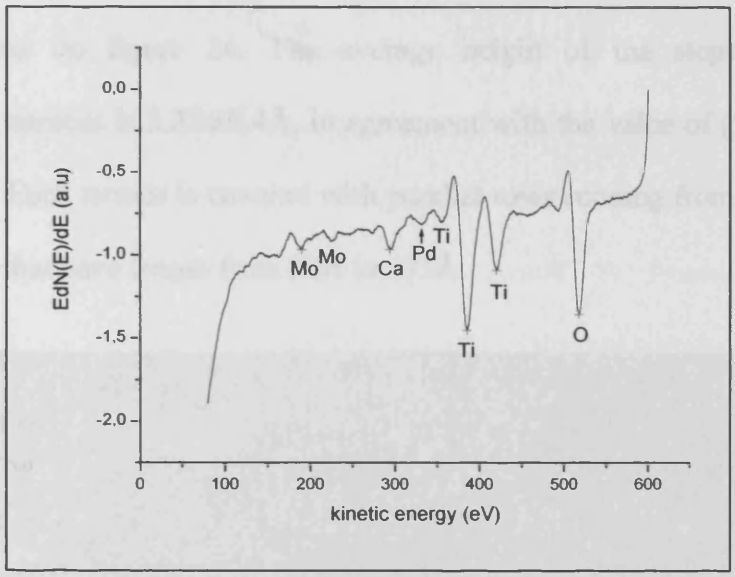

Figure 22: Auger spectrum of the TiO_2 surface after cleaning treatments.

The peaks at 190eV and 225eV are coming from the Molybdenum from the sample holder block. Calcium is present at 295eV (8.7%). A little Pd remains at 333eV (0.9%) but in very low amount compared to the TiO_2 crystal (Ti: 53.23%; O: 37.08%). The LEED pattern shows the (1×1)-TiO_2 pattern (figure 23). The white rectangle represents the unit cell. Very faint spots are present in between the (1×1) pattern, in the vertical direction, coming from the (1×2) reconstruction.

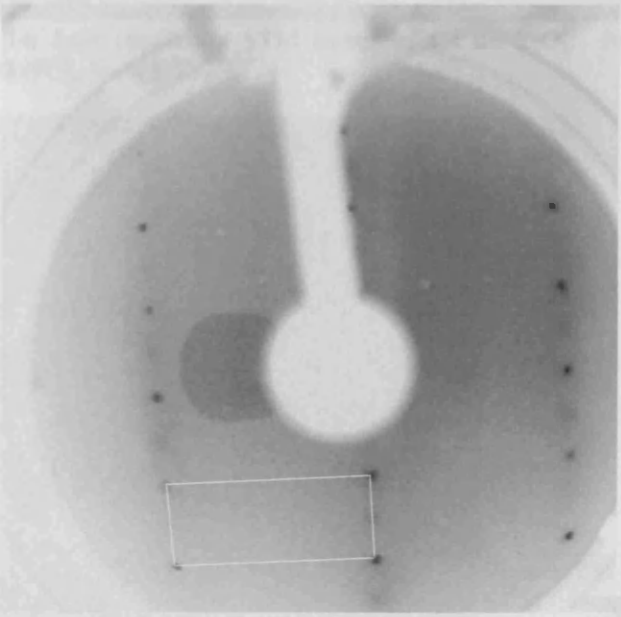

Figure 23: LEED pattern (66eV) of theTiO_2 surface after cleaning treatments.

STM images from a Ca-segregated surface are shown on figure 24 and 25. Many terraces appear on figure 24. The average height of the steps between two neighbouring terraces is 3.2Å±0.4Å, in agreement with the value of (1×1)-TiO_2(110) surface steps. Each terrace is covered with parallel rows running from the lower right to the top left that have length from 30Å to 175Å.

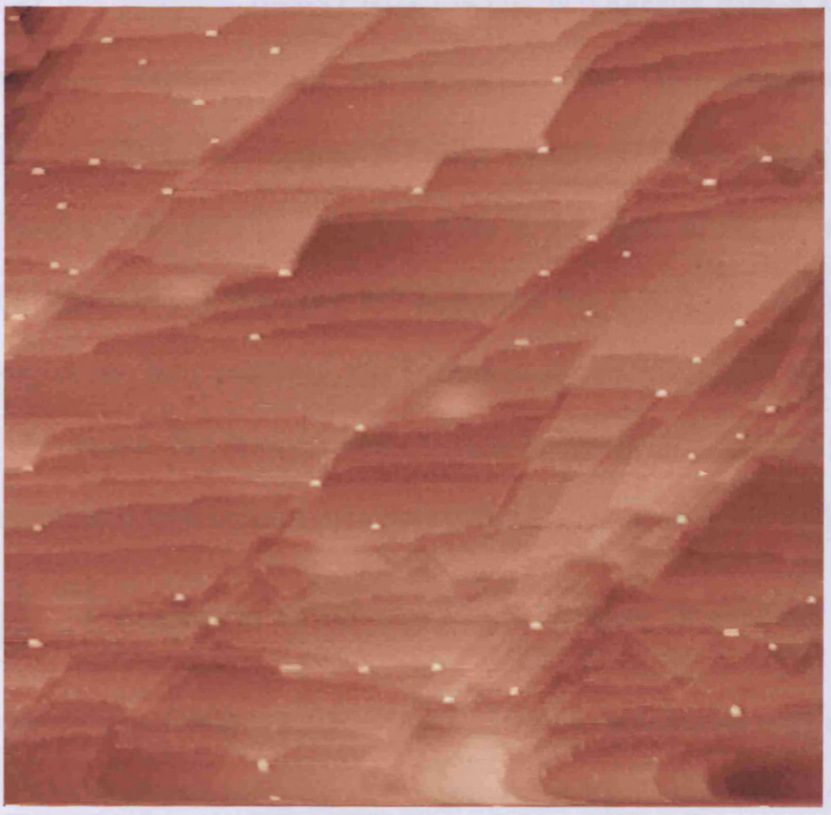

Figure 24: Low resolution STM image of Ca on TiO_2. Parameters: 2497Å×2497Å, 1nA, 1.5V, RT.

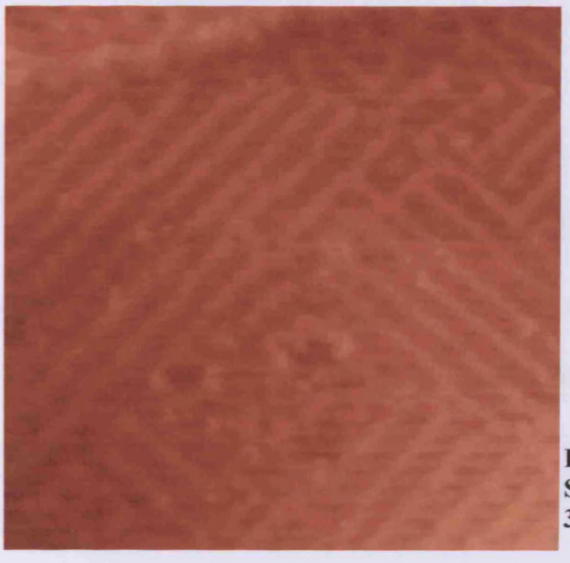

Figure 25: High resolution STM image. Parameters: 373.5Å× 373.5Å, 1nA, 1V.

They are intersected by rows perpendicular to them. These rows have length from 30Å up to 300Å. A zoom in figure 24 is shown on figure 25 where these characteristics are much clearer. The spacing of the parallel rows is not completely regular. A distance of 20.5Å±0.7Å is measured. This is about three times the distance 6.5Å, which is the periodicity along the [1$\bar{1}$0] direction of the clean (1×1)-TiO_2(110) surface. Under this structure, parallel rows running horizontally have a spacing of 13.8Å±0.6Å. This corresponds to the periodicity the [1$\bar{1}$0] direction of the reconstructed (1×2)-TiO_2(110) surface. A feature clearly visible on image 24 is the presence of bright white particles of ~50Å width at the edges of the terraces. They consist of Ca agglomerates that have diffused from the bulk to the surface of the crystal. Zhang et *al.* [61] proposed the formation of a $CaTiO_3$-like surface after observing STM images. The structure was identical to the experimental one presented here. They observed a well ordered overlayer that was clearly observed in LEED and reported a $\begin{pmatrix} 6 & 0 \\ 3 & 1 \end{pmatrix}$ structure in LEED. The LEED in figure 23 does not show the same characteristics as Zhang one. However, during the experiments with palladium deposition, a LEED pattern identical to the one shown by Zhang was found and is shown later in this chapter.

3.1.2. Palladium on TiO_2

Palladium was deposited at the surface by metal vapour deposition. The values of the current and the time required to evaporate the metal depend on the state of the filament. A new filament contains more palladium than an older one. That way, a low current and a short time will be sufficient to deposit metal at the surface. Once the filament is aged, for the same current, a longer time of deposition is necessary to deposit the same amount of metal.

The Auger spectrum (figure 26) shows a large peak of palladium at 331eV. Palladium shows other peaks at 281eV, 247eV and 164eV. Peak at 190eV and 225eV correspond to molybdenum and is coming from the sample holder block. A thick film of palladium has been evidently deposited because titanium and oxygen peaks are not visible in the spectrum.

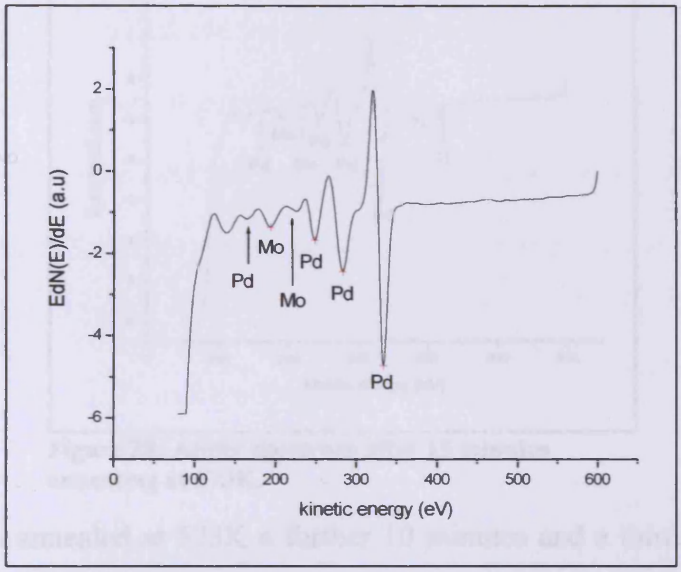

Figure 26: Auger spectrum after Pd deposition. From the size of the palladium peak, this corresponds to a high coverage.

The main feature of the LEED is an hexagonal pattern corresponding to the Pd(111) surface, as shown in figure 27.

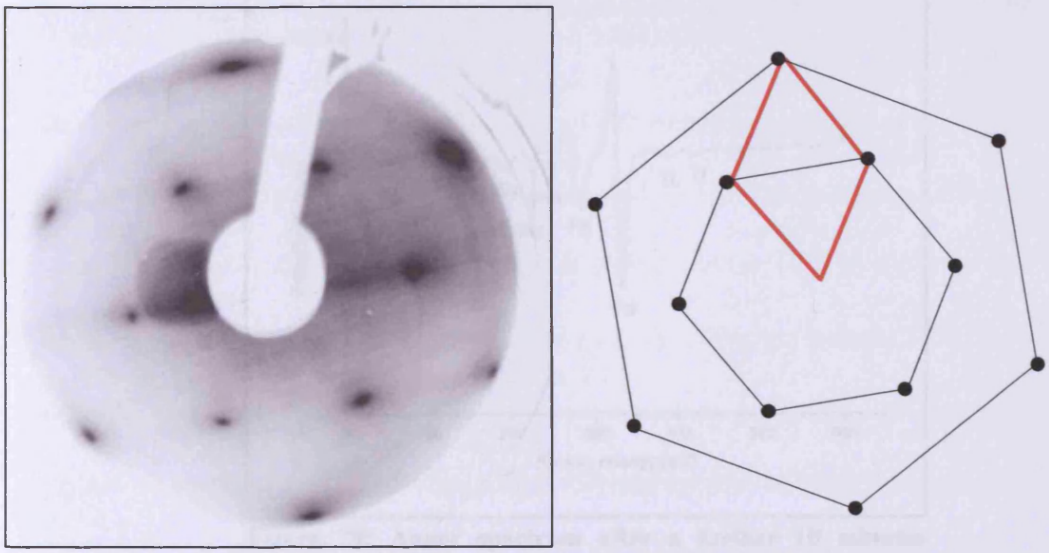

Figure 27: (a) LEED pattern taken at 155eV. (b) Schematic representation of the pattern. The black spots correspond to the spots of the Pd(111) on the LEED. The unit cell is shown in red.

The sample was annealed at 573K for 15minutes and the Auger spectrum on figure 24 was obtained. Titanium is present on the surface showing peaks at 386eV and 421eV. The peak at 421eV appeared as a spike due to an artefact. The same palladium and molybdenum peaks as figure 26 are present on figure 28.

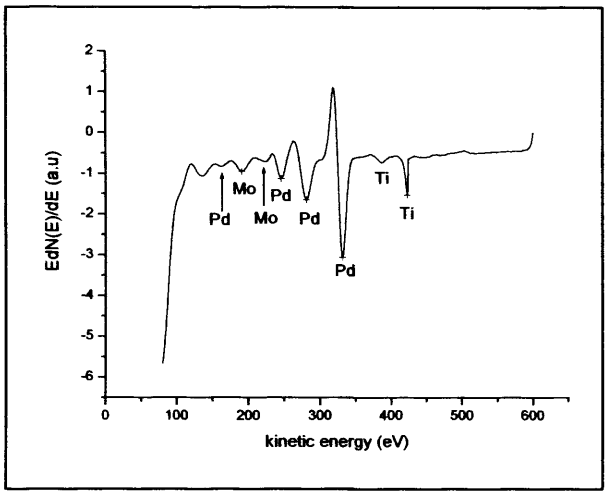

Figure 28: Auger spectrum after 15 minutes annealing at 573K.

The sample was annealed at 573K a further 10 minutes and a third Auger spectrum was recorded (figure 29). The two peaks of titanium were visible but still no significant oxygen peak is seen. Titanium and oxygen have similar sensitivity factor of 1.2155 and 1.2571 respectively.

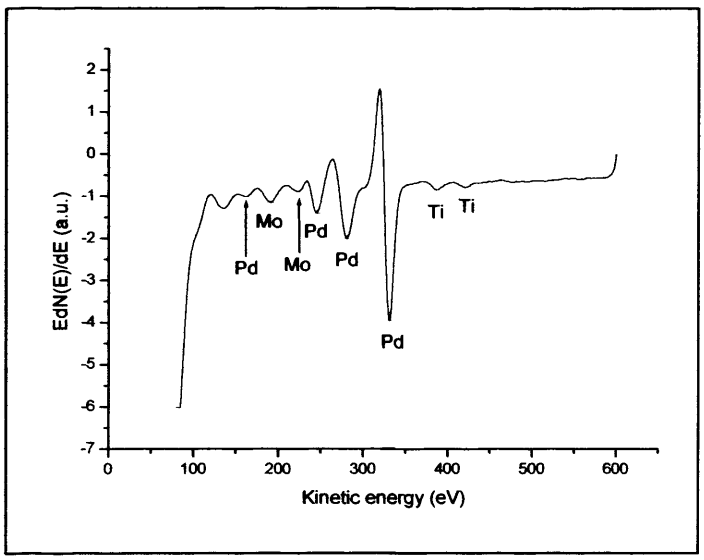

Figure 29: Auger spectrum after a further 10 minutes annealing at 573K.

Their relative cross sections differ a little with $\sigma = 0.529Å^2$ for Ti and $0.822Å^2$ for O thus a slightly bigger peak of oxygen is expected. In a fully oxidised crystal, the Ti:O ratio is 1:2, thus an oxygen peak twice bigger than the titanium one should be seen.

It is therefore probable that the surface is highly reduced which can account for the loss of the oxygen peak.

Further annealing was carried out for 10minutes at 673K, then at 773K and finally at 873K but no oxygen peak was detected. The peaks of Ti slightly increased with annealing temperature and the Pd peak slightly decreased. Calculations of the film thickness of palladium and the concentration of species at the surface are summarised in the table 1 below.

Annealing treatment	Palladium film thickness in Å	[Ti] in %	[Pd] in%
573K, 15mins	17.4	11	88.9
573K, 10mins	17.5	11.7	88.2
673K, 10mins	16.5	12.3	87.6
773K, 10mins	16.3	12.8	87.1
873K, 10mins	16.2	12.9	87

Table 1: the thickness is calculated from the equation $I=I_0e^{-d/\lambda}$ (refer to chapter 2 paragraph 6). The concentrations of the species were calculated from the Ti peak at 390eV and Pd peak at 333eV. The sensitivity factor for Ti is 1.2155 and 3.2842 for Pd.

The details of the calculation are explained in chapter 2 paragraph 6. The Mo peak was not taken into account for the determination of the concentration of Ti and Pd.

It has been shown that the growth mode of palladium on TiO_2 (110) is by the Volmer Weber growth (see chapter 3 for details and [2]). The palladium first deposited as particles that grow in height and diameter as more palladium is deposited. If the deposition continues, the particles will finally merge but without fusing together. This was observed for Cu (Chapter 3) and palladium behaves in an identical way. Annealing treatment may allow the fusion of the particles into a flat film.

Different explanations can account for the appearance of Ti peaks and the decrease in Pd coverage. High coverage (10-20ML) deposition of palladium produces 3D islands of Pd which exhibits the (111) facets [2]. The first possibility is that the palladium particles sinter with annealing into a thin film. Sintering occurs at 773K [9, 65] and, as seen in chapter 3, this has for effect to increase the surface area of each particle but to reduce the total surface area of the metal at the surface. The film may have holes where the substrate is visible and thus detected on the Auger (figure 30A). This structure has been previously seen by Bennett [3].

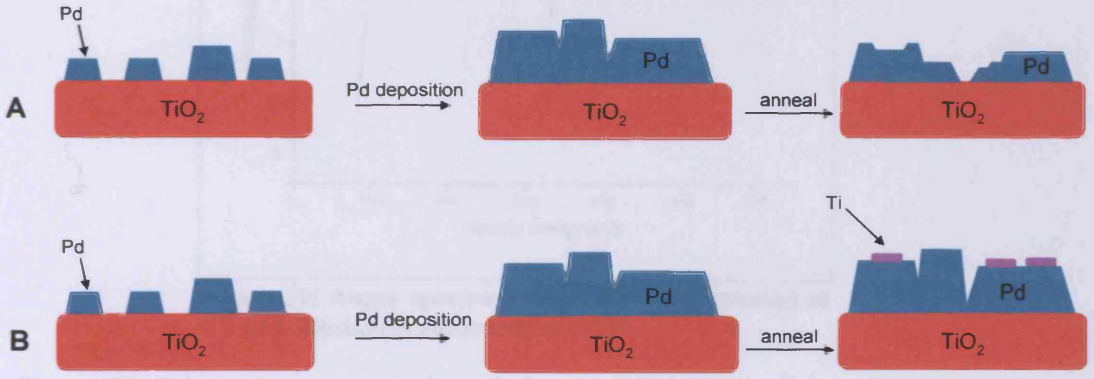

Figure 30: Schematic representation of the possible effects of annealing on a film of palladium. The red rectangle corresponds to the TiO_2 substrate, The green trapezoid is the Pd(111) film and the purple rectangle corresponds to the titanium atoms.

A second possibility is the transfer of Ti atoms through the large palladium particles or film onto the top of the Pd substrate (figure 30B) thus lowering the intensity of the palladium peak. The diameter of a Ti ion is 1.28Å and oxygen diameter is 2.8Å. Oxygen ion is twice bigger than a Ti ion thus Ti ions are the most likely to transfer through the film of metal deposited. This may explain the absence of oxygen on the Auger spectrum. Another explanation of this effect is that oxygen is less sensitive than titania. On the Auger spectrum of the clean titania (figure 15), oxygen peak is smaller than the titania (ratio Ti:O is 1.2:1) one despite the presence of twice more

oxygen than titania at the surface. Despite the sharpness of the LEED, STM imaging was not successful for the above surface.

The next treatment consisted in short sputtering followed by annealing at 873K for 30 minutes. Following this treatment, the Auger spectrum shown in figure 31 and the LEED represented in figure 32 were obtained.

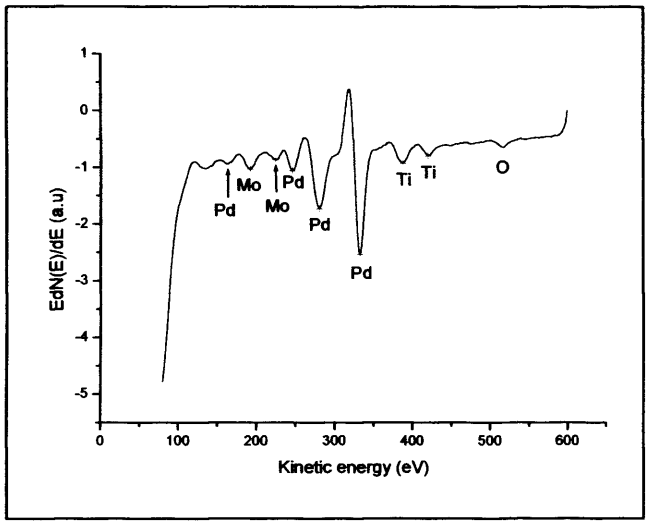

Figure 31: Auger spectrum after 30mins sputtering at RT and 30minutes annealing at 873K.

The Auger spectrum finally shows some oxygen at 510eV. The film, after this treatment, is 11.4Å thick. The two peaks of titania have increased also a little compared to the previous spectrum. The concentrations in Ti and Pd are 24.8% and 75.2% respectively.

The LEED pattern on figure 32A show the presence of a hexagonal pattern, labelled **a** and represented by a solid black hexagon on figure 32D. It corresponds to the Pd(111) substrate which has the real space nearest neighbour distance of 2.75Å as seen on the LEED shown on figure 27. The second feature is a pair of dashed red hexagons labelled **b** on figure 32D. They are rotated ±3° with respect to the Pd(111) hexagon. Figure 32B shows a LEED taken at 37eV. Three hexagonal patterns of different size are visible. The spots are quite broad and may consist of 2 spots instead

of 1. The two smallest sets of hexagons are aligned. The largest pattern (external one) is rotated of ~30° from the other hexagons. On figure 32C, which is schematically represented on figure 32D, extra spots have appeared on the LEED screen. The first set of extra spots is labelled **c** and is represented by the blue hexagon on figure 32D. The hexagon **c** is smaller than the hexagon of the Pd(111) substrate.

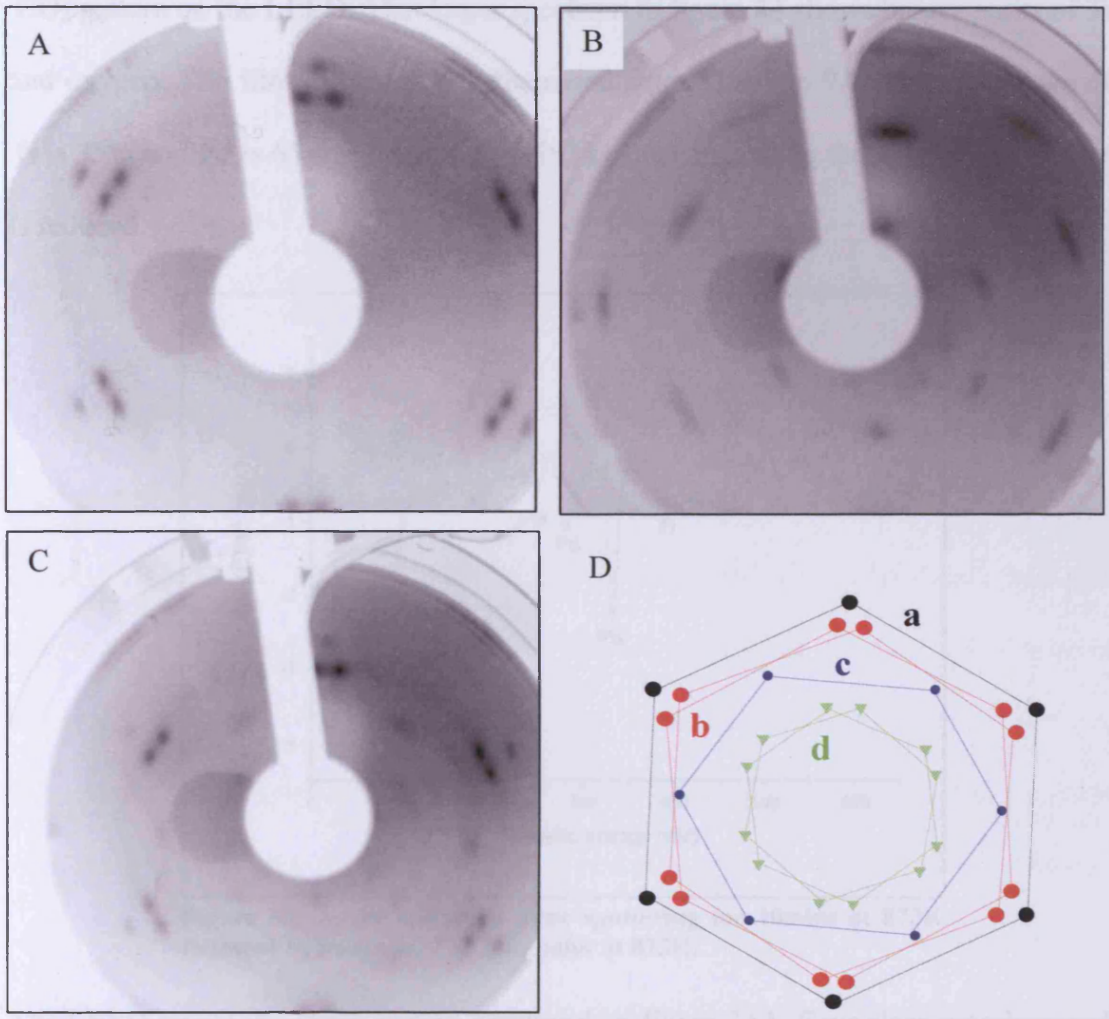

Figure 32: LEED pattern after annealing at 873K. A) Beam energy at 90eV, B) at 37eV, and C) 98eV. D) Schematic representation of the LEED pattern figure 32C.

This means that in real space, a bigger structure is present at the surface. Another set of spots is visible, labelled **d** on figure 32D, and is even smaller than **c**. It seems that this last series of spots is composed of 2 sets of hexagons. The LEED is not sharp

enough to differentiate clearly the set of hexagons. These extra spots have a real space structure even bigger than the structure labelled **c**.

In order to obtain a pattern of the TiO_2 substrate and to sharpen the LEED pattern the surface was further sputtered for 10minutes and annealed at 873K for 30 minutes. The sputtering treatment was carried out in order to remove some palladium and observe TiO_2 pattern on the LEED. The Auger spectrum in figure 33 shows bigger peaks of Ti and oxygen. The film thickness has decreased from 11.4Å to 9Å. The percentage of Ti is 35% and Pd is 65%. The ratio for Ti:O is 1.6:1 indicating that the TiO_2 substrate is reduced.

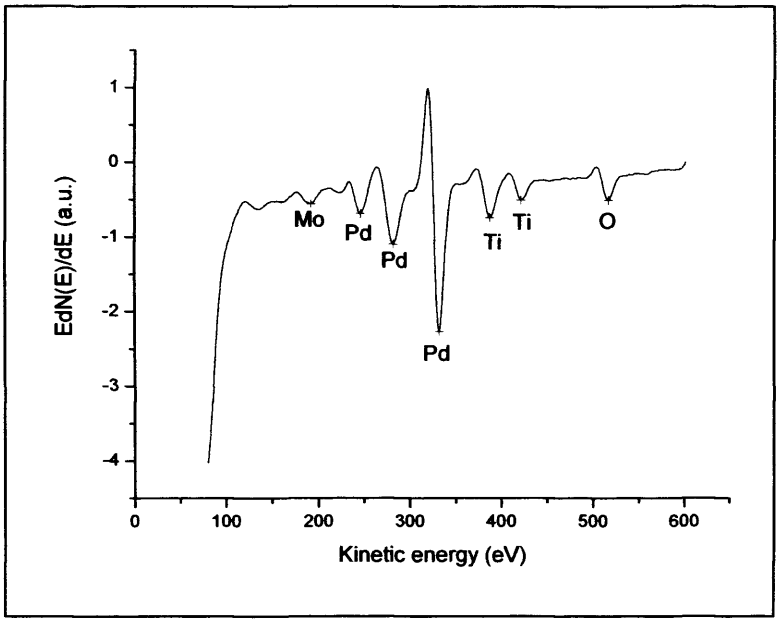

Figure 33: Auger spectrum after sputtering for 10mins at 873K followed by annealing for 30minutes at 873K.

The LEED revealed a sharp pattern displayed on figure 34A. Four clear superimposed patterns are distinguished.

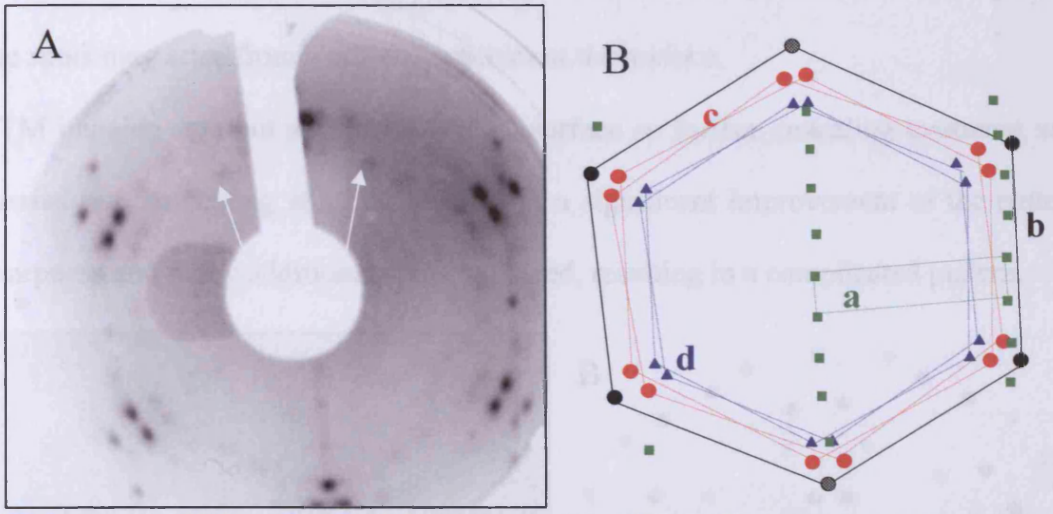

Figure 34: A) LEED pattern at 88eV after annealing at 873K. The white arrows are pointing at the faint additional spots. B) A schematic representation of the LEED pattern shown on figure 34A. The green squares represent the (1×2)-TiO_2(110) substrate, the black circle are the Pd(111), the red circles are the pinwheel spots and the blue triangles are from another kind of pinwheel structure.

Figure 34B shows schematically and to scale the different structures of the LEED pattern for clarity. The dashed green rectangle labelled **a** is the unit cell generated by the exposed region of the (1×2)-TiO_2(110) substrate. The solid black hexagon labelled **b** corresponds to the (111) Pd surface which has the real space nearest neighbour distance of 2.75Å. From the known dimension of the TiO_2 and Pd lattices, it is possible to determine the unit cell of the new structures. The real space nearest neighbour distance for the red hexagon structure **c** is 3.20Å±0.10Å and the structure possesses a hexagonal unit cell. It corresponds to the pinwheel structure as observed by Bowker group [4]. Finally, another set of hexagons, labelled **d** and represented by the blue pair of hexagons may belong to another kind of pinwheel structure. They are aligned with the pinwheel structure and have a larger unit cell. The nearest neighbour distance for this structure is 3.64Å±0.03Å and the hexagons are also rotated ±3° with respect to the Pd(111) underlayer. This structure was not observed in previous publications. Additional faint spots within the set of hexagons **d** were detected and

are shown with the white arrows. However, those two last patterns are very faint and the spots may arise from a minority species at the surface.

STM imaging was not successful on this surface so further annealing treatment was carried out. Annealing at 973K resulted in a significant improvement of the pattern sharpness and many additional spots appeared, resulting in a complicated pattern.

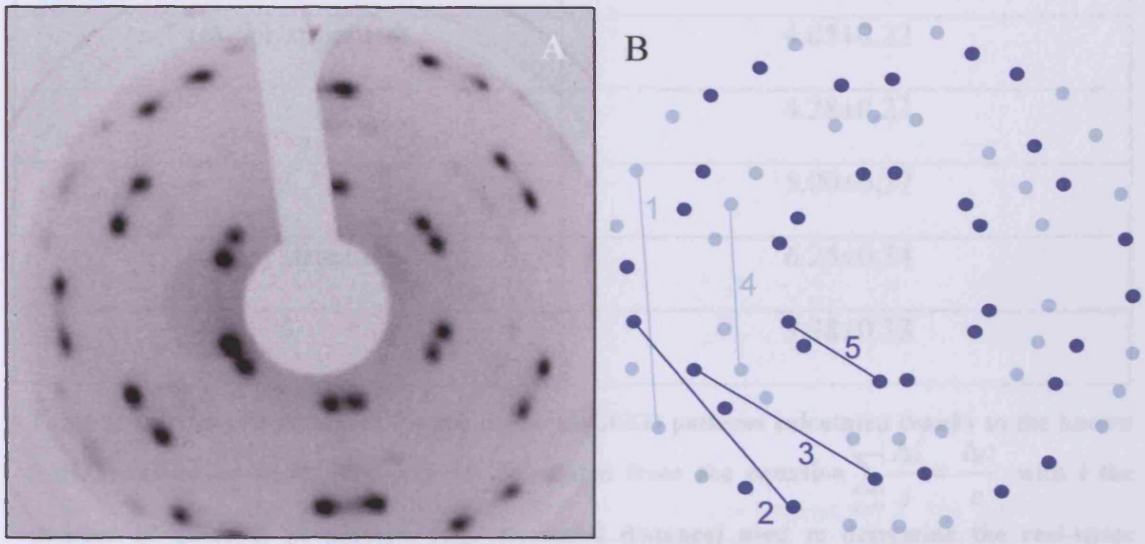

Figure 35: A) LEED pattern at 34eV after annealing 25 minutes at 973K. B) Schematic representation of the LEED pattern shown on figure 31A. The blue circles correspond to the spots of the set of hexagons. The interest in this LEED is the presence of a clear pattern at low beam energy which indicates that large structures, much larger than the Pd(111), are present on the surface.

At low energy (figure 35), a reasonably sharp pattern is visible, which, since the energy is low, must relate to structures with a large unit cell. It consists of three sets of hexagons that resemble the pinwheel pattern and the external set has a ~30° rotation from the others. The pattern figure 35A is the same as 33B but much sharper. It is possible to determine the distances of their unit cells by using the known distance of the Pd unit cell at a known beam energy value. The beam energy is related to the interatomic distance by the relation:

$$x' = x_0 \sqrt{\frac{V_0}{V_{0'}}} \qquad (2)$$

Where x' is the reciprocal distance at a beam energy V_0· (eV) and x_0 is the reciprocal distance at a beam energy V_0. Thus, the reciprocal distance for the Pd substrate at 34eV was calculated. From this value, the interatomic distances of the 3 sets of hexagons on figure 35 were determined and are shown in the table 2.

Structure label	Real space nearest neighbour distance (Å)
1 (minor structure)	4.05±0.22
2	4.28±0.23
3	5.00±0.27
4(minor structure)	6.25±0.24
5	9.38±0.33

Table 2: Interatomic distances for the different LEED patterns calculated thanks to the known Pd(111) lattice constant. The error is calculated from the equation $\sum_{a\to i}\frac{\Delta i}{i}=\frac{\Delta c}{c}$ with i the number of different parameters (e.g. measured distance) used to determine the real-space distance, c.

The labels 2, 3 and 5 correspond to the three dominant patterns in figure 35A. Looking closely at those values, label 5 has approximately the double distance of label 2. It may be suggested that label 5 corresponds the spacing for the STM structure with a size ~10Å and that label 2 is the continuation of the lattice. The LEED pattern is arising from a curved screen and the distances are thus not accurate at the edges of the screen. The pattern 3 does not show distances that could be related to the other structure. The only indication about this structure is its larger size compared to the hexagonal Pd(111).

At 93eV, a very complex pattern is observed with a large number of spots, which seem to be all related to the hexagonal or pinwheel structure. This is shown in figure 36A, which was obtained after the film was annealed for 25mins at 973K. Figure 37 consists in an exploded schematic of the LEED pattern drawn on figure 36B and

helps to differentiate and analyse the different structures. Three of the patterns were present on the previous LEED (figure 34). They were labelled **b**, **c** and **d**. The pattern of the TiO_2 structure (labelled **a**) is not visible on this LEED pattern because of the low energy.

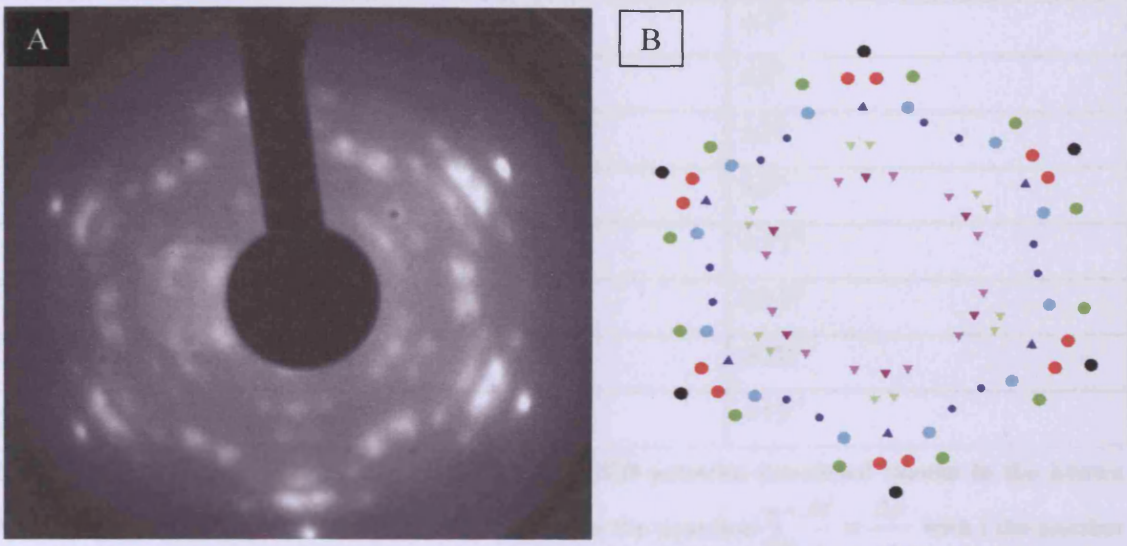

Figure 36: A) LEED pattern at 93eV after 25 minutes annealing at 973K. B) Schematic representation of the LEED pattern shown on figure 36A.

Two of the patterns, **b** and **c**, were assigned to the Pd(111) substrate (black spots) and the pinwheel structure (red spots) which were identified earlier [4].

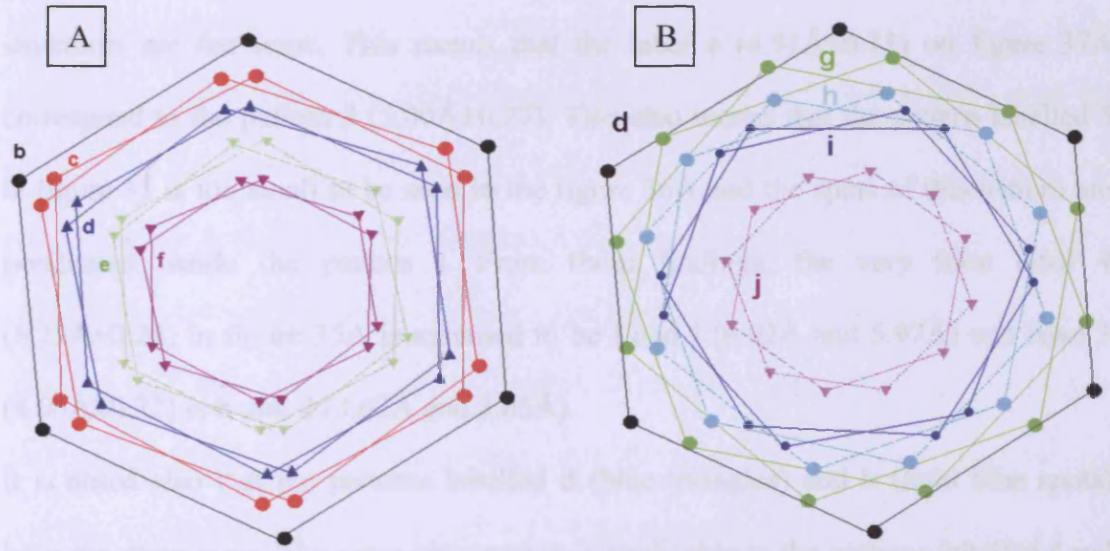

Figure 37: Exploded schematic of the LEED pattern on figure 36B for clarity. The black spots correspond to the spots of the Pd(111) substrate. The red ones show the pinwheel structure. The other structures represented by the triangles and spots of various colour may be related to pinwheel-like structures.

The real space nearest neighbour distances for each structures and their rotation with respect to Pd(111) are summarised in the table below:

Structure label	Real-space nearest neighbour distance (Å)	Rotation angle with respect to Pd(111) pattern
b: Pd(111)	2.75	-
c : Pinwheel	3.20±0.05	±3°
d	3.62±0.03	±3°
e	4.91±0.11	±3°
f	6.02±0.12	±3°
g	3.01±0.01	±15°
h	3.65±0.07	±15°
i	3.94±0.16	±30°
j	5.97±0.16	±15°

Table 3: Interatomic distances for the different LEED patterns calculated thanks to the known Pd(111) lattice constant. The error is calculated from the equation $\sum_{a \to i} \frac{\Delta i}{i} = \frac{\Delta c}{c}$ with i the number of different parameters (e.g. measured distance) used to determine the real-space distance, c.

The distances calculated in table 3 were compared with those on table 2. It can be suggested that the label 2 (table 2: 4.28Å±0.23) and label **i** (table 3: 3.94Å±0.11) structures are the same. This means that the label **e** (4.91Å±0.11) on figure 37A correspond to the pattern 3 (5.00Å±0.27). This also means that the pattern labelled 5 in figure 35 is too small to be seen in the figure 36A and the spots of this pattern are positioned inside the pattern **j**. From these findings, the very faint label 4 (6.25Å±0.24) in figure 35A is assumed to be **f** and **j** (6.02Å and 5.97Å) and label 1 (4.05Å±0.22) is **h** and **d** (3.62Å and 3.65Å).

It is noted also that the patterns labelled **d** (blue triangles) and **h** (light blue spots) have the same sizes. The same observation is applicable to the patterns labelled **f** and **j** (dark and light purple triangles). The real space nearest neighbour distance of the

pattern **g** is half the one of pattern **j**. It probably corresponds to the continuation of the lattice as the energy beam increases.

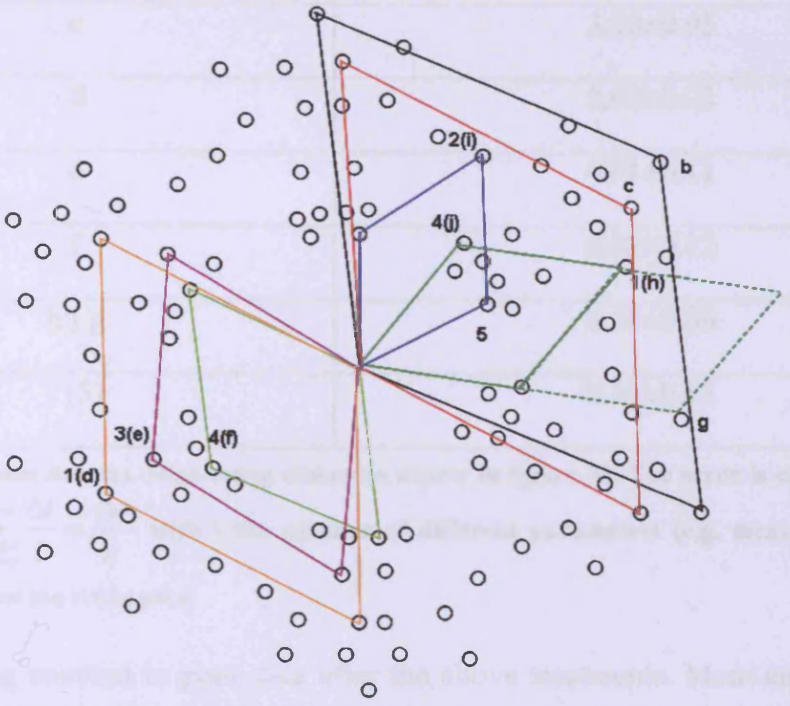

Figure 38: Schematic of the LEED pattern taken at 93eV same as figure 36B. The different unit cells present at the surface are drawn on the schematic. The numbers corresponds to the labels in table 2. The letter labels in table 3 are shown in bracket. The spots indicated as 5 are drawn to show the unit cell but are not present in the rest of the structure for clarity.

From the schematic on figure 38, various unit cells are present at the surface of the crystal. The know structures are the hexagonal Pd(111) (b shown in black) and the pinwheel (c shown in red) and their unit cell are indicated as in table 3. The other unit cells are either derived from the pinwheel structure with a ±3° rotation with respect to the Pd(111) unit cell (**d** shown in orange, **e** in purple and **f** in light green), either from the hexagonal structure with a ±15° rotation (**i/5** in blue) and ±15° rotation (**h/j/g** in dark green). Some unit cells have distances different from the real space nearest neighbour distance calculated in table 4. All the unit cell distances are shown in table 4. All those unit cells are bigger than the Pd(111) one. It is suggested that the surface is covered with large structures or superstructures.

Structure label (unit cell)	Unit cell (Å)
b (Pd(111))	2.75
c	3.20±0.05
d	3.62±0.03
e	4.91±0.11
f	6.02±0.12
h/j/g	6.36±0.09
i (5)	9.35±0.15

Table 4:Real space nearest neighbourg distances shown in figure 38. The error is calculated from the equation $\sum_{a\to i}\frac{\Delta i}{i}=\frac{\Delta c}{c}$ with i the number of different parameters (e.g. measured distance) used to determine the real-space

STM imaging resulted in poor data after the above treatments. More annealing was thus carried out in order to obtain a better ordered structure at the surface. Annealing at 1073K for 25minutes was completed. The LEED pattern is shown on figure 39(a) where most of the previous spots are not visible. The pattern consists of 4 sets of spots. The brightest set form a rectangular pattern, which originates from the clean (1×1)-TiO_2 (110) substrate. It is represented by the green circles on figure 39(b). The unit cell corresponds to the green rectangle. Between these spots, there is a set of weaker spots, which, relative to the (1×1)-TiO_2(110) substrate structure has a c(6×2) unit cell. This superstructure was previously observed by Zhang et *al.* [61] who found two possible unit cells on their LEED patterns. The two unit cell A and B were labelled $\begin{bmatrix}3 & 1\\ 3 & -1\end{bmatrix}$ and $\begin{bmatrix}6 & 0\\ 3 & 1\end{bmatrix}$ respectively and they are on the LEED figure 39. However, their STM images could not support an overlayer structure with a $\begin{bmatrix}3 & 1\\ 3 & -1\end{bmatrix}$

unit cell (or c(6×2)). Instead their images could be explained by using the $\begin{bmatrix} 6 & 0 \\ 3 & 1 \end{bmatrix}$ structure. However, according to Nörenberg, the unit cell corresponds to a c(6×2) on a reconstructed (3×1)TiO_2 where Ca substitute Ti every three atoms. The real distances of A and B unit cells on figure 35 are ~5.5Å×~5.5Å and ~6.5Å×~5.5Å respectively. The two other sets of spots have an hexagonal pattern. One corresponds to the Pd(111) structure (black spots) and the other to the pinwheel structure (red spots) which has a ±3° rotation from the Pd(111) substrate.

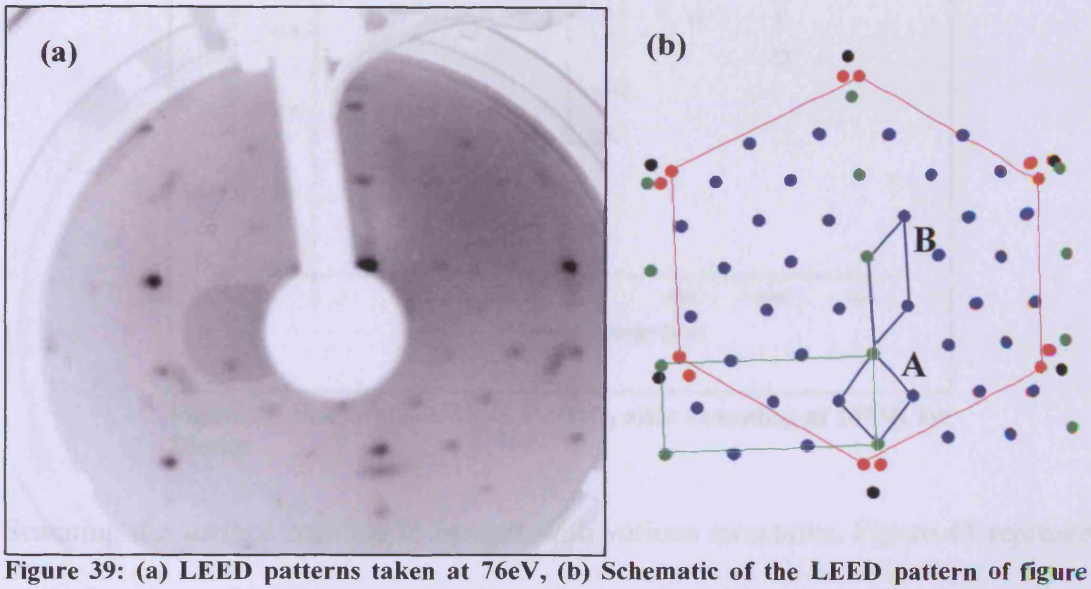

Figure 39: (a) LEED patterns taken at 76eV, (b) Schematic of the LEED pattern of figure 39(a). The black circles correspond to Pd(111); the red circles correspond to the pinwheel structure, the green circle to the (1×1)-TiO_2(110) substrate and the blue circle to the c(6×2) calcium structure. Blue circles are added on the schematic for clarity of the pattern.

The Auger spectrum on figure 40 shows a broad peak starting from 256eV to 306eV. The peak of palladium at 283eV is not sharp as in the previous Auger spectra. This broadness is coming from overlapping of peaks from different elements. Those elements are carbon and calcium which are detected at 295eV at 275eV respectively. A big change appears in the Pd/Ti ratio. The various sputtering and annealing treatment removed palladium from the surface. The concentration of Ti at the surface is 58% and 42% for palladium. The thickness of the film is 5.3Å. When compared with image 33 (where the concentrations of Ti/Pd were 35/65% and the thickness of

the film 9Å thick), the concentration of Ti has increased, Pd has decreased and thus the film thickness. Another change appears also on the Ti:O ratio. In the previous Auger spectra the ratio showed always more titanium than oxygen. In this case the ratio is 0.68:1. The interpretation of this observation can rely on the fact that $TiO_2(110)$ reconstructs upon annealing into a Ti_2O_3 configuration.

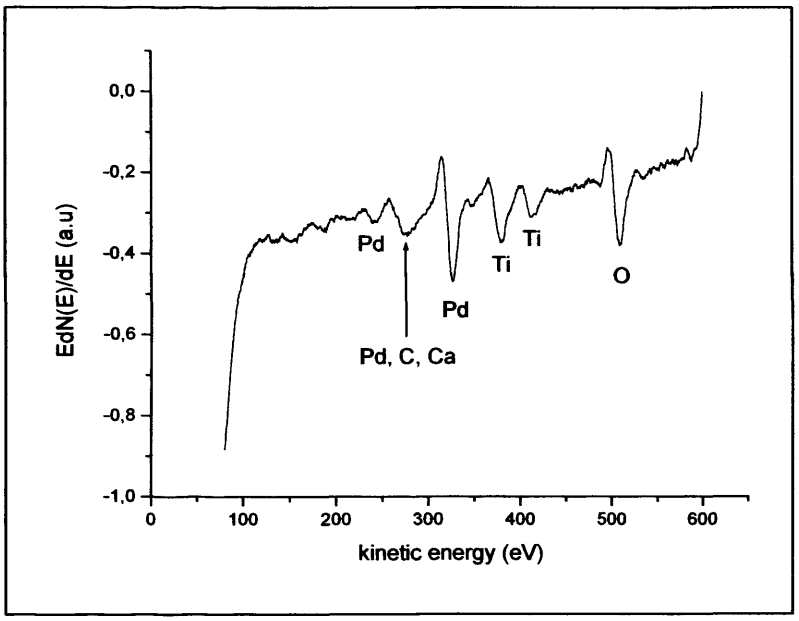

Figure 40: Auger spectrum of Pd/TiO_2 after annealing at 1073K for 25mins

Scanning the surface resulted in images with various structures. Figure 41 represents a large area image of the surface after the succession of sputtering and annealing treatments.

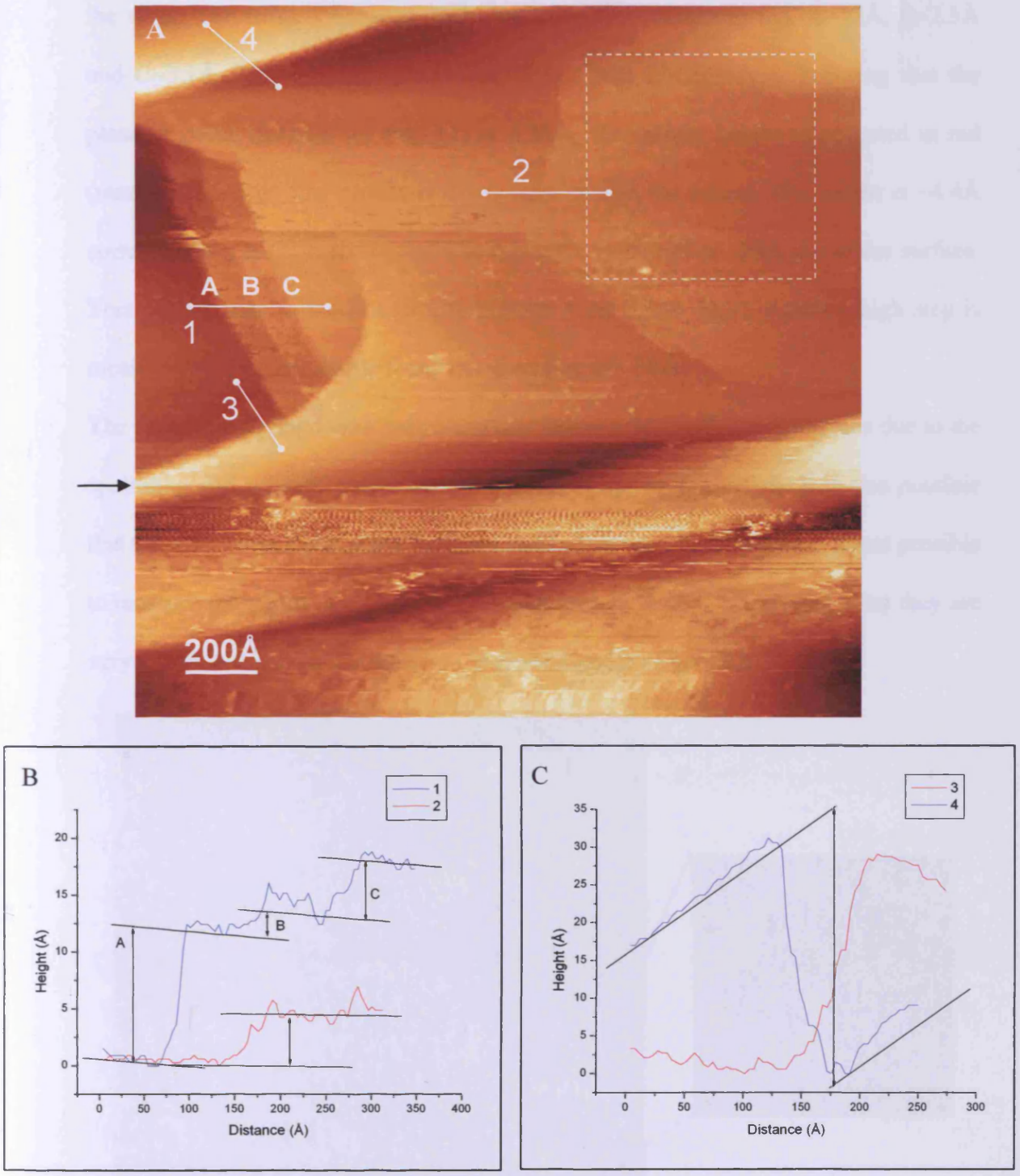

Figure 41: A) Low resolution STM image of Pd on TiO_2 (110). Parameters: 2000Å×2000Å, 1nA, 2V, RT. The lines across the image are line profiles of the images and are represented in figure 41B. The dashed square represents the surface shown on figure 42A. B) and C) Line profiles across the image 41A. The black arrow indicates changes induced by the tip.

A tip change is indicated by the black arrow. Below the arrow, the surface is blurry and noisy. Above it, it is possible to distinguish steps. Line profile 1 is taken across

the steps. The heights between each step are, from bottom to top, A~12Å, B~2.5Å and C~5.1Å. This consists of terraces of 5, 1 and 2 monolayers knowing that the plane to plane distance for Pd(111) is 2.26Å. The terrace height represented in red (number 2) on the line profile is much smaller than the others. The height is ~4.4Å corresponding to ~2 monolayers. The top left terrace sits at ~36Å above the surface. This corresponds to the line profile number 4 on figure 41(c). Another high step is measured by the line profile 3 and has the value of ~30Å.

The surface is covered with palladium that forms a film with many terraces due to the sputtering and annealing treatment that created gaps in the surface. It is also possible that the surface consists of big particles stacked on top of each other. It is not possible to measure the width of a particle. The scan area of 2000Å^2 proves only that they are very broad. A zoom of the image 41 is represented on figure 42.

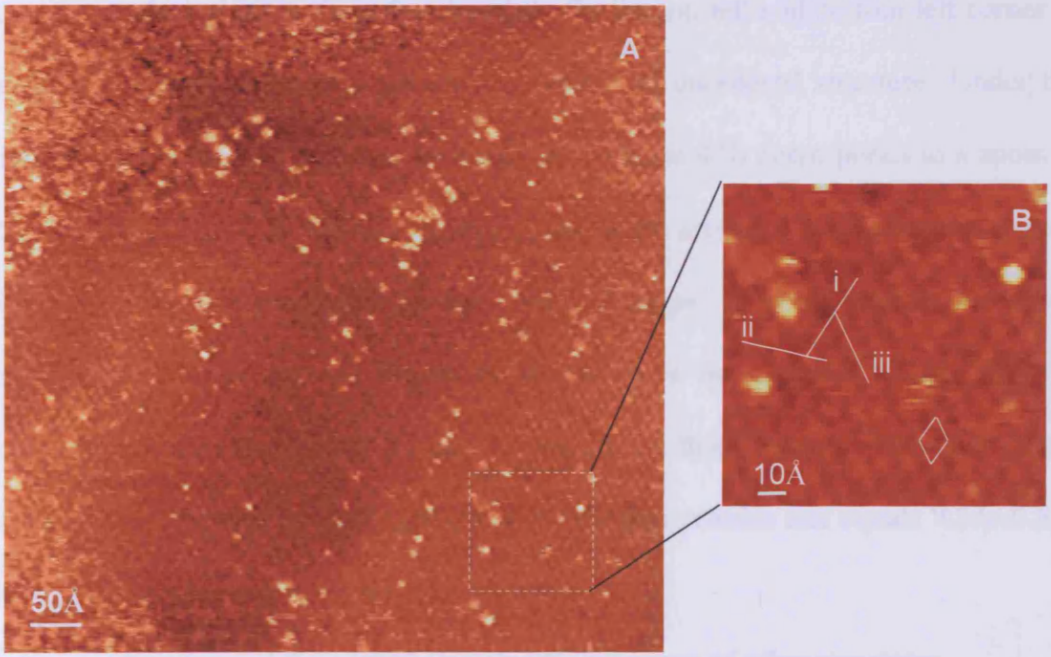

Figure 42: A) High resolution STM image represented by the black dashed square on figure 32. Parameters: 632Å×632Å, 1nA, 2V, RT. B) Zoom in figure 42A represented by the dashed square. Parameters: 115Å×115Å, 1nA, 2V, RT. The lines correspond to the line profile shown on figure 43. The diamond shape corresponds to the unit cell of the structure.

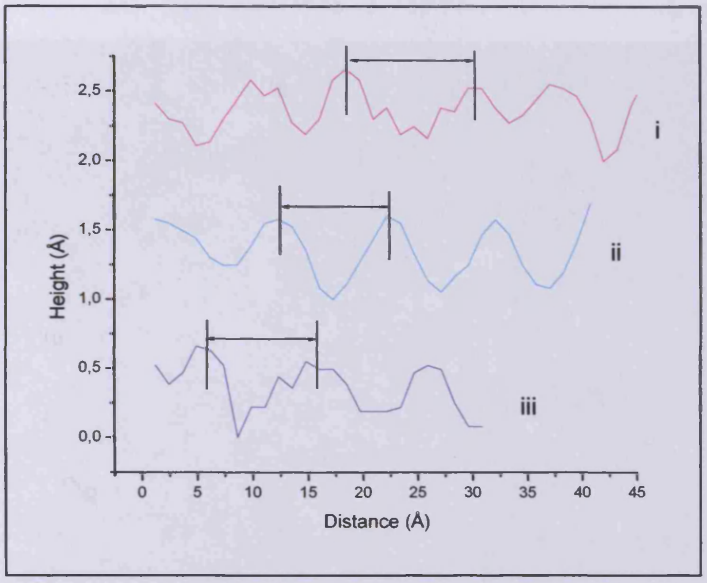

Figure 43: Line profile across image 42. The arrows represent the distance between each group of atoms.

Several features are distinguished on figure 42A. First, bright spots are visible which are randomly distributed on the surface. They may correspond to impurities such as oxygen or carbon coming from the chamber. On the top left and bottom left corner of the image, another feature is present consisting of unordered structure. Under the bright spots, the surface seems to be structured. Figure 42B corresponds to a zoom in 42A. On this image, it seems that groups of atoms are arranged in a hexagonal pattern with the unit cell represented by the diamond shape. It is not atomic resolution because the features are too big to be atoms. It is not possible at this stage to determine the amount of Pd, Ti and O present in those groups. The inter group distance is represented by the black arrow on the line profiles and equals 9.5Å±0.5Å. The size of the unit cell is 9.5Å×9.5Å.

Scanning other parts of the crystal revealed the presence of other structures.

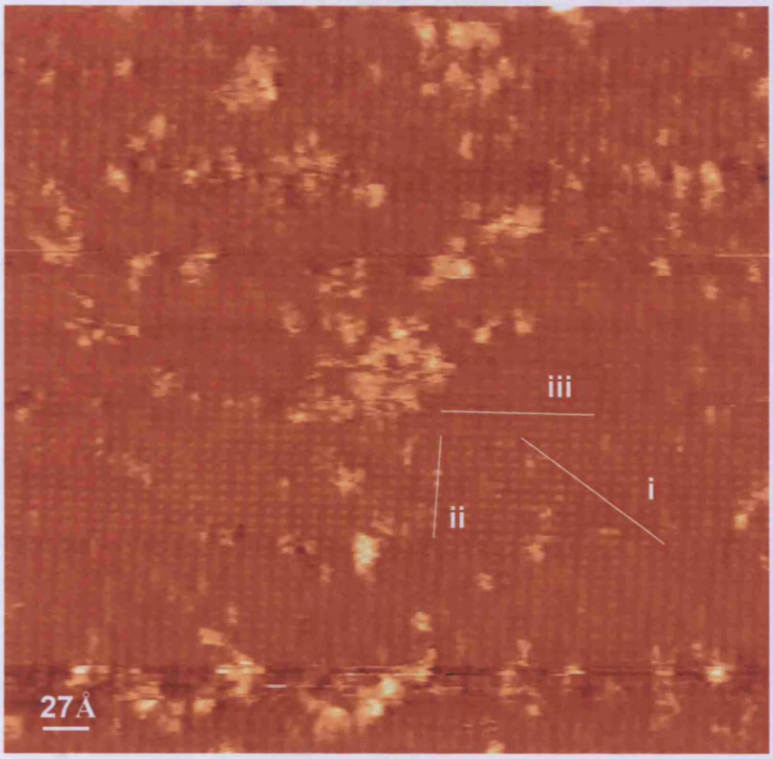

Figure 44: high resolution STM image at 298K. Parameters: 450Å×450Å, 1V, 1nA.

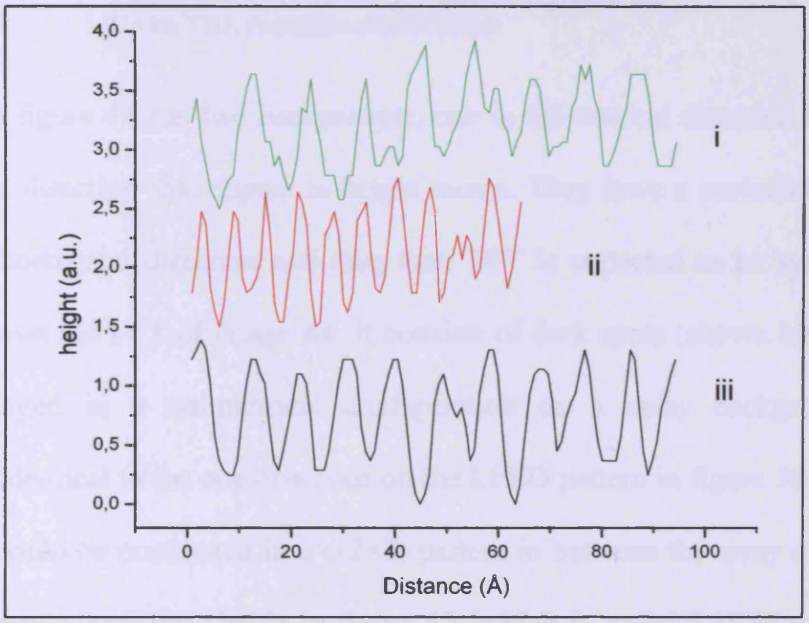

Figure 45: Line profile across image 44. The peak to peak widths are i- 10.67Å±0.06Å, ii- 6.26Å±0.04Å and iii- 9.09Å±0.06Å respectively.

The main feature visible on figure 44 is a well ordered surface showing a regular array of white spots of unit cell 6.26Å±0.04Å by 9.09Å±0.06Å. The distances were calculated from the line profiles on figure 45. The distance of 6.26Å is similar to the

distance, in the [110] direction, of the unit cell of the (1×1)-TiO_2(110). The distance of 9.09Å is three times the distance of the [001] direction. This suggests a (3×1) TiO_2 surface reconstruction as seen by Nörenberg et *al.*[62, 63]. This image on figure 44 implies that there are still areas of TiO_2 substrate not covered with palladium.

The Fast Fourier Transform (FFT) on this image is shown in figure 46.

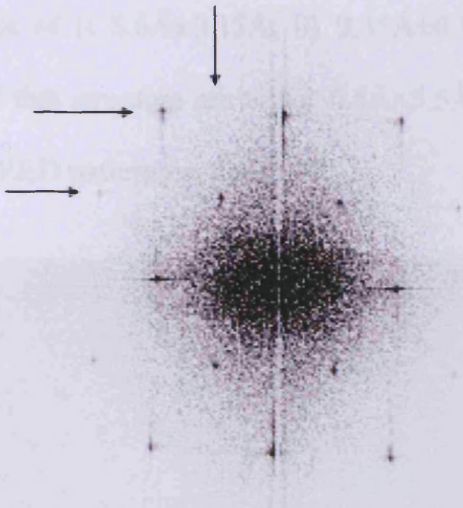

Figure 46: Fast Fourier Transform (FFT) of the Ca on TiO_2 reconstructed surface.

The image in figure 44 has two components, one in the vertical direction and one in the horizontal direction that appear as bright atoms. They have a periodicity in both vertical and horizontal direction and thus their FFT is expected to be symmetrical. Figure 46 shows the FFT of image 44. It consists of dark spots (shown by the black arrows) arranged in a symmetrical configuration on a noisy background. The symmetry is identical to the one observed on the LEED pattern in figure 39. From the FFT, spots should be positioned in a c(2×2) pattern in between the array of atoms in figure 44. Those atoms are visible in figure 47 (which is a zoom of image 44) and which is consistent with the FFT image.

The next figure is a zoom in figure 44. The top of the image is blurry due to noise. The changes in the image are due to tip changes. The lower part of the image shows a

poorly resolved structure. However it shows a feature not noticeable on a larger image. Extra spots have appeared in between the rectangular unit cell determined on figure 44. The unit cell is then changed and is drawn on figure 47. The unit cell can take two forms. Those two unit cells have the same shapes as the ones detected on the LEED pattern on figure 39. A line profile in each direction of the structure gives the peak to peak distances of i) 5.6Å±0.15Å, ii) 9.35Å±0.34Å and iii) 6.58Å±0.21Å. Thus, the unit cells of this structure are either 6.5Å×5.5Å or 5.5Å×5.5Å which is in accordance with the LEED pattern on figure 39.

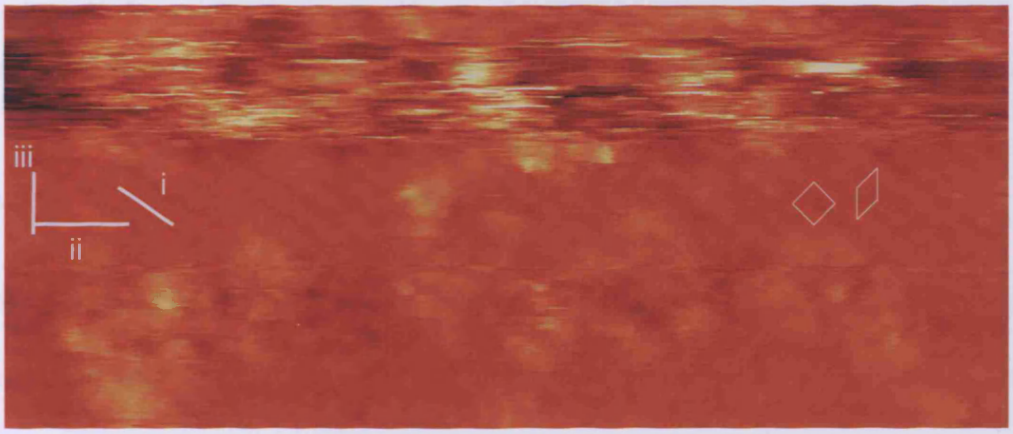

Figure 47: High resolution STM image. Parameters: 205Å×98.5Å, 1.2nA, 0.75V. The diamond and the parallelogram correspond to the possible unit cells. The white lines correspond to the line profiles shown on figure 47.

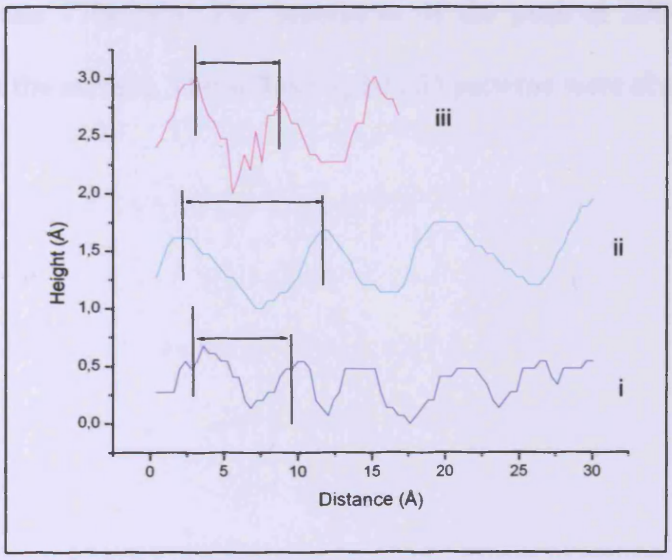

Figure 48: Line profile across the image on figure 47.

Zhang et *al.* proved, in a detailed experimental analysis, that Ca segregates to the $TiO_2(110)$ surface [61]. Based on their experimental results, they proposed a $CaTiO_3$-like $\begin{bmatrix} 6 & 0 \\ 3 & 1 \end{bmatrix}$ surface structure with the Ca sitting on top of the surface. This structure was questioned by Nörenberg et al who proposed that the reconstruction was due to c(6×2) Ca segregating at the surface of $(3\times1)TiO_2$. Looking at the deposition of Ca overlayer on $TiO_2(110)$, Thornton showed that bulk segregation and vapour deposited Ca formed a similar c(6×2) overlayer [64]. The LEED patterns from the various authors were similar to the LEED pattern presented here. Here, the STM images support both unit cell described earlier and therefore the $\begin{bmatrix} 6 & 0 \\ 3 & 1 \end{bmatrix}$ or c(6×2) $CaTiO_3$ and $\begin{bmatrix} 3 & 1 \\ 3 & -1 \end{bmatrix}$ structures can be considered as being present at the surface.

The main aim of this experiment was the observation of the SMSI effect between palladium and titania. In an attempt to remove some of the Ca without removing much of the palladium, more annealing was carried at 1073K for 15 minutes. The Auger spectrum showed a change in the Ti/Pd ratio. The film thickness was 3.2Å and the ratio Ti/Pd was 77%/23%. The broadness of the peak at 290eV indicated the presence of Ca at the surface. The following LEED patterns were observed.

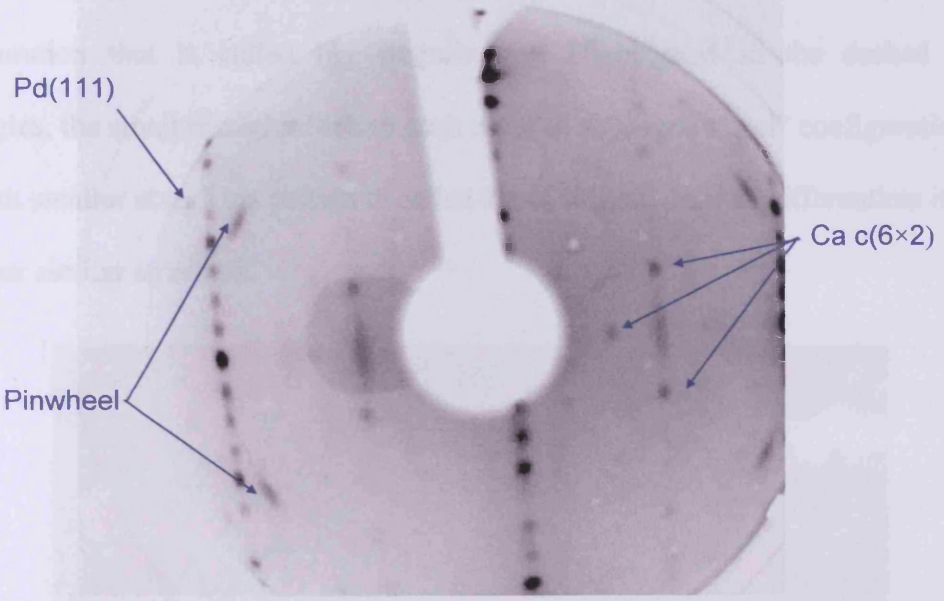

Figure 49: LEED pattern at 62eV.

The LEED pattern on figure 49 shows the presence of TiO_2. When compared with the pattern of a clean (1×1)-TiO_2(110) substrate, this new pattern has distances that correspond to a (1×4) reconstruction. This reconstruction had been observed by Nörenberg that appeared as a disordered reconstruction that followed the (3×1) reconstruction arising from Ca contamination [63]. Additional faint spots are present in between the (1×4) rows and form faint rows. Some spots are arising from the (6×2) Ca pattern. These observations from the LEED and Auger showed that the annealing treatment was not successful to remove the calcium. Moreover, on the LEED pattern, the pinwheel is present as a diffused elongated spot and the hexagonal pattern from the Pd(111) film is visible on the left hand side of the pattern only.

A high magnification image of the surface (290Å×290Å) is shown on figure 50. Two features, closely linked, are shown separately and in more detail in figure 51 and 53. One feature consists of bright spots forming small triangles which are dispersed all over the surface. The small triangles are shown in the white and the black dashed rectangles. The solid white rectangle surrounds the second feature that forms a

hexagonal structure with 6 triangles that interlock together in a "wagonwheel" configuration that is called big wagonwheel. Highlighted in the dashed black rectangles, the small triangles lock to each other in a "wagonwheel" configuration too but with smaller size. This pattern is called small wagonwheel to differentiate it from the other similar structure.

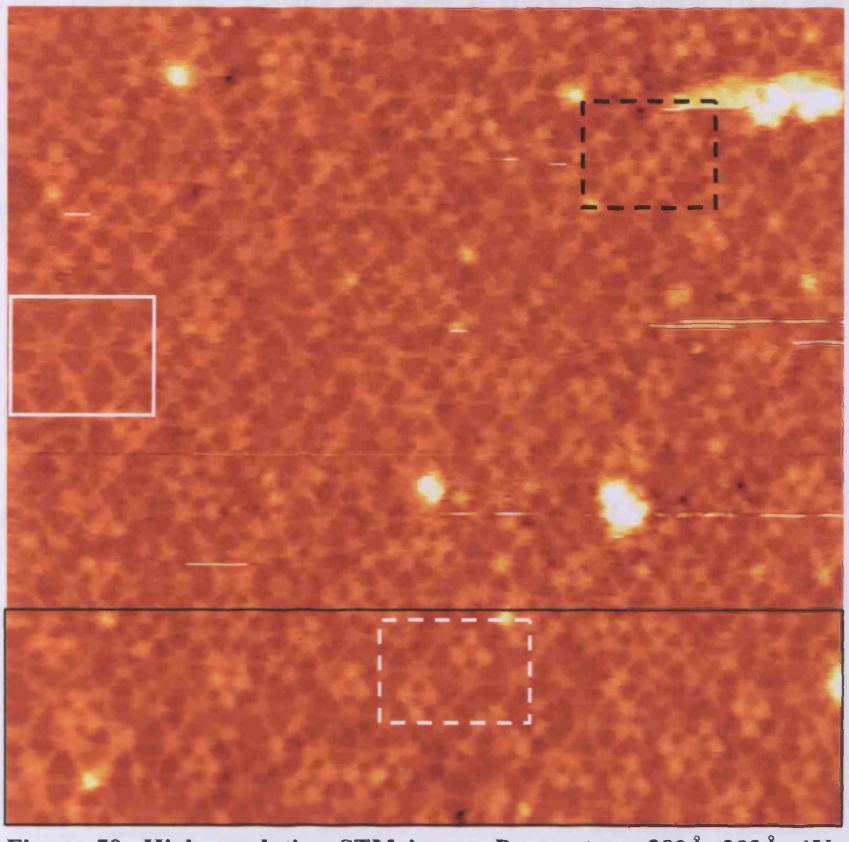

Figure 50: High resolution STM image. Parameters: 289Å×289Å, 1V, 1nA. The white rectangle corresponds to the image on figure 51, the white dashed one to figure 52 and the black dashed rectangle shows a part where the small triangle feature attach to each other to form an hexagonal array of spots.

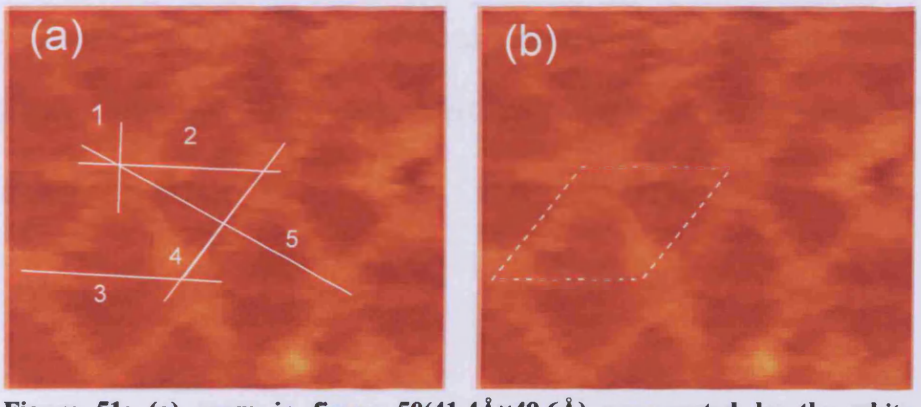

Figure 51: (a) zoom in figure 50(41.4Å×49.6Å) represented by the white rectangle. (b) Same image as (a). The dashed black shape corresponds to the unit cell.

Looking at the big wagonwheel structure on figure 51a, the line profile across the bright centre of the structure gives a distance of (1) 10.3Å. The measurement of the centre was repeated on various part of the surface. The same measures were found at ±1.0Å. An interesting point is that the centre is hollow as it can be seen on line profile 1 figure 52. The maximum peak to peak height of the clusters of atoms is 0.61Å±0.07Å. The unit cell of this structure is shown in figure 51(b) and measures 18Å×18Å (±0.5Å). The distance across the long axis of the unit cell is represented by the line 5 on figure 52 and equals 28.43Å±0.50Å. The axis angles of the unit cell are 60° and 120°.

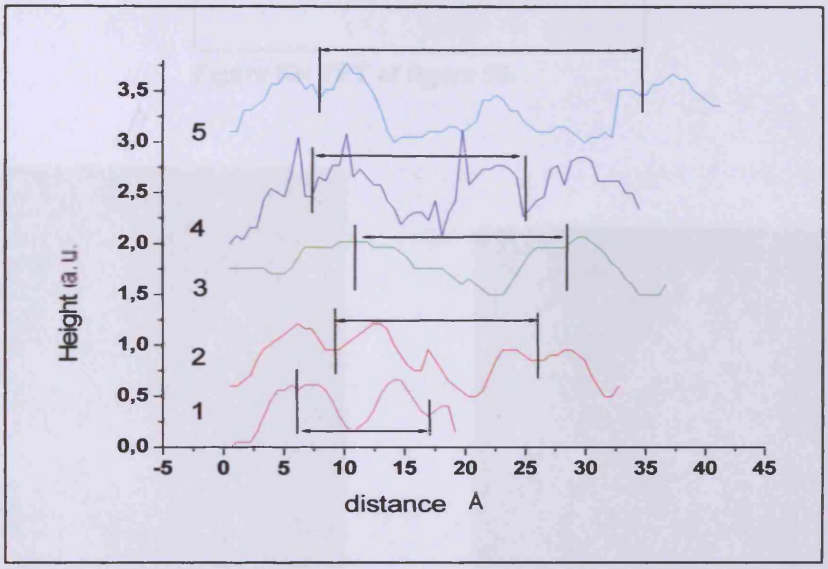

Figure 52: Line profiles along the lines marked on figure 51(a). The black arrow show the distances centre to centre of the hexagons.

The Auger spectrum showed the presence of Pd, Ti, O, C and Ca. It was seen in figure 44 that Ca reconstruct into a c(6×2) structure. Carbon appears at the surface as disordered agglomerates. Thus it is expected that the structure above consist of Pd, Ti and oxygen only.

The FFT of figure 50 is shown in figure 53. It shows a weak hexagonal pattern slightly distorted because of the poor resolution and the structure distortion in the STM image.

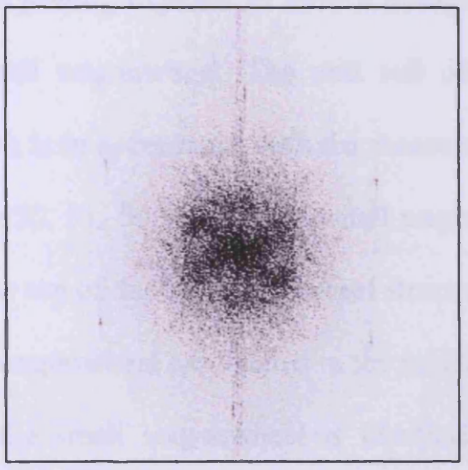

Figure 53: FFT of figure 50.

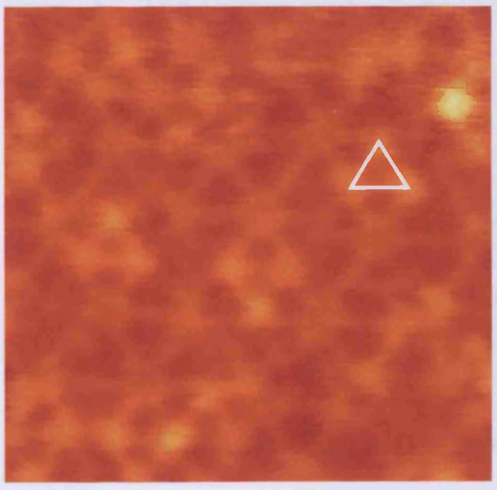

Figure 54: Zoom in figure 50 (76.5Å×76.5Å) represented by the dashed white rectangle

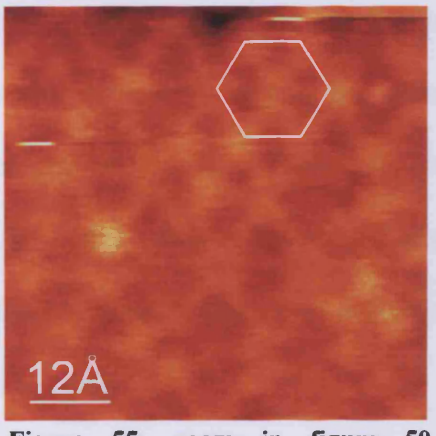

Figure 55: zoom in figure 50 (64.6Å×64.6Å). The hexagon shows the joined small triangle to form a small wagonwheel

Looking at the small wagonwheel on figure 54 and 55, two features are observed. The first one consists of 3 bright spots arranged in a triangular manner. The distance between 2 apices of the triangle is 9.5Å±0.2Å. This triangular feature is brighter than the big wagonwheel one and has a peak to peak height of 1.4Å±0.2Å which is much

bigger than the height of the centre in figure 51a. It sits in the middle of the arms of the big wagonwheel structure.

The second feature, present on another area of the image 50 (black dashed rectangle), shows the small triangles joining together to form a hexagonal structure (figure 55, white pattern) called small wagonwheel. The unit cell of this structure measures 9.5Å×9.5Å (±0.2Å) which is in accordance with the measures of figure 54. From the analysis of images figure 50, 51, 54 and 55, the small wagon wheel structure of unit cell 9.5Å×9.5Å sits on the top of the big wagonwheel structure of unit cell 17Å×17Å. The centres of the small wagonwheel are located in the middle of the big wagonwheel arms. The unit cell of the small wagonwheel is identical to the unit cell of the structure in figure 38. Figure 56 corresponds to a zoom of the black rectangle on image 50. The colours were changed for clarity using Paintshop Pro software. Atomic resolution was obtained on this image. Looking at the big wagonwheel structure (highlighted by the white square), it seems that the arms of the structure consist of 5 atoms and that the cluster centres form a hexagon of 6 atoms. The small clusters sitting at the top and forming small triangles are not atomically resolved. However, by comparing them with the centre clusters of the big wagonwheel, they seem to have the same size and therefore may as well consist of 6 atoms.

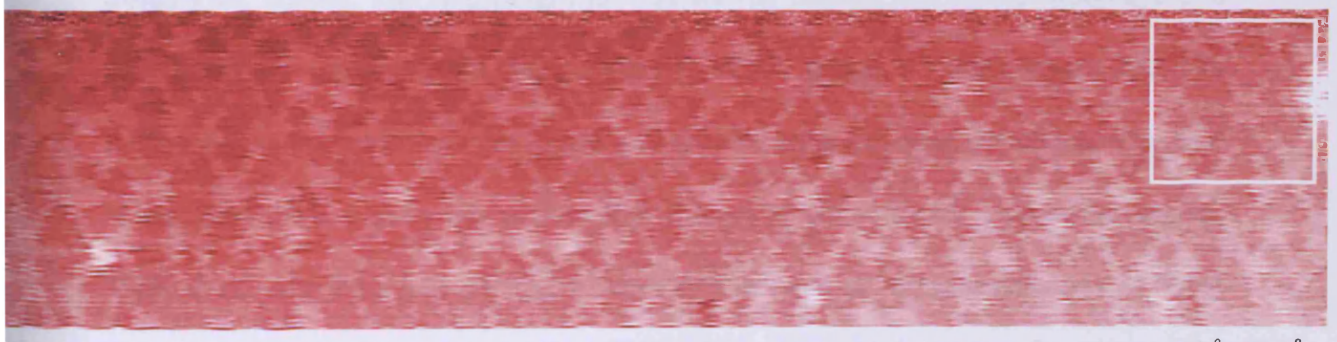

Figure 56: Zoom in figure 50 showing near atomic resolution of the wagonwheel structure. Parameter: 289Å×67.4Å

The sample was then heated up in the STM head to 573K overnight and the crystal was scanned at this temperature. A large number of different features are present at the surface at 573K as seen in figure 57. The colours in figure 57 have been equalised with Paint shop Pro software to obtain a better contrast.

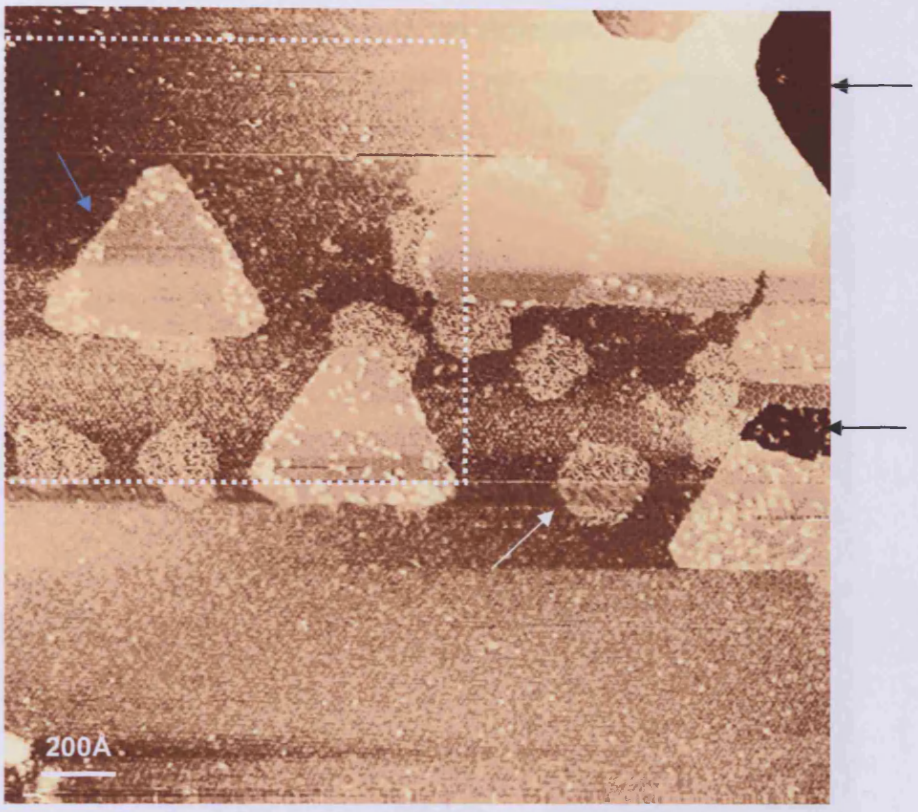

Figure 57: Low resolution STM image at 573K. Parameters: 2427Å×2427Å, 1nA, 1.5V. The white rectangle corresponds to the area shown on figure 56. The arrows indicate the different features.

A contrast is present on the right side of the image as shown by the arrows. Two troughs are visible. The step height is ~4Å for the bottom one thus 2 monolayers of palladium. The top one has a step height of ~11.5Å which is 5 monolayers. Particles are located in the middle of the image and they possess different structures. One type of particles (blue arrow) has a truncated triangular shape and is pseudo-hexagonal. Their sizes vary from one particle to another but have an approximate size of 530Å (length of side). The other type of particles, indicated by the white arrow, has a more or less rounded shape of ~200Å in diameter. They are located on the surface but also

on the edge of the pseudo-hexagonal particles. A zoom in figure 57 is shown on figure 58 where the different structures are clearer. The truncated triangular particles seem to have an ordered structure at their surfaces. Another ordered structure, indicated by the white rectangle is present on the surface. The last feature shown by the black rectangle seems to be a semi-ordered structure.

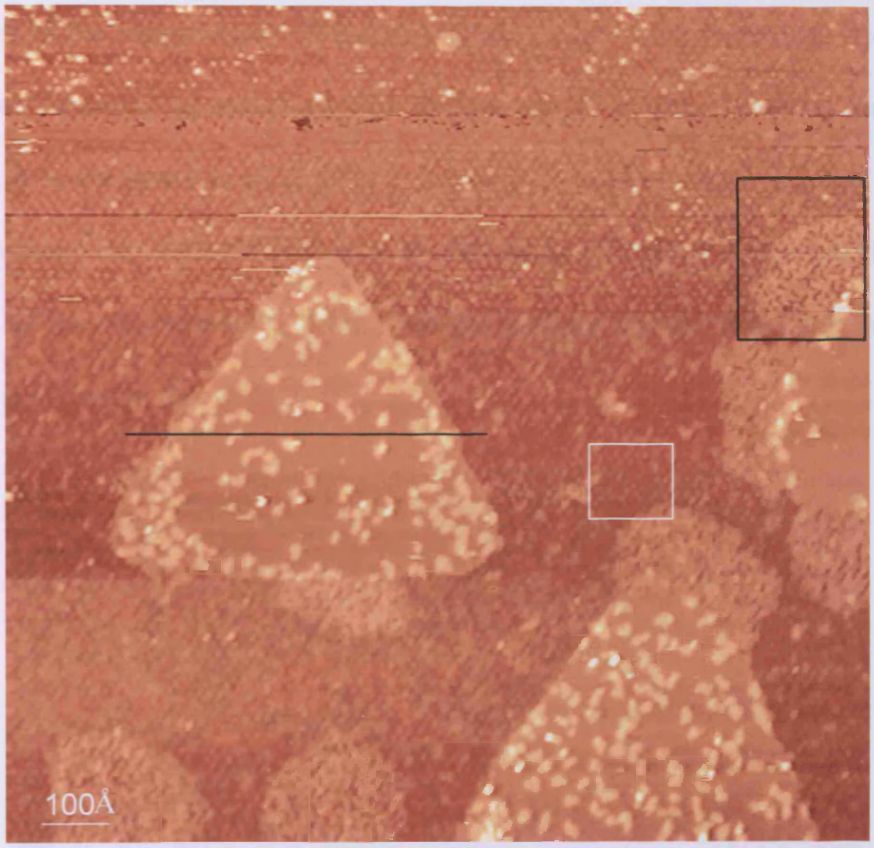

Figure 58: Low resolution STM image at 573K. Parameters: 1299Å×1299Å, 1.5V, 1nA. The black line across the particle corresponds to the line profile on figure 59, the black rectangle highlight the semi ordered structure and the white one another kind of structure.

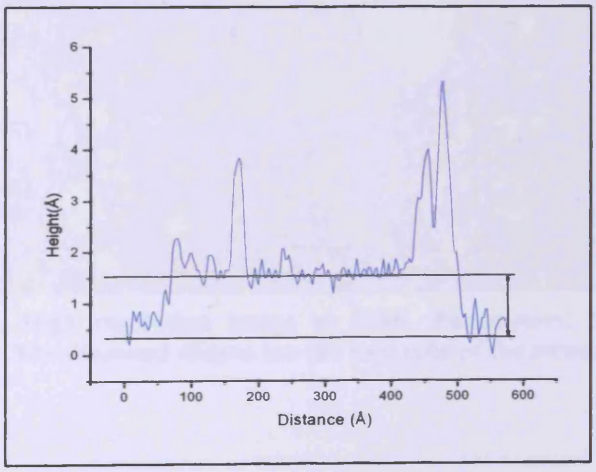

Figure 59: Line profile across image 58

The truncated triangular particle is not in the plane of the surface as shown by the line profile on figure 59. The step height is ~1.2Å. Clusters of atoms are present on the top of the particle. They correspond to the spike on the line profile and have a height of ~2.35Å and ~3.84Å for the highest one. They appear as the bright features on figure 58. The semi ordered feature, located at the edge of the particles and on the bottom left of the image figure 58 is highlighted by the black rectangle. There seems to be a semi ordered structure on this feature which sits at ~1Å from the surface. However, it is not possible to identify a unit cell. A zoom of the truncated triangular particle in figure 58 is shown in figure 60. The diamond shapes correspond to the two unit cells of the two structures present on the particle and the substrate. A zoom of figure 60 is shown in figure 61.

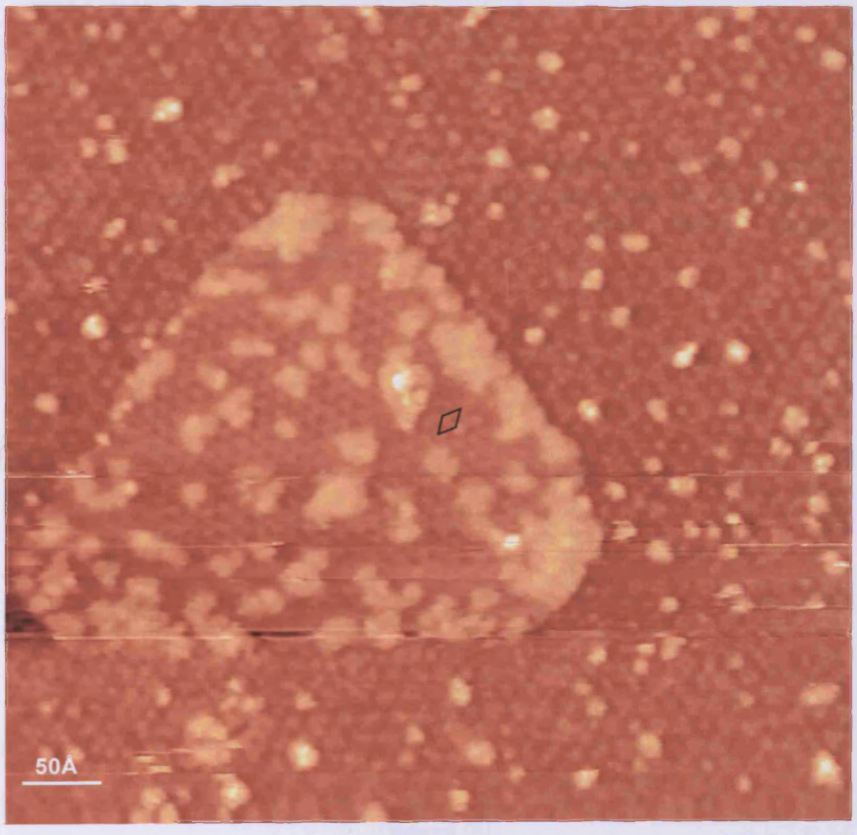

Figure 60: High resolution image at 573K. Parameters: 534Å×534Å, 1.5V, 1nA. The diamond shapes are the unit cells of the structures.

The structure at the top of the particle is hexagonal. A zoom on this structure is shown on figure 61B. The unit cell, calculated from the line profile 1, is represented in black and measures 10.3Å×10.3Å (±0.5). The height of the atoms on the particles varies from 0.6Å to 1.2Å as seen on the line profile figure 62. The distance across the unit cell measure 17.8Å (±0.5Å). The unit cell distance is similar to the small wagonwheel unit cell.

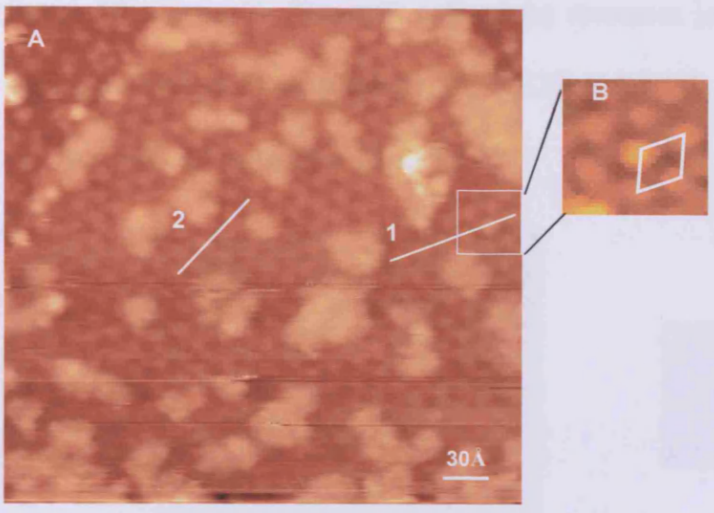

Figure 61: A) Zoom of figure 60 of the structure on the pseudo hexagonal particle (250Å×250Å). B) Image showing the hexagonal pattern formed by the structure. The white dashed shape corresponds to the unit cell.

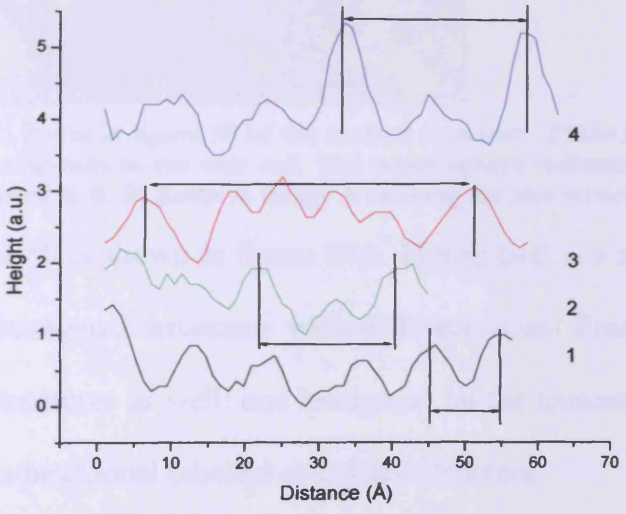

Figure 62: Line profile across both structures. The numbers are shown on figure 61 and 63. The arrow on line profile 1 and 4 correspond to the inter group distance. The arrow on line profile 2 is the distance across the long axis of the unit cell of the hexagonal structure and on the line profile 3 is the distance between two centre of the star shape in diagonal.

The surface around the particle shows another kind of much larger structure and is named, to differentiate it from the hexagonal and wagonwheel, "star shape". The structure consists of 6 groups of 3 clusters around a central larger cluster of 11.7Å±2.0Å in size (highlighted in figure 61B).The centre of the star can be in the same plane as the rest of the structure but also can have an atom at its top as seen on line profile 4 in figure 60. The peak to peak height distances vary from ~0.7Å, ~1.2Å to ~1.75Å (figure 60: curve 5). The unit cell of the structure is represented by the white shape on figure 60A and measures 25.3Å×25.3Å (±0.60Å). The distance across the long axis of the unit cell measures 43Å±0.5Å.

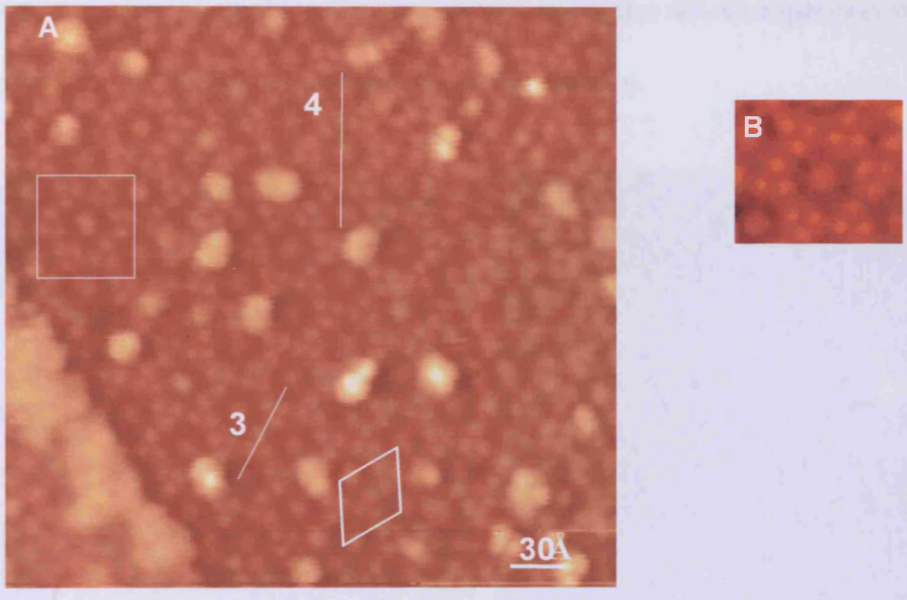

Figure 63: A) Zoom in figure 58 of the surface structure (250Å×250Å). The white diamond corresponds to the unit cell. The white square indicated the location of the zoom showed in B. B) Zoom in image A showing the star structure.

The FFT of image 60 is shown in figure 64A. Figure 64B is a schematic of the FFT that shows two hexagonal structures with different sizes. From the image 60, the surface has two structures as well: one hexagonal on the truncated triangular particle and another bigger hexagonal labelled star shape structure.

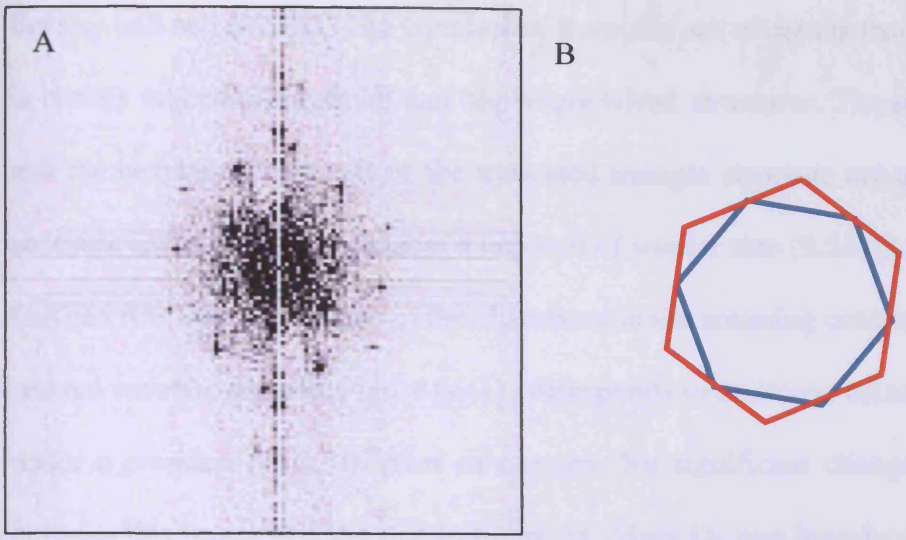

Figure 64: A) FFT of figure 60. Two hexagonal patterns are clearly visible. B) Schematic representation of the two hexagons.

This superstructure resembles the one shown on figure 49. Comparison was done in attempt to identify the structures present at the surface.

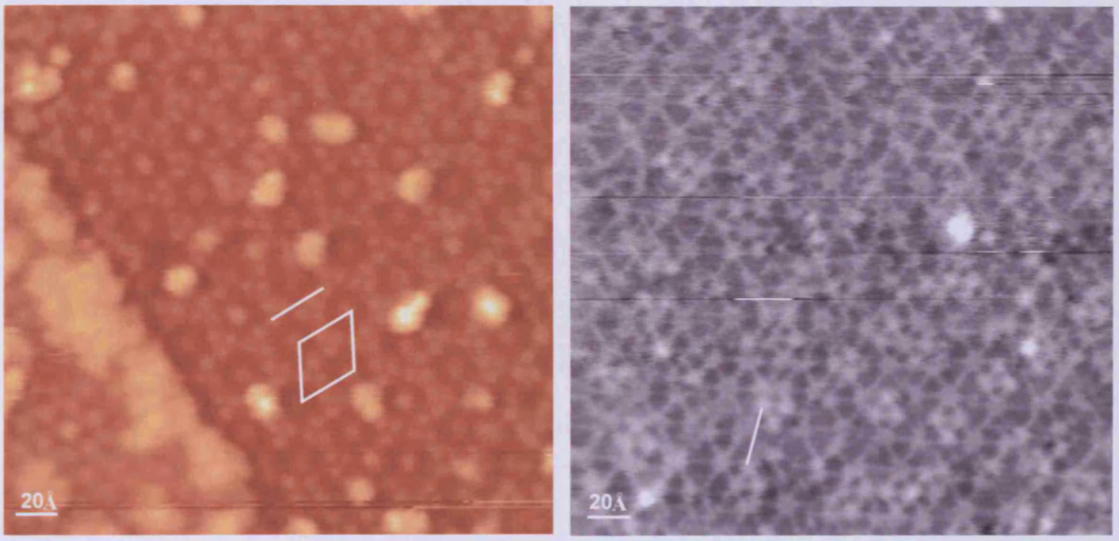

Figure 65: A) Zoom in figure 58. Parameters: 252Å×252Å. B) Same image as figure 50. Parameters: 252Å×252Å. The white line between two apices of the star in A has the same distance as the line from one apex of the small triangle to another one on another triangle on B. The unit cell in A fits two cluster centres of the big wagonwheel in B (top ones) but the below apices do not sits on any clusters. It is difficult to see since the image B shows a distorted structure.

The distance represented by the white line on figure 65A, measures ~28±0.5Å. On figure 65B the same line corresponds to the distance between two central groups of the clusters forming small triangles. This distance is a bit larger than the distance of

the star unit cell (~25Å). The conclusion from this set of data is that the star structure is closely related to the small and big wagonwheel structures. The small wagonwheel and the hexagonal unit cell of the truncated triangle structure are also related to the structure in figure 42 that possess a unit cell of similar size (9.5Å×9.5Å).

Oxygen was then introduced in the chamber and the scanning continued while oxygen reacted with the surface. Figure 66(1) corresponds to an image taken after 60 minutes under a pressure of 1×10^{-8}mbar of oxygen. No significant changes were observed between this image and the one in figure 58. More O_2 was introduced in the chamber at a pressure of 5×10^{-8}mbar. The truncated hexagonal particle got covered a little as seen on figure 66 (2 and 3). A sudden change occurred between image 3 and 4 where the particle got covered in 2 minutes time.

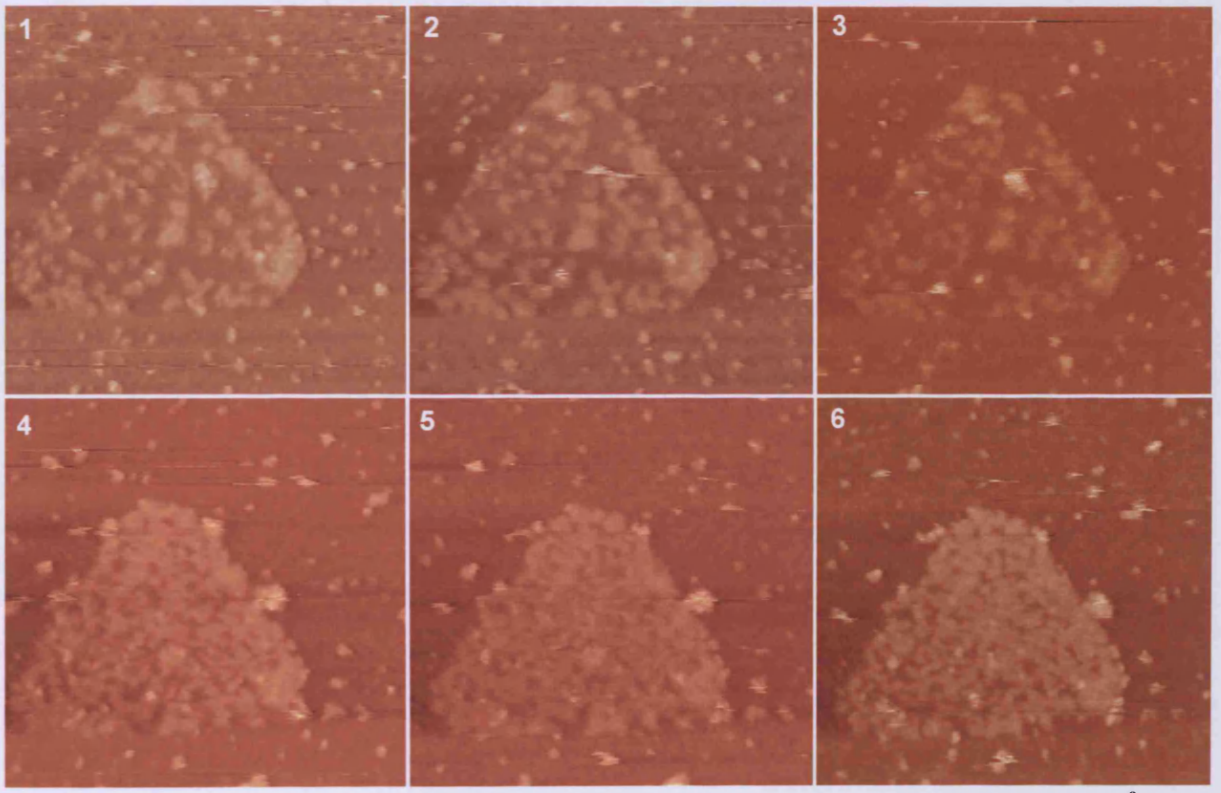

Figure 66: High resolution STM images. Parameters: 534Å, 1V, 1nA. 1) After 60mins at 1×10^{-8}mbar O_2. From 2) to 6) 5×10^{-8}mbar O_2 with images taken every 2 minutes. Data acquired in collaboration with Federico Grillo.

As the pressure increases, the impingement rate of oxygen molecules increases allowing a faster coverage at the surface. At 1×10^{-8}mbar of oxygen, the surface would have probably been covered too but on a much longer time scale. From image 4 to 6, oxygen was still introduced in the chamber and the particle got slightly more covered. The surface was scanned for a further 18 minutes. An interesting feature of this experiment is the location of the deposited oxygen. It only deposited on particles showing a truncated triangular shape.

The tip was moved to other areas on the surface. The scanning resulted in images showing that oxygen has completely covered other particles. In figure 67, large and bright particles are present. Their peak to peak height distances vary from ~5Å to ~8Å and their widths from ~35Å to ~90Å. A terrace is present on the right side of the image. It sits at 4.9Å±0.1Å from the underlayer surface. Looking at the line profile in figure 65 and the image, groups of atoms are present along the edge of the terrace. Their height is indicated by the green line on the line profile figure 65. They are not in the same plane of the terrace, nor of the surface. They are located at 2.1Å and 3.6Å (±0.1Å) above the surface.

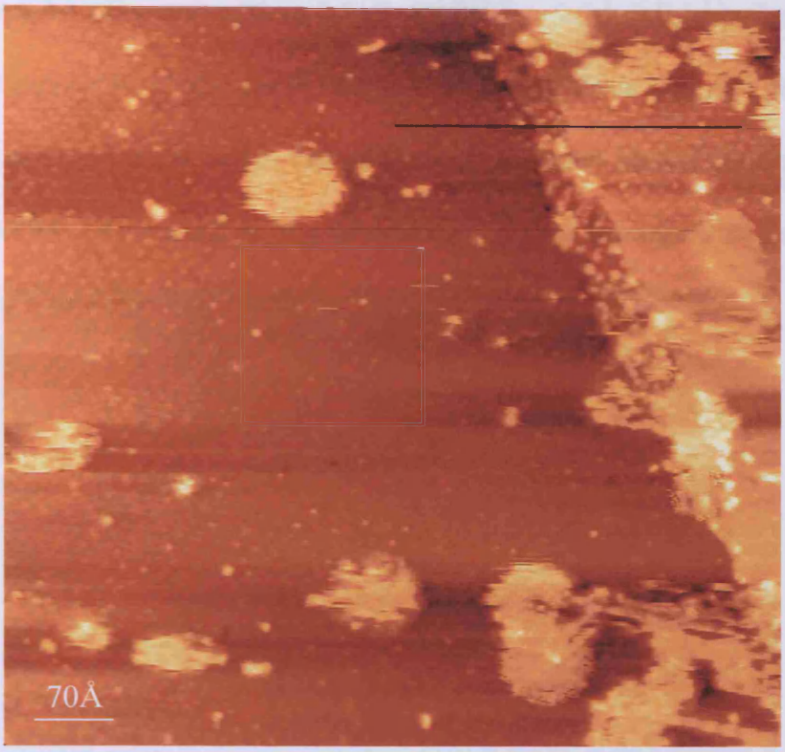

Figure 67: Low resolution STM image after oxygen deposition. Parameters: 702Å×702Å, 1nA, 1V, RT. The white square corresponds to the location of the image in figure 69.

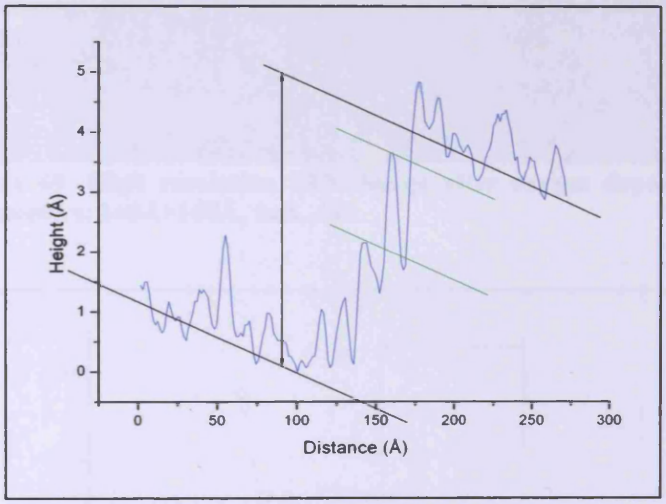

Figure 68: Line profile across the surface represented by the black line across figure 67.

The image in figure 69 is a zoom of figure 67. This is a higher resolution image that shows an ordered structure. The unit cell is represented in white on the image. The peak to peak width distances of i) is 9.6Å±0.1Å, ii) is 9.3Å±0.1Å and iii) is 14.8Å±0.5Å (line profile figure 70, black arrow). The peak to peak height for the

spots is 0.7Å±0.3Å. The unit cell size is thus ~9.5Å×~9.5Å (±0.1Å). Once again, the unit cell is comparable to the small wagonwheel one. From the line profile iii, the distance across 3 centres is ~28Å that is close to distance across the unit cell of the star shape structure. It seems that this structure is derived from the star shape one.

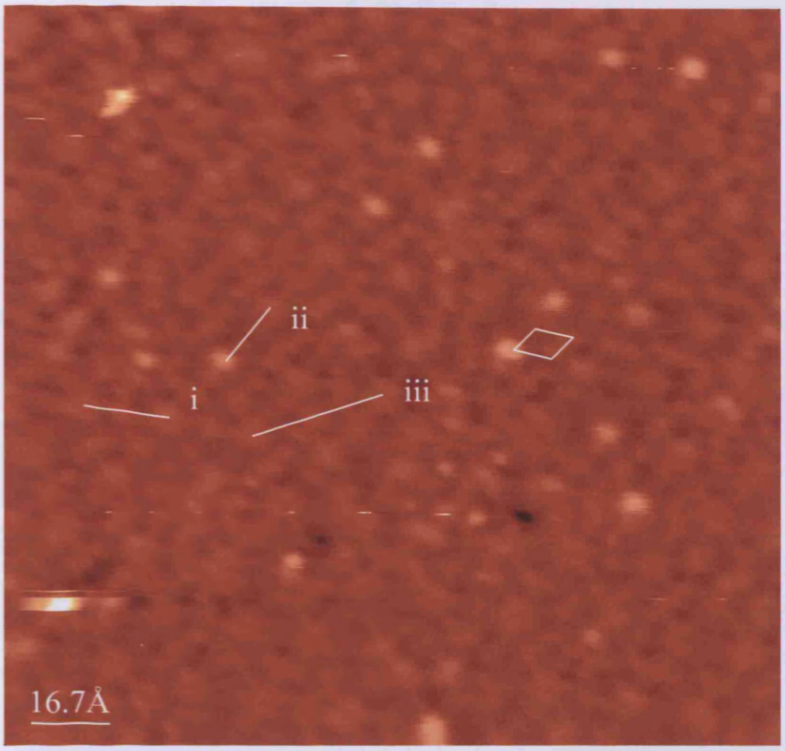

Figure 69: High resolution STM image after oxygen deposition. Parameters: 168Å×168Å, 1nA, 1V.

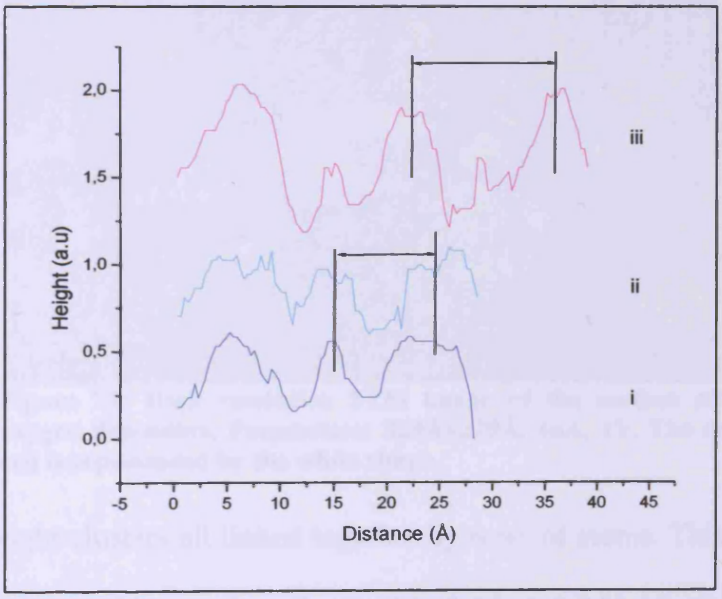

Figure 70: Line profiles along the lines marked on figure 69. Profiles are taken from a processed image for clarity and thus height information is not maintained. The black arrows correspond to the peak to peak distance.

Figure 71 shows the FFT of image 69. A hexagonal pattern is visible despite the noisy background structure that is visible on the image 69.

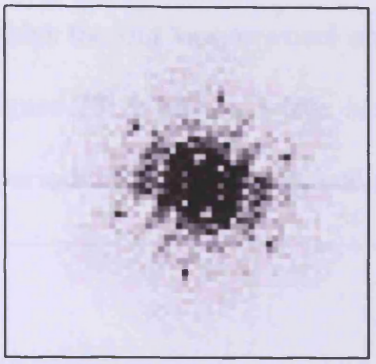

Figure 71: FFT of image 69.

Figure 72 shows a surface with various structures. First, very bright islands indicated by the white arrows are present at the surface. Under this bright layer of disordered structure, an ordered structure is clearly visible.

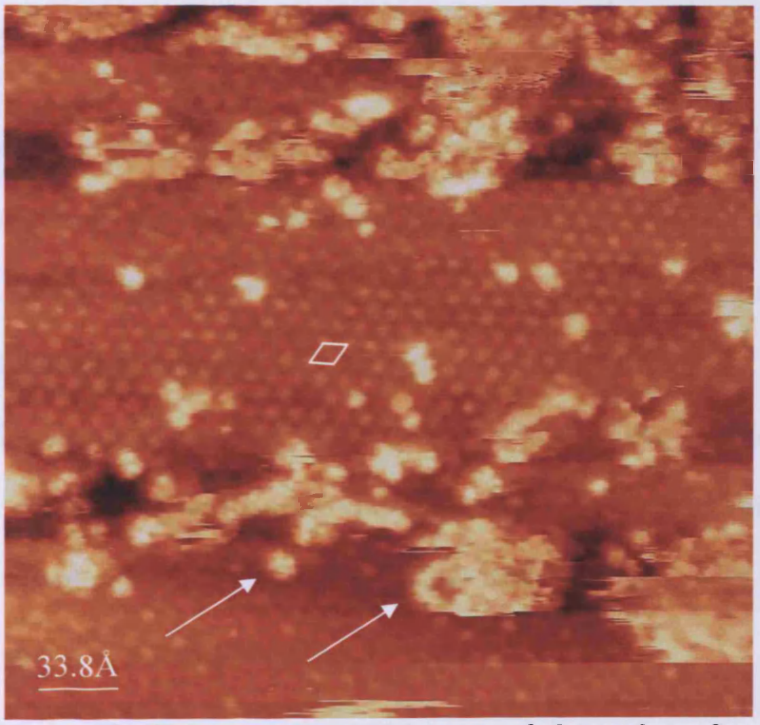

Figure 72: High resolution STM image of the surface after oxygen deposition. Parameters: 329Å×329Å, 1nA, 1V. The unit cell is represented by the white shape.

It consists of bright clusters all linked together by rows of atoms. This structure forms a hexagonal pattern with a unit cell of ~9.5×9.5Å (±0.2Å) identical to the small

wagonwheel one that was obtained before oxygen deposition. The peak to peak height showed a height of ~1.5Å and ~0.71Å. The top and bottom of the image shows ordered structure that resembles the big wagonwheel observed in figure 50.The FFT of the image is shown in figure 73. It shows a true hexagonal structure on a noisy background confirming the periodicity of the hexagonal structure.

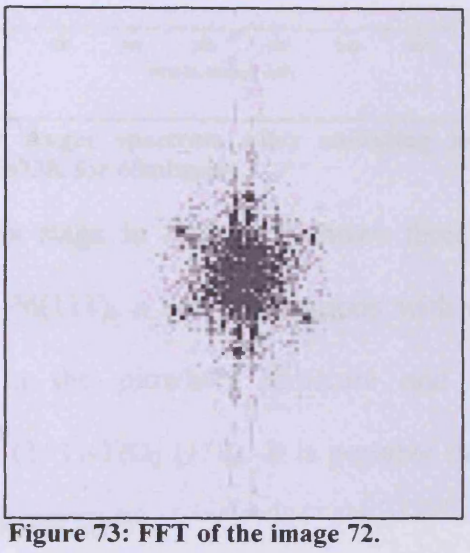

Figure 73: FFT of the image 72.

The crystal was then annealed again to 1073K in an attempt to remove the oxygen from the surface. From the Auger spectrum in figure 74 a large amount of Pd is still present at the surface. The Ti:Pd ratio is 0.5:0.5. The peak of the Pd appears much bigger than the titanium one and we would expect more Pd than Ti. However the sensitivity of the elements is 3.2842 for Pd and 1.2155 for Ti so the peak of Pd will appears bigger despite its lower concentration because it is more sensitive than Ti to detection. The broad peak at 280eV indicates that still some calcium is present at the surface and presumably some carbon too.

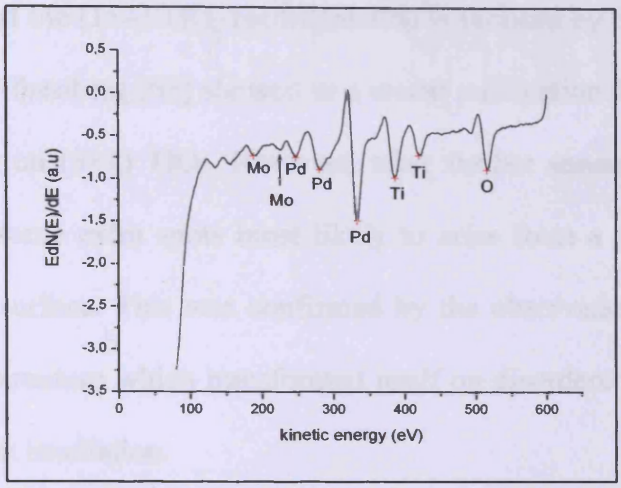

Figure 74: Auger spectrum after annealing the crystal at 1073K for 45minutes.

The LEED pattern at this stage in figure 75 shows three patterns: an hexagonal pattern arising from the Pd(111), a set of hexagons with a ±3° rotation from the Pd(111) corresponding to the pinwheel structure and a (1×4) reconstruction presumably related to the (1×1)-TiO_2 (110). It is possible that a layer of (1×4) TiO_2 has reconstructed under the Pd layer.

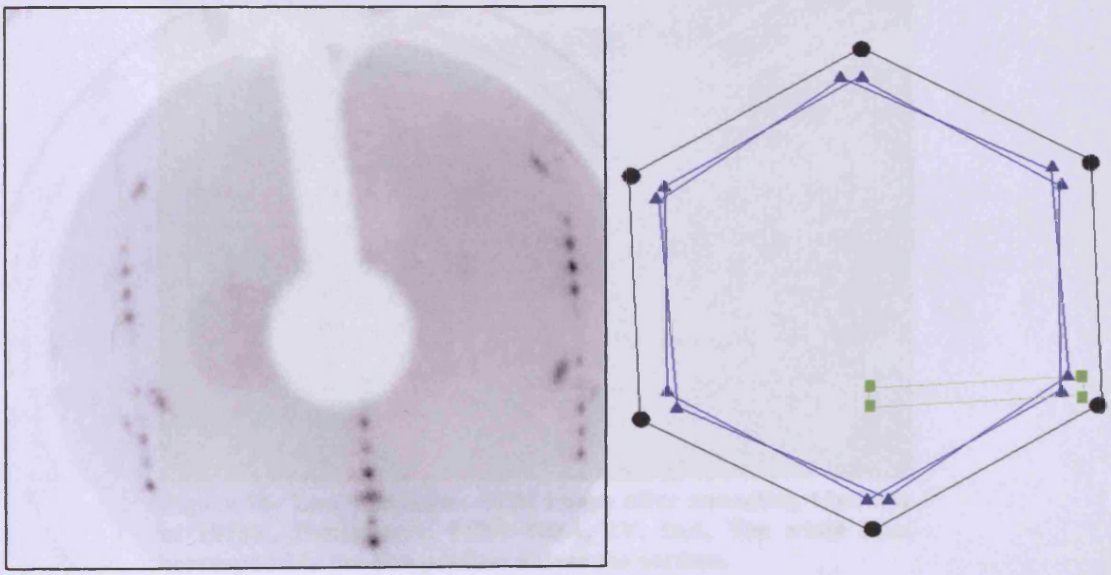

Figure 75: LEED pattern at 93eV. On the right hand side, the schematic of the LEED is drawn.

It is possible that the (1×4) TiO_2 reconstruction is induced by the presence of calcium at the surface. Nörenberg [63] showed in a recent publication that Ca reconstructed in a (6×2) pattern on (3×1) TiO_2. However, after further annealing, he noticed in his LEED pattern some extra spots most likely to arise from a (1×4) structure patches present on the surface. This was confirmed by the observation of STM images that showed (3×1) structure which transformed itself on disordered (1×4) upon annealing or electron beam irradiation.

STM images were obtained after this annealing session and shown in figure 76, 78 and 80.

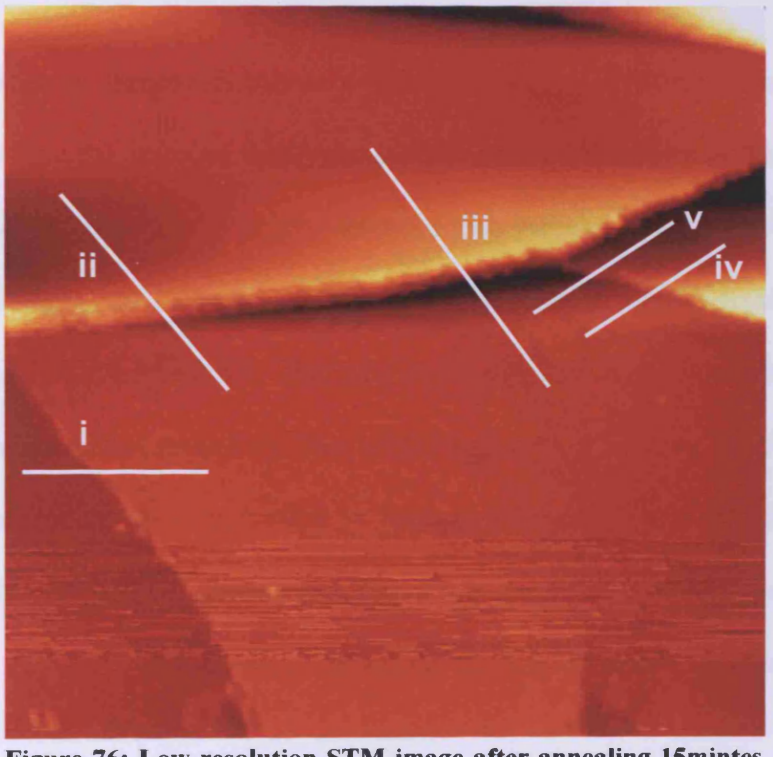

Figure 76: Low resolution STM image after annealing 15mintes at 1073K. Parameters: 968Å×968Å, 2V, 1nA. The white lines correspond to the line profiles across the surface.

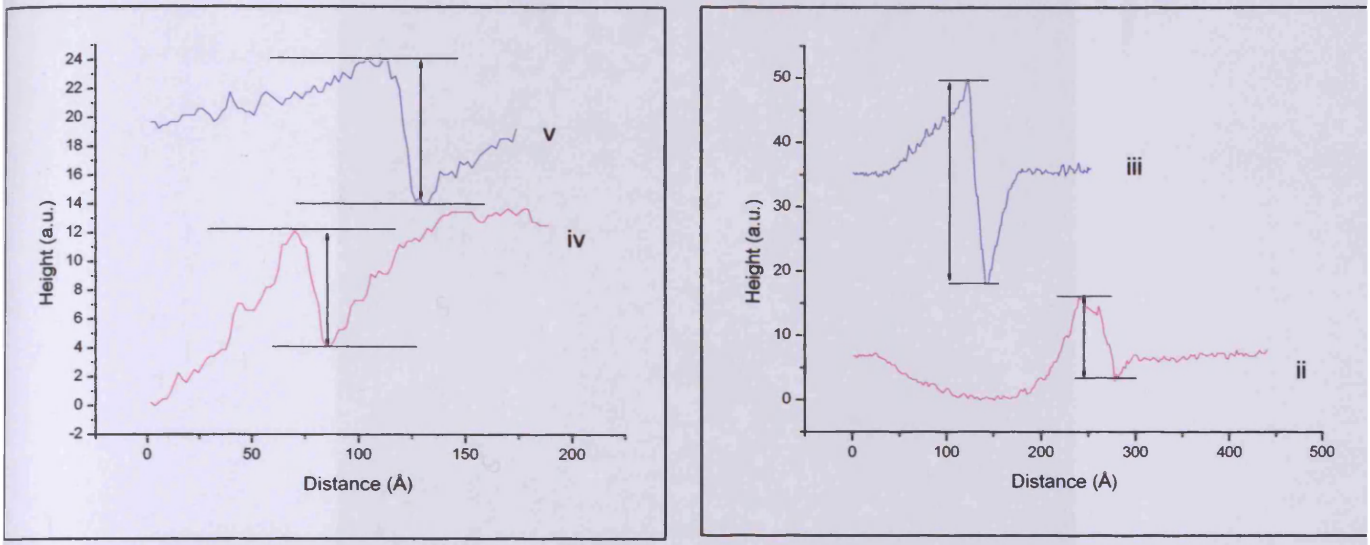

Figure 77: Line profiles across image 76. Profiles are taken from a processed image for clarity and thus height information is not maintained

The STM image in figure 76 shows a superimposition of terraces having different inclinations due to the terraces thickness and position on the surface. The line profiles labelled ii and iii show a step height distance that increases from left to right of the image. The distance varies from ~12.7Å to ~31.5Å. The second step (shown as i) has a constant height of 4.5Å±0.5Å. The step at the right of the image also presents an inclination (line profiles iv and v). The height varies from ~8Å to 10.7Å. The surface shows an ordered surface structure at high resolution (figure 78).The pattern is hexagonal with varying brightness features. They are clusters composed of groups of atoms. The unit cell, represented in white on the image, measures 9.8Å×9.8Å (±0.6Å).

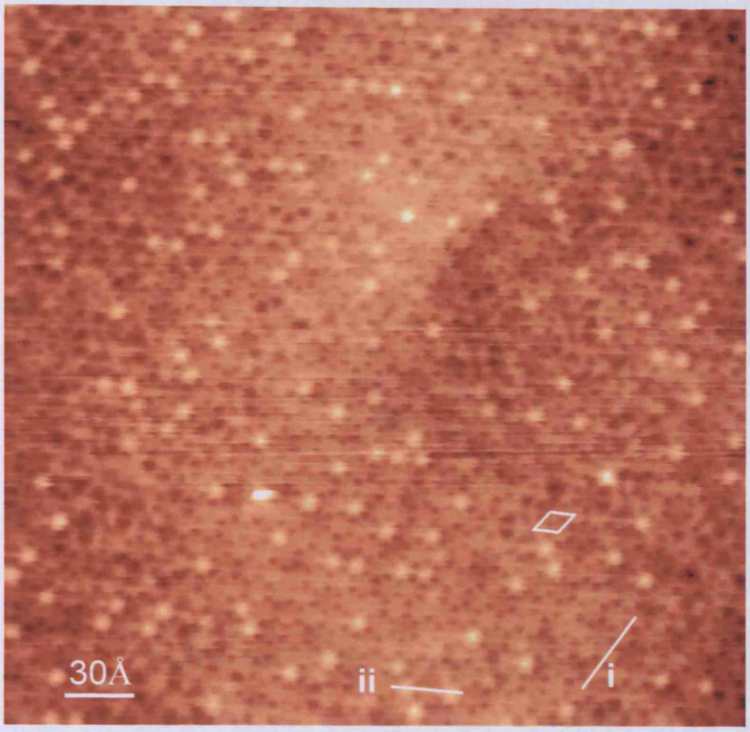

Figure 78: High resolution STM image after 15minutes annealing at 1073K. Parameters: 322Å×322Å, 1nA, 1.5V.

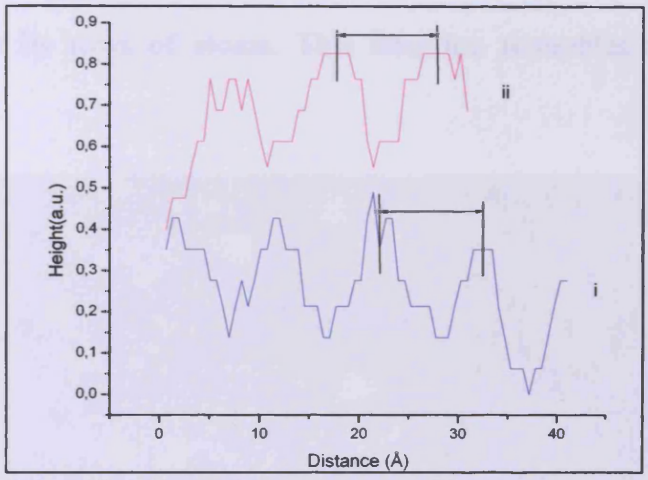

Figure 79: Line profile across image 78.

The unit cell is hexagonal and similar to the small wagonwheel structure. The error in measurements is due to the difficulty of getting well-ordered, complete unit cells in a string. The FFT image in figure 80 shows two hexagonal patterns arising from the surface. A small one 30° rotated from the larger one. Looking at the image on figure 78, only one hexagonal structure is visible. However, the groups of atoms forming the

hexagonal pattern are possibly small hexagonal arrangement of atoms. The FFT may confirm this arrangement.

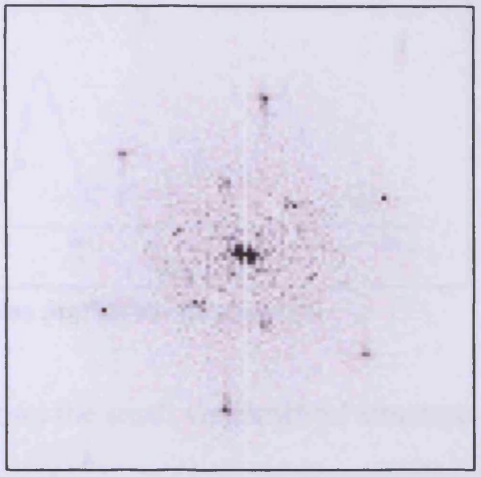

Figure 80: FFT image of figure 78.

A smaller area image (figure 81) shows a peak to peak height of ~0.4Å for the darkest groups. The peak to peak height for the brightest groups is 1.0±0.2Å. All the groups are linked together by rows of atoms. This structure resembles the wagonwheel structure.

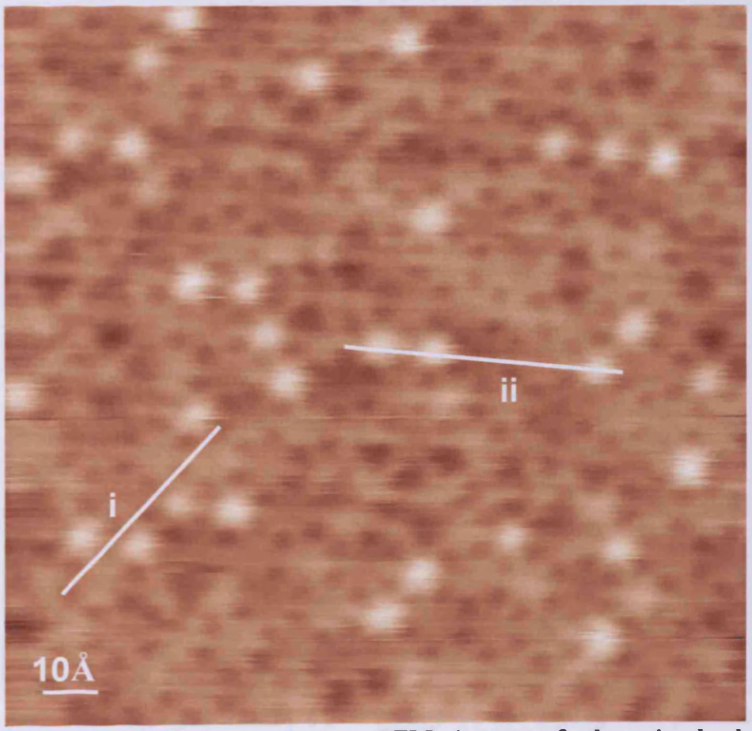

Figure 81: High resolution STM image of the pinwheel structure. Parameters: 134Å×134Å, 1nA, 1.5V, RT.

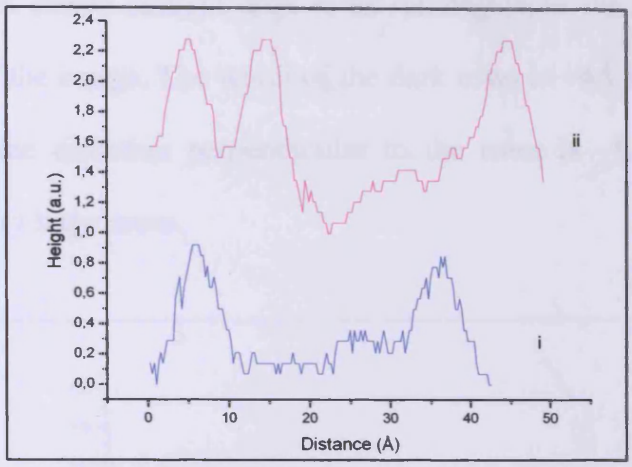

Figure 82: Line profiles across image 81.

The image in figure 83 shows the small wagonwheel structure and a zigzag area. The wagonwheel structure is on the same plane as the zigzag area as seen on the line profile figure 84 except for the hubs of the wagonwheel that sits, for some of them higher than the zigzag structure. The two structures are locked together and it seems that the sides of the zigzag are a continuation of the arms of the wagonwheel.

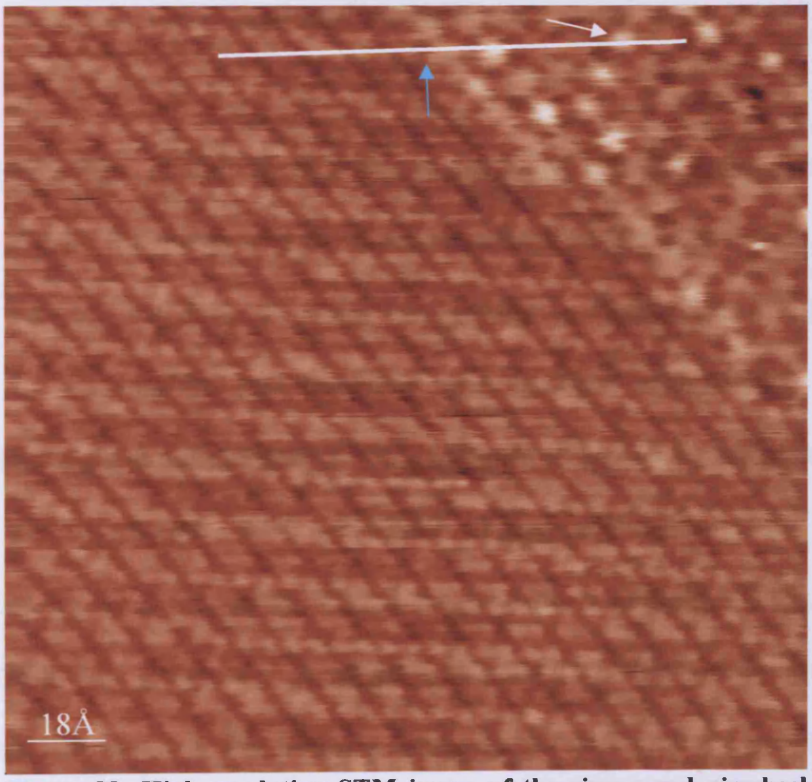

Figure 83: High resolution STM image of the zigzag and pinwheel structure. Parameters: 188Å×188Å, 1nA, 0.6V, RT.

The zigzag area shows straight dark rows running from the top left corner to the bottom right of the image. The width of the dark rows is ~4Å with ~0.8Å depth. The periodicity in the direction perpendicular to the rows is ~8.1Å. This structure is present over very large areas.

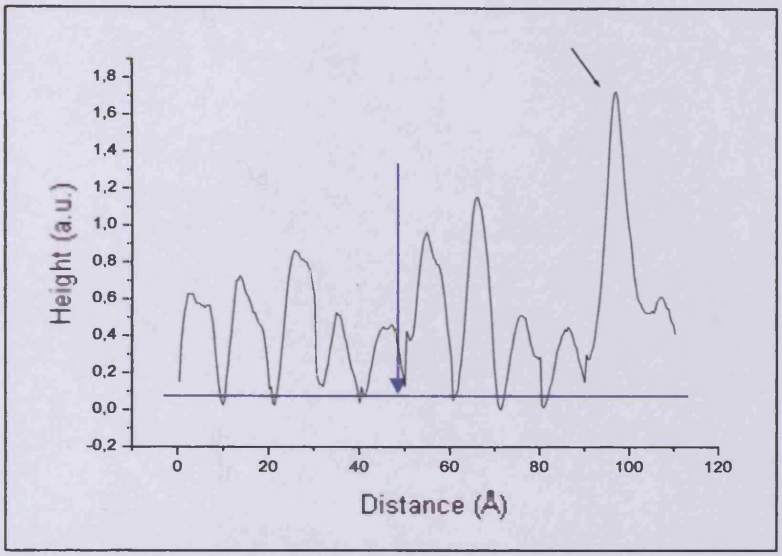

Figure 84: Line profile across image 83. The blue arrow indicates the limit between the zigzag structure and the wagonwheel one. The black arrow highlights a bright cluster, shown by the white arrow in figure 83.

The sample was then heated up to 573K in the STM head and more scanning was carried out. Figure 85 shows a high resolution image of the zigzag area. The zigzag are located between the dark rows and run parallel to them. The zigzags consist of three spots in the diagonal and one faint spot between each zigzag. The atomic spacing in the longitudinal direction of the zigzag rows is ~3.2Å, highlighted in figure 85(iii), but the intermediate spots are barely visible on the line profile (figure 86). Along the zigzag diagonal, figure 85(ii), the spacing is slightly shorter, ~2.9Å and ~3.0Å for 85(i). This structure is identical to the one found by Bowker group [4] who explained this difference in this lattice spacing by the presence of a pseudohexagonal structure. The unit cell of the zigzag structure is represented by the white rectangle on

the figure 85 and has the dimensions 8.1Å×6.3Å. According to Bowker, the contrast across the zigzag could arise from relaxations which result in the buckling of the surface.

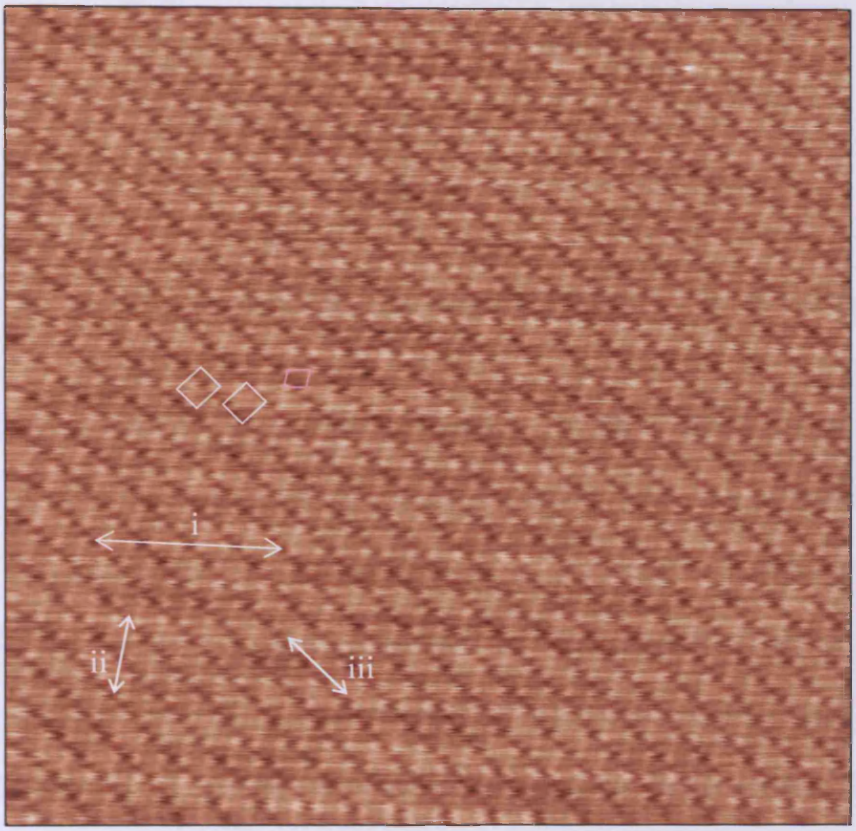

Figure 85: High resolution STM image of the zigzag structure. Parameters: 200Å, 1V, 1nA at 573K. The rectangles show the unit cell.

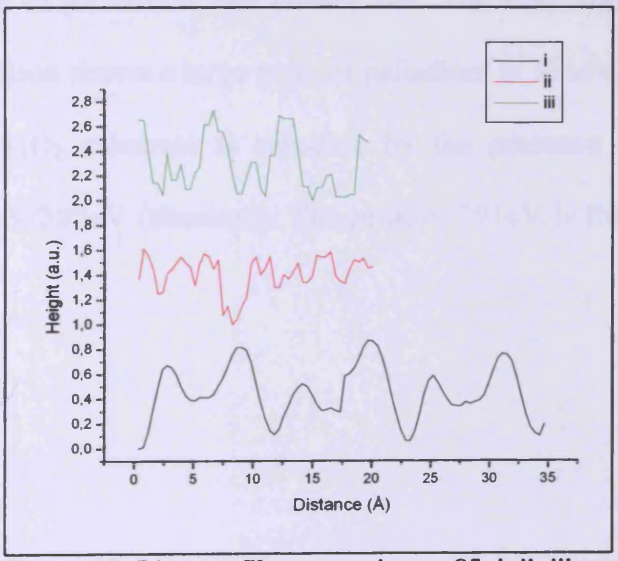

Figure 86: Line profiles across image 85. i, ii, iii are shown on figure 85. Profiles shown are taken from a processed image for clarity and therefore the information about the height is not maintained.

The FFT of the zigzag structure is shown in figure 87.

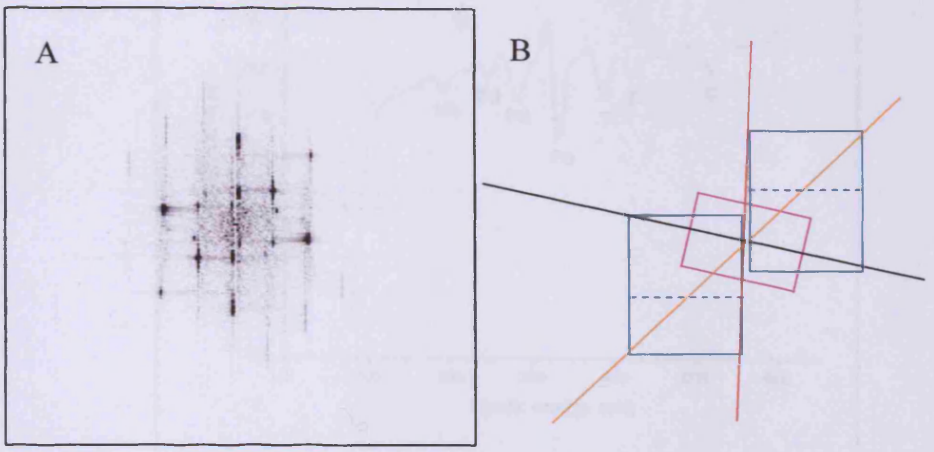

Figure 87: A) FFT image of the zigzag structure. B) Schematic of the FFT image.

It shows a nice and sharp image with periodicity. The three axes corresponds to the periodicity in the directions i (orange line), ii (yellow line) and iii (black line) in image 86. The zigzag structure has two domains as shown by the two blue rectangles on the FFT and by the two white rectangles on the image 86. The last rectangle (purple) could come from the unit cell shown by the pink rectangle in figure 85.

The crystal was cleaned by successive cycles of sputtering and annealing. The Auger spectrum showed that a little Pd remained (~2%) and a little Ca (~2%) contamination. Another deposition of palladium was carried out. The first Auger spectrum (figure 88) after the deposition shows a large peak of palladium at 331eV and peaks at 279eV and 245eV. The TiO_2 substrate is revealed by the presence of peaks at 519eV (oxygen) and 420eV/385eV (titanium). The peak at 191eV is from the molybdenum block.

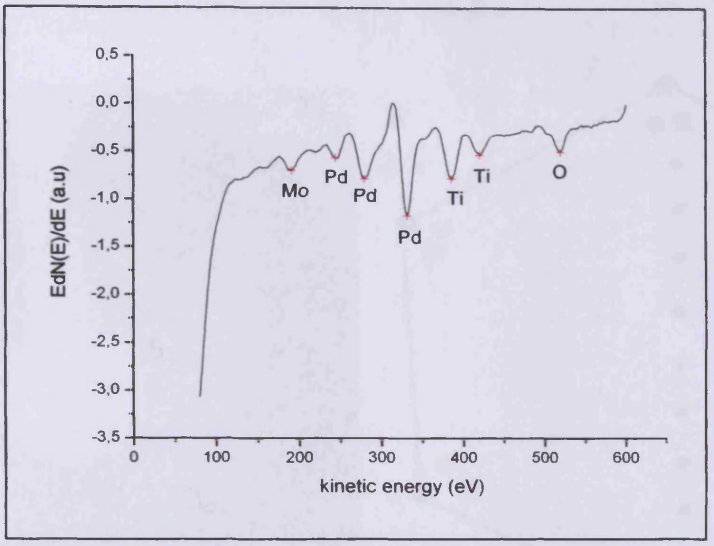

Figure 88: Auger spectrum after Pd deposition.

The thickness of the layer deposited was calculated from the equation $I_t = I_0 \exp^{-d/\lambda}$ (chapter 2). A 4.3Å thick layer was deposited, corresponding to nearly 2 monolayers of palladium (interplanar distance of Pd is 2.24Å) assuming that the layer was homogeneously spread on the surface. The Pd:Ti ratio is 1.22:1.

The LEED pattern (figure 89) after deposition consists of a blurry (1×2) pattern which indicates that palladium has deposited in a disordered way on the TiO_2 substrate. The film was annealed 15 minutes at 673K and 773K but it resulted in no improvement of the sharpness of the LEED. This was followed by 30 minutes annealing at 873K and 973K in an attempt to obtain an ordered palladium layer. The LEED on figure 90 was obtained after 30 minutes annealing at 1073K.

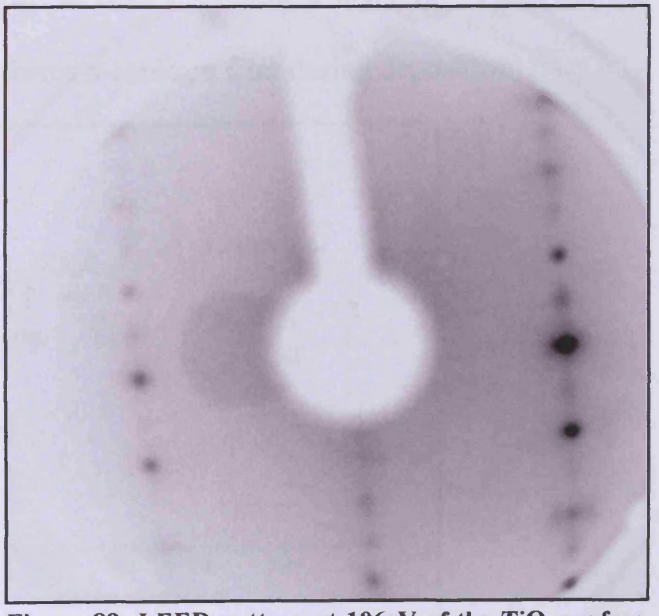

Figure 89: LEED pattern at 106eV of the TiO_2 surface after Pd deposition.

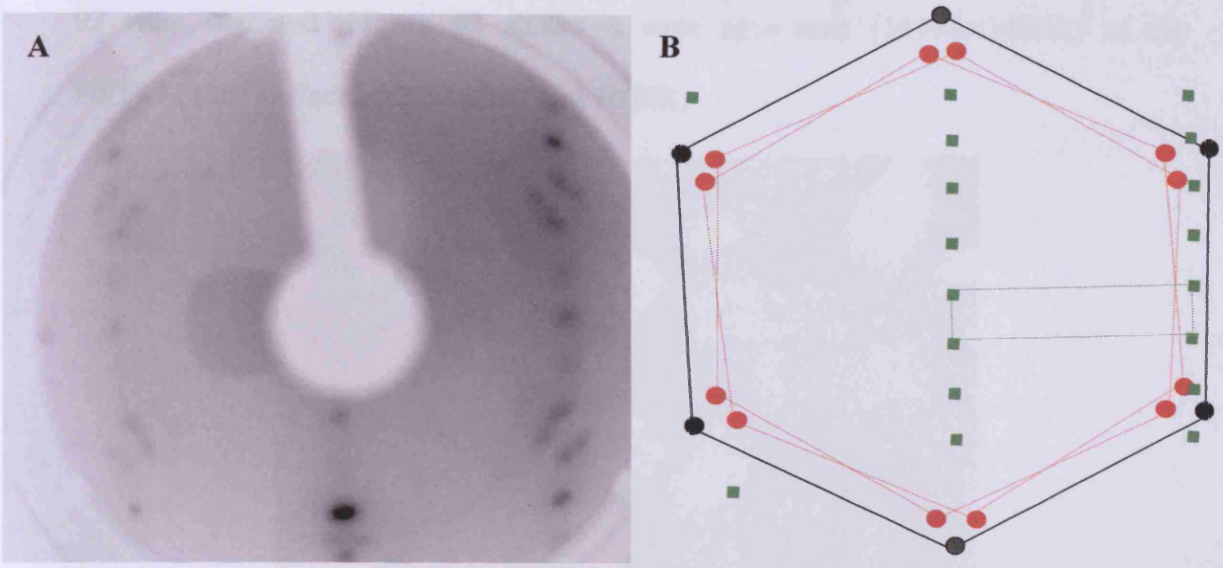

Figure 90: A) LEED pattern at 100eV of the annealed surface. B) Schematic representation of the LEED pattern figure 83A. The black spots are Pd(111), the red one the pinwheel structure and the green squares the (1×2)TiO_2 surface.

The LEED pattern figure 90 shows the presence of an hexagonal unit cell arising from the Pd(111) surface, another hexagonal pattern, having a ±3° rotation from the Pd(111) pattern. The last pattern is the (1×2) TiO_2 structure. This last one is very faint the (1×1) spots are more visible. The Auger spectrum in figure 91 showed that the Pd:Ti ratio has changed considerably to 0.42:1 leaving a layer of 3.85Å on the surface (considering that palladium forms a constant film during deposition).

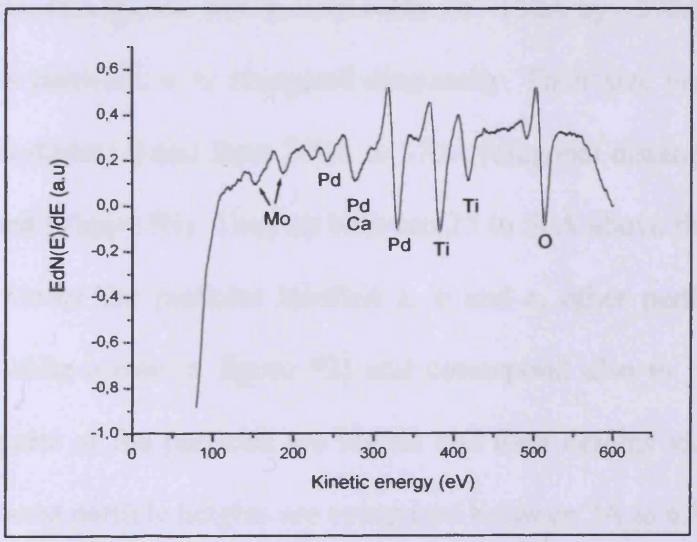

Figure 91: Auger spectrum after annealing 30minutes at 1073K.

Scanning was carried out after this treatment and pictures as the one shown in figure 92 were obtained. Figure 92 shows a wide area scan (1499Å×1499Å) of the $Pd/TiO_2(110)$ surface after annealing at 1073K.

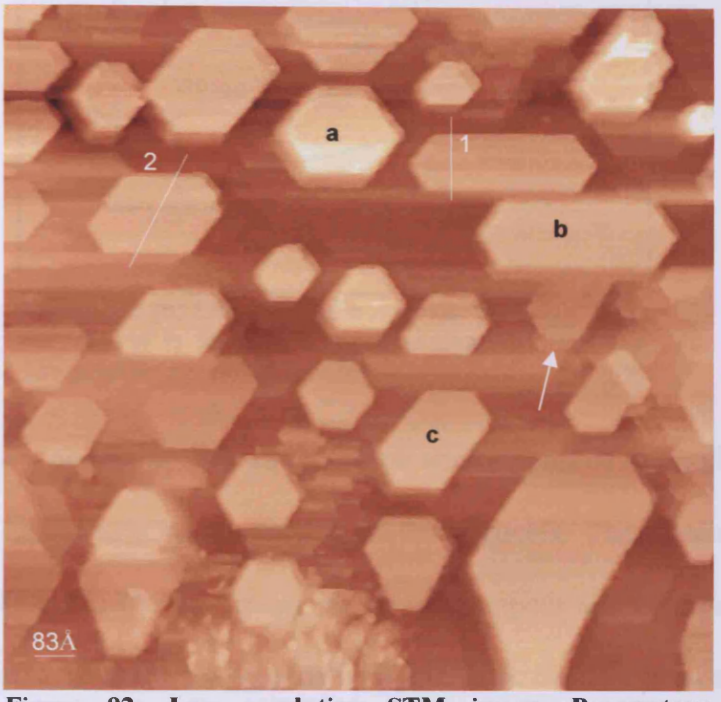

Figure 92: Low resolution STM image. Parameters: 1499Å×1499Å, 1nA, 1V. 1, 2 are line profiles shown in figure 86. a, b and c label the different particle types.

Particles of various sizes and height have formed on the surface. Some have a nearly perfect hexagonal structure, e.g. **a**, with widths varying from 125Å to 220Å. Other particles are pseudohexagonal, like **b**, with width of ~130Å by ~390Å. A third type of pseudohexagonal particles, **c**, is elongated diagonally. Their size vary from 190Å to 250Å (horizontal distance) and from 270Å to 370Å (diagonal distance). The particles are not flat topped (Figure 93). They sit between 25 to 50Å above the surface for the brightest ones. Under the particles labelled a, b and c, other particles are present (shown by the white arrow in figure 92) and correspond also to pseudohexagonal particles. Only parts of the particles are visible and their heights vary between 15Å and 20Å. The lowest particle heights are comprised between 3Å to 6Å.

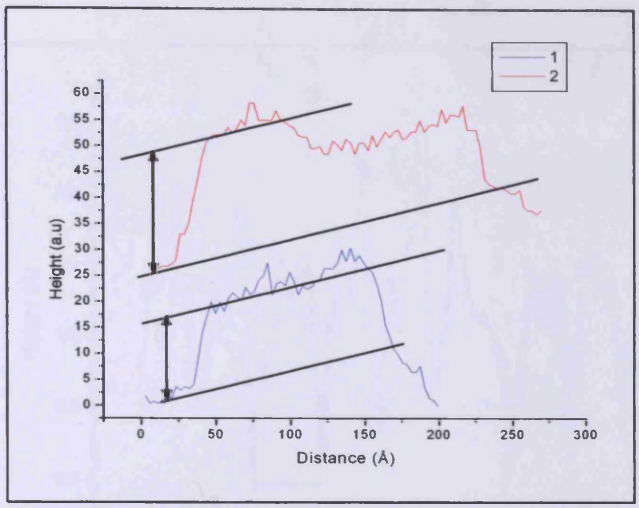

Figure 93: (b) Line profiles across the particles. They correspond to the lines 1 and 2 on figure 92. The two line profiles are offset for clarity.

The next STM image (figure 94) was taken on another part of the surface with similar particles. This image is a zoom on one of the particles. The distance between the groups is 17.5Å±0.5Å. On the image, the groups appear as dark spots and thus the peak to peak distance on the line profile in figure 95 is the distance between two gaps as shown by the black arrow.

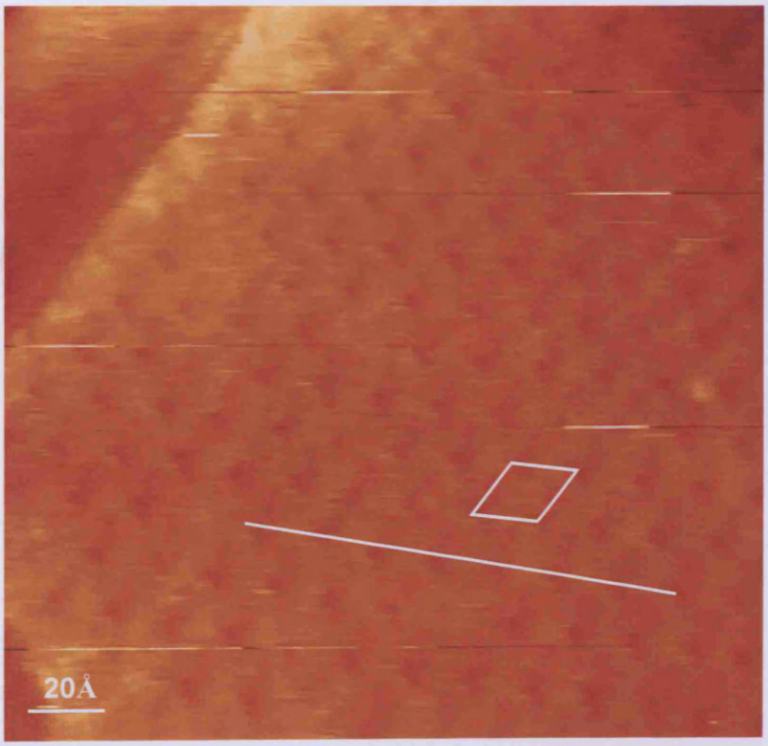

Figure 94: High resolution STM image of a Pd particle. Parameters: 221Å×221Å, 1nA, 1V.

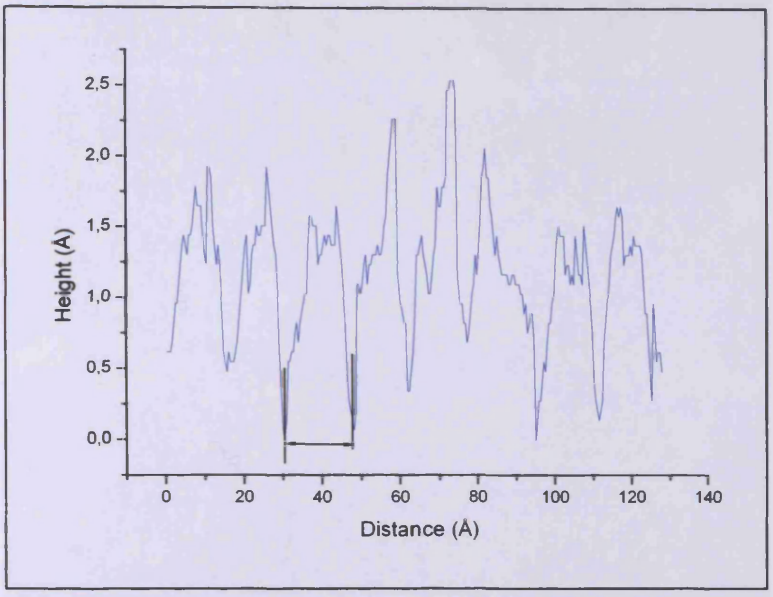

Figure 95: Line profile across figure 94 (white line).

The dispersion of Pd particles is not constant at the surface as seen on figure 96 where the coverage is higher than figure 92. The shapes of the particles are the same as above with approximately the same size range. A zoom of figure 96 is shown in figure 97.

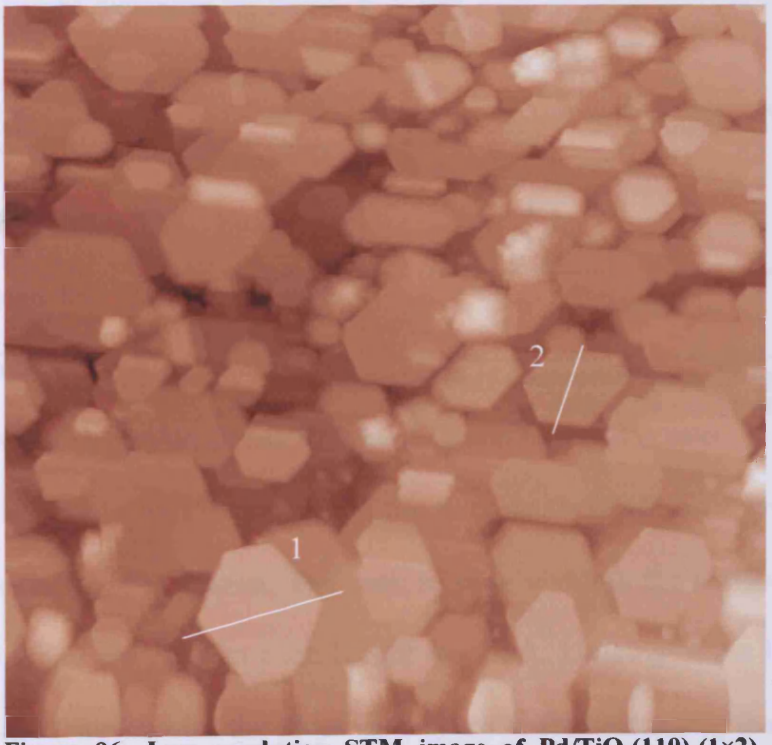

Figure 96: Low resolution STM image of $Pd/TiO_2(110)$-(1×2). Parameters: 2000Å×2000Å, 1.5nA, 1V, RT. 1 and 2 are the line profile across the particles and are shown on figure 98.

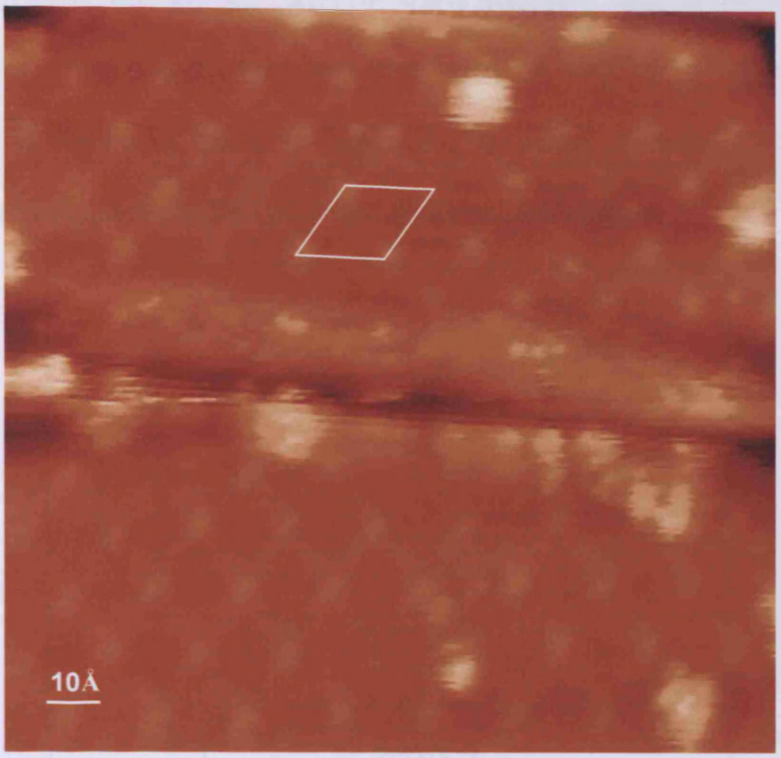

Figure 97: High resolution STM image of the Pd particle. Parameters: 144Å, 1nA, 1.5V

The particles are flat-topped as seen on the line profile in figure 98. The peak to peak height distances for those particles are 50Å. Other particles are present at lower heights which vary between ~15Å and ~50Å. Scanning the top of those flat particles showed some structure. A zoom on one of the particles above is shown on figure 97.

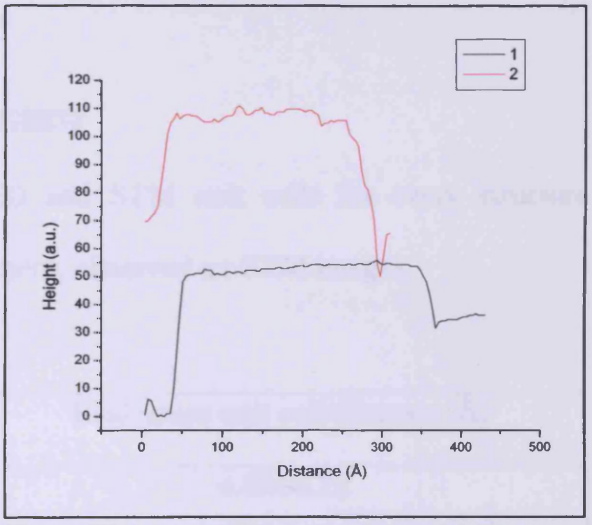

Figure 98: Line profiles across image 96. The height has been shifted for clarity of the plot. The height is thus in arbitrary units.

One pattern is visible on the surface of the particle. It consists of rows of groups arranged in an hexagonal pattern. The peak to peak width in the horizontal direction is 17.5Å±0.5Å and the peak to peak height is ~1.5Å. Looking at the line profile in figure 99, peaks (shown with the black arrow) are visible indicating that features are

present in between the groups. In this case, the unit cell is halved and thus corresponds the small wagonwheel structure observed after the previous deposition. The unit cell is drawn in white in figure 97. The large feature in the horizontal direction is due to a previous tip crash that damaged the surface.

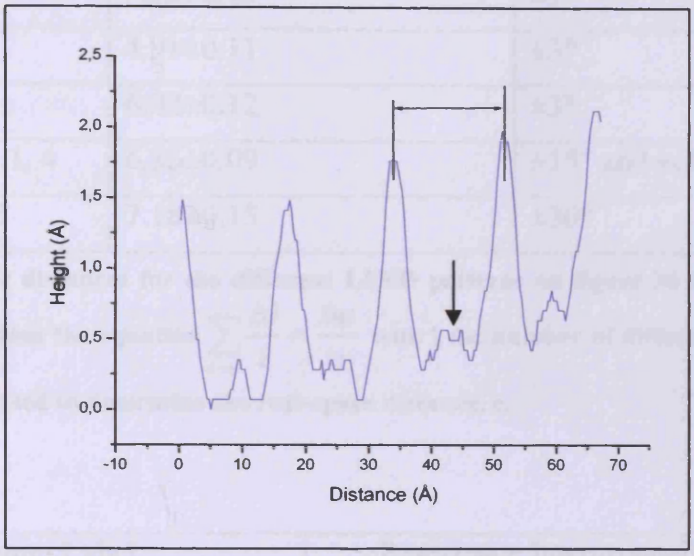

Figure 99: Line profile across figure 97.

3.2. Discussion and modelling of the structures

The tables below summarize the LEED and STM unit cells for every structure detected at the surface, and for some of them, observed on STM images.

Structure label	Real space unit cell distance (Å)
1 (minor structure)	4.05±0.22
2	4.28±0.23
3	5.00±0.27
4 (minor structure)	6.25±0.24
5	9.38±0.33

Table 5: Interatomic distances for the different LEED patterns on figure 35 labelled 1 to 5.

Structure label	Real-space unit cell distance (Å)	Rotation angle with respect to Pd(111) pattern
b: Pd(111)	2.75	-
c : Pinwheel	3.20±0.05	±3°
d	3.62±0.03	±3°
e and table 1: 3	4.91±0.11	±3°
f	6.02±0.12	±3°
h, j,g and table 1:1, 4	6.36±0.09	±15° and ±60°
i and table 1: 2, 5	7.18±0.15	±30°

Table 6: Interatomic distances for the different LEED patterns on figure 36 labelled b to j. The error is calculated from the equation $\sum_{a \to i} \frac{\Delta i}{i} = \frac{\Delta c}{c}$ with i the number of different parameters (e.g. measured distance) used to determine the real-space distance, c.

Structure Label	Real-space intergroup distance (Å)
Hexagonal (figure 42B)	9.4±0.5
Large wagonwheel (figure 50)	18±0.5
Small wagonwheel (figure 52)	9.5±0.2
Hexagonal (figure 59)	10.3±0.5
Star shape (figure 63)	25.3±0.5
wagonwheel (figure 66)	9.5±0.5
Hexagonal (figure 69)	9.5±0.2
Hexagonal (figure 78)	9.6±0.4
Zigzag (figure 85)	8.1×6.3
Hexagonal (figure 94)	17.5±0.5
Hexagonal (figure 96)	9±0.5

Table 7: Interatomic distance of the main structures calculated from the analysis of the STM images.

The main observations in those tables are the similarities in the intergroup distances of the structures. From the table, there may be only four structures:

- A hexagonal of ~9.5Å
- A hexagonal centrosymmetric of ~18Å
- A "star shape" (hexagonal) of ~25Å
- A zigzag structure of unit cell 8.1Å×6.3Å

In addition, there is a large difference between the size of the unit cells calculated from the LEED patterns that vary between 2.75Å×2.75Å and 9.4Å×9.4Å. The largest unit cell size detected on the LEED patterns has a hexagonal structure of size ~9.4Å which is close to various structures listed in the table above. It is therefore possible that all those structures are identical but appear different on the STM images due to different electronic effects on the scanned areas. The small wagonwheel image in figure 52 is probably related to the hexagonal structures in figures 66, 69, 78 and 96.

Larger structures are also present at the surface. One possibility is the presence of an underlayer having bigger structure. A large wagonwheel structure has been located under the small wagonwheel structure as seen in figure 50. The continuous annealing treatment at high temperatures (up to 1073K) may have brought up atoms at the surface of the big wagonwheel structure which stabilised by organising themselves into smaller structures. The LEED pattern showing the (1×4)-TiO_2 reconstruction is a good example of rearrangement for the surface stability. From the LEED and STM images, it seems that this (1×4) layer is arising from the reconstruction of (1×3) structure due to high reduction treatment.

A structure that has been previously observed is the zigzag structure which possess identical unit cell to the one found by Bowker group [4]. The wagonwheel structure present on the same terrace as the zigzag one (figure 83) showed a unit cell of

~9.5Å×9.5Å which is much smaller than the unit cell found by Bowker group [62] for its pinwheel structure (~17Å). However, the large wagonwheel structure (~18Å unit cell) resembles the pinwheel one. In figure 56, the number of atoms of the large wagonwheel arms consists of apparently 5 atoms that lock to each other in a centrosymmetric configuration. From the previous images and distance measurements, some models were proposed for the various structures. Figure 100 shows a schematic of the superstructure. A hexagonal lattice of periodicity ~3.5Å is rotated 15° to an underlying 2.75Å lattice. This is consistent with the LEED pattern labelled g/h/j which is rotated at15° to the Pd (111) lattice. However, the unit cell of this structure has a real space nearest neighbour distance of 6.4Å±0.1Å.

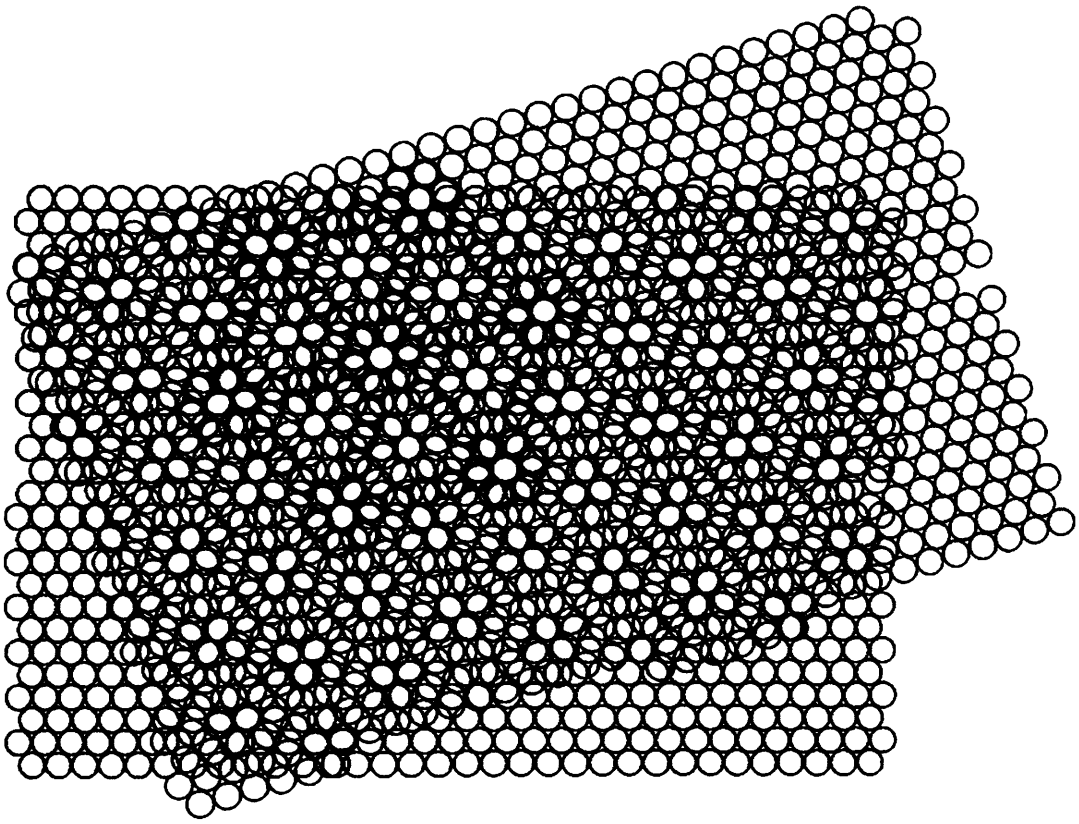

Figure 100: A hexagonal lattice of Ti atoms is rotated by ~15,5° upon a lattice of 2.75Å periodicity giving rise to the superstructure drawn in bold. This pattern is identical to the wagonwheel structure represented in figure 101.

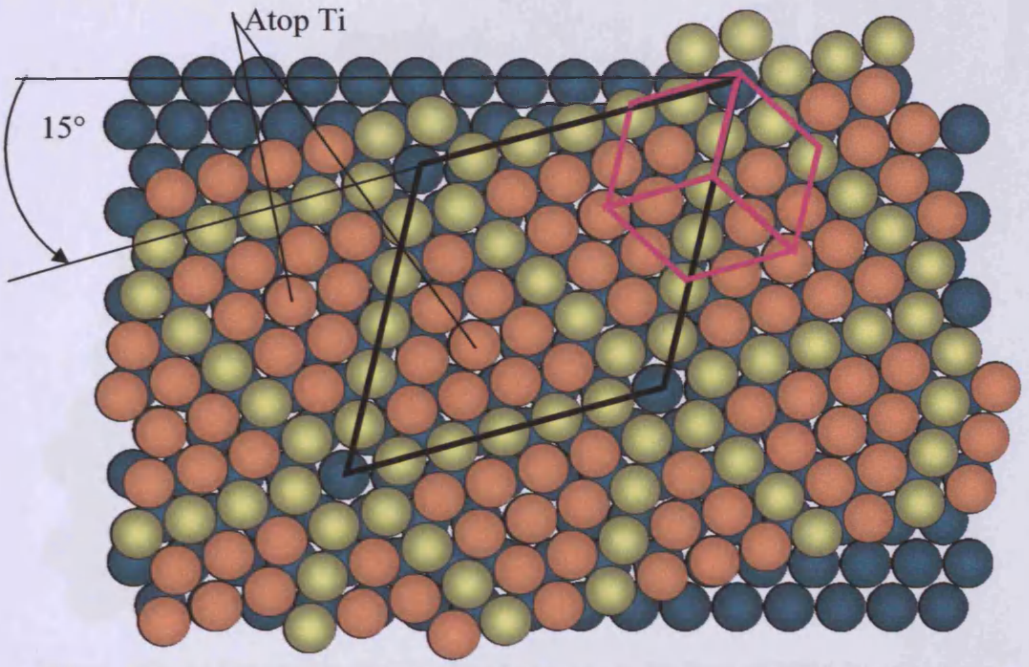

Figure 101: Model of the large pinwheel structure. The radius of covalent Ti is 1.36Å and the one for Pd is 1.31Å. This model is based on the assumption that Ti is on the top of Pd atoms. The black parallelogram shows the wagonwheel unit cell. The magenta one corresponds to the unit cell determined on the LEED pattern.

From the Schematic in figure 100, one can see that the wagonwheel structure contains atop atoms as indicated in figure 101, located in the centre of the triangles forming the wagonwheel. The structure comprising the atop atom is a repeat unit of the wagonwheel hub. Its unit cell is drawn in magenta for clarity and measure ~6.3Å which is consistent with one LEED pattern unit cell distance (labelled in table 2 h,j,g) and rotation of ±15° and ±60° from the underlying Pd structure.

This model allowed also to explain some deformation of the structure seen on STM images. Two examples in figure 102 and 103 are shown below.

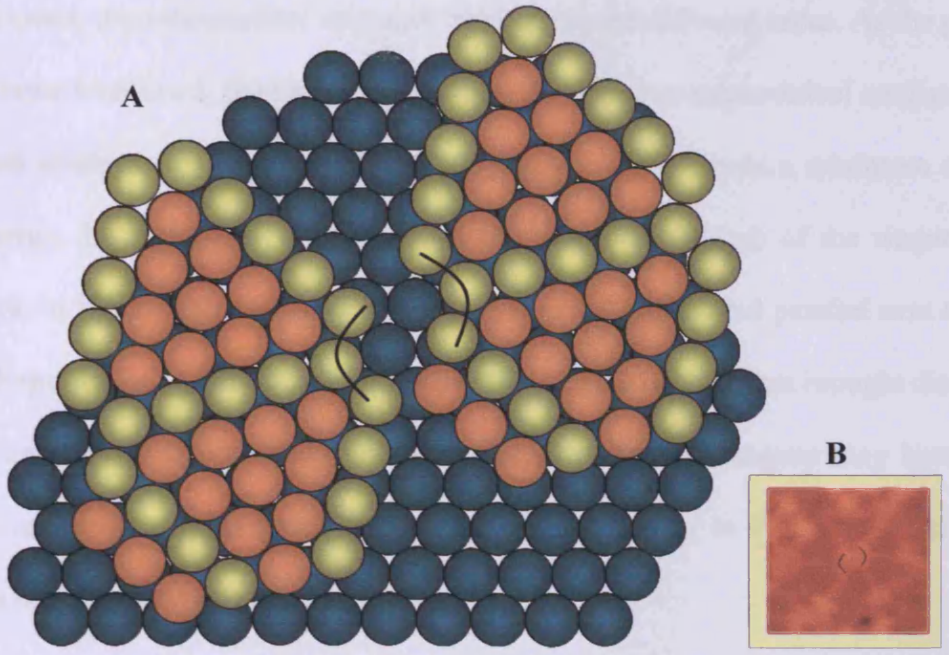

Figure 102: A) Schematic of disordered structure. B) Part of STM image when such deformation is visible.

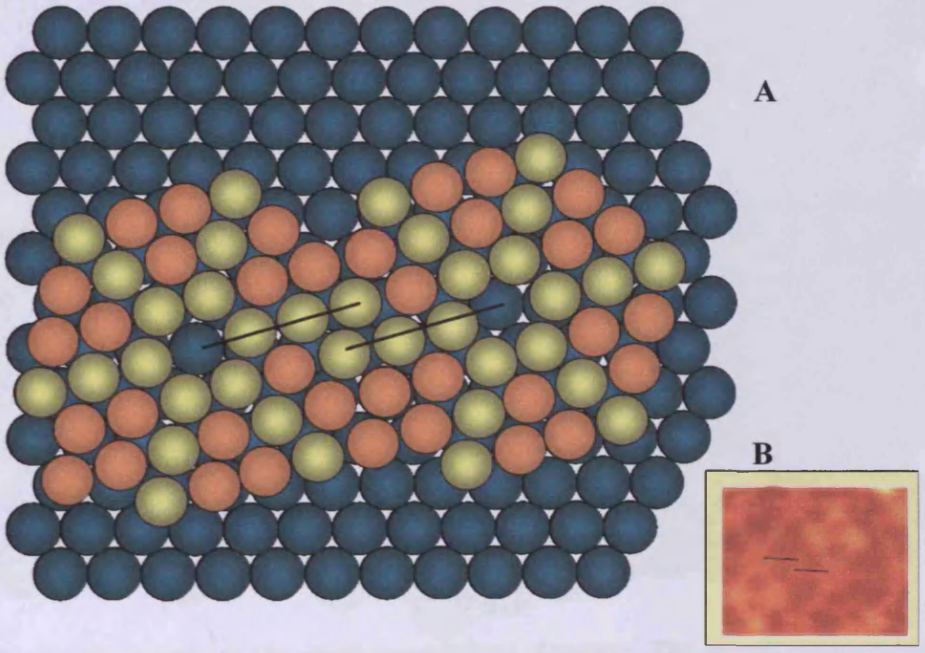

Figure 103: A) Schematic of rearranged structure where two arms of the wagonwheel are located next to each other. B) Part of STM image when such deformation is visible.

In both cases, the wagonwheel structure has built up on different areas. As the growth of this layer continued, the two domains may not join in a symmetrical configuration and such arrangement (figure 102 and 103) may arise to obtain a minimum surface free energy. In figure 101, the distortion is located on the hub of the wagonwheel structure. In figure 102, two arms of the wagonwheel are located parallel next to each other. From the image in figure 56, other features were noticed that brought distortion in the structure. The proposed explanation was that some hexagons may have arms with 4 or 3 atoms. This would affect the model showed in figure 101 and could explain the distortion of the structure.

The second modelled structure is the small wagonwheel structure located on the top of the large wagonwheel one, with a unit cell distance of ~9.5Å. The figure 104 shows a schematic of the proposed model.

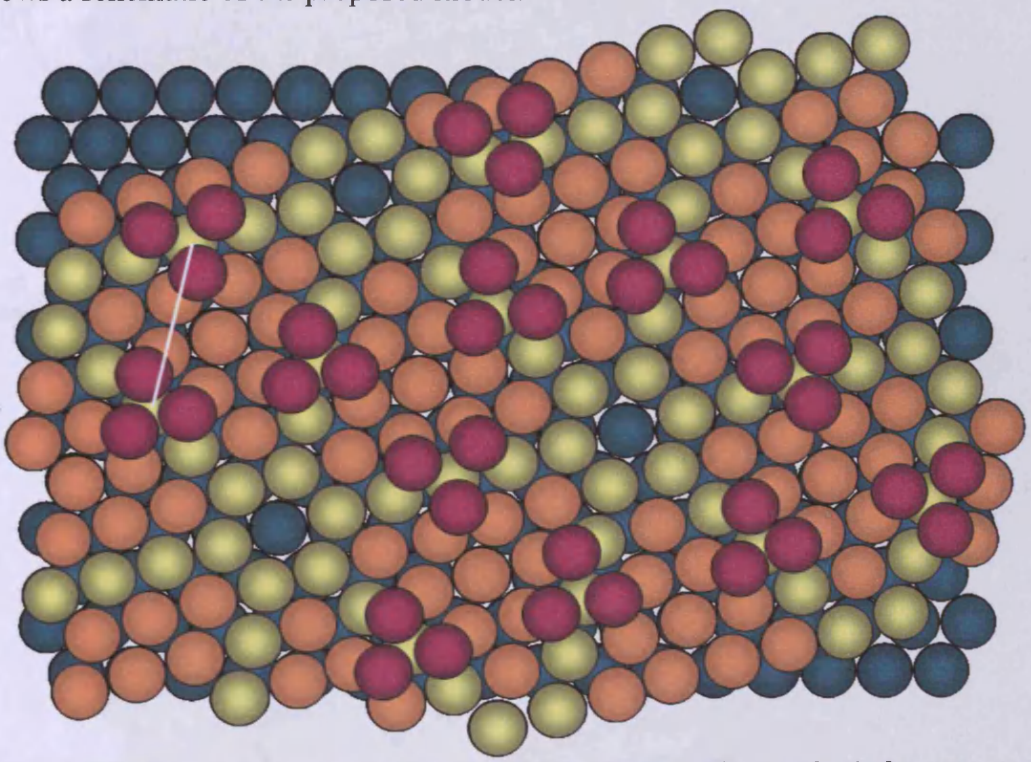

Figure 104: Schematic of the small wagonwheel structure. The purple circles represent the possible small triangle structure.

If this model is correct then 9.5Å/3 equals 3.1Å which could corresponds to the atom periodicity, with the white line representing the distance between the apices of the

triangles. The small wagonwheel structure may be arising from the small triangle and the hubs of the large wagonwheel underneath. The hub may have atop atoms and thus may be on a similar height as the small wagonwheel structure. The structure is in the same plane as the large wagonwheel structure and 15° rotated from the underlying Pd(111) surface. In the LEED pattern in figure 35, the unit cell of the structure i/5 measured 9.4Å±0.3Å and is 15° rotated from the Pd(111) pattern which is the case here. This model then could correspond to the small wagonwheel structure. The atoms could be either palladium or titanium.

The star shape feature differs from the two above due to its larger unit cell, ~25Å×25Å. The following model was proposed to explain the structure.

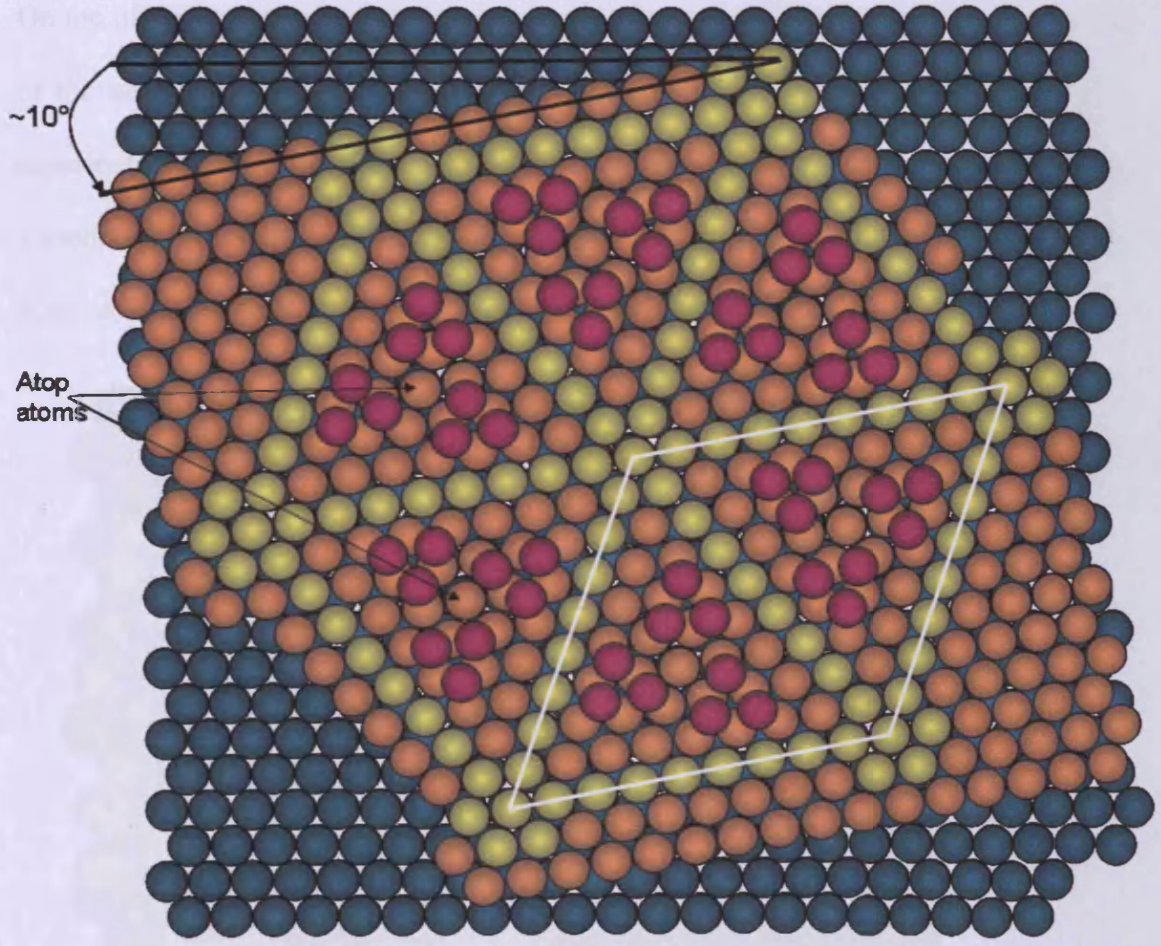

Figure 105: Schematic of the star shape structure. The unit cell is shown by the white parallelogram and measures 24.5Å if the atoms are titanium. The hubs of the star shape are atop atoms on Pd as well as the atoms shown by the arrows. The yellow atoms may be atop or 2-fold and the orange one, 3-fold or atop.

The structure consists of 8 atoms that are locked to each other in a centrosymmetric configuration. It is rotated ~10° from the underlying Pd(111) that has a 2.75Å periodicity. If the structure is correct, the periodicity of the 8 atoms wagonwheel is ~2.8Å which could be possible for Pd or Ti atoms. The unit cell is represented in white and measures ~24.5Å×24.5Å. The unit cell is too large to be seen in the LEED pattern in figure 38. The hubs of this structure contain atop atoms. Other atop atoms are located within the structure (indicated by the black arrows). According to the line profile 4 in figure 62, atoms can sit on the hub of the wagonwheel showing a peak to peak height of ~1.8Å from the wagonwheel surface. However, not all the centre has additional atoms.

On top of this wagonwheel structure, groups of atoms are present that form the apices of the star shape. From the line profile 3 in figure 62, the apices of the star shape, represented by the purple atoms in figure 105 are in the same plane as the hubs of the 8-atoms wagonwheel and may contain 3 atoms. For stability, they would be positioned around the atop atoms and be in 3-fold position.

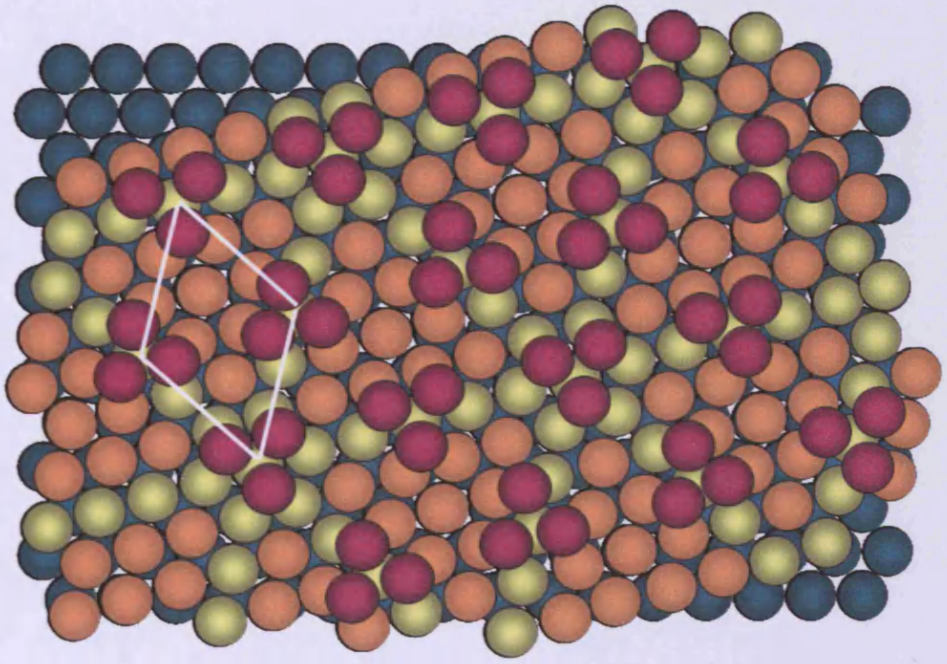

Figure 106: Schematic of the hexagonal structure after annealing at 800°C. The unit cell is shown by the white parallelogram and measures 9.5Å if the atoms are titanium. The yellow atoms may be atop or 2-fold and the orange one, 3-fold or atop. The pink ones are the top layer 3-fold titanium atoms forming the small wagonwheel structure.

After annealing to high temperature (800°C), the structure observed by STM was different from the ones above but the unit cell was similar to the small wagonwheel structure (figure 81). Starting from the model in figure 104, it was possible to draw a new model where all the triangles are linked together to form a hexagonal pattern of unit cell~9.5Å×9.5Å. It is shown in figure 106.

The last structure imaged consisted of a zigzag structure which was also linked to the small wagonwheel structure of unit cell 9.5Å×9.5Å (model in figure 106). In the paper published by Bowker [66], the model proposed for the zigzag included a layer of oxygen underneath the Ti atoms. It is also possible that the zigzag structure is located directly onto the palladium surface without any intermediate layer. From the line profile in figure 85, the zigzag structure is in the same plane as the large wagonwheel structure and the arms of the wagonwheel fit with the zigzag structure. The STM image showed very bright spots on the small wagonwheel hub (figure 83). They are probably Ti or Pd atoms that diffused during the annealing or oxidation treatment on top of the structure.

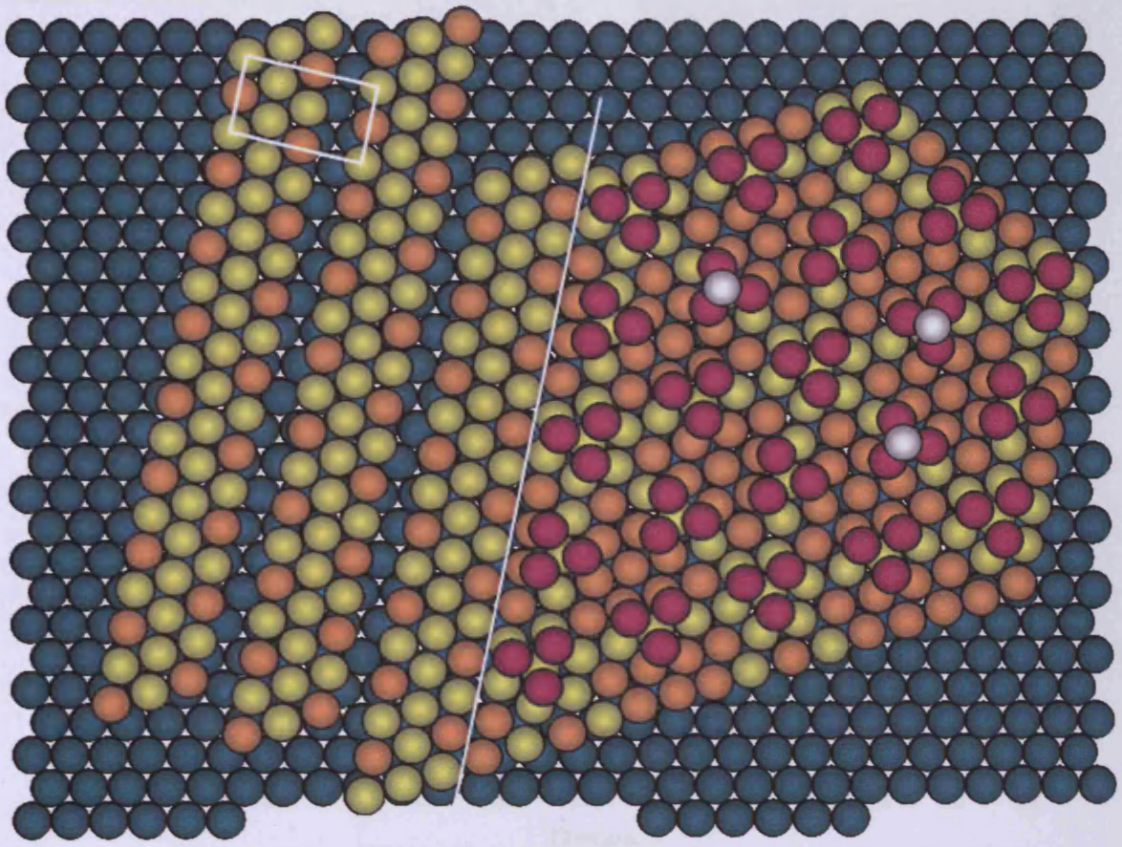

Figure 107: Schematic of the zigzag and small wagonwheel structures. The unit cell is shown by the white rectangle for the zigzag and measures 8.1Å×6.3Å. The yellow spheres may be atop or 2-fold and the orange one, 3-fold or atop. The pink ones are the 3-fold Ti atoms from the small wagonwheel structure and the white spheres are more Ti atoms that sit in a 3-fold position on the small wagonwheel.

3.3. High area, powdered catalyst

3.3.1. Catalyst reduced at 200°C

The catalyst was first reduced at 200°C in a pulsed flow of H_2. The results of the experiment are shown on figure 108.

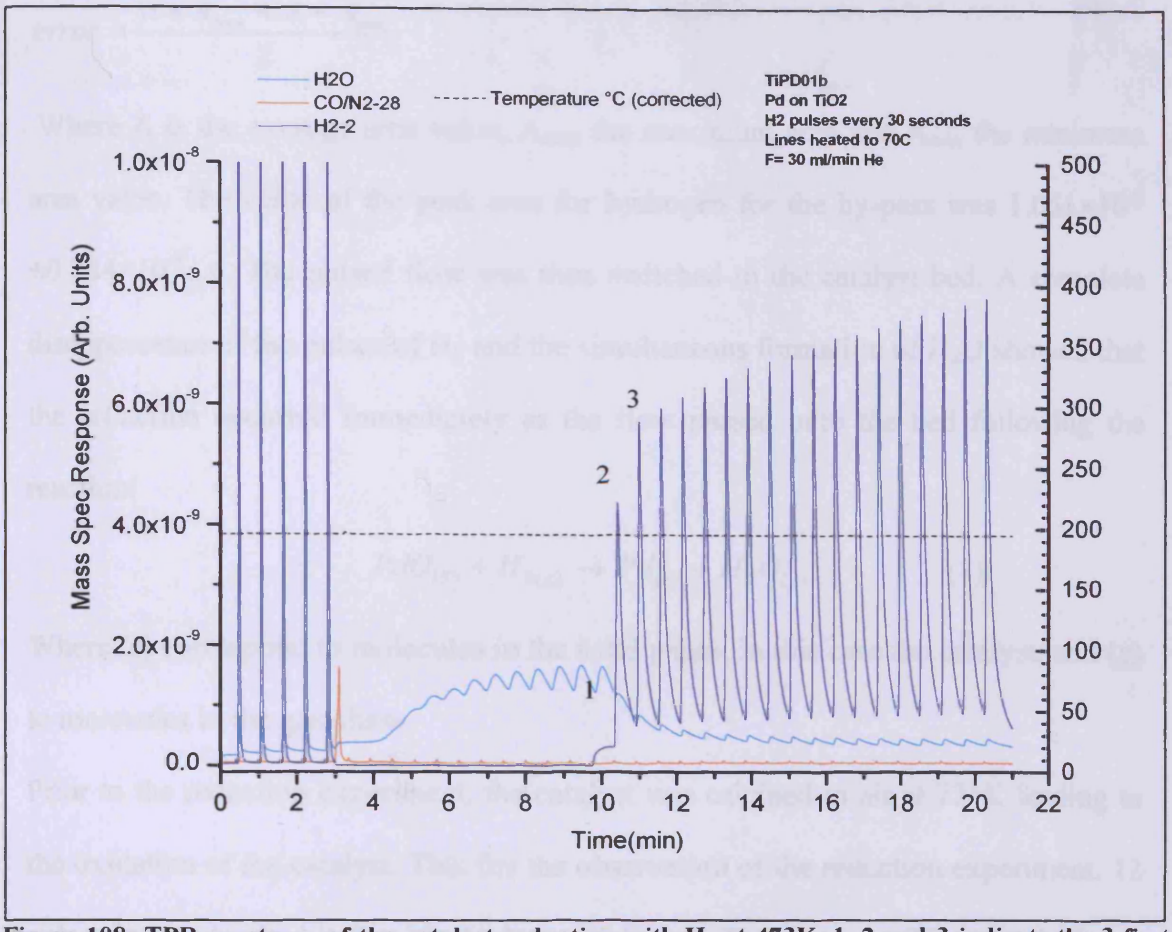

Figure 108: TPR spectrum of the catalyst reduction with H_2 at 473K. 1, 2 and 3 indicate the 3 first peaks arising from H_2 after the uptake. The light blue spectrum arises from the water, the dark blue from H_2, and the orange from CO/N_2. The x-axis is the real time of the experiment. The y-axis is the response of the mass spectrometer and is in arbitrary units. The z-axis is the temperature of the catalyst bed in Kelvin. The scale of the mass spectrometer response has been changed to clarify the H_2 peaks from 10 to 20mins. However, the by-pass pulses are not shown completely. The tips of the peaks vary around 7×10^{-8}a.u.

The five first pulses correspond to pulses through the by pass. They look constant but vary in reality. This is due to the change in the data acquisition. When the peaks were small and broad, more points were measured for one peak than when they were sharp and fast. The number of measured points for each pulse being smaller, the error on the calculation of the peak area was then bigger. This brings some uncertainties on the peak area calculation through the by-pass. The average by-pass peak area was determined by calculating the average area of the five by-pass pulses. The areas were formed by using the peak fitting module in Origin lab software. The error was calculated by:

$$error = \frac{A + A_{max} + A - A_{min}}{2}$$

Where A is the average area value, A_{max} the maximum area and A_{min} the minimum area value. The value of the peak area for hydrogen for the by-pass was 1.061×10^{-9} $\pm0.284\times10^{-9}$a.u. The pulsed flow was then switched to the catalyst bed. A complete disappearance of the pulses of H_2 and the simultaneous formation of H_2O showed that the reduction occurred immediately as the flow passed onto the bed following the reaction:

$$PdO_{(S)} + H_{2(g)} \rightarrow Pd_{(S)} + H_2O_{(g)} \qquad (1)$$

Where (s) correspond to molecules in the solid phase, in this case the catalyst, and (g) to molecules in the gas phase.

Prior to the reduction experiment, the catalyst was calcined in air at 773K leading to the oxidation of the catalyst. This fits the observation of the reduction experiment. 12 pulses were adsorbed before the hydrogen take off. The amount of H_2 adsorbed was calculated by measuring the surface area of the peaks. Knowing that each pulse contains $0.53cm^3$, it was then possible to calculate the volume of H_2 reacted. However, a feature concerning all the H_2 reduction experiments and that would have an effect on the volume measurements was noticed. There was a continuous increase of the height of H_2 pulses with time. During the second reduction at 200°C, the reaction was carried out for a longer time (figure 109) and a definite increase was seen. Looking at the pulses of hydrogen they consist of 2 parts: a straight upward line followed by an exponential decay. However, the signal did not return to the baseline before another pulse started. A continuous increase of the peak height with time was observed. The increase of the peak does not mean a larger amount of hydrogen. The peaks may be higher but narrower and so have an identical area. In order to measure

those areas, the integral of each peak of H_2 was calculated and the method followed is shown on figure 110.

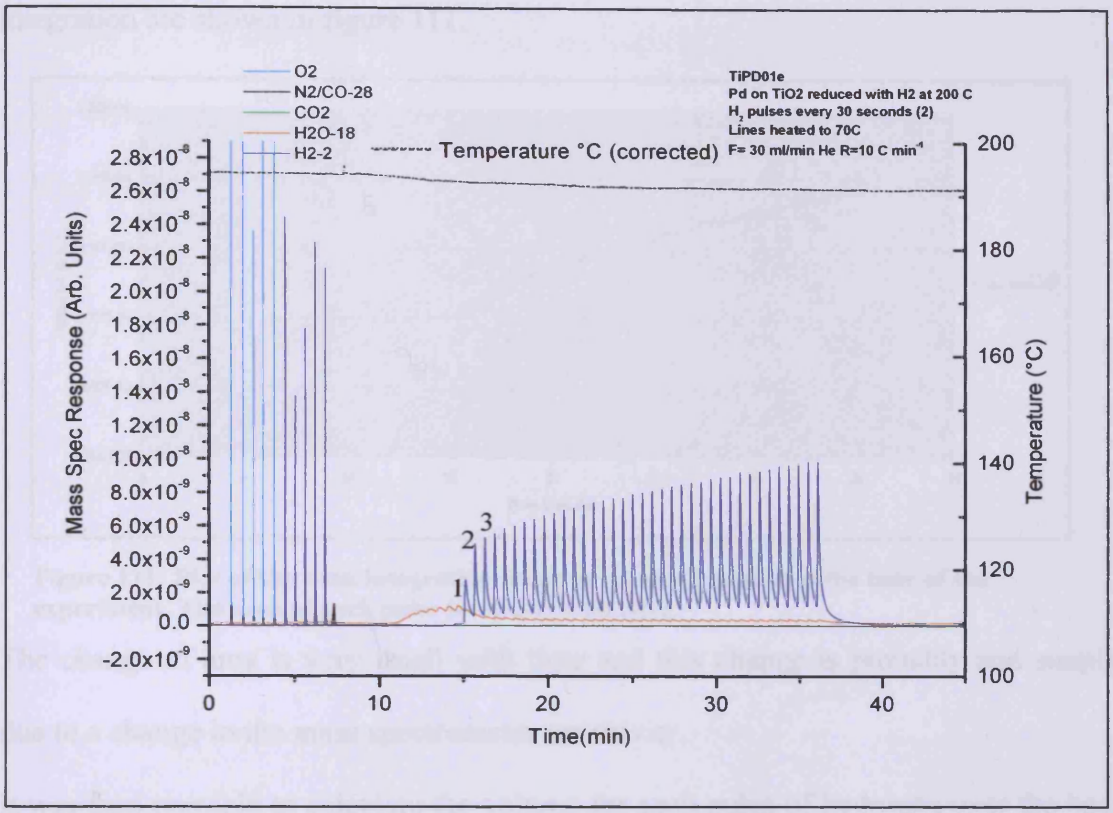

Figure 109: spectra of the second reduction in H_2 of 5%Pd/TiO_2 catalyst at 473K. The light blue by-pass pulses preceding the hydrogen ones are oxygen pulses. The catalyst was oxidised before the second reduction as explained in the experimental paragraph. As for the first reduction, water was produced as hydrogen was consumed. 1, 2 and 3 are related to the first, second and third peak after the reduction has occurred.

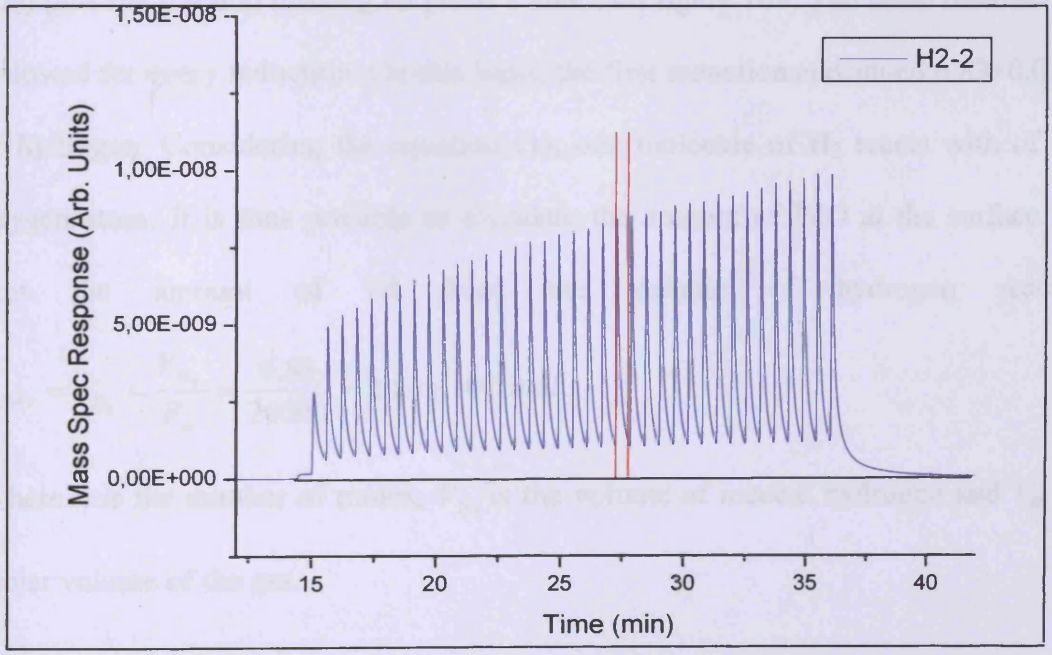

Figure 110: spectrum of the hydrogen. The black line is the baseline for the integration. The red lines comprise the area integrated.

The baseline was set so that it follows the baseline of the spectrum. The area integrated is comprised between the two red lines in figure 110 and the results of the integration are shown in figure 111.

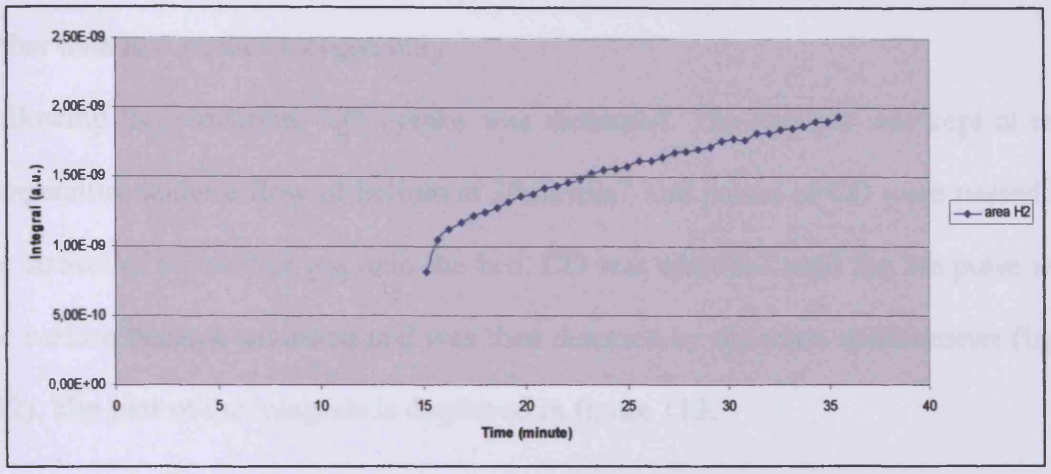

Figure 111: Plot of the peak integration (peak area) as a function of the time of the experiment. The area of each pulse increases with time.

The change of area is very small with time and this change is probably and simply due to a change in the mass spectrometer sensitivity.

It was then possible to calculate the volume for each pulse of hydrogen over the bed. Similar to the areas, the volume of hydrogen kept increasing with time. However, the amount of hydrogen reacted was the sum of the adsorbed peaks (12 pulses in figure 109) plus the fraction missing on pulse 1 and 2 on figure 109. The same method was followed for every reduction. On this basis, the first reduction consumed 6.83±0.07ml of hydrogen. Considering the equation (1), one molecule of H_2 reacts with of one oxygen atom. It is thus possible to calculate the amount of PdO at the surface and thus the amount of Pd from the volume of hydrogen reacted.

$$n_{PdO} = n_{H_2} = \frac{V_{H_2}}{V_m} = \frac{6.83}{24000} = 2.84 \times 10^{-4}\, mol$$

Where n is the number of moles, V_{H_2} is the volume of reacted hydrogen and V_m the molar volume of the gas.

So, $m_{PdO} = n_{PdO} \times M_{PdO} = 2.84 \times 10^{-4} \times 132.2 = 3.76 \times 10^{-2}\, g$ and $m_{Pd} = 3.02 \times 10^{-2}\, g$

The loading of palladium was 5% on 0.5g of catalyst which corresponds to $2.5 \times 10^{-2}\, g$ of Pd. This reasonably close agreement indicates that bulk PdO is reduced rather than just surface oxygen only.

Following the reduction, CO uptake was measured. The catalyst was kept at room temperature under a flow of helium at 30ml.min^{-1} and pulses of CO were passed into the stream of the carrier gas onto the bed. CO was adsorbed until the 5th pulse when the surface became saturated and was then detected by the mass spectrometer (figure 112). The plot of the integrals is displayed in figure 113.

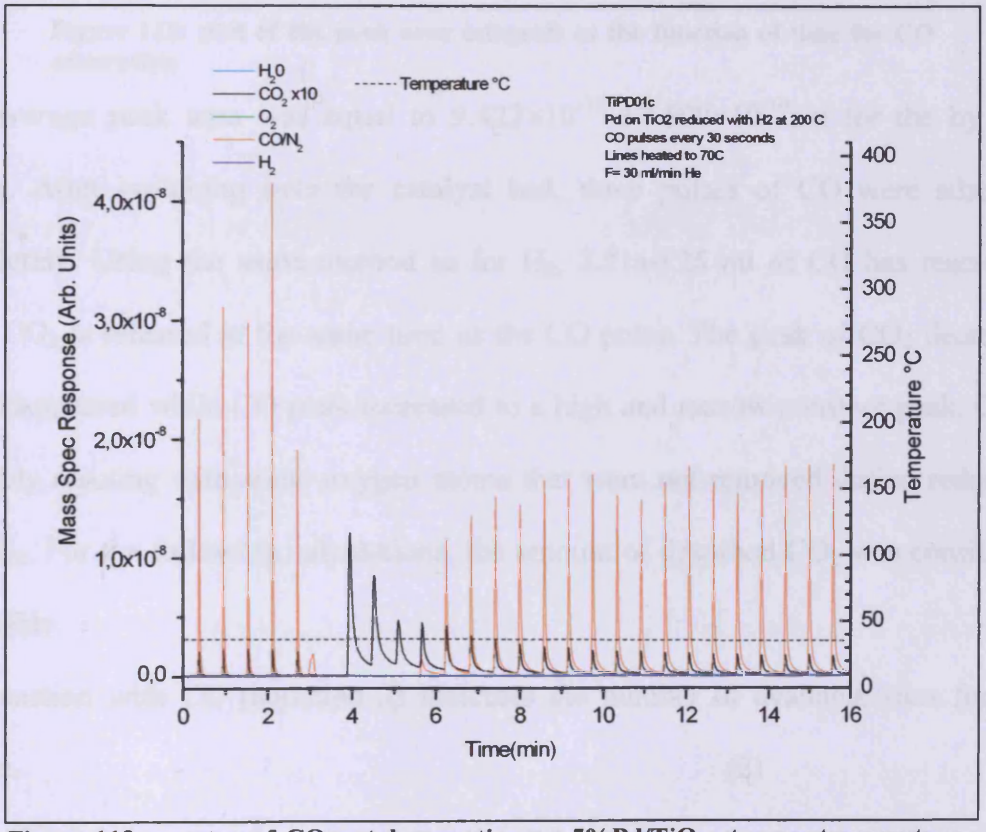

Figure 112: spectra of CO uptake reaction on 5%Pd/TiO_2 at room temperature. The CO pulses are represented in orange. The five first pulses are over the by pass.

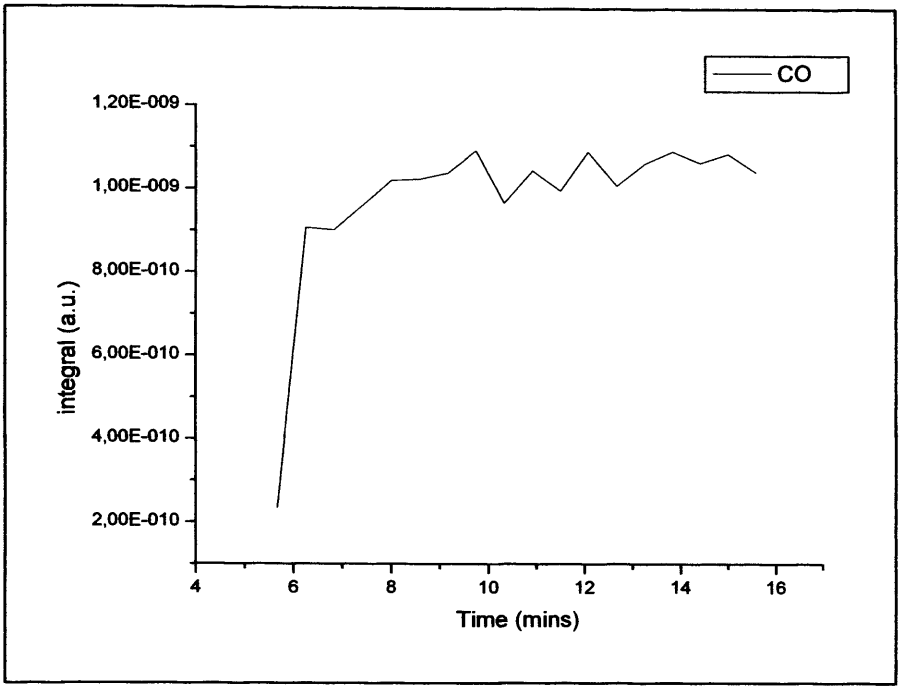

Figure 113: plot of the peak area integrals as the function of time for CO adsorption

The average peak area was equal to 9.423×10^{-10} $\pm7.590\times10^{-10}$a.u for the by pass pulses. After switching over the catalyst bed, three pulses of CO were adsorbed completely. Using the same method as for H_2, 2.21±0.26 ml of CO has reacted in total. CO_2 is released at the same time as the CO pulse. The peak of CO_2 decreased and disappeared while CO peak increased to a high and narrow constant peak. CO is probably reacting with some oxygen atoms that were not removed during reduction with H_2. For the following calculations, the amount of desorbed CO_2 was considered negligible.

The reaction with CO (equation 2) indicates the number of available sites for CO uptake. (2)

$$Pd_s + CO_g \rightarrow Pd_s + CO_s$$

Where Pd_s is the amount of surface Pd, CO_g is the CO in the gas phase and CO_s is the surface CO. Considering that one molecule of CO adsorbs at 1 site of Pd, so

$$n_{CO_g} = n_{Pd_s} = \frac{V_{CO_g}}{V_m} = \frac{2.21}{24000} = 9.21 \times 10^{-5} mol$$

Thus, $N_{Pd} = n_{Pd_s} \times A = 5.54 \times 10^{19}$ surface atoms

Where N_{Pd} is the number of surface atoms and A is the Avogadro constant.

Approximately 0.5g of catalyst covered with 5% of palladium was loaded in the tube.

Thus the number of moles of Pd deposited is

$$\frac{m_{catalyst} \times 0.05}{M_{Pd}} = 2.35 \times 10^{-4} \text{moles}$$

$$= 1.41 \times 10^{20} \text{ atoms.}$$

Therefore the dispersion of palladium at the surface equals:

$$\frac{5.54 \times 10^{19}}{1.41 \times 10^{20}} = 0.39$$

The dispersion of the palladium atoms is ~40% at the surface. As seen on chapter 3, the smaller the radius of the particle, the smaller its surface area. Thus the palladium deposited consists of very small particles.

3.3.2. Reduction at higher temperatures and CO uptake experiments

Each reduction experiments in hydrogen were followed by CO uptake and by CO oxidation reaction. The CO oxidation reactions are described in the paragraph 3.2.4. Then, the catalyst was reduced to higher temperature and the same set of experiments was carried out (CO uptake followed by CO oxidation reaction).

After reduction at 400°C, the volume of H_2 reacted was similar to the one at 473K. 6.42ml of H_2 were used to reduce the catalyst.

Table 4 summarises the different H_2 and CO uptake at different reduction temperatures. The CO uptake was always carried out at room temperature.

Temperature of reduction (°C)	H_2 uptake (ml)	CO uptake (ml)	Surface Pd sites available
200	6.82	2.21	5.54×10^{19}
400	6.51	0.97	2.43×10^{19}
500	7.99	0.70	1.75×10^{19}
550	6.77	0.28	7.02×10^{18}
600	5.53	0.04	1.00×10^{18}

Table 8: Hydrogen uptake at different reduction temperatures and carbon monoxide uptake at room temperature in ml

Increasing the reduction temperature of the catalyst to 873K coincided with a decrease in CO uptake and a decrease of surface Pd sites, especially the highest temperatures. However, the reduction temperature had none or little effect on the H_2 reaction. In their work, Tauster and co-workers [47] considered chemical interaction changes between the metal and the support to explain the loss of sorption of CO and also of H_2. They referred to this effect as the Strong Metal Support Interaction (SMSI) and associated it with the formation of bonds between the metal and the Ti cations or Ti atoms. They proposed that the metal-metal bonding resulted from the overlapping of the occupied d orbital of the metal with the vacant d orbital of the Ti^{4+}. They considered also another kind of interaction between the noble metal and the support Ti atoms which was the formation of intermetallic compounds.

They reported the possibility of the formation of hydrides with the noble metal-titanium intermetallics and that H_2 adsorption would take place at the surface of such compounds. This latter interpretation is consistent with the results presented here indicating that H_2 was still adsorbed despite the loss of CO uptake. This would indicate that intermetallic compounds have been formed at the surface and that

hydrogen is adsorbed at the surface of such particles. It is also possible that a part of this amount of H_2 was necessary to reduce the surface which was left oxidised from the preceding CO oxidation reaction. Each hydrogen reaction occurred with a desorption of H_2O confirming the reduction of PdO to the Pd state.

3.2.4. CO oxidation reactions

Finally, in order to test the activity of the catalyst, CO oxidation was carried out. The catalyst was kept under a flow of $10\%O_2$/He at $30ml.min^{-1}$ and CO was pulsed every 30 seconds in the stream of the carrier gas. The temperature on the bed was then ramped to 773K with a rate of 10°C/min.

Catalyst reduced at 200°C

The oxidation reaction did not occur at room temperature as it is seen on figure 114. Figure 115 and 117 display a zoom in the spectrum, from 30mins to 60mins and

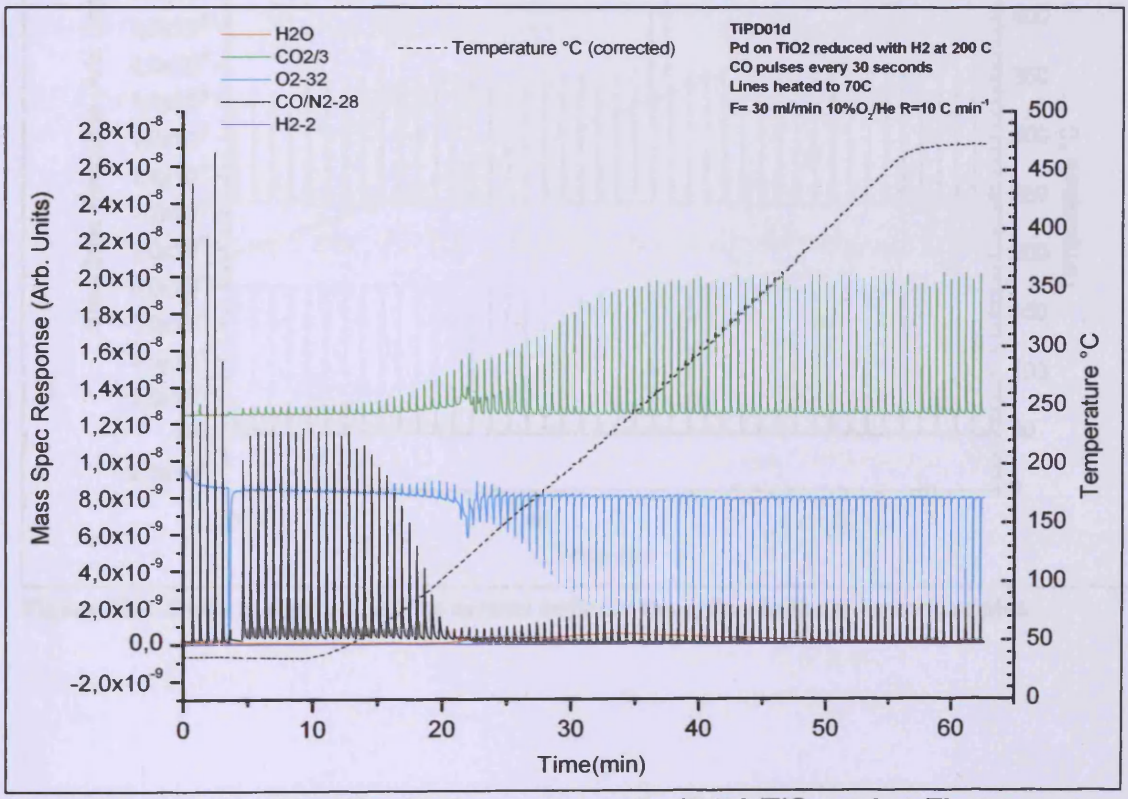

Figure 114: spectrum of the CO oxidation reaction on the 5%Pd /TiO_2 catalyst. The temperature ramp is of $10°C.min^{-1}$.

19mins to 27mins. The evolution of the amount of CO, CO_2 and O_2 was estimated through the calculation of the peak areas, which were then plotted as a function of time and temperature (figure 116).

Looking at the temperature plot, it is first linear and then spikes appear at ~220°C until ~380°C. This indicates that an exothermic reaction is taking place.

Looking at figure 114, there was no formation of CO_2, neither consumption of O_2 nor CO at room temperature. The slight formation of CO_2 was coming from the reaction of CO with O_2 at the filament of the mass spectrometer. As the temperature increased, CO and O_2 were progressively adsorbed and CO_2 was produced. The pulses of CO remained short and sharp until the temperature of the bed was raised.

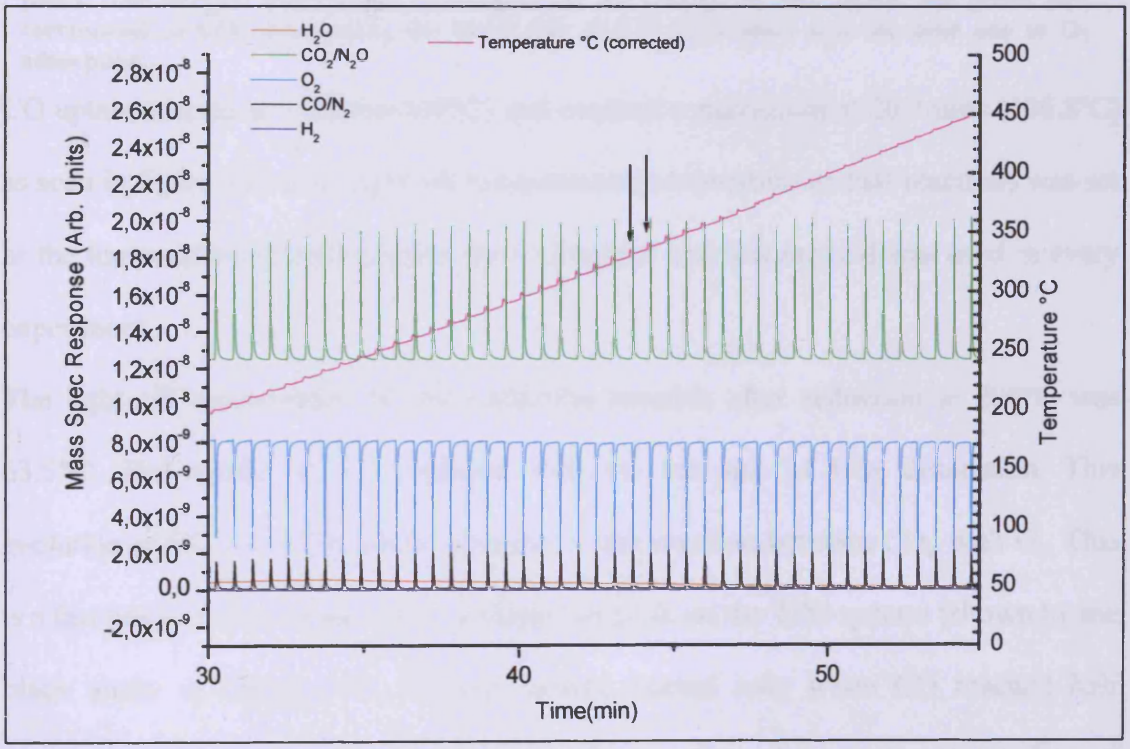

Figure 115: Zoom in figure 114. The arrows indicate the spikes in the temperature plot.

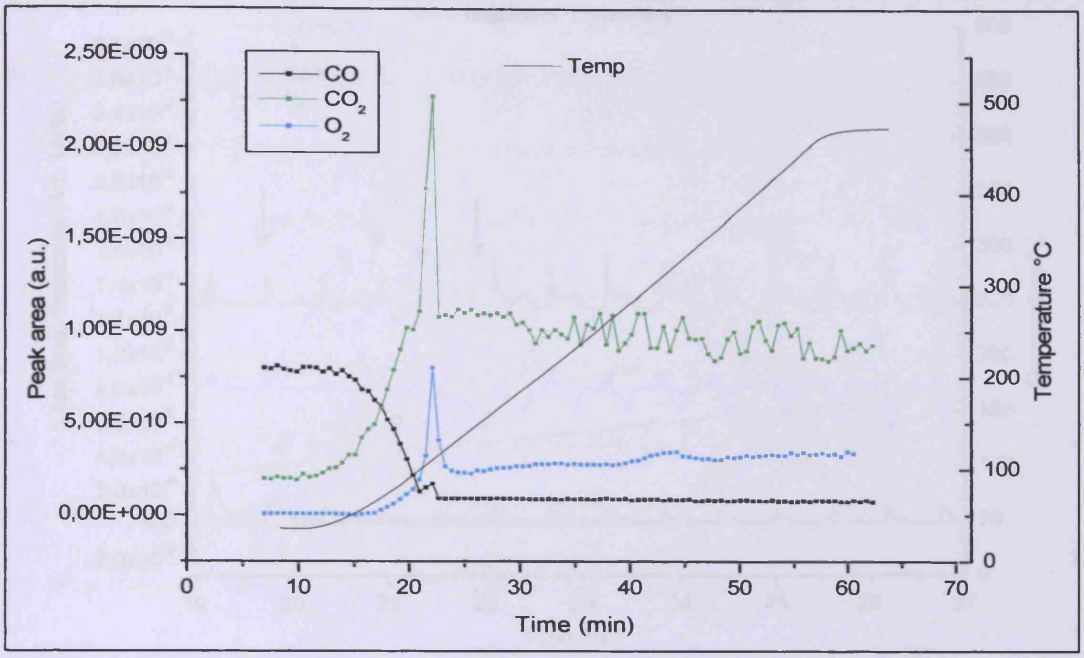

Figure 116: Peak areas of CO, CO_2 and O_2 calculated from the integrals of their spectrum peaks. The oxygen integral has been inversed for clarity. In this figure, the green plot correspond to CO_2 desorption, the black one to CO adsorption and the blue one to O_2 adsorption.

CO uptake started at ~13mins (48°C) and reached a maximum at 20.3mins (106.8°C) as seen in figure 116. The light off temperature (temperature of half reaction) was set as the temperature of half reaction for CO uptake and this method was used in every experiment.

The light off temperature for the oxidation reaction after reduction at 200°C was 63.5°C. The uptake of CO matched with the increase of CO_2 desorption. This evolution of CO and CO_2 can be assigned to the reaction between CO_g with O_s. This is a fast reaction that comes out as a sharp fast peak on the TPD spectra (shown by the black arrow in figure 117). Oxygen uptake started only when CO reached half conversion at 16mins (63.5°C) confirming the presence of oxygen at the surface of the metal particles.

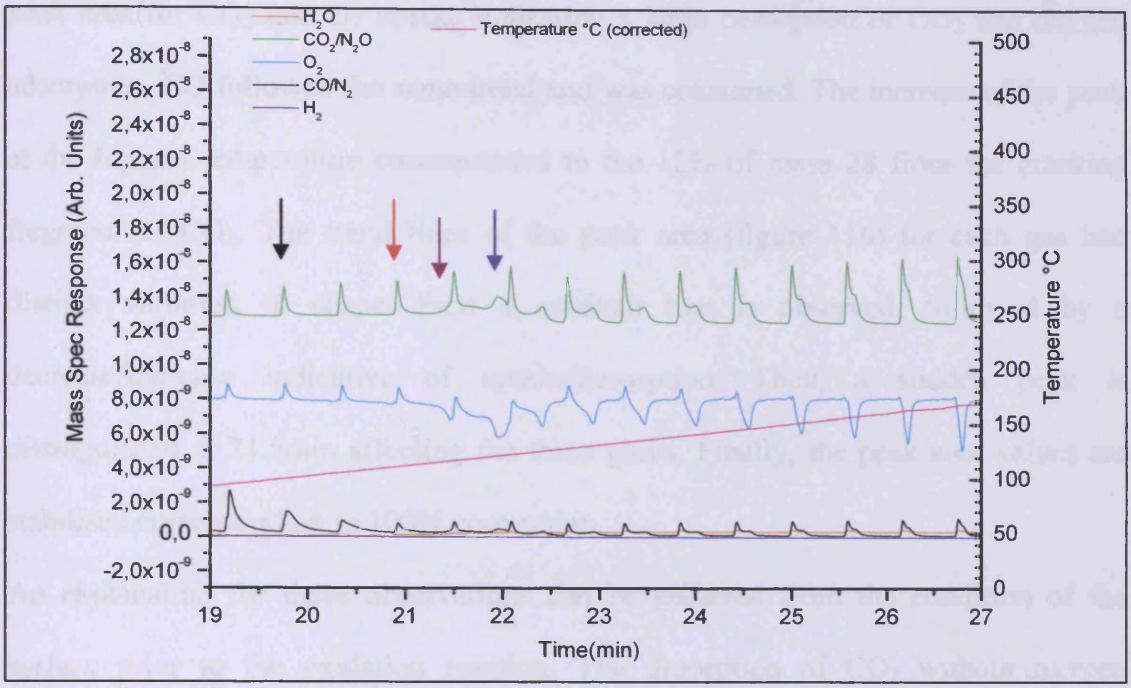

Figure 117: Zoom in figure 114 between 19 and 27 minutes. The back and the red arrows indicate the fast reaction. The purple one indicates the slow release.

On figure 117, CO_2 peaks evolved showing a sharp peak first (red arrow), followed by a slow release with an elevation of the baseline (purple arrow). A visible uptake of CO coincided with oxygen and CO_2 changes. As explained above, the sharp peaks are coming from the reaction between CO_g and O_s. The following slow uptake for oxygen and release for CO_2 could only be the result of a reaction between CO_s and O_2 which is a slow and difficult reaction. It is well known that CO_s blocks oxygen dissociation. At 21.5mins (106.5°C), the CO peak varied in shape and 2 peaks were detected for each pulse of gas injected: a sharp first peak followed by a lagged broad and small peak. Then, the time gap between the two peaks decreased at each pulse as the temperature increased until they merged into one peak. A similar pattern was observed for the formation of CO_2 starting at the same temperature. O_2 uptake followed a similar trend with an irregular uptake at the beginning of the reaction.

Looking at figure 116, the progress of the reaction was shown by the large increase of peak area for CO_2 and O_2 uptake indicating a large desorption of CO_2 and oxygen adsorption. CO followed the same trend and was consumed. The increase of the peak at the highest temperature corresponded to the 12% of mass 28 from the cracking fragment of CO_2. The trend lines of the peak area (figure 116) for each gas had distinct variation in shape. First a constant line is observed, followed by a decrease/increase indicative of uptake/desorption. Then, a sudden peak is distinguished at 21.5min affecting the three gases. Finally, the peak area values are stabilised corresponding to 100% conversion.

An explanation for these observations can be gathered from the condition of the surface prior to the oxidation reaction. The desorption of CO_2 without oxygen adsorption is explained by the slow reaction of the adsorbed O_s with the gas phase CO (figure 119a).

The temperature increases the speed of the surface reaction. As CO_2 desorbs, free sites become available for oxygen and CO to compete for from the gas phase. Peak areas evolution on figure 116 showed that CO was adsorbed first. CO_2 continued to desorb but without oxygen consumption. It means that CO adsorbs at the surface and reacts with dissociated oxygen already at the surface (figure 119).

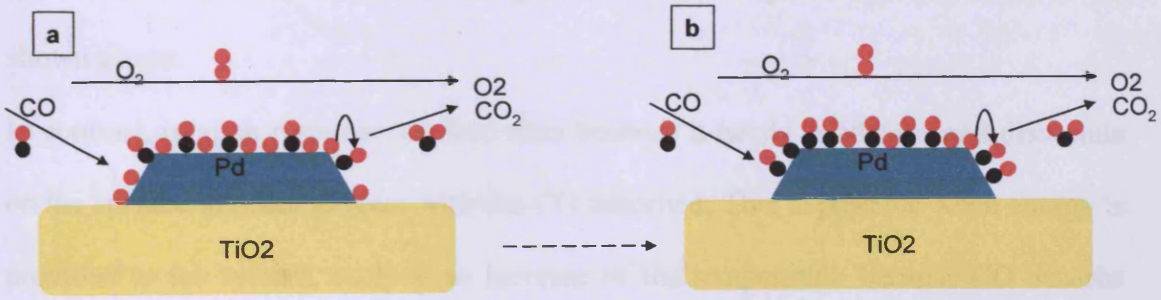

Figure 119: Schematic of CO oxidation reaction on Pd supported on TiO_2. The arrows represent the gas flow through the catalyst. (a) State of catalyst surface when CO start to be adsorbed. (b) State of the surface after CO adsorption and before oxygen uptake.

The surface progressively becomes covered with CO which partly reacts with dissociated oxygen. This reaction is fast which is seen as the fast peak as seen on the spectra of figure 117 (black arrow).

This fast reaction can be written as follow:

$$CO_{(g)} \rightarrow CO_{(s)}$$
$$CO_{(s)} + O_{(s)} \rightarrow CO_{2(s)}$$
$$CO_{2(s)} \rightarrow CO_{2(g)}$$

Oxygen uptake started at 70.4°C because CO previously blocked the surface sites. The surface is dominated (and poisoned) at low temperature by CO molecules and by oxygen atoms (not poisoned) at high temperature. Raising the temperature of the bed will decrease the poisoning of the surface by CO (CO desorption) and will allow the adsorption and dissociation of oxygen at the surface. The uptake of oxygen coincided with a change in the shape of the CO_2 peak (figure 117 shown by the red and blue arrows) from one sharp peak to one sharp and one lagged (shifted) broad peak.

Carbon monoxide adsorbs but does not dissociate on the surface due to its high internal bond strength (1076 kJ.mol^{-1}) while oxygen easily dissociates (500 kJ.mol^{-1}). It then requires little energy to produce CO_2 from the reaction between $CO_{(g)}$ with oxygen adsorbed at the surface and this appears as a fast and sharp peak on the spectrum (black and red arrow on figure 117). The steps of this fast reaction are shown above.

In contrast, oxygen requires two free sites because it needs to adsorbs and dissociate on the surface in order to react with the CO adsorbed. This is possible when energy is provided to the system, such as an increase of the temperature because CO desorbs and frees up sites. The reaction can be written as follow:

$$O_{2(g)} \rightarrow O_{2(s)}$$
$$O_{2(s)} \rightarrow O_{(s)} + O_{(s)}$$
$$CO_{(s)} + O_{(s)} \rightarrow CO_{2(s)}$$
$$CO_{2(s)} \rightarrow CO_{2(g)}$$

This reaction is slow and appears as the large peak (blue arrow) observed at 21.5mins on figure 117.

Finally, CO_2 formation, oxygen and CO consumption stabilised at 100% conversion until the ramp finished as seen in figure 116. At that stage only one fast sharp peak was arising for each pulse. What happened here is that as the temperature increased, all the $CO_{(s)}$ have reacted with $O_{2(g)}$ (slow reaction) and the CO has progressively free up sites (figure 120) while O atoms have covered the surface. This happened because CO desorbs with the increase in temperature. The free sites of the surface can now be occupied by dissociated oxygen that then reacts catalytically with the CO from the $CO+O_2$ gas phase.

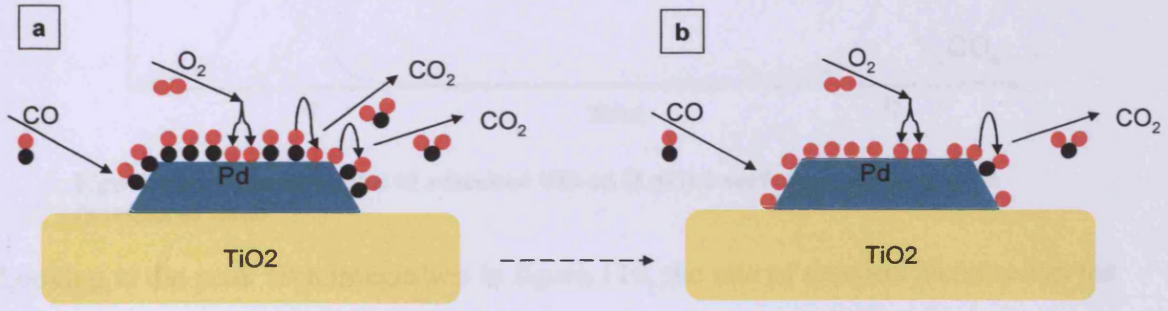

Figure 120: Schematic of CO oxidation reaction on Pd supported TiO_2. The arrows represent the gas flow through the catalyst bed. (a) State of the catalyst surface when both CO and O_2 react at the surface. (b) State of the catalyst surface at the end of the reaction.

The mechanism of CO oxidation on Pd has been definitively established by the work of Ertl [66]. The reaction occurs via the Langmuir-Hinshelwood scheme and the rate can be written as follow:

$$\text{Rate} = k[CO_a][O_a]$$

Where k is the rate constant, $[CO_a]$ and $[O_a]$ the concentration of adsorbed CO and O.

The rate constant, k, is dependent on the temperature and, for most reactions, it increases when the temperature is increased. Thus, the reaction rate will speed up when the temperature is raised. However, the speed of the reaction will be the highest when $[CO_a][O_a]$ is at a maximum. Therefore, looking at figure 121, it is evident that the CO_2 formation will reach a maximum at time t_1 and t_2, where $[CO_a]$ and $[O_a]$ are equal. At time $t<t_1$, $[CO_a]$ is lower than $[O_a]$ and is thus $CO_{(g)} \rightarrow CO_{(s)}$ is the limiting step of the reaction. At time time $t>t_1$, $[CO_a]$ is higher than $[O_a]$ and not enough dissociated oxygen atoms are present at the surface to react with adsorbed CO.

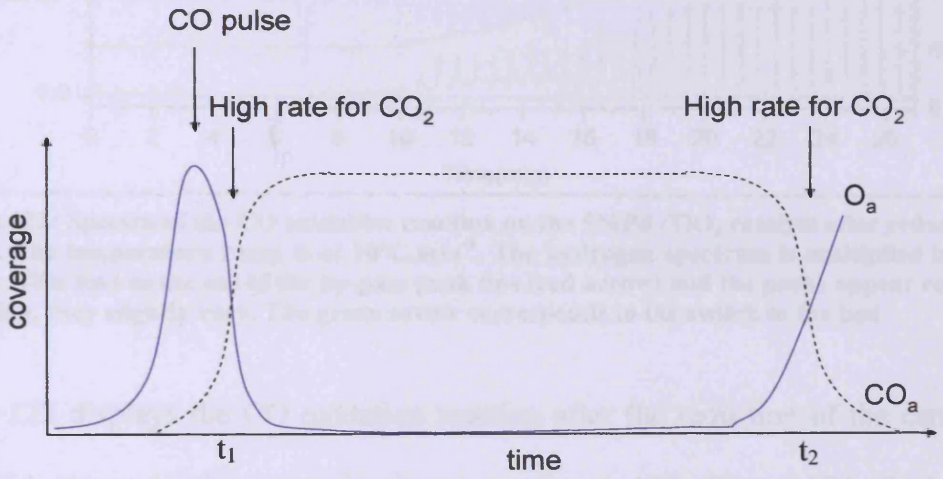

Figure 121: Schematic plot of adsorbed CO ad O at the surface of the metal as a function of time.

Looking at the peak area integration in figure 116, the rate of reaction increased as the temperature of the bed was raised. The reaction reached its maximum at 106°C when 100% conversion of CO into CO_2 was achieved.

Catalyst reduced at 400°C

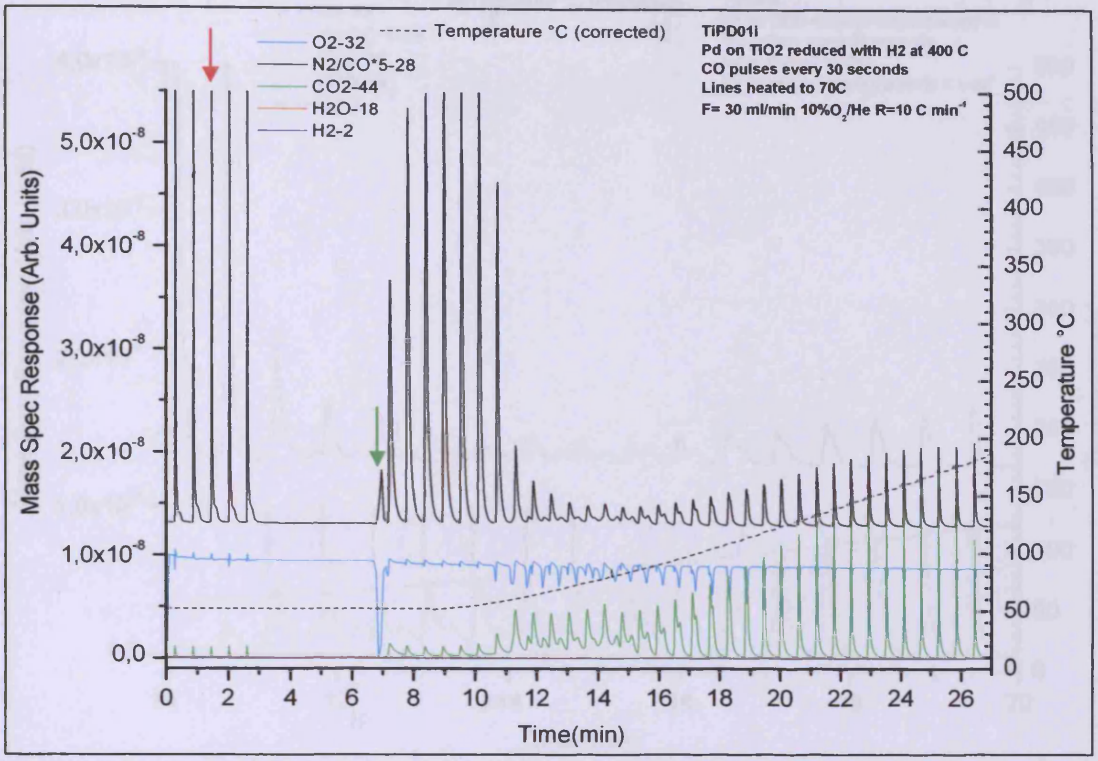

Figure 122: Spectra of the CO oxidation reaction on the 5%Pd /TiO_2 catalyst after reduction at 400°C. The temperature ramp is of 10°C.min^{-1}. The hydrogen spectrum is multiplied by 5 for clarity. This lead to the cut of the by-pass peak tips (red arrow) and the peaks appear constant. In reality, they slightly vary. The green arrow corresponds to the switch to the bed.

Figure 122 displays the CO oxidation reaction after the reduction of the catalyst at 400°C. A zoom in the graph is shown on figure 123. Figure 124 displays the evolution of the peak areas for each gas as a function of time and temperature.

A little CO reacted at room temperature showed by the reduction of the peak area of CO and the increase of CO_2 at 7mins (figure 124). This was followed by an immediate decrease of CO peak area, corresponding to CO uptake, as the temperature was increased. The light off temperature started much earlier than previously with a temperature shift from 63°C to 47.8°C. The catalyst reduced at 200°C showed the presence of a double peak of CO_2 at 117.7°C whereas the same feature appeared at 41.2°C for the catalyst reduced at 400°C. As before, the doublet consisted of a fast sharp peak and a lagged broad one.

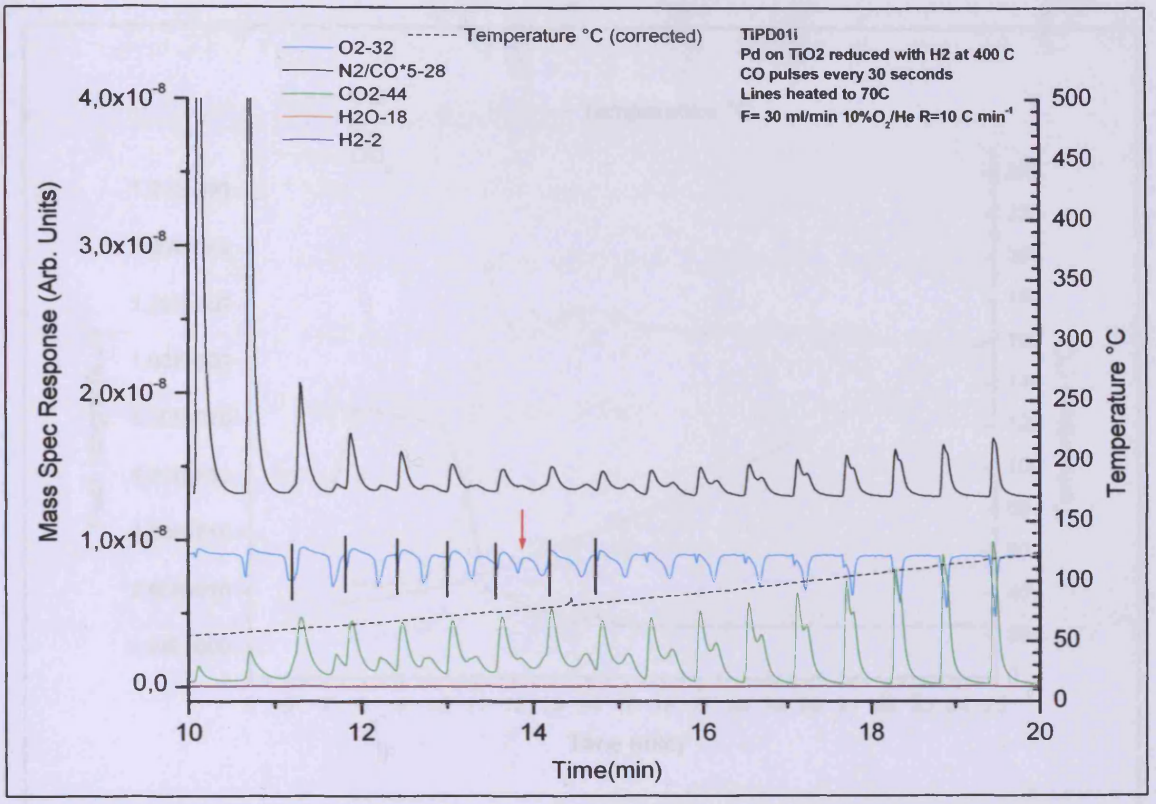

Figure 123: Zoom in spectra figure 87. The red arrow indicates the change from doublet to triplet state for CO_2 and O_2. The vertical black lines correspond to the areas chosen for integration. The black arrow shows the lagged peak at 14.6mins.

The oxygen showed a little triplet, arising from the broadening of the second peak into a doublet at 13.6mins (65.3°C) (shown by the red arrow).

From 13.6mins, the CO_2 peak still shows doublet state with a very small lagged peak that nearly combines with the first sharp peak. Interestingly, at the following pulse, 14.2mins (69.5°C) the lagged peak is then again well separated from the first one. It also corresponds to a small spike on the temperature plot as seen in figure 123. This little isolated change is probably due to an error in the measurement. Looking at the CO spectrum, the trend followed the same changes but on a much smaller scale.

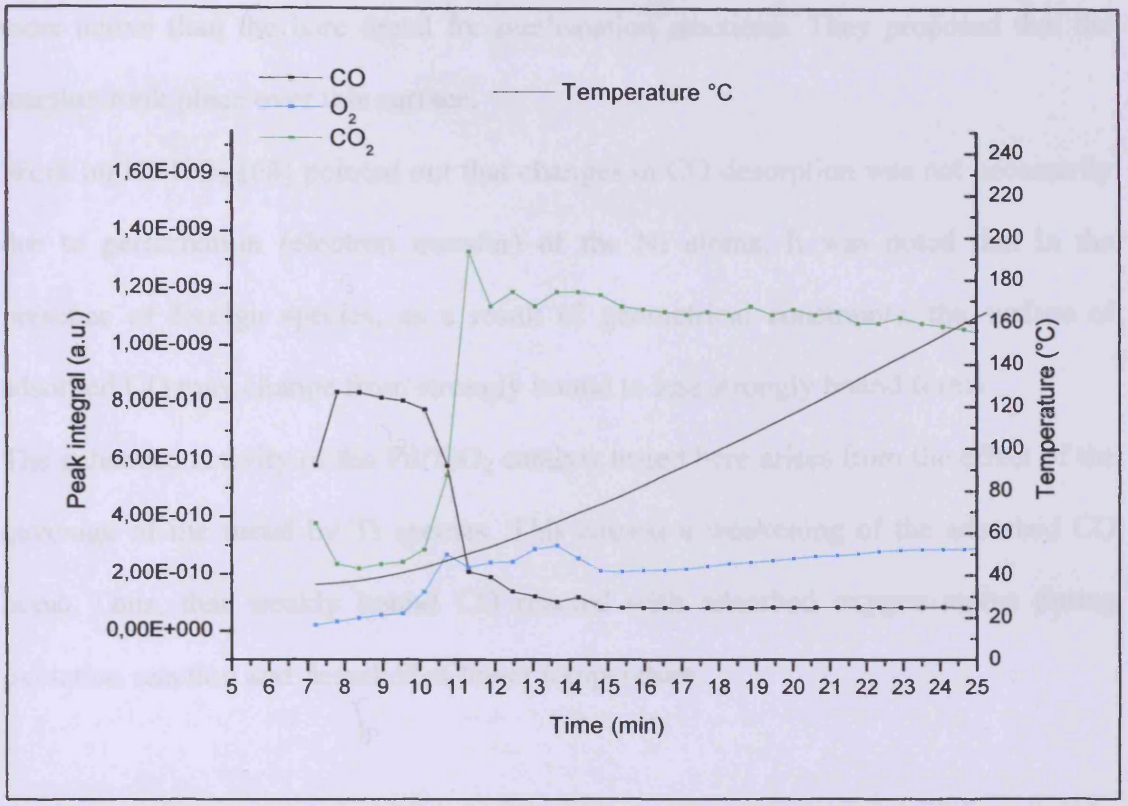

Figure 124: Peak areas of CO, CO_2 and O_2 (inversed) calculated from the integrals of their spectrum peaks. The data start when the gas flow is switched on the catalyst bed.

On figure 124, a larger amount of CO_2 is produced at 50.1°C. It corresponded also to an increase in oxygen uptake. A little CO is adsorbed at the beginning of the reaction and the reaction really starts at 10mins. 100% conversion is reached at ~11mins at a temperature of ~50°C.

The reduction of Pd/TiO_2 catalyst at 400°C did not lead to sintering of the Pd particles which generally occurs at higher temperatures (above 500°C). The possible explanation for the improvement of the catalytic activity of CO oxidation probably comes from changes of the surface structure. It was shown from the STM measurements that the Pd supported TiO_2 surface reconstructed upon annealing into various structures. The possible structure involved the migration of Ti on top of the Pd metallic layer. It was reported by Ko and Gorte [67] that Pt surfaces almost

completely covered (i.e. 95%) by thin layers of titanium oxide (TiO_x) were much more active than the bare metal for methanation reactions. They proposed that the reaction took place over this surface.

Work on Ni/TiO_2 [68] pointed out that changes in CO desorption was not necessarily due to perturbation (electron transfer) of the Ni atoms. It was noted that in the presence of foreign species, as a result of geometrical constraints, the surface of adsorbed CO may change from strongly bound to less strongly bound forms.

The enhanced activity of the Pd/TiO_2 catalyst tested here arises from the effect of the coverage of the metal by Ti species. This caused a weakening of the adsorbed CO bond. Thus, that weakly bound CO reacted with adsorbed oxygen atoms during oxidation reaction and desorbed at lower temperature.

Catalyst reduced at higher temperatures

The graph obtained after reduction at 500°C, 550°C and 600°C were also analysed in order to bring additional information regarding the adsorption sites, and the change of the surface. Figure 125 displays the CO oxidation reaction after reducing the catalyst at 500°C. Figure 126 displays a zoom of the spectra between 0 and 30mins.

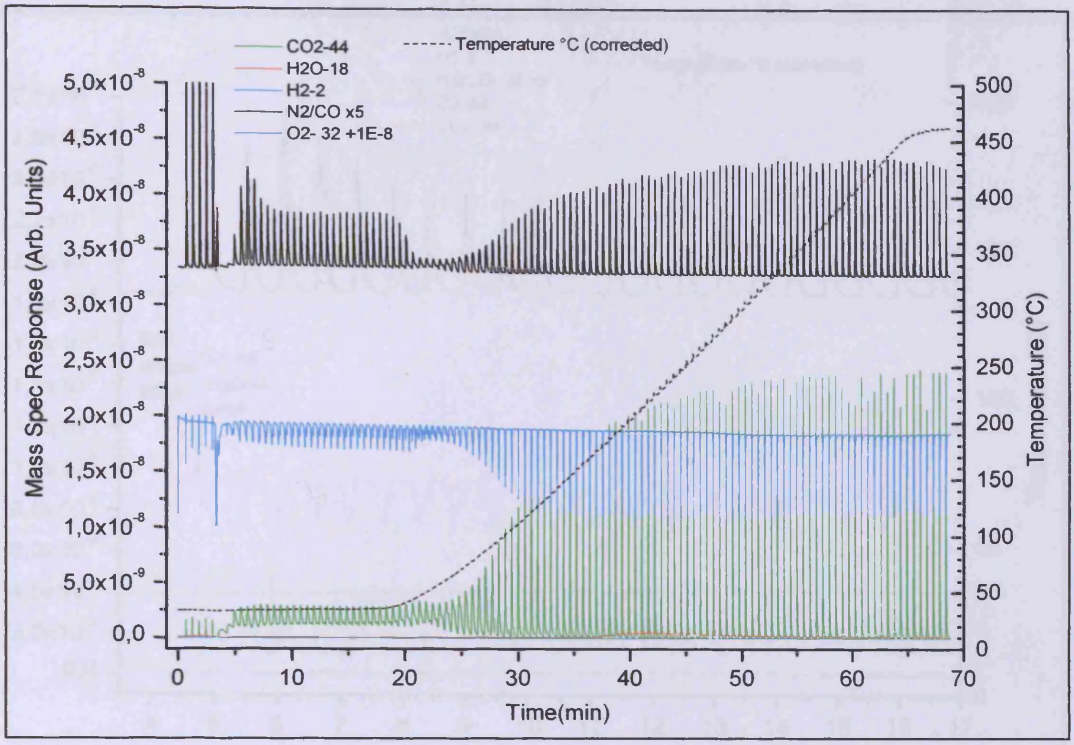

Figure 125: Spectra of the CO oxidation reaction on the 5%Pd /TiO_2 catalyst after reduction at 500°C. The temperature ramp is 10°C.min^{-1}. The hydrogen spectrum is multiplied by 5 for clarity. This lead to the cut of the by-pass peak tips and the peaks appear constant. In reality, they slightly vary.

As for the catalyst reduced at 400°C, as soon as the flow was switched to the bed, oxygen was consumed and CO_2 released indicating that the oxidation reaction started. This is shown on the first part of the spectrum, until 16mins.

The storage of CO started at room temperature (3.5mins) where about1.2ml of CO was adsorbed at the surface. From this adsorption, CO_2 was produced, showing a broad and slow peak that did not reach back the baseline. Looking at the oxygen uptake, 2 peaks were present immediately after the first pulse was flowed onto the bed (Figure 126: 3.7mins). For each pulse, a first sharp peak appeared followed by a broad lagged peak. The broad and lagged peak was slightly separated from the following pulse.

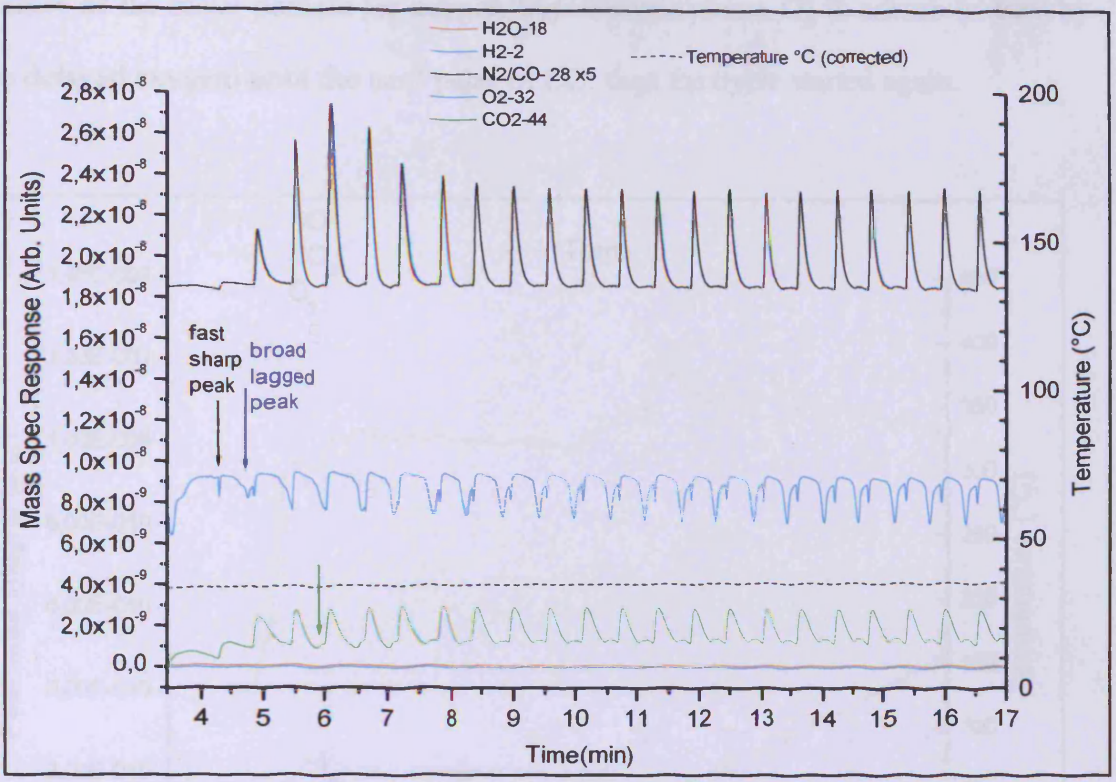

Figure 126: spectrum from 3 to 17 minutes.

At 5.4mins, some CO is coming through leading to an increase in the CO peak area (figure 127). A second peak (figure 126: green arrow) appeared in the CO_2 spectrum, lagged from the first one and merging with the next pulse. The lagged peak of O_2 followed the same trend.

At 6.6mins the CO uptake kept increasing and stabilised at 8.4mins (34.3°C). The peak areas on figure 127 showed clearly this evolution. O_2 also stabilised and showed 2 peaks on figure 126; one small sharp and a broad lagged peak. Respectively, CO_2 was produced as regularly, showing 2 broad peaks. Looking closely at each pulse, the oxygen uptake was delayed from the CO and CO_2 peaks. No oxygen was adsorbed when CO_2 was produced initially with the CO pulse. This implied that CO_g was reacting with O_s leading to desorption of CO_2. Free sites were then available at the

surface of the metal particle for oxygen from the gas phase, O_g to adsorb (shown by the delayed oxygen) until the next pulse of CO. then the cycle started again.

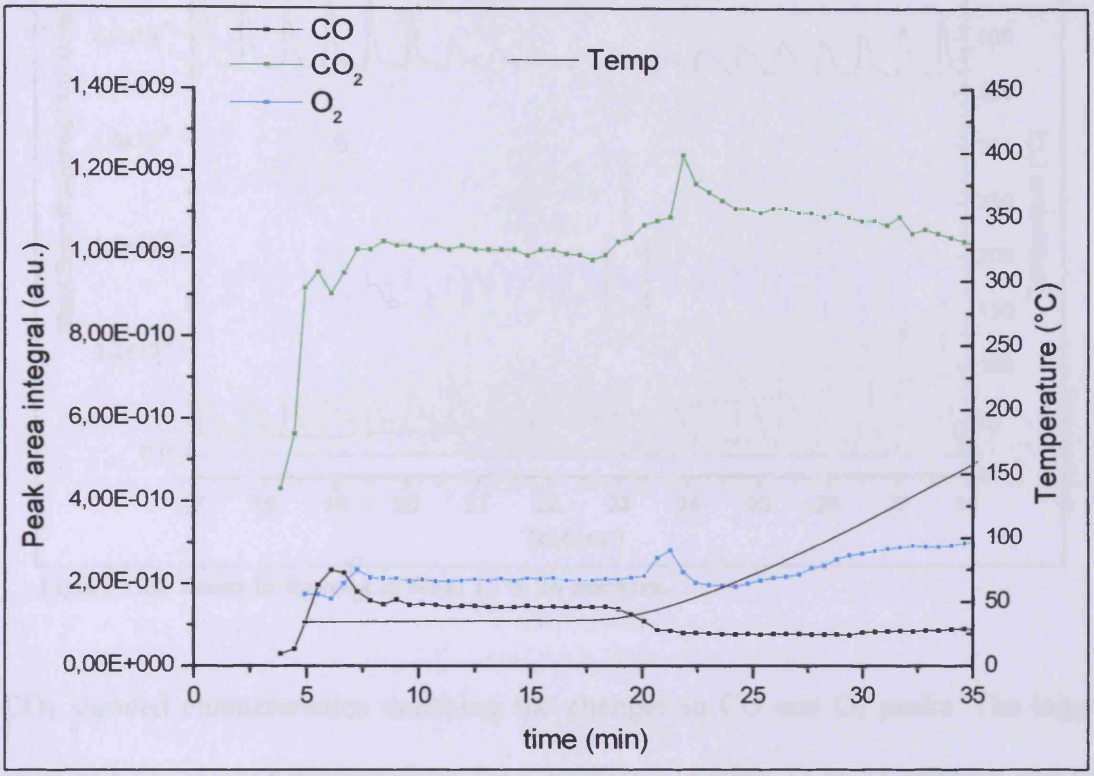

Figure 127: Peak area of CO, CO_2 and O_2 calculated from the integral of their spectrum peaks

As soon as the temperature increased, CO_2 formation increased and the CO peaks decreased until a constant minimum at 20.6mins (figure 128), this minimum being dictated by the cracking fragment of CO_2.

The sharp quick peaks of CO became broad and slow and a second lagged peak appeared on the spectrum. At the same time, O_2 showed a triple peak (figure 128, black arrow) with the third peak becoming more defined as the temperature increased. The appearance of this triplet coincided with the appearance of the lagged peak of CO.

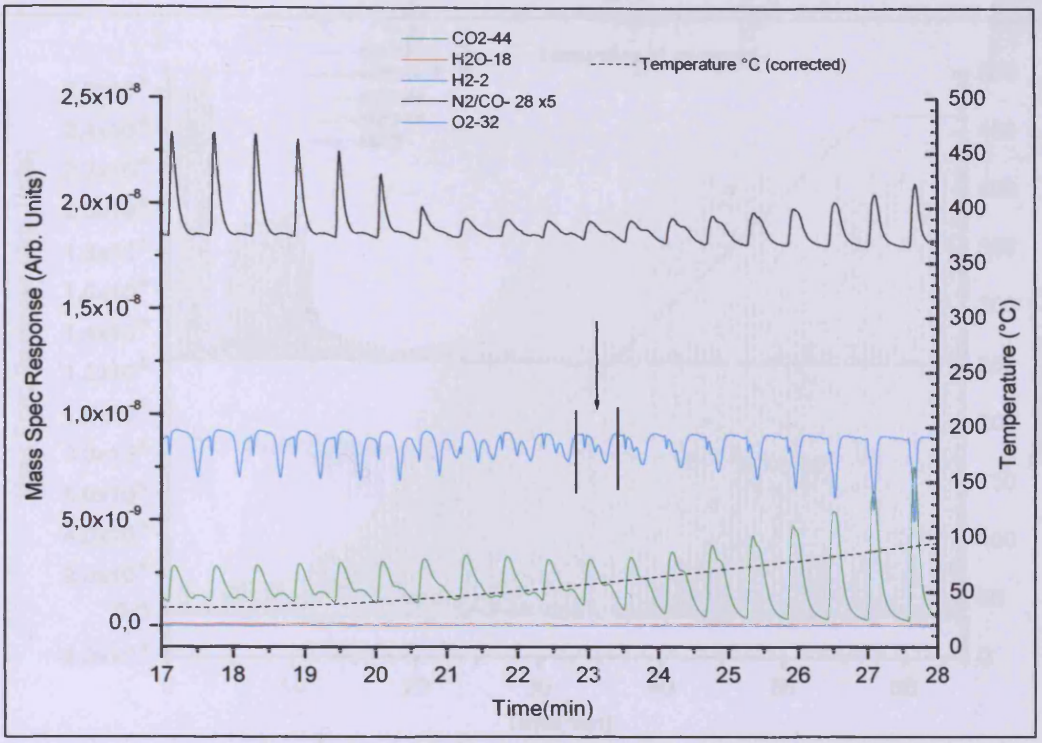

Figure 128: Zoom in figure 125 from 17 to 28 minutes.

CO_2 showed characteristics matching the changes in CO and O_2 peaks. The lagged peak of CO_2 merged progressively into the first one from 17 to 21 minutes and this during the uptake of CO. A new lagged peak appeared in the CO_2 spectrum at 22mins and the same feature was observed in the CO spectrum certainly due to the cracking fragment of CO_2. Finally, the peak shape for the three gases changed again before reaching a steady state. The CO_2 doublet merged and the same behaviour was observed for CO (cracking fragment) as well as O_2. Only one peak was detected for each pulse for every gas and they all coincided with each other at 27mins (180°C) due to the high rate of the reaction. The light off of the reaction was ~33°C, the reaction started as soon as the gas flow was switched to the bed.

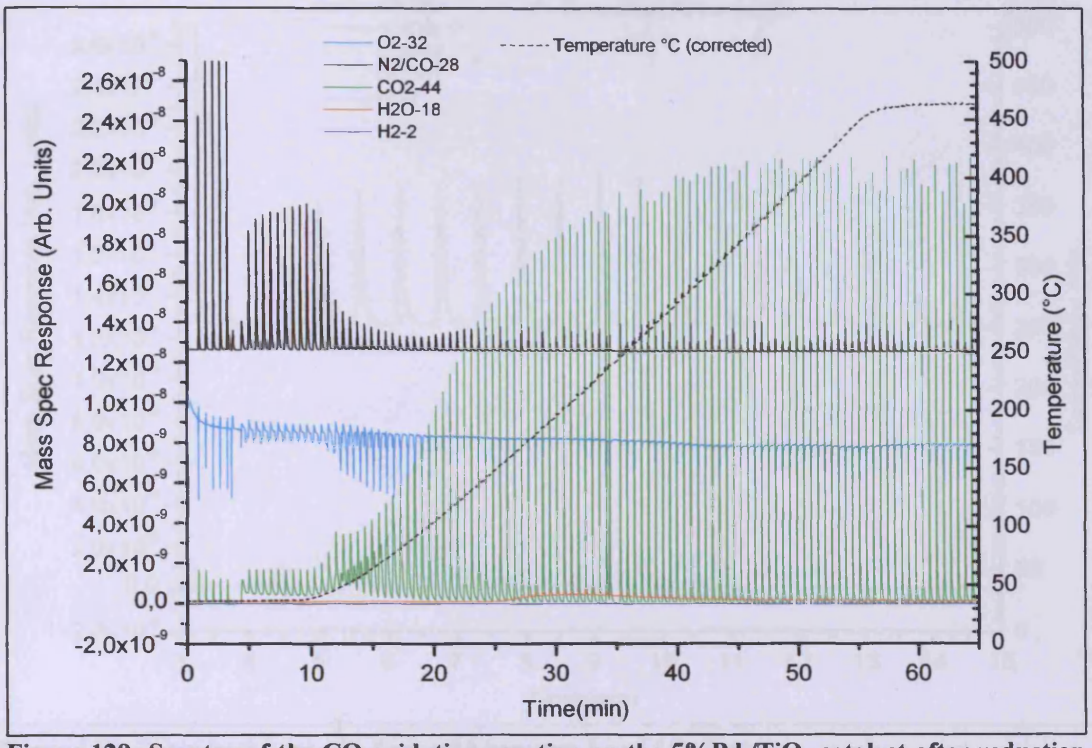

Figure 129: Spectra of the CO oxidation reaction on the 5%Pd /TiO_2 catalyst after reduction at 550°C. The temperature ramp is 10°C.min^{-1}. On the N_2/CO peaks, the by-pass peak tips are cut and the peaks appear constant because of the shift of the spectrum upward for clarity of the three spectra.

The reduction at 550°C led to more changes (figure 129). When the gas flow was switched to the bed, CO_2 was produced and O_2 was consumed at room temperature indicating the start of the reaction. A little CO was adsorbed but instantly returned into a large peak showing a similar behaviour to the catalyst reduced at 500°C. However, the integration of the CO peak showed that only 23% of the CO pulse put in was adsorbed. The calculation took into account the fraction of CO coming from the cracking fragment of CO_2. The oxygen peak shape was different from the previous reactions (figure 130). It consisted this time of a first sharp peak (when a pulse of CO was inserted) followed by a slight decrease of the baseline and then by a broad peak that merged with the peak of the next pulse.

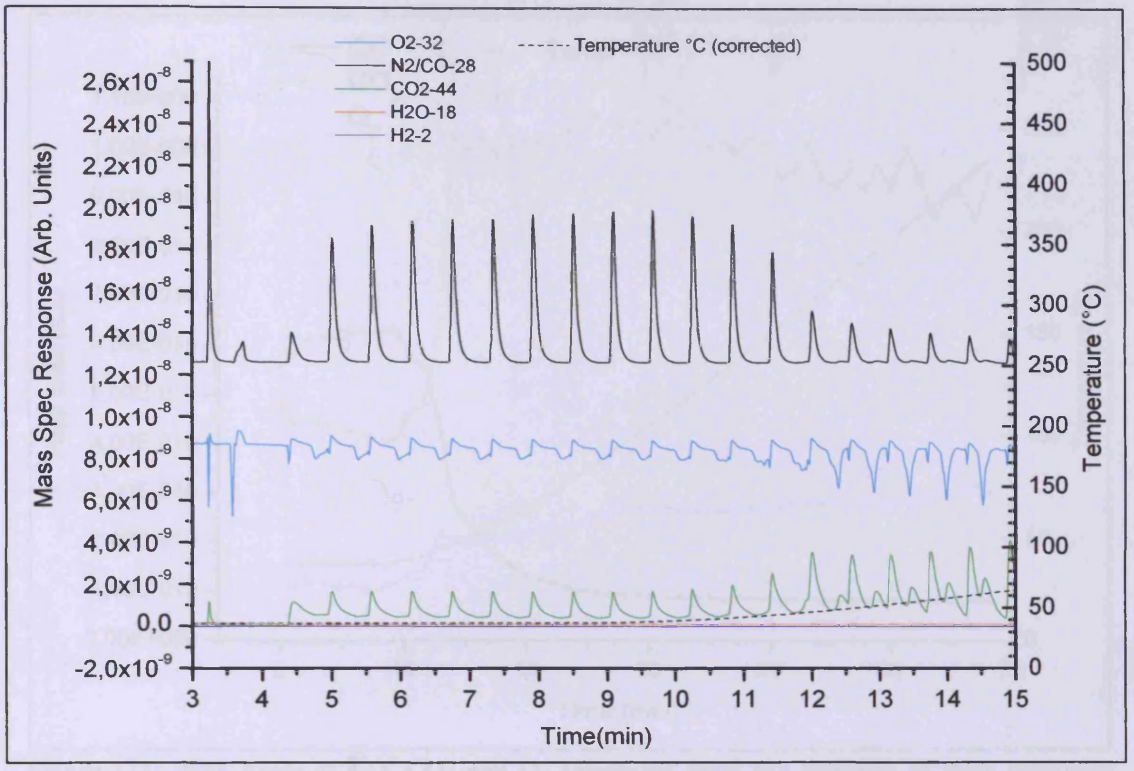

Figure 130: Zoom in the spectra figure 23 between 3 and 15minutes

This group of peaks evolved as the temperature increased. Between ~12 and 18mins, the shape of the lagged broad peak changed until it formed a sharp fast peak. The oxygen may have adsorbed at the surface on different sites and may account for the diverse shapes of oxygen peaks. From the integration of the peaks (figure 131), a significant amount of CO_2 was produced at 30°C and it looked like ~40% conversion. As the temperature increased, the behaviour was the same as for the previous reduction temperatures. Figure 131 shows the evolution of the peak areas of the 3 main gases. The reaction started at 37°C and half reaction was reached at 42°C which is nearly room temperature. While CO_2 reached a maximum, CO peak area kept decreasing until a minimum at 96°C.

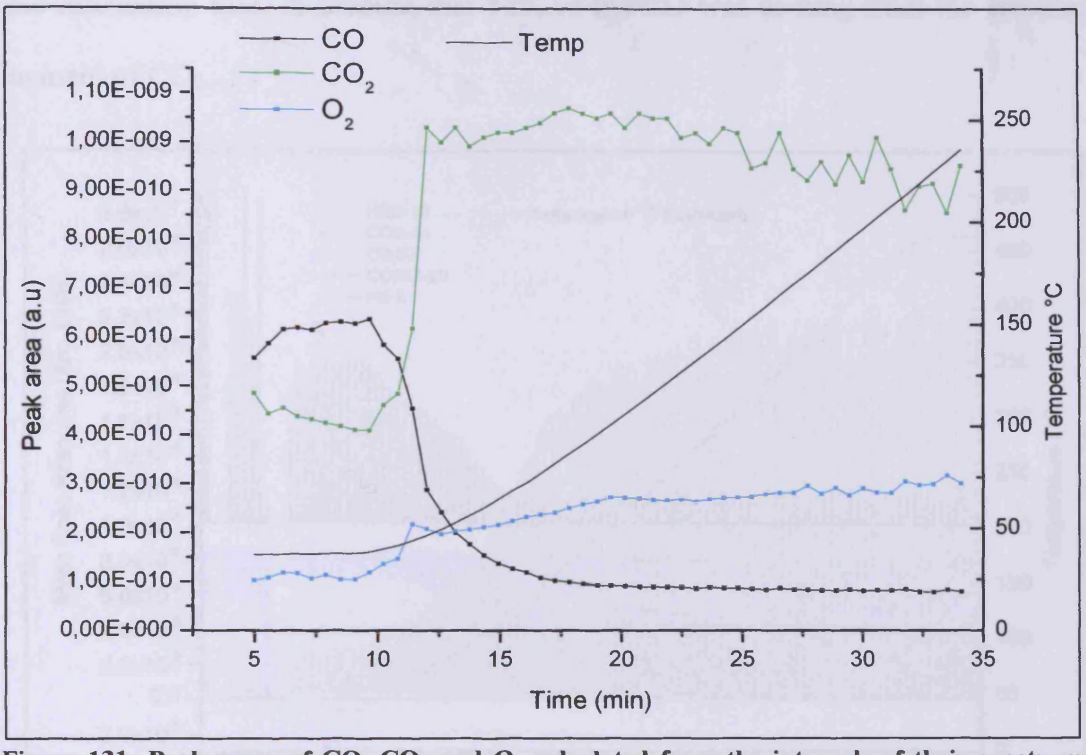

Figure 131: Peak areas of CO, CO_2 and O_2 calculated from the integrals of their spectrum peaks. After 30mins CO_2 peak area plot is not constant. This is due to changes in the data acquisition as explained previously.

Finally the catalyst was reduced at 600°C (figure 132). The same behaviour was observed as the catalyst reduced at 550°C. The half reaction is difficult to assess because the reaction started as the gases were flowed to the bed at a temperature of 36°C. This reaction is a bit faster than for the catalyst reduced at 550°C. The shapes of the peaks were slightly different (figure 133). Oxygen showed one sharp peak, when the pulse of CO was inserted on the bed, followed by a sharp lagged peak which merged into a single peak at ~22mins. CO_2 showed 2 peaks for each CO pulse starting as soon as the pulsed flow was switched to the bed. Similarly to oxygen, the doublet of CO_2 merged into a single sharp peak at ~22mins. CO was partially adsorbed at room temperature. From the integral of CO peaks over the by-pass and over the bed at room temperature, ~21% of the pulsed was adsorbed (figure 134).

This calculation took in account that 12% of the CO was coming from the cracking fragment of CO_2.

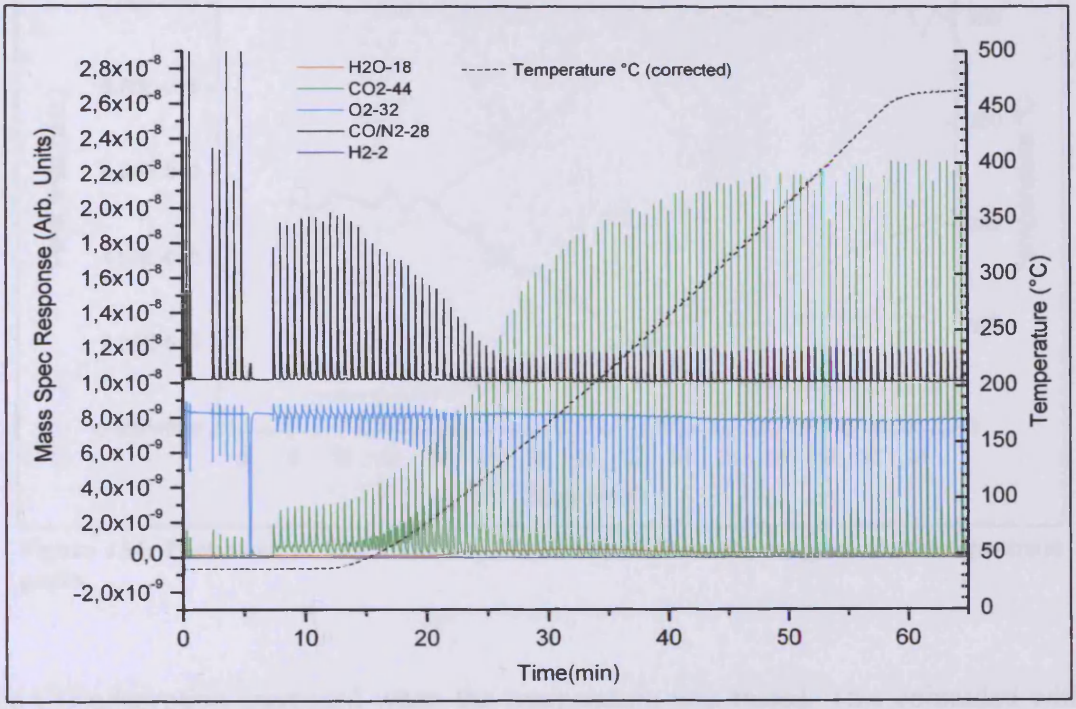

Figure 132: Spectra of the CO oxidation reaction on the 5%Pd /TiO_2 catalyst after reduction at 600°C. The temperature ramp is 10°C.min^{-1}.

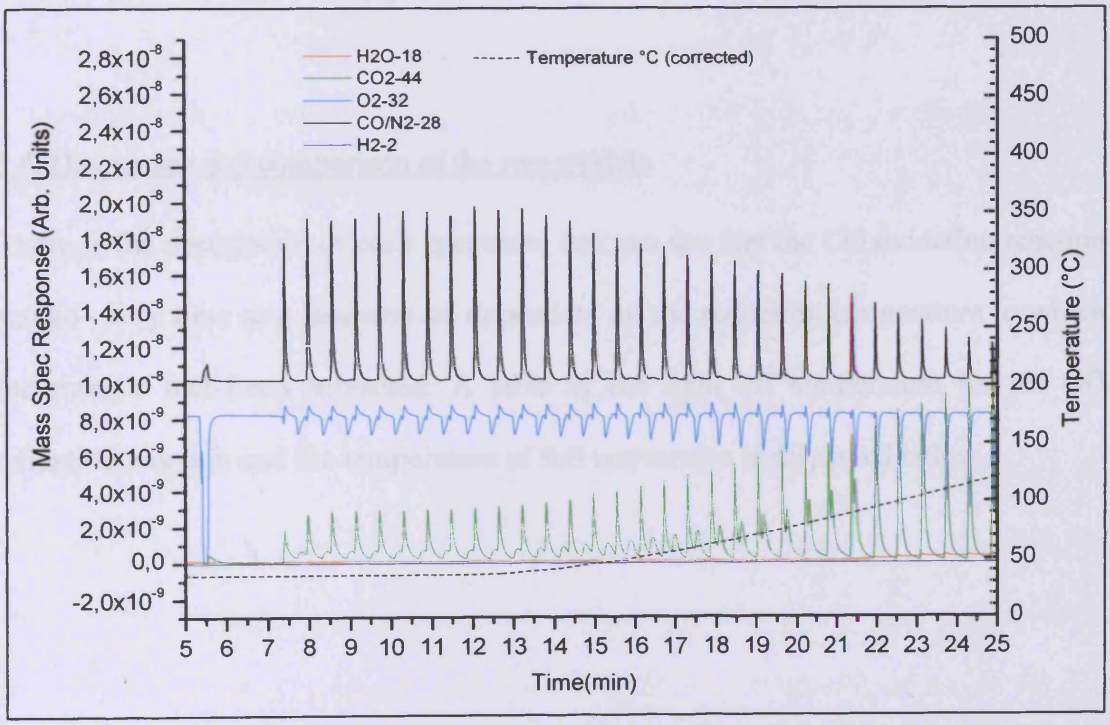

Figure 133: Zoom in the spectra in figure 132 from 5 to 25 minutes.

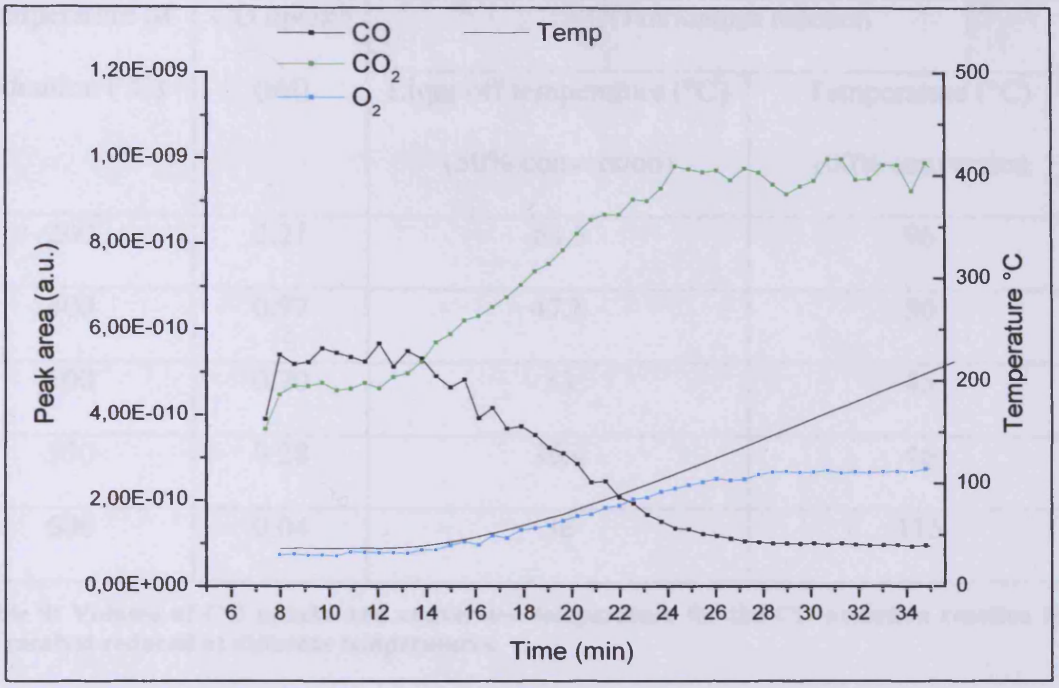

Figure 134: Peak area of CO, CO2 and O2calculated from the integral of their spectrum peaks.

The CO adsorption increased when the temperature was raised. This coincided with an increase in intensity of the peaks of CO_2 and a decrease in the peaks of O_2 until they merged into single sharp peaks. 100% conversion was reached at 115°C.

3.4. Discussion and comparison of the two models

Through the description of each spectrum, one can see that the CO oxidation reaction started every time at a temperature dependent on the reduction temperature to which the catalyst had been subjected. A table of the light off temperature for the CO oxidation reaction and the temperature of full conversion is displayed below.

Temperature of reduction (°C)	CO uptake (ml)	CO oxidation reaction	
		Light off temperature (°C) (50% conversion)	Temperature (°C) 100% conversion
200	2.21	63.5	96
400	0.97	47.8	50
500	0.70	33	45
550	0.28	36.4	46
600	0.04	36	115

Table 9: Volume of CO uptake and conversion temperature for the CO oxidation reaction for the catalyst reduced at different temperatures.

The observation of spectra showing doublets, usually under the form of a sharp and fast peak and a broad lagged one was one of the main feature common to all the spectra. The double peaks were interpreted by the fast reaction of CO_g with O_s for the first sharp peak; the second and broad peak is coming from the reaction between CO_s and O_{2g}. Once the reduction temperature had increased to 400°C, an important observation was the loss of CO uptake from 2mls to 0.97mls and the decrease of the light off temperature from 93.2°C to 47.8°C of the CO oxidation reaction. This phenomenon, explained earlier, was due to weakly bound CO adsorbed on the low-temperature reduced supported Pd. The weakening of the CO bond was due to the Pd surface disordering or steric effects caused by its partial decoration by reduced TiO_x species.The disordering of the metal surface led to the creation of new active centres. Those active centres consisted of defects that could bind to the CO molecules but with weak bond strengths. The more the surface was reduced, the more defects were present on the surface (oxygen vacancies for example). Further decrease in the CO uptake was observed after reducing the sample above 400°C and reduction at 600°C

suppress the CO adsorption property. This was probably due to the encapsulation of the Pd particles, the effect of the disordering of the metal surfaces but also to the sintering of the Pd particles. As seen in chapter 3, the bigger the particles, the bigger their specific surface area. However, the total surface area decreases when the radius of the particles increases. Thus, even less sites are available for CO adsorption. It also affected the CO oxidation reaction by shifting the 100% conversion temperature from 46°C (catalyst reduced at 550°C) to 115°C.

After reduction at high temperature (≥500°C), Pd supported on TiO_2 has undergone a change in the metal-support interface probably due to the SMSI effect. This effect has been assessed through observation of the CO chemisorption with reduction temperature and has been attributed to both electronic and geometrical effects (metal decoration) [44]. DRIFT characterisation indicated that CO oxidation on Pd/TiO_2 took place between the weakly bound CO and oxygen atoms on metallic Pd sites through the Langmuir-Hinshelwood mechanism [69], which was in agreement with the Kochubey and Pavlova work [51, 70, 71]. The DRIFTS indicated that CO adsorption on Pd/TiO_2 is weak at ambient temperature, especially after the reduction pre-treatment. This observation explains the decrease of the light off temperature which was observed after the different reduction treatments. The strength of the CO bond being weak at ambient temperature, the CO coverage was reduced leaving sites for O_2 dissociation and thus it was easy for the reaction to occur and for the CO_2 to desorb at low temperature. In a previous publication, the authors showed, from DRIFT and TPR studies, that the reduction of PdO over TiO_2 by CO is limited within the outermost layer at ambient temperature and the core PdO could be reduced further with the increase of temperature [41].

The appearance of small triple peaks for the catalysed reduced at 400, 500 and 550°C indicated changes in the surface uptake process. Reducing the surface to higher temperature led to changes of the surface structure, or created new defects sites for CO and O atoms to adsorb. It was observed that the defects could affect CO bonding strengths [70] and thus leading to changes in the distribution of adsorbed CO forms. This could explain why the peak shape would change on the spectrum at a specific temperature.

It was also observed on the LEED pattern of the model catalyst and also on the STM images that various structures had formed on the surface when it was annealed in vacuum from 600°C to 800°C. They were mainly hexagonal and wagonwheel like structures.

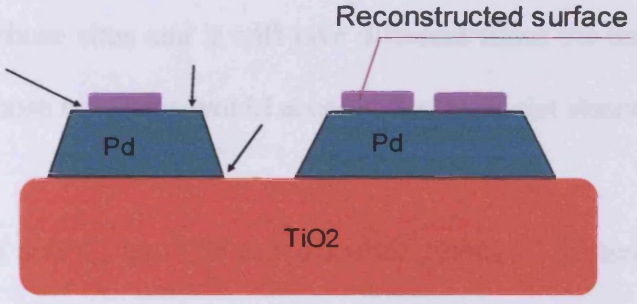

Figure 135: Schematic of the catalyst surface after reducing treatment. The palladium surface has reconstructed into a new layer. Less palladium is available but new sites are created for CO oxidation reaction. The arrows show the new reaction sites in addition to the palladium itself.

The formation of a wagonwheel structure at the surface may be responsible for the decrease of available Pd sites. However, as calculated earlier, there are still 1.75×10^{19} available sites after the reduction at 500°C. Those sites can be of different types: the palladium atoms, the Pd atoms at the interface with TiO_2, the reconstructed surface (figure 135) at the interface with Pd and the reconstructed surface itself. The reconstructed surface can take different form as seen on the STM images obtained

from the crystal surface. The wagonwheel possess various structures that were modelled in the section 3.2. A small wagonwheel structure of unit cell 9.5Å×9.5Å and a large wagonwheel one of unit cell ~17.5Å×17.5Å were obtained. This larger structure also showed some disordering and could have an effect on the reactivity of the surface. Another structure called "star shape" has a unit cell of ~25Å×25Å. An hexagonal structure of same unit cell as the wagonwheel was detected. This structure reacted when oxidation occurred on the surface and led to a disordered structure. Other parts of the surface, on the contrary, showed well defined structure after oxidation. Finally a zigzag structure was imaged on top of the surface of unit cell 8.1Å×6.3Å. Defect centres can also take part in the process: oxygen vacancies, kink, steps or adatoms. All those various sites would possess different properties and would interact with CO and O_2 more or less strongly. The CO oxidation reaction would therefore vary at those sites and it will take different times for the reaction to occur. The presence of those new sites would account for the triplet states as it was supposed above.

After annealing at 600°C, less CO was adsorbed (0.04ml). Sintering had occurred at the surface as indicated by the surface area. The BET measurements are shown in the table below.

Catalyst	Surface area ($m^2.g^{-1}$)
fresh 5%Pd/TiO_2	46
5%Pd/TiO_2 after reduction at 600°C	30

Table 10: BET measurements of the fresh and used catalyst.

Despite the smaller amount of available Pd sites, the CO oxidation still occurred with a low light off temperature (39°C). Some weakly bound CO is responsible for the

maintenance of the CO oxidation reaction. The reduced TiO_x species arising from reduction to higher temperature poison Pd sites and are responsible for the loss in CO uptake, results in weaker binding CO sites on Pd and high temperature treatment results in some limited sintering.

4. Conclusion

The structure and reactivity of palladium deposited on TiO_2 and the effect of reducing treatment has been studied in this chapter. The work was carried out on a single crystal of $TiO_2(110)$ and on a powdered Pd/TiO_2 catalyst. The aim of the work was to look at the SMSI effect on such system. The chapter started with the description of the titania surface and the SMSI effect in an introductory section through the account of various publications done on the subject.

The study of the clean $TiO_2(110)$ gave results that were in agreement with the various paper published previously. Clean $TiO_2(110)$ has a (1×1) termination that is stable and very close in size to the bulk termination (2.95Å×6.5Å). Annealing treatment led to a (1×2) reconstruction of the surface. The loss of oxygen during annealing is responsible for the reorganisation of the surface into its lowest energy state. Ca segregation occurs on the surface after long annealing treatment at high temperature. Ca is a common contaminant in bulk titania and diffuse through the bulk to the surface upon annealing. Ca tends to reconstruct on the surface into a $\begin{pmatrix} 6 & 0 \\ 3 & 1 \end{pmatrix}$ structure. The STM images were obtained after annealing at 700°C. The surface displayed superstructures with various unit cells. A hexagonal structure of unit cell ~9.5Å×9.5Å that was located on truncated triangular particles was first imaged. Those particles were sitting on top of a "star shape" structure of unit cell ~25Å×25Å. The hexagonal structure was reactive during oxidation treatment and Ti or Pd atoms

diffused on the top to form disordered clusters. The "star shape" structure, in contrary, did not react with the oxygen. Other superstructures were observed on other area of the surface: a large wagonwheel of unit cell ~17.5Å×17.5Å and a small wagonwheel of ~9.5Å×9.5Å unit cell. The small wagonwheel appeared first as 3 groups of 3 atoms forming an equilateral triangular structure of distance 9.5Å. Annealing to 800°C allowed this structure to reconstruct into a small wagonwheel structure of hexagonal unit cell.

The results from CO adsorption and CO oxidation reaction on the powdered catalyst showed that reduction pre-treatment affected the adsorption capacities of CO but improved the CO reaction by lowering the light off temperature from 93°C to 36°C after annealing at 200°C and 550°C respectively. It was shown that the decrease in CO uptake was probably due to the weakening of the CO sites on Pd. The disordering of the metal surface led to the creation of new centres and CO molecules could bind to those sites with different bond strength (depending on the type of the site). The loss of CO uptake was also due to the encapsulation of the Pd particles, the effect of the disordering of the metal surface but also the sintering of the Pd particles. The encapsulation of Pd was observed in the STM images where the reconstructed surface (that may be Ti atoms) was covering the palladium surface by one or more layers. The sintering process was studied in chapter 3 where the same system was used. It showed that the total surface area of the particles decreased as the particle radius increased (so when the annealing temperature increased). The decrease in the total surface area led to a decrease in the activity of the catalysts since less active sites were available for CO to adsorb and for the reaction to take place. This was also observed on the powdered catalyst, which had a lower surface area (BET measurements) and an increase in 100% conversion temperature (46°C after

annealing at 550°C and 115°C after annealing at 600°C). The reduction of CO was also due to the lowering in the strength of the CO bond, especially after reduction pre-treatment. This weak metal CO bond allowed CO oxidation at low temperature (room temperature in the case presented here) due to reduced self-poison of the surface. It was also exposed that, at room temperature, CO reduced only the outermost layer of PdO, an increase in temperature was necessary to reduce the core PdO and that Pd was only metallic on TiO_2 surfaces.

Weakly bound CO, reconstruction and encapsulation due to the SMSI effect seem to be the most important factors in the lost of CO adsorption and enhancement in the CO oxidation activity.

5. References

1. Henrich V.E. and Cox P.A., *The surface science of metal oxides.* Cambridge University Press, 1994.
2. Diebold U., *The surface science of titanium dioxide.* Surface Science Reports, 2003. **48**: p. 53-229.
3. Suzuki T. and Souda R., *The encapsulation of Pd by the supporting $TiO_2(110)$ surface induced by strong metal-support interactions.* Surface Science, 2000. **448**: p. 33-39.
4. Bennett R.A., Pang C.L., Perkins N., Smith R.D, Morrall P., Kvon R.I., and Bowker M., *Surface Structures in the SMSI State; Pd on (1×2) reconstructed $TiO_2(110)$.* Physical Chemistry B, 2002. **106**(18): p. 4688-4696.
5. Bennett R.A., Stone P., and Bowker M., *Pd nanoparticle enhanced re-oxidation of non-stoichiometric TiO_2: STM imaging of spillover and a new form of SMSI.* Catalysis Letters, 1999. **59**: p. 99-105.
6. Bennett R.A., Newton M.A., Smith R.D., Evans J. and Bowker M., *Titania surface structures for directed growth of metal nanoparticles via metal vapour deposition and metal organic chemical vapour deposition.* Material Science and Technology, 2002. **18**: p. 710-716.
7. Bennett R.A., Stone P. and Bowker M., *Scanning tunnelling microscopy studies of the reactivity of the $TiO_2(110)$ surface: Re-oxidation and the thermal treatment of metal nanoparticles.* Faraday Discussions, 1999. **114**: p. 267-277.
8. Bowker M., Stone P., Bennett R.A., Perkin N., *CO adsorption on a $Pd/TiO_2(110)$ model catalyst.* Surface Science, 2002. **497**: p. 155-165.

9. Bowker, M., Stone P., Bennett R.A., *Formic acid adsorption and decomposition on TiO_2(110) and on Pd/TiO_2(110) model catalysts.* Surface Science, 2002. **511**: p. 435-448.

10. Jak M.J.J., Konstapel C., Van Kreuningen A., Verhoeve J. and Frenken J.W.M., *Scanning tunnelling microscopy study of the growth of small palladium particles on TiO2(110).* Surface Science, 2000. **457**: p. 295-310.

11. Howard A., Mitchell C.E.J., and Edgell R.G., *Real time STM observation of Ostwald ripening of Pd nanoparticles on TiO_2(110) at elevated temperature.* Surface Science Letters, 2002. **515**: p. L504-L508.

12. Haller G.L. and Resasco D.E., *Metal support interactions group VIII: metals and reducible oxides.* Advanced catalysis, 1989. **36**: p. 173-235.

13. Dachille F., Simons P.Y., and Roy R., *Pressure-temperature studies of anatase, brookite, rutile and TiO_2-II.* American Mineralogy, 1968. **53**: p. 1929.

14. Smyth J.R., http://ruby.colorado.edu/~smyth/Home.html.

15. Li M., Hebenstreit W. and Diebold U., *The influence of the bulk reduction state on the surface structure and morphology of rutile TiO_2(110) single crystals.* Journal of physical chemistry B, 2000. **104**: p. 4944-4950.

16. Chung Y.W., Lo W.J. and Somorjai G.A., *Low energy electron diffraction and electron spectroscopy studies of the clean (110) and (100) titanium dioxide (rutile) crystal surfaces.* Surface Science, 1977. **64**: p. 588-602

17. Ramamoorthy M. and Vanderbilt D., *First-principle calculations of the energetics of stoichiometric TiO_2 surfaces.* Physical Review B, 1994. **49**(23): p. 16721-16727.

18. Kao C.C., Tsai S.C., Bahl M.K. and Chung Y.W, *Electronic properties, structure and temperature dependence composition of nickel deposited on rutile titanium dioxide (110) surfaces.* Surface Science, 1980. **95**: p. 1-14.

19. Asari E. and Souda R., *Atomic structure of TiO_2(110)-p(1x2) and p(1x3) surfaces studied by impact collision ion scattering spectroscopy.* Physical Review B, 1999. **60**(15): p. 10719-10722.

20. Sander M. and Engel T., *Atomic level structure of TiO_2(110) as a function of surface oxygen coverage.* Surface Science Letters, 1994. **302**: p. L263-L268.

21. Asari, E. and Souda R., *Atomic structures of TiO_2(110) surface between p(1x1) and p(1x2) studied by scanning tunneling microscopy.* Applied Surface Science, 2002. **193**: p. 70-76.

22. Bennett R.A., Stone P. Price N.J., Bowker M., *Two (1x2) reconstruction of TiO_2(110): surface rearrangement and reactivity studied using elevated temperatures scanning tunnelling microscopy.* Physical Review Letters, 1999. **82**(19): p. 3831-3834.

23. Pang C.L., Haycock A., Raza, H., Murray P.W., Thornton G., *Added row model of TiO_2 (110)1×2.* Physical Review B, 1998. **58**(3): p. 1586-1589.

24. Onishi H. and Iwasawa Y., *STM-imaging of formate intermediates adsorbed on a TiO_2(110) surface.* Chemical Physics Letters, 1994. **226**: p. 111-114.

25. Diebold U. and Hebenstreit W., *High Transient Mobility of Chlorine on TiO_2(110): Evidence for "Cannon-Ball" Trajectories of Hot Adsorbates.* Physical Review Letters, 1998. **81**(2): p. 405-408.

26. Diebold U., Anderson K.O.N. and Vanderbilt D., *Evidence for the tunnelling site on transition -metal oxides: TiO_2(110).* Physical Review Letters, 1996. **77**(7): p. 1322-1325.

27. Tasker P., *The stability of ionic crystal surfaces.* Journal of Physics: Condensed Matter, 1979. **12**: p. 4977-4884.

28. Lafemina J.P., Critical Review in Surface chemistry, 1994. **3**: p.297.

29. Møller P.J. and Wu M.-C., *Surface geometrical structure and incommensurate growth: ultrathin Cu films on TiO_2(110).* Surface Science, 1989. **224**(1-3): p. 265-276.

30. Szabo A. and Engel T., *Structural studies of TiO_2(110) using scanning tunnelling microscopy.* Surface Science, 1995. **329**(3): p. 241-254.

31. Murray P.W., Condon N.G., and Thornton G., *Effect of stoichiometry on the structure of TiO_2(110).* Physical Review B, 1995. **51**(16): p. 10989-10997.

32. Novak D., Garfunkel E. and Gustafsson T., *Scanning tunneling microscopy study of the atomic scale structure of TiO_2(110)-(1×1).* Physical Review B, 1994. **50**(7): p. 5000-5003.

33. Onishi H. and Iwasawa Y., *Reconstruction of the TiO_2(110) surface: STM study with atomic scale resolution.* Surface Science, 1994. **313**: p.L783-L789.

34. Ashino M., Uchihashi T., Yokoyama K., Morita S. and Ishikawa M., *STM and atomic resolution non-contact AFM of an oxygen-deficient TiO_2(110) surface.* Physical Review B, 2000. **61**(20): p. 13955-13959.

35. Bennett R.A., Poulston S., Stone P. and Bowker M., *STM and LEED observations of the surface structure of TiO_2(110) following crystallographic shear plane formation.* Physical Review B, 1999. **59**(15): p. 10341-10346.

36. Bennett R.A., *The re-oxidation of sub-stoichiometric TiO_2(110) surface in the presence of crystallographic shear planes.* Physical chemical Communication, 2000. **3**.

37. Gao W., Chen J., Guan X., Jin R., Zhang F. and Guan N., *Catalytic reduction of nitrite ions in drinking water over Pd–Cu/TiO_2 bimetallic catalyst.* Catalysis Today, 2004. **93-95**: p. 333-339.

38. Kim W.J. and Baer D.R., *Deactivation behaviour of a TiO_2-added Pd catalyst in acetylene hydrogenation.* Journal of Catalysis, 2004. **226**(1): p. 226-229.

39. Wang C.-B., Lee H.-G, Yeh T.-F, Hsu S.-N and Chu K.-S., *Thermal characterization of titania-modified alumina-supported palladium and catalytic properties for methane combustion.* Thermochemica Acta, 2003. **401**(2): p. 209-216.

40. Lin W., Zhu Y.X., Wu N.Z., Xie Y.C., Murwani I. and Kemnitz E., *Total oxidation of methane at low temperature over Pd/TiO_2/Al_2O_3: effects of the support and residual chlorine ions.* Applied Catalysis B: Environmental, 2004. **50**(1): p. 59-66.

41. Zhu H., Qin Z., Shan W., Shen W. and Wang J., *Pd/CeO_2–TiO_2 catalyst for CO oxidation at low temperature: a TPR study with H_2 and CO as reducing agents.* Journal of Catalysis, 2004. **225**(2): p. 267-277.

42. Macleod N., Cropley R. and Lambert R.M., *Efficient reduction of NO_x by H_2 under oxygen-rich conditions over Pd/TiO_2 catalysts: an in situ DRIFTS study.* Catalysis Letters, 2003. **86**(1-3): p. 69-75.

43. Bowker, M., et al., *Catalysis at the metal-support interface: exemplified by the photocatalytic reforming of methanol on Pd/TiO_2.* Journal of Catalysis, 2003. **217**(2): p. 427-433.

44. Tauster S.j., Fung S.C. and Garten R.L., *Strong metal-support interaction. Group 8 noble metals supported on TiO_2.* Journal of the American Chemical Society, 1978. **100**(1): p. 170-175.

45. Simoens A.J., Baker R.T.K., Dwyer D.J., Lund C.R.F. and Madon R.J., *A study of nickel-titanium oxide interaction.* Journal of Catalysis, 1984. **86**(2): p. 359-372.

46. Sadeghi H.R. and Henrich V.E., *SMSI in Rh/TiO_2 model catalysts: Evidence for oxide migration.* Journal of Catalysis, 1984. **87**(1): p. 279-282.

47. Tauster S.J., *Strong metal-support interactions.* Accounts of Chemical Research, 1987. **20**(11): p. 389-394.

48. Herrmann J.M., *Electronic effect in strong metal-support interactions on titania deposited metal catalysts.* Journal of Catalysis, 1984. **89**(2): p. 404-412.

49. Baker R.T.K., Prestridge E.B. and McVicker G.B., *The interaction of palladium with alumina and titanium oxide supports.* Journal of Catalysis, 1984. **89**: p. 422.

50. Sun Y.M., Belton B.N. and White J.M., *Characteristics of platinum thin films on titanium dioxide (110).* Journal of Physical Chemistry, 1986. **90**(21): p. 5178-5182.

51. Kochubey D.I., Pavlova S.N., Novgorodov B.N., Kryukova G.N. and Sadykov,V.A., *The influence of support on the low-temperature activity of Pd in the reaction of CO oxidation: 1- The structure of supported Pd.* Journal of catalysis, 1996. **161**(2): p. 500-506.

52. Van de Loosdrecht J., van der Kraan A.M., van Dillen A.J. and Geus J.W. *Metal-support interaction: titania-supported and silica-supported nickel catalysts.* Journal of Catalysis, 1997. **170**(2): p. 217-226.

53. Dulub O., Hebenstreit W. and Diebold U., *Imaging cluster surfaces with atomic resolution: The strong metal-support interaction state of Pt on $TiO_2(110)$.* Physical Review Letters, 2000. **84**(16): p. 3646-3649.

54. Boffa A.B., Galloway H.C., Jacobs P.W., Benítez J.J., Batteas J.D., Salmeron M., Bell A.T. and Somorjai G.A., *The growth and structure on titanium oxide films on Pt(111) investigated by LEED, XPS, ISS and STM.* Surface Science, 1995. **326**(1-2): p. 80-92.

55. Sedona F., Eusebio M., Rizzi G.A., Granozzi G., Ostermann D. and Schierbaum K, *Epitaxial TiO_2 nanoparticles on Pt(111): a structural study by photoelectron diffraction and scanning tunneling microscopy.* Physical Chemistry Chemical Physics, 2005. **7**(4): p. 697-702.

56. Lai X., Clair P.St., Valden M., Goodman D.W, *Scanning tunneling microscopy of metal clusters supported on TiO_2(110): morphology and electronic structure.* Progress in Surface Science, 1998. **59**(1-4): p. 25-52.

57. Jennison D.R., Dulub O., Hebenstreit W. and Diebold U., *Structure of an ultrathin TiO_x film, formed by the strong metal support interaction (SMSI), on Pt nanocrystals on TiO_2(110).* Surface Science, 2001. **492**(1-2): p. L677-687.

58. Jak M.J.J., Konstapel C., van Kreuningen A., Chrost J., Verhoeve J. and Frenken J. W. M., *the influence of substrate defects on the growth rate of palladium nanoparticles on a TiO_2 (110) surface.* Surface Science, 2001. **474**(1-3): p. 28-36.

59. Zhang, L., van Ek J. and Diebold U., *Highly ordered nanoscale surface alloy formed through Cr-induced Pt(111) reconstruction.* Physical Review B, 1998. **57**(8): p. R4285-R4288.

60. Fu Q., Wagner T., Olliges S. and Carstanjen H.-D, *Metal-oxide interfacial reactions: encapsulation of Pd on TiO_2(110).* Journal of Physical chemistry B, 2005. **109**: p. 944-951.

61. Zhang L.P., Li M., and Diebold U., *Characterisation of Ca impurity segregation on the TiO_2(110) surface.* Surface Science, 1998. **412/413**: p. 242-251.

62. Nörenberg H. and Harding J.H., *Ordered structures of calcium oxide on TiO_2(110) studied by STM and atomistic simulation.* Physical Review B, 1999. **59**(15): p. 9842-9845.

63. Nörenberg H. and Harding J.H., *Ca-induced surface reconstructions on TiO_2(110) studied by scanning tunneling microscopy, reflection high-energy electron diffraction and atomistic simulation.* Surface Science, 2001. **473**(1-2): p. 151-157.

64. Bikondoa O., Pang C.L., Muryn C.A., Daniels B.G., Ferrero S., Michelangeli E. and Thornton G.,*Ordered overlayers of Ca on TiO_2(110)-1×1.*Journal of Physical Chemistry B, 2004. **3108**: p. 16768-16771.

65. Stone P., Bennett R.A., Poulston S. and Bowker M., *Scanning tunnelling microscopy and Auger electron spectroscopy study of Pd on TiO_2(110).* Surface Science, 1999. **433-435**: p. 501-505.

66. Engel T., Ertl G., *Surface residence times and reactions mechanism in the catalytic oxidation of CO on Pd(111).* Chemical Physics Letters, 1978. **54**(1): p.95-98.

67. Ko C.S. and Gorte R.J., *A comparison of titania overlayer on Pt, Pd and Rh.* Surface Science, 1985. **161**(2-3): p.597-607.

68. Raupp G.B. and Dumesic J.A., *Effects of titania on the coadsorption of H_2 and CO on nickel surfaces: Consequences for understanding methanation over titania-supported nickel catalysts.* Journal of Catalysis, 1984. **96**(2): p.597-612.

69. Zhu H., Qin Z., Shan W., Shen W., Wang J., *Low-temperature oxidation of CO over Pd/CeO_2-TiO_2 catalysts with different pretreatments*. Journal of Catalysis, 2005. **233**(1): p.41-50.

70. Pavlova S.N., Sadykov V.A., Razdobarov V.A. and Paukshti E.A., *The influence of support on the low-temperature activity of Pd in the reaction of CO oxidation. 2- Adsorption properties and reactivity of adsorbed species.* Journal of catalysis, 1996. **161**(2): p.507-516.

71. Pavlova S.N., Sadykov V.A., Razdobarov V.A. and Paukshti E.A., *The influence of support on the low-temperature activity of Pd in the reaction of CO oxidation. 3- Kinetics and mechanism of the reaction.* Journal of catalysis, 1996. **161**(2): p.517-523.

Chapter 5

Conclusion

This thesis has focused on the nature of metals supported on a TiO_2 surface. Palladium and copper were deposited on a titania single crystal (model catalyst) and a powdered catalyst (real catalyst) composed of Pd nanoparticles on titania. The Metal Vapour Deposition (MVD) technique was used in the case of the crystal and the experiments were carried out in a UHV (Ultra High Vacuum) system consisting of an STM chamber with LEED/Auger equipment. The crystal studied was a TiO_2 surface cut in the 110 plane. The powdered catalyst was a TiO_2 P25 powder and was prepared by incipient wetness with palladium chloride.

The aim of the work was to look at catalyst phenomena from both a real and a model catalyst point of view. In chapter 1, the importance of such studies was highlighted. It indicated that surface science and catalysis were closely linked. In order to improve the efficiency of a catalyst, it is essential to understand how the molecules and atoms behave at the surface during the different catalytic steps. This is where surface science becomes essential providing the right tool to gain such information. The advantage of using single crystals is the limitation of variables. Single crystals are one plane surfaces with a limited number of well defined sites and a smaller surface area than powdered catalysts. The fundamental difference is usually the pressure at which experiments are carried out and thus the finite residence time of species at the surface. At high pressure, reactions take place that would not occur in UHV conditions but they may not be noticed by the analytical methods used in this environment. The study of surface science gives a restricted but optimised approach of heterogeneous catalysis. UHV is necessary in order to keep the surface of the crystal to analyse clean for a certain period of time.

Some of the fundamental properties of nanoparticles were examined from a mathematical point of view in chapter 3. An analysis of the geometrical aspects of monolayers and nanoparticles and the relation between particle spacing and size was given. It was established that for a fixed volume (V) of material deposited, the total surface area of particles (S_T)

decreased as the radius of the particle increased despite the fact that the area of one particle increased with its radius (r). The particle density was also found to be dependent on the coverage, θ; the lower the coverage, the lower the particle density. This makes sense since the volume was dependent on the coverage. The relation between particle spacing (R) and particle radius (r) was established. It was assumed that the particle were 3D hemispherical particles with same size and same surface arrangement (square) with a constant volume of material deposited and a constant area (A). The resulting equation stated that the interatomic distance increased as the radius increased and was dependent on coverage. At coverage $\theta = 1$, then ideally R=0 because all the particles are arranged over the surface in a square arrangement and are touching each other. At coverage $\theta > 1$, more than one layer of material is present at the surface. Thus, annealing will be needed for the radius of the particle to increase and to create space between the particles. For $\theta < 1$, then $R \neq 0$ for a minimum particle radius because the surface is only partially covered. So as Θ decreases, then R increases for the same particle radius.

Those equations were tested by analysing two materials, Cu/TiO_2 and Pd/TiO_2 both deposited by MVD. There are three main growth modes of thin film that are Volmer-Weber (3D island growth), Stranski-Krastanov (Monolayer followed by 3D particle) and Frank Van der Merwe (Monolayer by monolayer). Those modes can be distinguished by analysing the Auger spectra during deposition of a metal. STM imaging was used to confirm the Auger analysis. We showed from the Auger spectra analysis that both metals followed a VW growth mode at the surface. The STM images confirmed this growth mode since particles were imaged after deposition with the substrate still visible under the particle in the case of palladium deposition.

The sintering process was then studied for those two models. The interest in looking at this process is due to its diverse applications such as catalysis or semiconductor industry. The two

main sintering mechanisms are coalescence and Ostwald ripening. The analysis of STM images and PSD calculations showed that Cu sintered via coalescence where bigger particles grow at the expense of small particles. This process was not obvious from the STM images but the PSD plot showed a loss of small particles and an increase of larger ones as sintering occurred. The PSD calculations resulted in the formation of one group of large particles after sintering for the Pd particles, which is consistent also with the coalescence process. When comparing the data from the PSD and the images analysis with the equations set in the section 2 of chapter 3, the results were related to each others. From the PSD analysis, the surface area of a particle increased with its radius but the total surface area decreased. In the case of copper, the total surface area at room temperature was 4500nm^2 and 3900nm^2 after annealing at 650°C(in a total area of 10,000 nm^2). For palladium, the same phenomenon was observed while the total volume of material remained constant. Then, looking at the STM images in the case of Pd (the coverage of Cu was too high to see this), the interparticle distance (R) increased with the increase of particle radius.

Those observations showed the importance of the nature of the interface in the efficiency of a process. Sintering leads to a loss of activity due to the decrease in the total surface area and thus in the density of active sites. This is why it is important to understand the growth mode of active particles and their stability towards sintering. The longer the particle remains small and dispersed on the support, the longer the catalyst will remain active.

The last section of this chapter focused on the relevance of such studies to catalysis. For example, it revealed that parameters can be changed to alter the properties of a reaction through the alteration of its surface. Such parameters can be the alteration of surface free energy, promotion of the surface, the type of support and its surface area or size particles.

In chapter 4, the structure and reactivity of Pd/TiO_2 real and modelled catalyst was studied. An introduction was given that outlined the structure of TiO_2 and explained the SMSI effect

through the analysis of various publications. From the study of the $Pd/TiO_2(110)$ crystal system, it was found that various structures arose from the annealing treatment to temperature up to 800°C. This was confirmed by LEED analysis. The different structures showed unit cell distances varying from 2.75Å (for Pd(111)) to 25Å for the " star shape" structure. Other structures were present at the surface and were modelled. The different structures and models are shown below. The first model (figure 2) corresponds to the large wagonwheel structure which has a unit cell of ~17.5Å×17.5Å. It consists of 5 atoms triangles that lock to each other in a centrosymmetric configuration. Small triangular features of unit cell ~9.5Å×9.5Å are located top of this large wagonwheel and this is displayed on the model figure 4.

igure 1: (a) High resolution STM
nage 41.4Å×49.6Å.

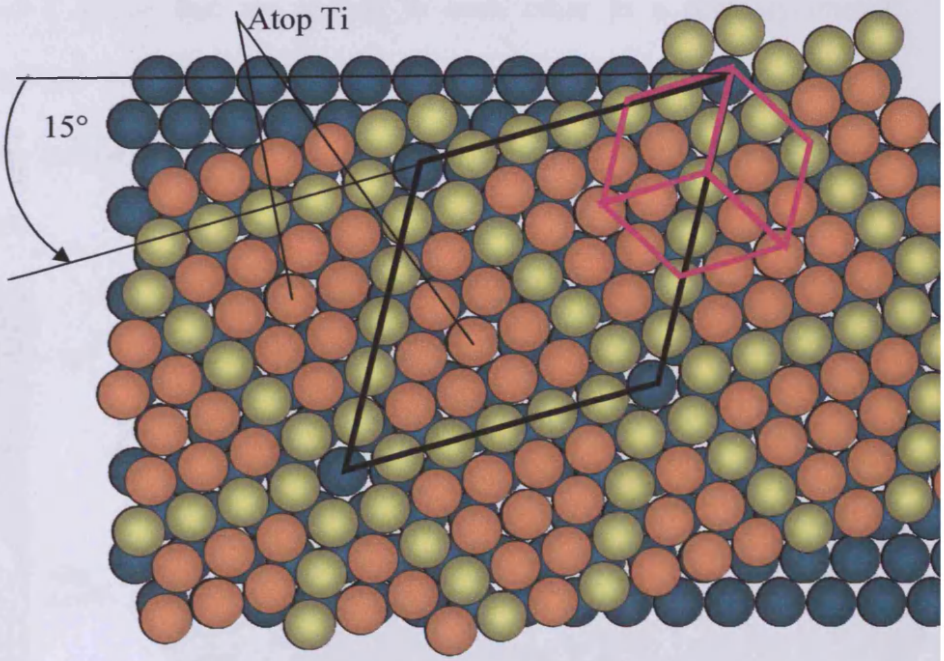

Figure 2: Model of the large pinwheel structure. The radius of covalen
1.36Å and the one for Pd is 1.31Å. This model is based on the assumptio
Ti is on the top of Pd atoms. The black parallelogram shows the wagon
unit cell. The magenta one corresponds to the unit cell determined c
LEED pattern.

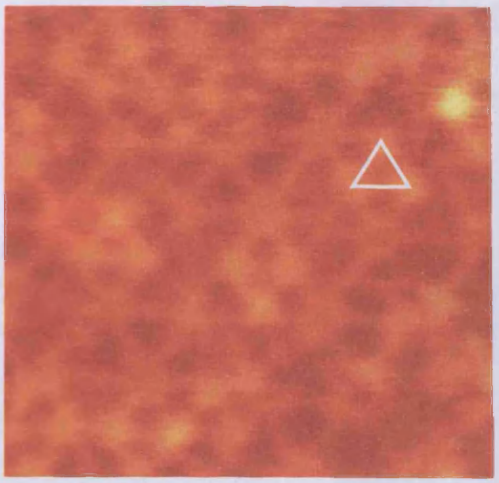

Figure 3: High resolution STM image (76.5Å×76.5Å) the triangular feature is represented by the dashed white rectangle.

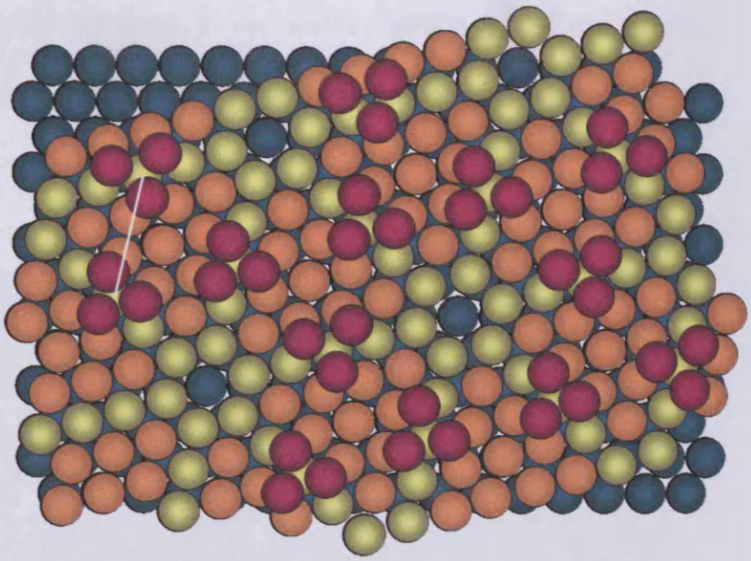

Figure 4: Schematic of the small wagonwheel structure. The purple circles represent the possible small triangle

The structure consists of 8 atoms that are locked to each other in a centrosymmetric configuration. It is rotated ~10° from the underlying Pd(111) that has a 2.75Å periodicity. If the structure is correct, the periodicity of the 8 atoms wagonwheel is ~2.8Å which could be possible for Pd or Ti atoms.

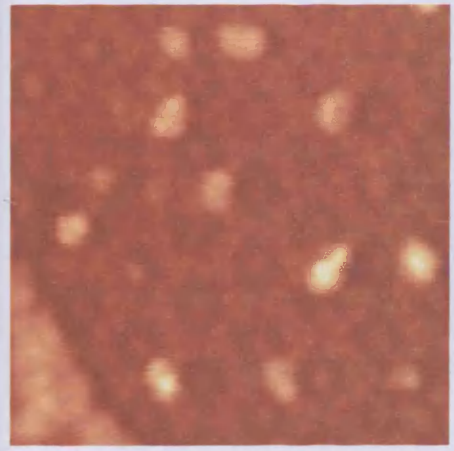

Figure 5: High resolution STM image (220Å×220Å) of the star shape structure.

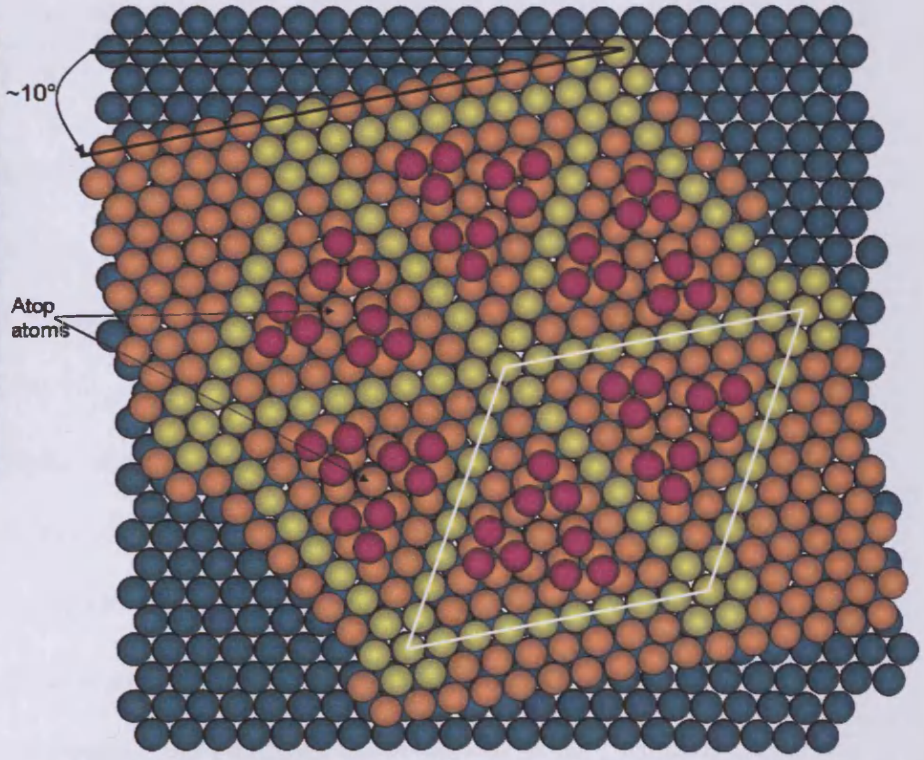

Figure 6: Schematic of the star shape structure. The unit cell is shown by the white parallelogram and measures 24.5Å if the atoms are titanium. The hubs of the star shape are atop atoms on Pd as well as the atoms shown by the arrows. The yellow atoms may be atop or 2-fold and the orange one, 3-fold or atop.

Annealing the surface to 800°C led to more changes in the surface structure and the model showed that the structure may well be an extension of the small triangle structure into a small wagonwheel structure.

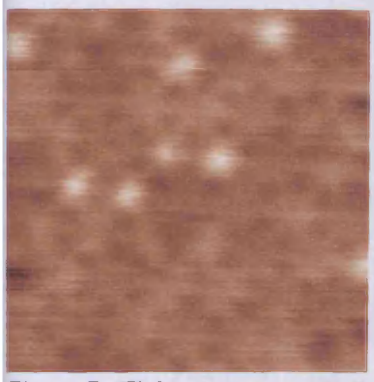

Figure 7: High resolution STM image of the small wagonwheel structure.

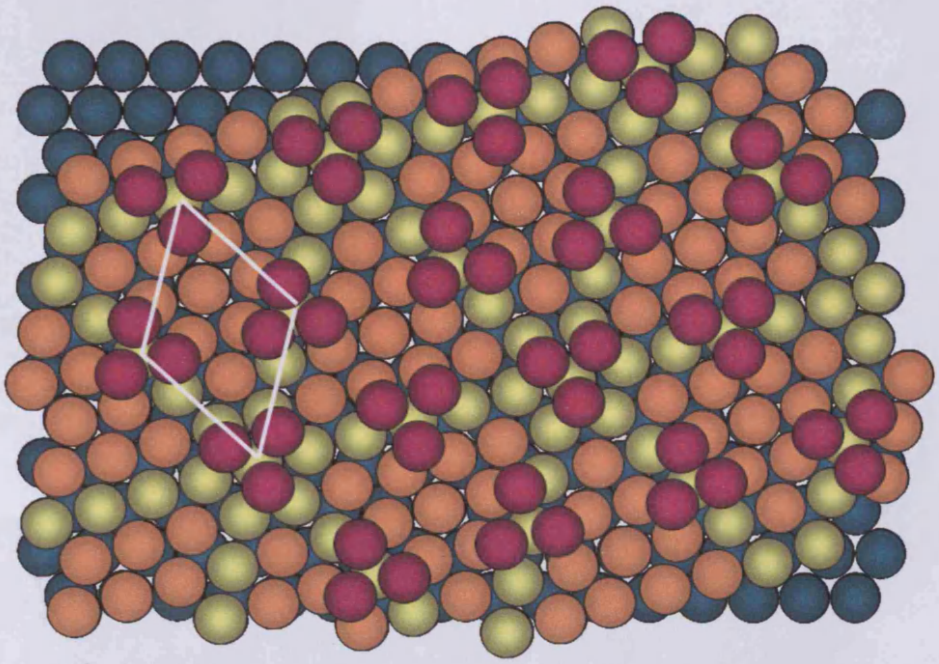

Figure 8 : Schematic of the hexagonal structure. The unit cell is shown by the white parallelogram and measures 9.5Å if the atoms are titanium. The yellow atoms may be atop or 2-fold, the orange one, 3-fold or atop and the purple ones are 3-fold.

The last structure to be observed was a zigzag structure of unit cell 8.1Å×6.3Å. This zigzag structure joined the small wagonwheel structure as shown in the model in figure 10.

From the model shown here, it was assumed that only Ti atoms were present on top of the Pd surface. The covalent radius of Ti and Pd being very similar, 1.36Å and 1.31Å respectively, then it is not possible, from the distance measurements, to differentiate the two elements. From the LDOS, the ground state electron configuration of Pd is $4d^{10}$ and Ti is $3d^2.4s^2$, thus at positive bias, the electron tunnelled from the tip to the empty state of the titanium atoms, that appeared as the bright features on the STM images. The dark area are possibly Ti 3-fold or Pd. They could be Pd atoms because the Pd atoms would appear as dark features at positive bias and would induce some distortion on the structure.

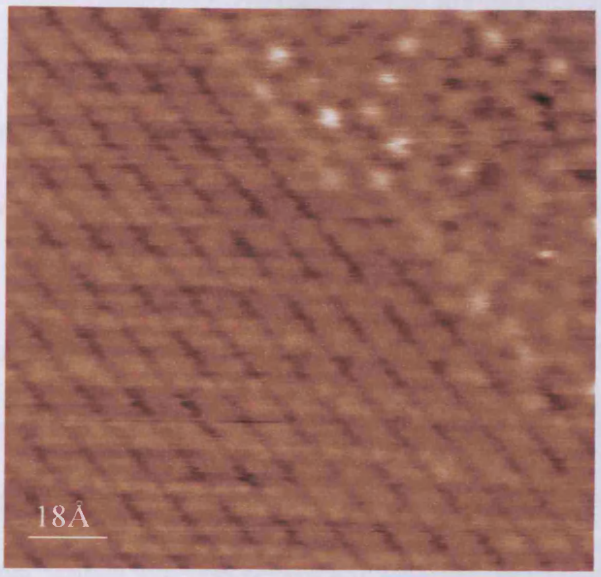

Figure 9: High resolution STM image of the zigzag and pinwheel structure. Parameters: 188Å×188Å.

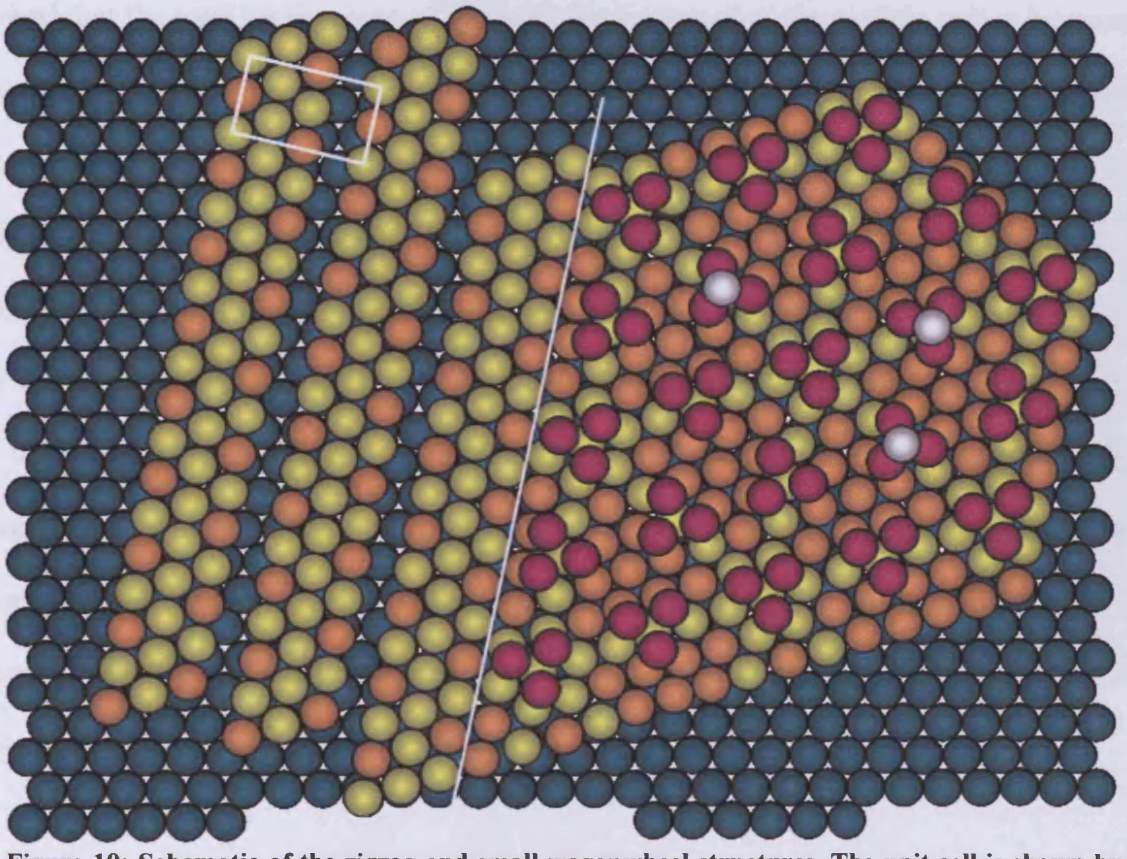

Figure 10: Schematic of the zigzag and small wagonwheel structures. The unit cell is shown by the white rectangle for the zigzag and measures 8.1Å×6.3Å. The yellow spheres may be atop or 2-fold and the orange one, 3-fold or atop. The pink ones are the 3-fold Ti atoms from the small wagonwheel structure and the white spheres are more Ti atoms that sit in a 3-fold position on the small wagonwheel.

The results from CO adsorption and CO oxidation reaction on the powdered catalyst showed that reduction pre-treatment affected the adsorption capacities of CO but improved the CO reaction by lowering the light off temperature of the reaction. It was assumed that the decrease in CO uptake was due to the partial decoration of the metal particles by TiO_x species. The disordering of the metal surface led to the creation of new active centres and CO molecules could bind to those sites with different bond strength.

The complete loss of CO uptake was due to the encapsulation of the Pd particles and also the sintering of the Pd particles (small effect). The encapsulation of Pd was observed in the STM images where the reconstructed surface was covering the palladium surface by one or more layers. The sintering process was studied in chapter 3 where the same system was used. It showed that the total surface area of the particles decreased as the particle radius increased (so when the annealing temperature increased). The decrease in the total surface area led to a decrease in the activity of the catalysts since less active sites were available for CO to adsorb and for the reaction to take place. This was also observed on the powdered catalyst, which had a lower surface area and an increase in the temperature for 100% conversion. The reduction of CO was also due to the lowering in the strength of the CO bond, especially after reduction pre-treatment. This weak metal CO bond allowed CO oxidation at lower temperatures. It was reported that, at room temperature, CO reduced only the outermost layer of PdO, an increase in temperature was necessary to reduce the core PdO. Weakly bound CO, reconstruction and encapsulation due to the SMSI effect seem to be the most important factors in the loss of CO adsorption and enhancement in the CO oxidation activity.